Université Fédérale

Toulouse Midi-Pyrénées

THÈSE

En vue de l'obtention du

DOCTORAT DE L'UNIVERSITÉ DE TOULOUSE

Délivré par :

Institut Supérieur de l'Aéronautique et de l'Espace

Présentée et soutenue par :
Laura Victoria ROLANDI
le lundi 13 décembre 2021

Titre :

Stabilité des écoulements compressibles à bas nombre de Reynolds

Stability of low Reynolds number compressible flows

École doctorale et discipline ou spécialité :
ED MEGeP : Dynamique des fluides

Unité de recherche :
Équipe d'accueil ISAE-ONERA EDyF

Directeur(s) de Thèse :

M. Laurent JOLY (directeur de thèse)
M. Thierry JARDIN (co-directeur de thèse)

Jury :
M. Jean-Christophe ROBINET Professeur ENSAM - Président
Mme Stefania CHERUBINI Professeure associée École polytechnique de Bari - Examinatrice
M. David FABRE Maître de conférences Université Paul Sabatier - Examinateur
M. Thierry JARDIN Ingénieur de recherche ISAE-SUPAERO - Co-directeur de thèse
M. Laurent JOLY Professeur ISAE-SUPAERO - Directeur de thèse
M. Kunihiko TAIRA Professeur Université de Californie Los Angeles - Rapporteur

Acknowledgements

It is with great emotion that I write this page, thanking the people who, during these years, have been close to me and have contributed to the realization of this thesis, carried out within the Department of Aerodynamics, Energetics and Propulsion of the Institut Supérieur de l'Aéronautique et de l'Espace (ISAE-SUPAERO).

First of all, I would like to thank my supervisors, Thierry, Jérôme and Jérémie, for their trust. Thank you for having been there for me sharing the beautiful and motivating moments, but also the difficult ones that a thesis can go through. I thank my thesis director, Laurent, for his advices, sometimes harsh, but right. I can see how much it was for my own good.

Many thanks to Professors K. Taira and J.-C. Robinet for having accepted to review my work and for their enriching comments and I also extend my gratitude to Dr. D. Fabre and Dr. S. Cherubini for having taken part of my jury.

These years would not have been the same without the friends, rather than colleagues, I found at DAEP. In particular I would like to thank my "original ones", Ramzi, Miguel, Jéromine, Gonzalo and Radouan who have welcomed me into the 118 office and made me feel part of the group from the very first moment. "Les TàRéS" Alessio, Massyl and Maxime, and also Manu, Francesco, Sam, Romain, Marta M., Claudia, Pietro, Ekhi, Sandrine and Ludo. Thank you for the support, the exchanges, and the everyday laughter. It is not obvious to find an environment like the one I found here three years ago, and that we have and continue to honor as a very strong group.
To my friends Narjes and Mina, thank you for your kindness and the magical thread that binds us.

Grazie alla mia famiglia per avermi incoraggiato, in particolare a mia sorella, Cristina, su cui ho sempre potuto contare e che mi ha ispirato fin da quando ero solo una bambina. Ai miei amici di tutti i giorni Luca, Michele e Alessandro, grazie infinitamente, perché la quotidianità insieme a voi é stata fantastica e con voi mi sono sempre sentita a casa. Gabriele, abbiamo vissuto questo periodo storico unico l'uno affianco all'altra e abbiamo passato momenti che ci hanno messo alla prova, ti ringrazio con tutto il cuore per l'aiuto, l'affetto e il ricordo indelebile di questi anni insieme. Marta, abbiamo condiviso questa esperienza fin dall'inizio e non avrei potuto sperare in un'amicizia più vera, completa e rassicurante di quella che ho trovato in te fin dal primo giorno, un grazie non basterà mai.

Thanks to you all, I have grown not only as a scientist, but also as a person. I come out of these years much stronger and prouder than I could have ever imagined.

Victoria
Toulouse, le 13/12/2021.

Abstract

The aim of this work is to investigate the compressibility effects on the wake dynamics of the circular cylinder and the NACA0012 airfoil at low Reynolds numbers. In particular, the focus is made on the primary and secondary instabilities that are responsible for the flow transition from a stationary two-dimensional state to an unsteady three-dimensional one. In order to perform the stability analysis, a global modal stability code is developed based on Krylov–Schur algorithm with a time-stepping approach.

In the first part, we focus on the NACA0012 airfoil primary instability, which develops on the stationary solution and yields the nonlinear development of a two-dimensional unsteady wake. This unsteady flow is characterized using Direct Numerical Simulations at different Reynolds numbers $Re \in [200; 1000]$ for various angles of attack $\alpha \in [0°; 20°]$, while the steady base flow used for the stability analysis is obtained using the Selective Frequency Damping (SFD) technique. The influence of both the angle of attack and the Reynolds number on the characteristics of the most amplified mode is first investigated in the incompressible regime, revealing in both cases a non-monotonic evolution of the perturbation growth rate, with a maximum at a given value of α and Re. Then, the compressibility effects in the low-subsonic regime are considered, with Mach numbers up to $M_\infty = 0.5$. Compressibility is observed to increase or decrease the mode growth rate with respect to its incompressible value depending on the angle of attack and the Reynolds number. For $\alpha < 20°$, compressibility has a destabilizing effect close to the critical threshold, which results in an earlier Hopf bifurcation, while increasing the Mach number always results in a decrease of the growth rate of the mode well above the critical threshold. Finally, the mode frequency decreases with the Mach number.

The second part is devoted to the three-dimensional secondary instabilities that arise on the two-dimensional unsteady wake. In this case, the base flow used for the stability analysis is the two-dimensional periodic solution calculated using Direct Numerical Simulations without resorting to the SFD technique. The three-dimensionalization of the circular cylinder through the development of mode A and mode B instabilities is investigated for Reynolds numbers up to $Re = 350$. Compressibility is found to have a stabilizing effect on both the modes close to the critical thresholds, delaying the 3D transition, without modifying the transverse wavelengths at which the flow becomes unstable. Conversely, above the critical threshold, compressibility has a stabilizing effect only on mode B, while the range of critical wavelengths of mode A shifts toward lower values. Compressibility effects on the secondary instability of the unsteady wake of the NACA0012 airfoil at angle of attack $\alpha = 20°$ are also considered.

Résumé

L'objectif de ce travail est d'étudier l'influence de la compressibilité sur la dynamique du sillage du cylindre circulaire et du profil NACA0012, à faibles nombres de Reynolds. L'attention est portée en particulier sur le développement des instabilités primaires et secondaires à l'origine de la transition de l'écoulement d'un état bidimensionnel stationnaire vers un état tridimensionnel instationnaire. Le développement d'un code basé sur l'algorithme de Krylov–Schur combiné à une approche itérative en temps est réalisé pour conduire l'analyse de stabilité modale globale.

La première partie est focalisée sur l'instabilité primaire à l'origine de la bifurcation du sillage du profil NACA0012 d'un état bidimensionnel stationnaire vers un état bidimensionnel instationnaire. Cet écoulement instationnaire est caractérisé à l'aide de simulations numériques directes pour différents nombres de Reynolds $Re \in [200; 1000]$ et pour différents angles d'incidence $\alpha \in [0°; 20°]$. L'écoulement de base stationnaire nécessaire à l'analyse de stabilité est obtenu à l'aide de la technique de Selective Frequency Damping (SFD). L'influence de l'angle d'incidence et du nombre de Reynolds sur les caractéristiques du mode le plus amplifié est d'abord étudiée dans le régime incompressible, révélant dans les deux cas une évolution non-monotone du taux de croissance dont le maximum est atteint pour un α et Re donné. L'influence de la compressibilité est ensuite explorée en régime compressible pour des nombres de Mach jusqu'à $M_\infty = 0.5$. Celle-ci produit un effet stabilisant ou déstabilisant sur le mode qui dépend de l'angle d'incidence et du nombre de Reynolds. Pour $\alpha < 20°$, la compressibilité a un effet déstabilisant près du seuil critique, qui se traduit par une bifurcation de Hopf plus précoce, tandis que l'augmentation du nombre de Mach entraîne toujours une diminution du taux de croissance du mode lorsqu'on s'éloigne du seuil critique. Enfin, la fréquence du mode diminue avec le nombre de Mach.

La deuxième partie est consacrée aux instabilités secondaires tridimensionnelles qui se développent dans le sillage bidimensionnel instationnaire. Dans ce cas, l'analyse de stabilité est conduite sur un écoulement de base instationnaire obtenu par des simulations numériques directes sans la SFD. Le développement des modes A et B responsables de la transition du cylindre circulaire vers un état tridimensionnel est d'abord étudié pour des nombres de Reynolds jusqu'à $Re = 350$. La compressibilité a un effet stabilisant sur les deux modes à proximité des seuils critiques, retardant le processus de tridimensionnalisation, mais ne modifie pas les longueurs d'onde des modes instables. En revanche, au-dessus des seuils critiques, seul le taux de croissance du mode B décroît avec le nombre de Mach, tandis que la plage des longueurs d'onde instables du mode A se déplace vers des valeurs plus faibles. La réponse à l'augmentation du nombre de Mach des instabilités secondaires 3D se développant dans le sillage instationnaire à l'aval d'un profil NACA0012 est étudiée dans un second temps.

Table of Contents

List of Tables

List of Figures

Chapter 1

Introduction

Abstract: This chapter is devoted to the description of the fundamental concepts presented in this thesis. In section §1.1, the context of this work is presented. We introduce the governing equations in section §1.2 and the framework of linear stability in §1.3 with the absolute/convective and local/global instability concepts. The description and formation of the primary two-dimensional and secondary three-dimensional wake flow instabilities are presented in §1.4. In section §1.5, we discuss the objectives of this PhD work and the organization of the present manuscript. In the last section, §1.6, we summarize the key points of the present chapter in French and will do so throughout the manuscript.

Contents:

1.1 Context

Wake flows have been of fundamental interest to scientists and engineers for more than a century. These flows can be found almost everywhere: the flow behind a body moving through a fluid, like behind cars or aircraft, as shown in figure 1.1.a, or the flow downstream of a body immersed in a stream, like behind simplified shapes, *i.e.* canonical objects, as reported in fig 1.1.b and also like wind-driven strained clouds developing in the wake of an island (figure 1.1.c). The incompressible flow regime behind a given body, can be characterized by the ratio between inertial and viscous forces. This ratio is a non dimensional number known as Reynolds number Re and allows the scaling of different flow configurations, which is of crucial importance for the representativeness of experimental studies of large-size problems. In figure 1.1.b the evolution of the wake behind the circular cylinder is fully characterized by the value of the Reynolds number Re, regardless of the characteristic size of the cylinder, speed or fluid viscosity.

The study of wake flows is of crucial importance for the design and the optimization of transportation

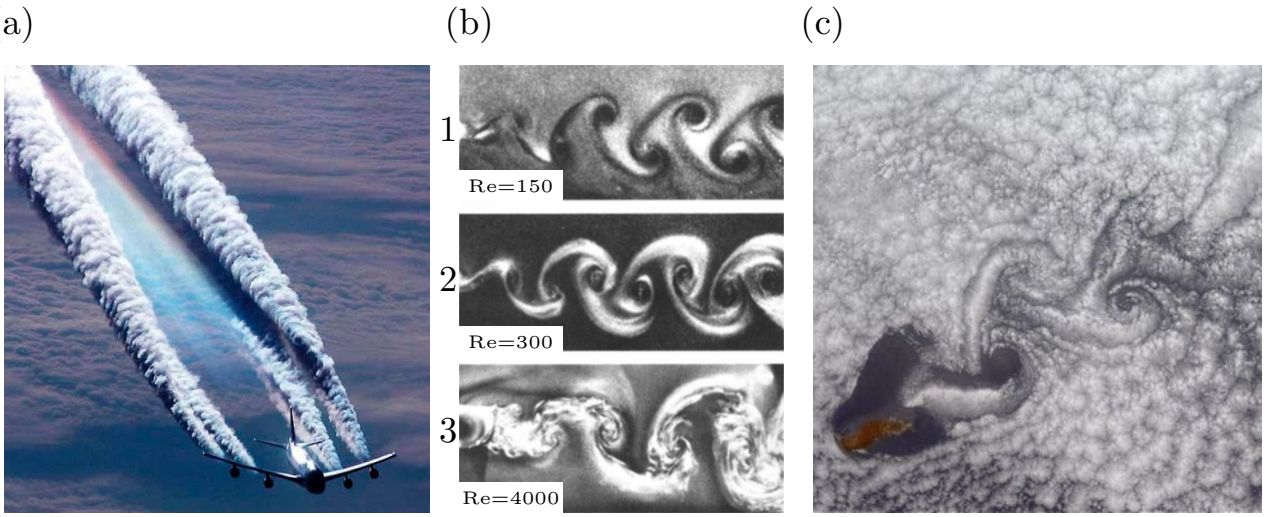

Figure 1.1 – (a) Turbulent wake flow behind an airplane, (b) wake behind a circular cylinder from laminar to turbulent [113] and (c) von Kármán street materialized by strained clouds in the wake of Alejandro Selkirk Island (The image was taken by the Landsat 7 satellite in September 1999. Credit: Bob Cahalan/NASA, USGS).

vehicles' shapes. It allows, for instance, to reduce the aerodynamic drag force and therefore fuel consumption, or to establish the flight envelope of an aircraft. High speed flows encountered in terrestrial transport applications (*i.e.* high Reynolds numbers) combined with complex shapes (figure 1.1.a), result in flows much more complex and chaotic than the one illustrated in figure 1.1.c, with well organized and smooth patterns. The combination of high speed and complex design, makes the study of these flows very challenging, this is where the need for a simplification of the problem comes from. A deep understanding of the flow dynamics around canonical bodies is a necessary first step before dealing with real-world applications in all their complexity.

We now focus our attention on figure 1.1.b, which illustrates the evolution of the flow behind a circular cylinder from a laminar to a turbulent regime. If we consider that turbulence is the result of the succession of qualitative and topological changes of the dynamical system, known as bifurcations, that progressively involve finer structures, we notice that the well organized and smooth patterns (fig. 1.1.b.1 and 1.1.b.2) are nothing less than the outcome of the very first bifurcations. These arise when progressively increasing the Reynolds number from a flow at rest, and therefore are the first stages on the route to turbulence (fig. 1.1.b.3). For this reason, studying the first bifurcations, and associated instabilities, that arise and modify the flow dynamics, is a key point for characterizing the fundamentals of flow evolution and understanding phenomena that persist even at higher Reynolds numbers, as in figure 1.1.c.

The study of fluid instabilities is the subject of a specific field of fluid dynamics, called hydrodynamic stability, that has emerged in the late 19th century with the pioneering works of Helmholtz, Kelvin, Rayleigh and Reynolds [32, 66, 88, 110]. Until recently, these studies have mostly considered atmospheric

	density ($\mathrm{kg\,m^{-3}}$)	mean temperature (K)	mean pressure (Pa)
Earth	1.225	288	101 325
Stratosphere (25 km)	0.0401	222	2549
Mars	0.0155	214	636

Table 1.1 – Average conditions encountered on Earth, Mars and the stratosphere at an altitude of 25 km.

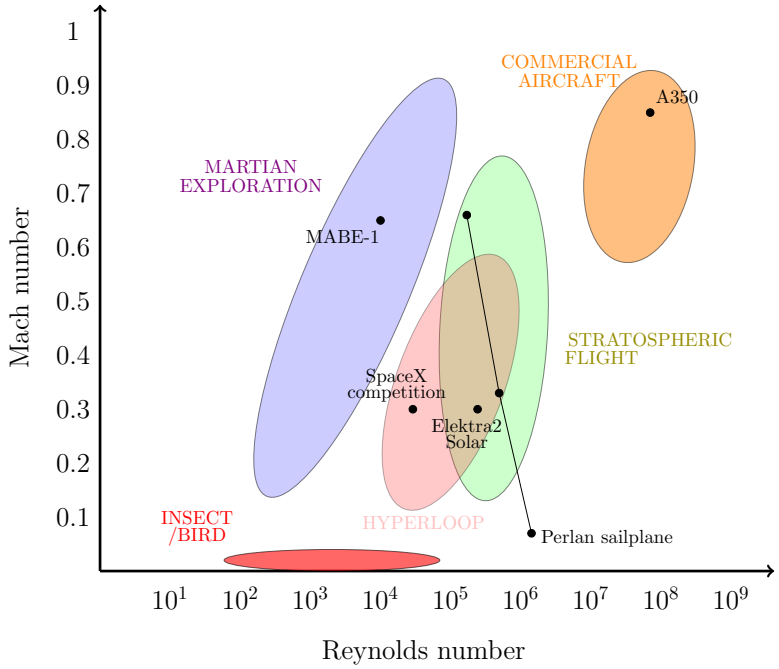

Figure 1.2 – Reynolds number vs Mach number chart for various applications and experiments [4, 30, 60, 83, 103]

conditions on Earth (see table 1.1), where flows at low Reynolds numbers are treated as incompressible. During the last decades, many technological limits have been overcome and prospective applications such as vactrains (*e.g.* Hyperloop concept), stratospheric flight, Martian exploration or optimization of liquid atomization have gained significant interest. Figure 1.2 shows the range of Reynolds-Mach numbers for some of those applications. The flows involved are different from conventional regimes and are typical of low density/pressure environments (Mars or stratosphere, see table 1.1) or of high-speed micro-objects. Compressibility, even at very low Reynolds numbers, is no more negligible in this context and may impact the wake dynamics.

For this growing number of engineering applications, compressible flows at low Reynolds numbers are becoming essential, but a fundamental knowledge on the physics underlying these conditions is lacking. The aim of this work is therefore to contribute to the understanding of this specific regime which has been very little explored so far, focusing our attention on how compressibility may affect the development of instabilities and the transition to turbulence of the wake of various bodies.

1.2 Governing equations

The motion of compressible Newtonian fluids is described by the Navier–Stokes equations, obtained by applying the laws of conservation of mass, momentum and energy. In this work, we consider the three-dimensional compressible Navier–Stokes (NS) equations in conservative form for an ideal gas:

$$\begin{aligned}
&\frac{\partial \rho}{\partial t} + \boldsymbol{\nabla} \cdot (\rho \mathbf{u}) = 0 \\
&\frac{\partial \rho \mathbf{u}}{\partial t} + \boldsymbol{\nabla} \cdot (\rho \mathbf{u} \otimes \mathbf{u}) = -\boldsymbol{\nabla} p + \boldsymbol{\nabla} \cdot \left[\mu \left(\boldsymbol{\nabla} \mathbf{u} + \boldsymbol{\nabla} \mathbf{u}^T \right) - \frac{2}{3} \mu \boldsymbol{\nabla} \cdot \mathbf{u} \, \delta_{ij} \right] \\
&\frac{\partial \rho E}{\partial t} + \boldsymbol{\nabla} \cdot (\rho \mathbf{u} E + p \mathbf{u}) = \boldsymbol{\nabla} \cdot (K \boldsymbol{\nabla} T) + \boldsymbol{\nabla} \cdot \left(\mathbf{u} \left[\mu \left(\boldsymbol{\nabla} \mathbf{u} + \boldsymbol{\nabla} \mathbf{u}^T \right) - \frac{2}{3} \mu \boldsymbol{\nabla} \cdot \mathbf{u} \, \delta_{ij} \right] \right)
\end{aligned} \tag{1.1}$$

where ρ is the fluid density, $\mathbf{u}$ the velocity vector, p the pressure, T the temperature and E the total energy. The viscosity μ and the thermal conductivity K are constant. The system can be written in the following compact form

$$\frac{\partial \boldsymbol{q}}{\partial t} = \mathscr{N}(\boldsymbol{q}) \tag{1.2}$$

with $\boldsymbol{q} = (\rho, \rho\mathbf{u}, \rho E)^{\mathrm{T}}$ representing the state vector and $\mathscr{N}$ the nonlinear NS dynamical operator. We introduce four nondimensional numbers:

$$Re = \frac{\rho_\infty U_\infty L}{\mu}, \quad M_\infty = \frac{U_\infty}{\sqrt{\gamma \frac{p_\infty}{\rho_\infty}}}, \quad St = \frac{fL}{U_\infty}, \quad Pr = \frac{\mu c_p}{K} \tag{1.3}$$

the Reynolds, Mach, Strouhal and Prandtl numbers, respectively. Here, the Prandtl number is taken constant ($Pr = 0.7$). Quantities with subscript $_\infty$ indicate upstream quantities, L is the characteristic length scale, c_p is the specific heat at constant pressure, γ is the ratio of specific heats and f is the shedding frequency. The corresponding convective time scale is $T = L/U_\infty$.

1.3 Linear stability theory

One of the fundamental approaches for investigating flow instabilities and transition to turbulence is the linear stability analysis. Within this theory, a flow state $\boldsymbol{q}$, governed by the dynamics of the nonlinear Navier–Stokes system (eq 1.2), can be seen as the superposition of a base state $\boldsymbol{q_b}$, a stationary or periodic solution of the Navier–Stokes equations, and a small-amplitude disturbance $\boldsymbol{q}'$. Through a Taylor expansion we can write:

$$\begin{aligned} \frac{\partial(\boldsymbol{q_b} + \epsilon \boldsymbol{q}')}{\partial t} &= \mathscr{N}(\boldsymbol{q_b} + \epsilon \boldsymbol{q}') \\ &= \mathscr{N}(\boldsymbol{q_b}) + \epsilon \left.\frac{\partial \mathscr{N}(\boldsymbol{q})}{\partial \boldsymbol{q}}\right|_{\boldsymbol{q_b}} \boldsymbol{q}' + O\left(\epsilon^2\right) \end{aligned} \tag{1.4}$$

where $\epsilon \ll 1$ to ensure small amplitude perturbations. The base state satisfies the NS equations, $\dot{\boldsymbol{q}}_b = \mathscr{N}(\boldsymbol{q}_b)$, therefore, equation (1.4) reduces to:

$$\frac{\partial \boldsymbol{q}'}{\partial t} = \mathscr{L}\boldsymbol{q}' \tag{1.5}$$

where $\mathscr{L} = \left.\frac{\partial \mathscr{N}(\boldsymbol{q})}{\partial \boldsymbol{q}}\right|_{\boldsymbol{q}_b}$ is the Jacobian of the Navier–Stokes operator computed at the base state. This means that, in the neighborhood of the base state $\boldsymbol{q}_b$, the dynamics of the perturbation can be described by the dynamics of the linearized system. It should be noticed that, considering an initial condition $\boldsymbol{q}'(0)$, the analytic solution of equation (1.5) is

$$\boldsymbol{q}'(t) = \mathscr{M}\boldsymbol{q}'(0) \tag{1.6}$$

where $\mathscr{M} = e^{\mathscr{L}t}$ is the exponential propagator. The damping or the growth, or in general the evolution of the perturbation, will characterize the stable or unstable nature of the base state. System (1.5) can be simplified depending on the base flow properties (*e.g.* if it is parallel or non parallel) and on assumptions made on the perturbation form. Depending on these assumptions, linear stability can be investigated by different approaches.

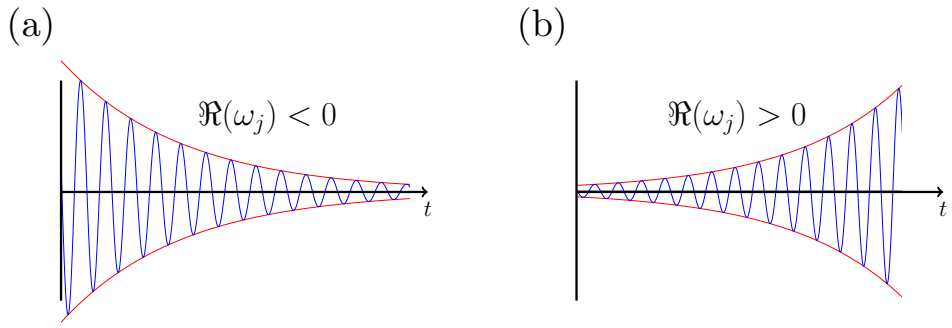

Figure 1.3 – (a) Damped or (b) amplified perturbation amplitude depending on the sign of the real part of ω.

Modal and non-modal approaches

For the moment, we consider that the damping/growth of perturbations has been defined in time[1]. We can first distinguish between *modal* and *non-modal* approaches. The *modal* analysis is based on the assumption of an exponential dependence on time and the perturbation can be seen as the sum of linearly independent perturbations under the form

$$\begin{aligned} \boldsymbol{q}'(\boldsymbol{x},t) = \sum_{j=1}^{\infty} \tilde{\boldsymbol{q}}_j(\boldsymbol{x}) e^{\omega_j t} + c.c. &= \sum_{j=1}^{\infty} \tilde{\boldsymbol{q}}_j(\boldsymbol{x}) e^{[\Re(\omega_j)+i\Im(\omega_j)]t} + c.c. \\ &= \sum_{j=1}^{\infty} \tilde{\boldsymbol{q}}_j(\boldsymbol{x}) e^{\Re(\omega_j)t} [\cos(\Im(\omega_j)t) + i\sin(\Im(\omega_j)t)] + c.c. \end{aligned} \tag{1.7}$$

ω_j is the complex frequency of the perturbation whose real part, $\Re(\omega_j)$, determines whether the perturbation is damped or amplified in time (whether $\Re(\omega_j)$ is negative or positive, respectively), and whose imaginary part, $\Im(\omega_j)$, is the pulsation of the perturbation which is related to its frequency $\Im(\omega_j) = 2\pi f_j$ (see figure 1.3). Given the linear independence and the exponential time dependence, *i.e.* each perturbation is autonomous with a monotonic amplitude temporal evolution, we can characterize the perturbation $\boldsymbol{q}'$ by its asymptotic behaviour. As $t \to \infty$, the perturbation $\tilde{\boldsymbol{q}}_j(\boldsymbol{x})e^{\omega_j t}$ associated to the highest $\Re(\omega_j)$, *i.e.* to the most amplified or least damped perturbation, will dominate and drive the dynamics of the flow. What is the $\tilde{\boldsymbol{q}}_j(\boldsymbol{x})$ structure and what does ω_j stand for?
Replacing the form of the perturbation (1.7) in the system (1.5), we obtain :

$$\frac{\partial \tilde{\boldsymbol{q}}_j(\boldsymbol{x}) e^{\omega_j t}}{\partial t} = \mathscr{L}\tilde{\boldsymbol{q}}_j(\boldsymbol{x}) e^{\omega_j t}. \tag{1.8}$$

The time derivative development and the simplification of the exponential lead to:

$$\omega_j \tilde{\boldsymbol{q}}_j(\boldsymbol{x}) = \mathscr{L}\tilde{\boldsymbol{q}}_j(\boldsymbol{x}). \tag{1.9}$$

This corresponds to an eigenvalue problem (EVP) and shows that ω_j and $\tilde{\boldsymbol{q}}_j(\boldsymbol{x})$ are the eigenvalue and corresponding eigenvector of $\mathscr{L}$. Therefore, through the modal approach, the linear stability reduces to a spectral analysis of the linearized operator.

The *non-modal* approach [93], instead, also known as the transient growth analysis, does not

[1]The damping/growth of perturbations can also be defined in space, in the context of *local* stability analysis, that will be treated at the end of this section

suppose an exponential time evolution and the perturbation

$$\boldsymbol{q}'(\boldsymbol{x},t) = \sum_{j=1}^{\infty} \tilde{\boldsymbol{q}}_j(\boldsymbol{x},t) + c.c. \tag{1.10}$$

is considered as the sum of no longer linearly independent perturbations. Interacting with each other, the decay/amplification of the disturbance may not be monotonic and exhibit a transient in the early time evolution. Therefore, this analysis concerns the evolution of the perturbation on time scales that are completely neglected by the modal approach. Moreover, this method does not suppose the base flow to be steady. Nevertheless, in the large-time limit $t \to \infty$, this analysis recovers the least stable mode, *i.e.* the modal response.
In this work, we adopted the modal approach.

Local and global approaches

Properties of the base flows can be used to further simplify the problem. If the base flow $\boldsymbol{q}_b$ exhibits one or more homogeneous directions, an exponential spatial dependence of the perturbation along those directions can be assumed. With respect to the number of homogeneous directions of the base flow in which we consider a modal evolution, the approach is said to be *local, bi-global* or *tri-global*. Thus, the spatial structure of the perturbation, defined by $\tilde{\boldsymbol{q}}_j(\boldsymbol{x})$ in (1.7), becomes:

$$\tilde{\boldsymbol{q}}_j(\boldsymbol{x}) = \tilde{\boldsymbol{q}}_j(x_1,x_2,x_3) = \begin{cases} \tilde{\boldsymbol{q}}_j(x_1)e^{i(\alpha x_2+\beta x_3)} & \text{if } \boldsymbol{q}_b = \boldsymbol{q}_b(x_1) \quad \text{local} \\ \tilde{\boldsymbol{q}}_j(x_1,x_2)e^{i\alpha x_3} & \text{if } \boldsymbol{q}_b = \boldsymbol{q}_b(x_1,x_2) \quad \text{bi-global} \\ \tilde{\boldsymbol{q}}_j(x_1,x_2,x_3) & \text{if } \boldsymbol{q}_b = \boldsymbol{q}_b(x_1,x_2,x_3) \quad \text{tri-global} \end{cases} \tag{1.11}$$

where x_1, x_2 and x_3 denote generic spatial coordinates, while α and β, in the temporal formulation, are real numbers that define the wavenumbers along the associated direction[2]. Introducing the perturbations form (1.7) with the local and bi-global spatial evolution in the system (1.5), we find a simplified eigenvalue problem, whose eigenvalues ω_j depend on the wavenumbers: $\omega_j = \omega_j(\alpha)$ or $\omega_j = \omega_j(\alpha,\beta)$. The relation between frenquency and wavenumber is called dispersion relation. In this work the tri-global, here simply called *global* approach[3], has been used: no assumption is made about the spatial dependence of the base flow, *i.e.* $\boldsymbol{q}_b = \boldsymbol{q}_b(x_1,x_2,x_3)$, and the spatial structure of the perturbation is free to evolve in space without imposing any periodicity *a priori*.

After these considerations, we can finally define the approach used in the present work: a modal global stability analysis, that defines temporal global modes. Thus, we are able to characterize the stable/unstable nature of the base flow depending on the spectral properties of $\mathscr{L}$. The stability of $\boldsymbol{q}_b$ is therefore expressed by the following criterion:

- the base state is said to be *globally stable* if $\Re(\omega_j) < 0 \; \forall j \in \mathbb{N}^*$. It means that any perturbation is damped in time and the perturbed flow will always relax to its initial equilibrium state;

[2]This is in the case of local temporal analysis. In local spatial analysis, instead, α and β are complex numbers, while ω is imaginary following our convention (1.7).

[3]The term *global* refers to the fact that all space variables are considered as eigendirections. With this definition the authors consider that in two-dimensional frameworks, global stability analysis does not necessarily reduce to bi-global stability, since the term bi-global, in its generic formulation, incorporates a modal spatial evolution assumption. This is not the case in our analysis. Either the problem is two-dimensional and the third dimension is completely neglected, or tri-dimensional and even if the third dimension is homogeneous, we can perform a tri-global analysis, different from the bi-global one, where the wavenumber has to be imposed *a priori*.

- the base state is said to be *globally unstable* if there exists at least one eigenvalue ω_j with $\Re(\omega_j) > 0$. This means that at least one perturbation grows in time and the perturbed flow will diverge from the base state, either indefinitely or converging toward another equilibrium state;

- the base state is said to be *marginally stable* if the leading eigenvalue ω_j satisfies $\Re(\omega_j) = 0$. In this case, the perturbation is neither damped nor amplified.

1.3.1 Temporal and spatial approaches

In the context of local stability analysis, we can distinguish between a *temporal* and a *spatial* analysis. In this case, the difference lies on whether we define the damping/growth of perturbations in space or in time. Although we resort to a global approach in the present work, implying that the damping/growth of the perturbations is defined in time, an introduction to the local stability analysis is useful to understand concepts that will be discussed in the next section. Indeed, in section 1.3.2 we will see that temporal and spatial local analysis lead to issues related to global stability. From equation (1.11), the perturbation is expressed as follows:

$$\boldsymbol{q}'(\boldsymbol{x},t) = \sum_{j=1}^{\infty} \tilde{\boldsymbol{q}}_j(x_1) e^{i(\alpha x_2 + \beta x_3)} e^{\omega t} + c.c. \tag{1.12}$$

Without loss of generality, we restrict the following discussion to a two-dimensional problem, *i.e.* :

$$\boldsymbol{q}'(\boldsymbol{x},t) = \sum_{j=1}^{\infty} \tilde{\boldsymbol{q}}_j(x_1) e^{i\alpha_j x_2} e^{\omega_j t} + c.c. \tag{1.13}$$

In the temporal local stability analysis, the temporal frequency ω is considered as complex, while the spatial wavenumber α is a given real number:

$$\begin{aligned} \boldsymbol{q}'(\boldsymbol{x},t) = \boldsymbol{q}'(\boldsymbol{x},t,\alpha) &= \sum_{j=1}^{\infty} \tilde{\boldsymbol{q}}_j(x_1) e^{i\alpha x_2} e^{\omega_j t} + c.c. \\ &= \tilde{\boldsymbol{q}}_j(x_1) \Big[\cos(\alpha x_2) + i \sin(\alpha x_2) \Big] \underbrace{e^{\Re(\omega_j)t}}_{\substack{\text{drives the} \\ \text{decay/growth}}} \Big[\cos(\Im(\omega_j)t) + i \sin(\Im(\omega_j)t) \Big] + c.c. \end{aligned} \tag{1.14}$$

The disturbance is then considered as a wavepacket consisting of the superposition of periodic waves along the x_2 direction, whose wavelength is given by $\lambda = \frac{2\pi}{\alpha}$. Each wave grows or decays in time at a specific rate, given by $\Re(\omega_j)$, and propagates at a constant phase speed, given by $v_\phi = \frac{\Im(\omega_j)}{\alpha}$. If all disturbances corresponding to a given wavenumber have the same phase velocity, the medium is said to be non-dispersive. The envelope of the wavepacket propagates at a speed defined by the group velocity, $v_g = \frac{d\Im(\omega_j)}{d\alpha}$. Through the resulting EVP, it is possible for each wavenumber α to identify the most amplified perturbation associated to the maximum growth rate $\Re(\omega_j)$.

In the spatial local stability analysis, the spatial wavenumber α is considered as complex, while the temporal frequency is a given pure imaginary number $i\omega$:

$$\begin{aligned} \boldsymbol{q}'(\boldsymbol{x},t) = \boldsymbol{q}'(\boldsymbol{x},t,\omega) &= \sum_{j=1}^{\infty} \tilde{\boldsymbol{q}}_j(x_1) e^{i\alpha_j x_2} e^{i\omega t} + c.c. \\ &= \tilde{\boldsymbol{q}}_j(x_1) \underbrace{e^{-\Im(\alpha_j)x_2}}_{\substack{\text{drives the} \\ \text{decay/growth}}} \Big[\cos(\Re(\alpha_j)x_2) + i \sin(\Re(\alpha_j)x_2) \Big] \Big[\cos(\omega t) + i \sin(\omega t) \Big] + c.c. \end{aligned} \tag{1.15}$$

Analogously, through the resulting EVP, we are able to see whether the resulting perturbation grows (negative $\Im(\alpha_j)$) or decays (positive $\Im(\alpha_j)$) in space.

The differences between temporal and spatial approaches will be discussed in section 1.3.2. In particular, the limitations of choosing one or the other as well as the need for a spatio-temporal analysis in the context of local stability of open flows, will be addressed.

1.3.2 Absolute and convective instabilities

The main difficulty in choosing either a spatial or a temporal approach when addressing the local stability of a given flow lies in the fact that one needs to decide *a priori* whether the spatial or temporal damping/growth of the perturbation is more relevant. In open flows, such as wake flows, in which fluid particles are continuously advected downstream, both approaches employed separately may not be representative of the global dynamics of the flow. In particular local spatial analysis may have no physical relevance and the stable/unstable characterization given by the local temporal analysis is not exhaustive. Hence, it is better to resort to a spatio-temporal analysis, where both ω and α are considered complex. The perturbation form (1.13) becomes then:

$$\begin{aligned}\boldsymbol{q}'(\boldsymbol{x},t) = \boldsymbol{q}'(\boldsymbol{x},t,\alpha) &= \sum_{j=1}^{\infty} \tilde{\boldsymbol{q}}_j(x_1) e^{i\alpha_j x_2} e^{\omega_j t} + c.c. \\ &= \tilde{\boldsymbol{q}}_j(x_1) \underbrace{e^{-\Im(\alpha_j)x_2 + \Re(\omega_j)t}}_{\substack{\text{drives the} \\ \text{decay/growth}}} \Big[\cos(\Re(\alpha_j)x_2) + i\sin(\Re(\alpha_j)x_2)\Big]\Big[\cos(\Im(\omega_j)t) + i\sin(\Im(\omega_j)t)\Big] + c.c.\end{aligned} \tag{1.16}$$

This analysis leads to the *absolute* and *convective instability* concepts, which are related to the *global instability* of the flow[25, 27, 50, 51].

For sake of simplicity and without loss of generality, we restrict expression (1.16) to a one-dimensional problem. We ignore the dependence along x_1, that only affects the initial wave amplitude, and we consider the spatio-temporal wave evolution in the (x_2, t) plane only, which hereinafter will simply be denoted by the (x, t) plane. From the work of Bers [13] and following [49, 50, 51], this analysis can be reduced to the study of the Green's function, $G(x,t)$, of the dispersion relation in the physical space (x,t). Function $G(x,t)$ contains all the information about the spatio-temporal dynamics of the system as a response to a localized initial impulse at (x,t)=(0,0).

The stationary-phase or steepest descent method [11, 38] allows to evaluate the $G(x,t)$ evolution over long times. With this method, the asymptotic response to the impulse corresponds to $G(x,t)$ estimated along each ray $\frac{x}{t} = \text{cst}$, considering the complex wavenumber α^* for which the phase velocity is stationary, *i.e.* real group velocity equal to $\frac{x}{t}$:

$$\frac{\partial \omega}{\partial \alpha}(\alpha^*) = \frac{x}{t} = V. \tag{1.17}$$

In this way, $G(x,t)$ identifies a wavepacket and the couple $(\alpha^*, \omega^* = \omega(\alpha^*))$ can be interpreted as the spatial wavenumber and associated temporal frequency perceived by an observer moving at velocity V along the spatio-temporal rays $\frac{x}{t} = V$[51]. Is this wavepacket growing along this ray? From the perturbation form (1.16), we have:

$$e^{-\Im(\alpha)x + \Re(\omega)t} = e^{-\Im(\alpha)Vt + \Re(\omega)t} = e^{(-\Im(\alpha)V + \Re(\omega))t}. \tag{1.18}$$

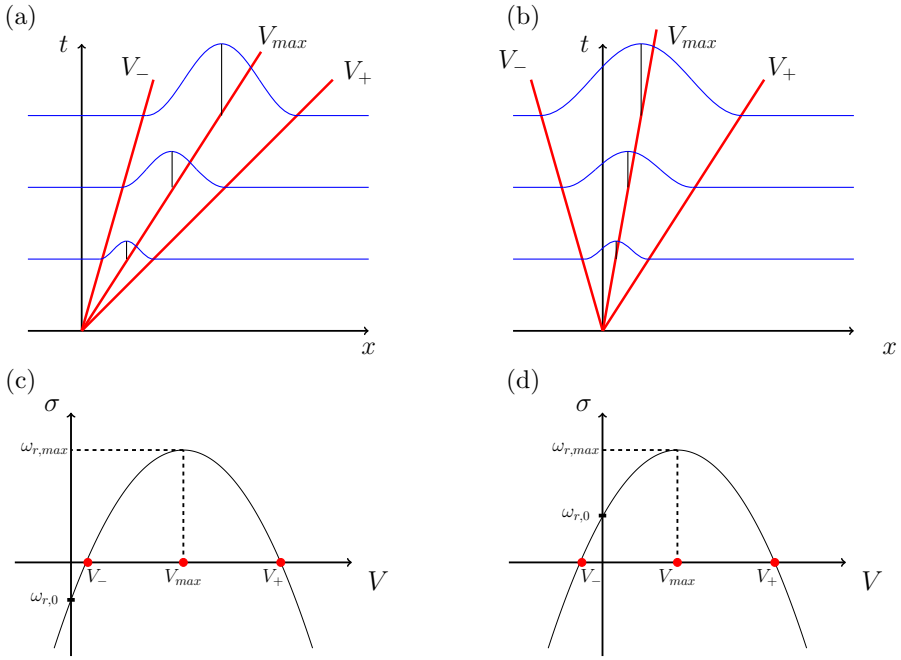

Figure 1.4 – Convective (a) and absolute (b) instability evolution in the (x,t) plane. Associated growth rate $\sigma(V)$, which defines the extremes rays V_-, V_+ and the absolute growth rate $\omega_{r,0}$, in the convective (c) and absolute (d) cases.

Therefore, along the ray, the perceived growth rate σ has the following expression:

$$\sigma = \sigma(V) = \Re(\omega^*) - \Im(\alpha^*)V \tag{1.19}$$

and the perturbation either grows ($\sigma < 0$) or decays ($\sigma > 0$). If now we consider a temporal analysis (α is real), the growth rate, given by $\Re(\omega(\alpha))$, presents a maximum ($\omega_{r,max}$) with respect to α. This maximum, is achieved for a wavenumber that we call α_{max}, and the corresponding group velocity is[4]:

$$\frac{\partial \omega}{\partial \alpha}(\alpha_{max}) = V_{max} \tag{1.20}$$

Hence, along $\frac{x}{t} = V_{max}$, the perceived wavenumber is real and the growth rate is $\sigma(V_{max}) = \omega_{r,max}$, which represents a global maximum for σ. The concepts of spatio-temporal instability are then defined as:

- the base flow is stable if $\lim_{t\to\infty} G(x,t) = 0$, *i.e.* $\sigma < 0$, along all rays $\frac{x}{t} = \text{cst}$;
- the base flow is unstable if $\lim_{t\to\infty} G(x,t) = \infty$, *i.e.* $\sigma > 0$, at least along one ray $\frac{x}{t} = \text{cst}$.

When the base flow is unstable, the range within which the wavepackets grow exponentially, is finite. The extremes of this range are denoted as V_- and V_+ and correspond to the rays along which $\sigma = 0$, as reported in figure 1.4. At this point, we should consider the wavepacket that remains at the point of impulse, *i.e.* the wavepacket with zero group velocity ($V = 0$). The wavenumber associated to this wavepacket, α_0, is a saddle point of the dispersion relation, *i.e.*

$$\frac{\partial \omega}{\partial \alpha}(\alpha_0) = 0. \tag{1.21}$$

[4]This derivative assumes both ω and α to be complex numbers. It is different from the one used for calculating α_{max}: $\frac{\partial \Re(\omega)}{\partial \alpha}(\alpha_{max}) = 0$.

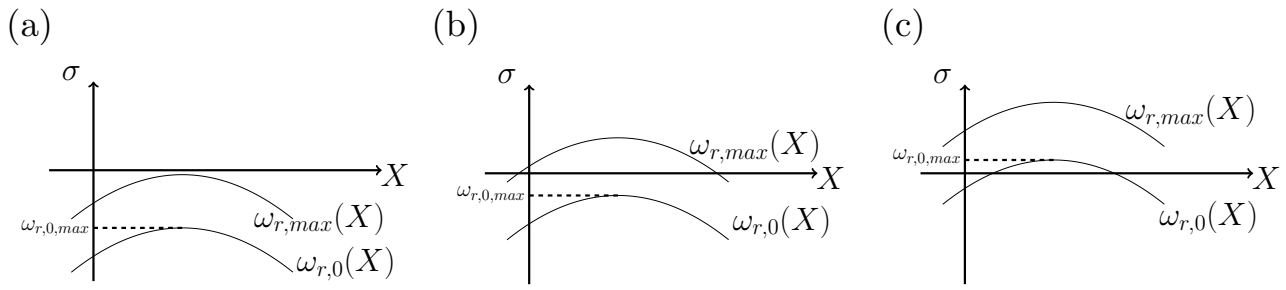

Figure 1.5 – Resulting scenarios of local stability analysis of weakly non-parallel flows: locally stable base flow (a), locally convectively unstable base flow (b), locally absolutely unstable base flow (c)

This wavepacket is associated with the so called absolute growth rate $\sigma(0) = \omega_{r,0}$, which defines the nature of the instability. Convective and absolute instability are then defined as follows:

- the base flow is convectively unstable, if $\lim_{t\to\infty} G(x,t) = 0$, *i.e.* $\sigma < 0$, along the ray $\frac{x}{t} = 0$;
- the base flow is absolutely unstable, if $\lim_{t\to\infty} G(x,t) = \infty$, *i.e.* $\sigma > 0$, along the ray $\frac{x}{t} = 0$.

Figure 1.4 schematically summarizes the difference between absolute and convective instability. If the absolute growth rate is negative, *i.e.* both V_- and V_+ are positive (figure 1.4.c), instabilities generated by the impulse are convected downstream (figure 1.4.a) and the flow behaves like a noise amplifier. Conversely, if the absolute growth rate is positive, *i.e.* V_- negative and V_+ positive (figure 1.4.d), the instabilities will gradually contaminate the whole domain (figure 1.4.b) and the flow will behave like an oscillator. We can now understand why local spatial theory may not have physical relevance. Indeed, it is meaningful only if the flow is convectively unstable. If the instability is absolute, so by definition any spatial location will be contaminated by the disturbance at long time, the concept of the asymptotic spatial behaviour ($x \to \infty$) looses its significance. Conversely, if the instability is convective, the perturbation oscillating in time will eventually emerge at $x \to \infty$ as represented by the spatial response.

1.3.3 Relation between local and global instability

Keeping in mind that the absolute/convective instability theory is local and therefore valid for parallel flows, it is reasonable to ask how these results can be used and extended to the case of non-parallel flows. Hence, in this section, we will see how these results are related to the global response of the flow.

We now address weakly non-parallel flows, *i.e.* flows that slowly evolve along the streamwise direction (x). The streamwise evolution of the base flow can be quantified by the variation of a characteristic local length scale, such as the momentum thickness θ [27]. The base flow is considered weakly parallel if

$$\epsilon = \frac{d\theta}{dx} \ll 1 \tag{1.22}$$

and it is supposed to vary over a slow space scale $X = \epsilon x$. This slow evolution allows to consider the flow dynamics at each streamwise station as locally parallel. With this approach, it is possible to analyze the streamwise evolution of the maximum and absolute growth rate, $\omega_{r,max}$ and $\omega_{r,0}$. Figure 1.5 presents the different scenarios that can be encountered. The flow is uniformly locally stable if $\omega_{r,0} < \omega_{r,max} < 0$ whatever streamwise position (figure 1.5.a). When a region of local convective instabilities arises (figure 1.5.b), $\omega_{r,0} < 0$ for all X but $\omega_{r,max} > 0$ for some X, the flow is locally convectively unstable and behaves like an noise amplifier. Nevertheless, this type of flow is globally stable, because no self-excited state can arise. If, on the contrary, there is a region of local absolute

instability (figure 1.5.c), nothing can be said *a priori* about the existence of a global instability, *i.e.* a self-sustained state that oscillates at a specific frequency ω_G.

There have been different theories proposed to identify the global frequency ω_G, among which:

- The initial resonance condition [74]: ω_G is the absolute frequency ω_0 at the upstream boundary between convective and absolute regions.
- The downstream resonance condition [59]: ω_G is the absolute frequency ω_0 at the downstream boundary between convective and absolute regions.
- ω_G is the predicted maximum absolute frequency $\omega_{0,max}$ [86].

A more general theory that relates global and local instability properties has been provided by the WKBJ (Wentzel–Kramers–Brillouin–Jeffreys) approach [25, 28, 40, 61, 76]. With this method, the global mode structure is considered in the form of WKBJ expansions [11] along the streamwise direction and the global frequency ω_G is defined as the absolute frequency ω_0 at a the saddle point X_s of $\omega_0(X)$ in the complex X-plane, such that [5]:

$$\frac{\partial \omega_0}{\partial X}(X_s) = 0 \tag{1.23}$$

likewise ω_0 has been derived for parallel flows, *i.e.* considering the saddle point of the dispersion relation $\omega(\alpha)$. In fact, in order to relate local to global analysis, the streamwise direction needs to be seen as an eigenvalue direction as well. Therefore, since $\omega_{r,0,max}$ represents the maximum absolute growth rate over the real axis X, the following inequalities hold:

$$\omega_{r,G} \leq \omega_{r,0}(X_s) \leq \omega_{r,o,max}. \tag{1.24}$$

The presence of a region of absolute local instability is a necessary but not sufficient condition for global instability to occur. The flow is found to be globally unstable if the zone of absolute instability is sufficiently large.
This theory, developed for weakly non-parallel flows, applies satisfactorily to wake flows, which can be strongly non parallel, especially in the case of wake behind bluff bodies [51, 75].

1.4 Wake instabilities behind bluff bodies

The evolution of the wake behind a circular cylinder has been widely studied during the last decades [9, 39, 111, 113]. At very low Reynolds numbers in the Stokes regime, $Re < 5$, the flow is attached to the cylinder (figure 1.6.a), until a first topological change occurs at $Re = 5$ and two steady counter-rotating vortices form behind the cylinder [5], giving rise to the recirculation region (figure 1.6.b). At this stage, the flow has been found to transition into a convective instability (figure 1.5.b), while at $Re = 25$, the first local absolute instability appears (figure 1.5.c) [51, 75]. Nevertheless, at this stage the region of local absolute instability is small and the flow is still dominated by local convective instability.

The two counter-rotating vortices become unsteady as the primary global instability appears, at $Re = Re_{c1} \approx 47$, due to the fact that the region of local absolute instability has become sufficiently large to make the flow globally unstable [26, 51]. The flow has entered into a self-sustained periodic vortex-shedding regime, with a pattern of swirling vortices called the von Kármán vortex street. Further increasing the Reynolds number, the amplitude of the oscillation increases. Then, a second bifurcation occurs at $Re = Re_{c2} \approx 180$, with the wake becoming three-dimensional, *i.e.* the two-dimensional periodic solution becomes unstable.

[5] Analogously to the derivative (1.20), this derivative considers both ω_0 and X complex.

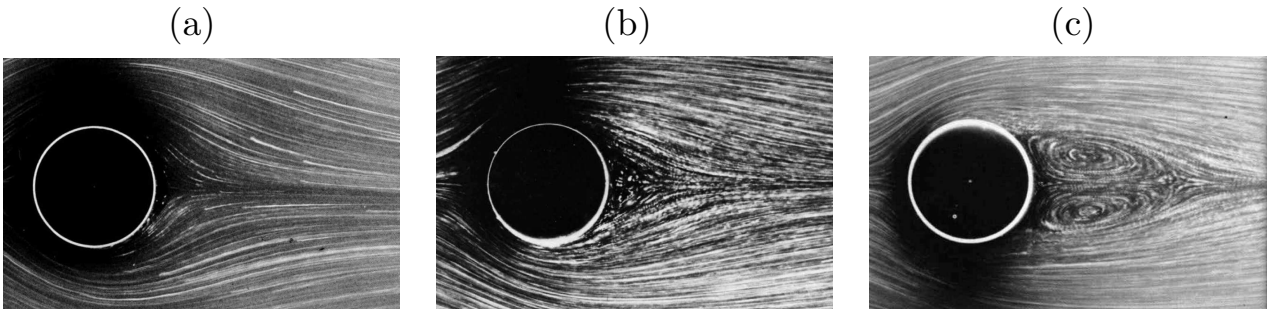

Figure 1.6 – Cylinder wake evolution : (a) $Re = 1.54$, (b) $Re = 9.6$ and (c) $Re = 26$. Adapted from pictures 24, 40 and 42 of Van Dyke's album; photographs by Sadatoshi Taneda [108].

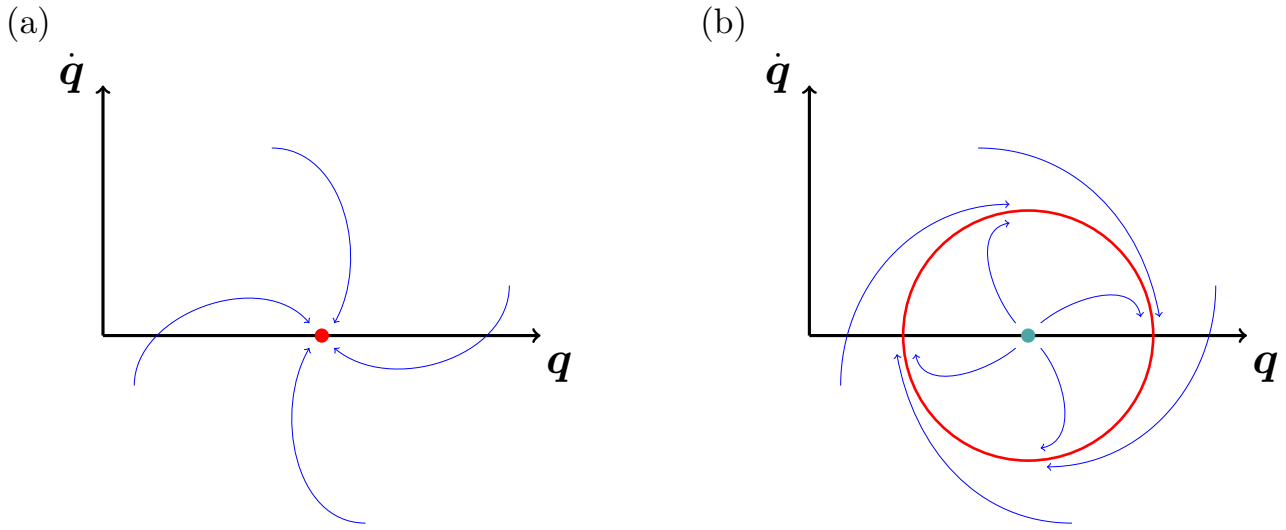

Figure 1.7 – Stable fixed point, $Re < Re_{c1}$ (a) and unstable fixed point with stable limit cycle, $Re_{c2} > Re > Re_{c1}$ (b), in the phase space $(\boldsymbol{q}, \dot{\boldsymbol{q}})$.

This description of the successive stages of the wake behind the circular cylinder as the Reynolds number is increased also applies to wakes behind other types of bodies, with the transition from a stationary to a two-dimensional periodic solution at a first critical value Re_{c1} and the three-dimensionalisation of the wake at a second critical value Re_{c2}. In particular, the evolution from a stationary to a periodic solution always corresponds to a Hopf bifurcation. The three-dimensional mechanism, on the other hand, can originate from different types of instabilities. The first Hopf bifurcation occurring on the stationary state and the different bifurcations occurring on the periodic solution are further described in the next subsections.

1.4.1 The first Hopf bifurcation

We have just described the qualitative and topological changes of the system with respect to the Reynolds number. For Re below the first critical value, Re_{c1}, the solution is stationary, while for $Re_{c1} < Re < Re_{c2}$ the solution is periodic, *i.e.* the von Kármán vortex street, with Re_{c2} representing the critical value above which the flow is three-dimensional. These two types of equilibrium solutions represent the so called attractors, towards which trajectories starting from a neighbouring initial state will converge as $t \to \infty$. These two attractors, *i.e.* the stationary and the periodic solutions, are both stable solutions for $Re < Re_{c1}$ and $Re_{c1} < Re < Re_{c2}$, respectively. They are referred to as a fixed point and a limit cycle solutions and can be represented in the phase space $(\boldsymbol{q}, \dot{\boldsymbol{q}})$ as shown in figure

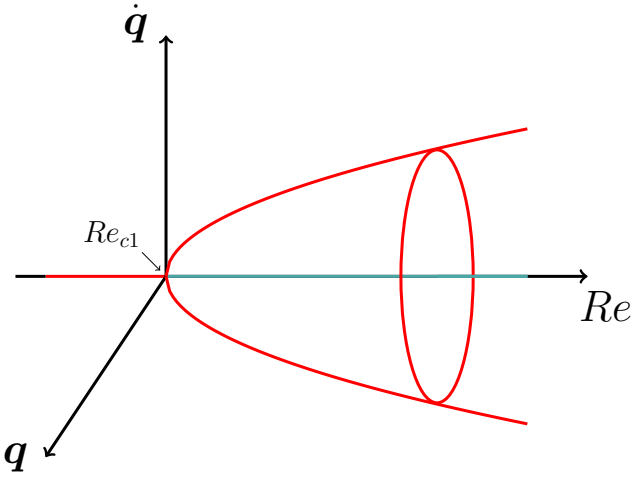

Figure 1.8 – Hopf bifurcation diagram. A slice at fixed $Re < Re_{c1}$ corresponds to figure 1.7.a, while at fixed $Re > Re_{c1}$ corresponds to 1.7.b

1.7. For $Re < Re_{c1}$ the fixed point solution is stable (figure 1.7.a), while for $Re_{c1} < Re < Re_{c2}$ the fixed point solution, *i.e.* the stationary solution (green dot in figure 1.7.b), is unstable, but the system presents a stable limit cycle, *i.e.* the periodic solution.

The transition from a stable fixed point to a stable limit cycle is well known as a supercritical Hopf bifurcation [97, 100], that is depicted in figure 1.8. Such a bifurcation is characterized by the fact that the leading eigenvalue of the Jacobian matrix $\mathscr{L}$ (see equation (1.9)) is a complex conjugate pair, $\omega = \omega_r \pm i\omega_i$, that crosses the real axis at $Re = Re_{c1}$[6], with

$$\left.\frac{d\omega_r}{dRe}\right|_{Re_{c1}} > 0. \tag{1.25}$$

At $Re = Re_{c1}$[7], the imaginary part of the eigenvalues gives the oscillation frequency [97].

1.4.2 Limit cycle instabilities

The stability of the limit cycle solution can be studied by means of Floquet theory, which describes the behaviour of linear differential equations with time-periodic coefficients. In this case, equation (1.5) becomes:

$$\frac{\partial \boldsymbol{q}'}{\partial t} = \mathscr{L}(t)\boldsymbol{q}' \tag{1.26}$$

where the Jacobian matrix is a periodic linear operator: $\mathscr{L}(t) = \mathscr{L}(t+T)$, with T indicating the oscillation period. Floquet analysis relates the study of the limit cycle to that of a fixed point through the so-called Poincaré map. The Poincaré map is a collection of points, obtained by storing a single point of the trajectory for each cycle of motion, *i.e.* the intersection of the trajectory with a Poincaré section, as depicted in figure 1.9. Looking at the evolution of the points of the Poincaré map, it is then possible to deduce if the periodic system is stable or not. Introducing the Floquet transition matrix

[6] A fixed point solution can become unstable through different types of primary bifurcations. Since the von Kármán instability is well known to arise from a Hopf bifurcation, the description of the other bifurcation types occurring for fixed point solutions is not presented here. The readers interested can refer to Charru [22] for details.

[7] As it will be seen later on in the manuscript, the frequency given by the imaginary part of the eigenvalue may diverge from the one observed in the nonlinear regime as the Reynolds number is increased beyond Re_{c1}, depending on the base state considered.

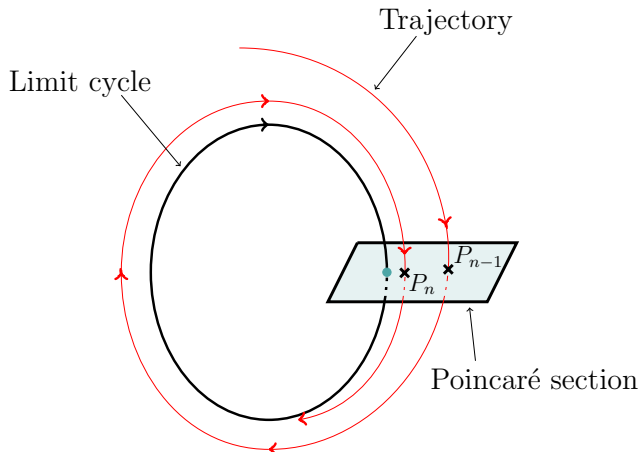

Figure 1.9 – Poincaré map, limit cycle and trajectory representation. The green dot indicates the fixed point solution representative of the limit cycle.

$\phi(0,T)$, that relates the states of the system at time $t=0$ and $t=T$, we have:

$$\boldsymbol{q}'(T) = \phi(0,T)\ \boldsymbol{q}'(0) \tag{1.27}$$

If now we compare this expression to the generic solution of the time-independent coefficient system (1.6) $\boldsymbol{q}'(t) = e^{\mathscr{L}t}\boldsymbol{q}'(0)$, we obtain that $\phi(0,T) = e^{\mathscr{L}T}$ [10, 48, 99]. The eigenvalues of the Floquet transition matrix, referred to as the characteristic Floquet multipliers, can be then interpreted in the same way as the eigenvalues of the exponential propagator matrix $\mathscr{M} = e^{\mathscr{L}T}$. In fact, due to its periodicity, $\mathscr{L}(t)$ results in a constant coefficient matrix on the Poincaré section.

The Floquet characteristic multipliers μ, eigenvalues of the exponential propagator $\mathscr{M}$, and ω, the eigenvalues of the Jacobian matrix $\mathscr{L}$, also called Floquet exponents, are related through

$$\mu = e^{\omega T}. \tag{1.28}$$

Hence, the stability of each mode can be either deduced from the real part of ω or the modulus of μ:

$$\text{Stable } \begin{cases} \omega_r < 0 \\ |\mu| < 1 \end{cases} \qquad \text{Unstable } \begin{cases} \omega_r > 0 \\ |\mu| > 1 \end{cases} . \tag{1.29}$$

There can be different bifurcations of the limit cycle, depending on how the characteristic Floquet multiplier crosses the unit cycle. Looking at figure 1.10, we have:

- when $\mu = +1$, *i.e.* $\omega = 0 + 0i$ (see Appendix A), the limit cycle presents a saddle-node bifurcation. A new stable periodic orbit (red cycle) emerges with the same periodicity of the original orbit (green cycle). In special cases, in particular for symmetric wakes, the saddle node bifurcation results in a pitchfork bifurcation [17];

- When $\mu \neq +1$, *i.e.* $\omega_i \neq 0$, the system presents a new frequency. The intersections of the original (green) and new (red) orbits with the Poincaré section, which are represented by the green and red dots respectively, can be seen as the unstable fixed point that bifurcates toward a limit cycle (blue cycle), see also figure 1.7.b. The new periodic orbit (red trajectory) can be then visualized as lying on a torus with periodicity $2\pi/\omega_i$. This bifurcation is called Secondary Hopf bifurcation or Neimark–Sacker bifurcation. Within this case, there is a particular condition, corresponding to $\mu = -1$, which results in $\omega_i = \bar{\omega}_i/2$, with $\bar{\omega}_i = 2\pi/T$ indicating the base flow frequency.

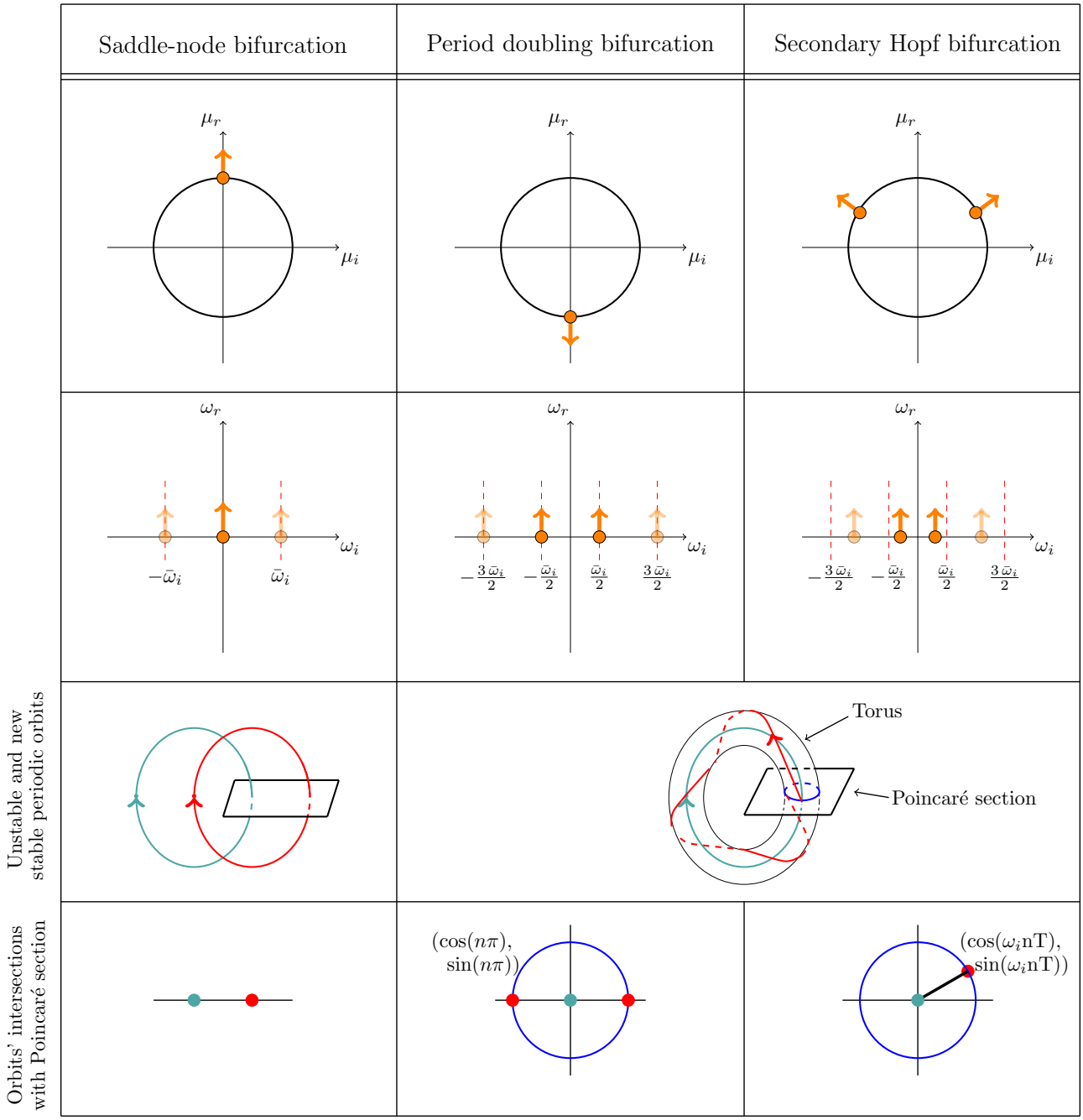

Figure 1.10 – Bifurcations of a periodic limit cycle through the Floquet multipliers μ (first row) and eigenvalues of the Jacobian matrix ω (second row). Visualization of the unstable periodic solution represented in green with the resulting stable one in red (third row) and the asymptotic intersections of trajectories with the Poincaré section (fourth row), $n \in \mathbb{N}$. $\bar{\omega}_i = 2\pi/T$ in the second row indicates the base flow frequency, while eigenvalues represented in opacity indicate other possible solutions that cannot arise due to the aliasing effect and the base state periodicity.

Hence, the emerging periodic orbit has exactly twice the periodicity of the original one. This bifurcation is called Period doubling bifurcation[8]. In this case, the intersections of the new orbit with the Poincaré map coincide with two stable points that, around the original orbit, define a Möbius band. The other particular condition, obtained for $\mu = \pm i$ and corresponding to a period quadrupling, is unlikely to appear, since it would produce a resonance with the period doubling

[8] In mathematics, the Feigenbaum phenomenon stands as a route to chaos going through an infinite sequence of period doubling bifurcations of periodic limit cycles.

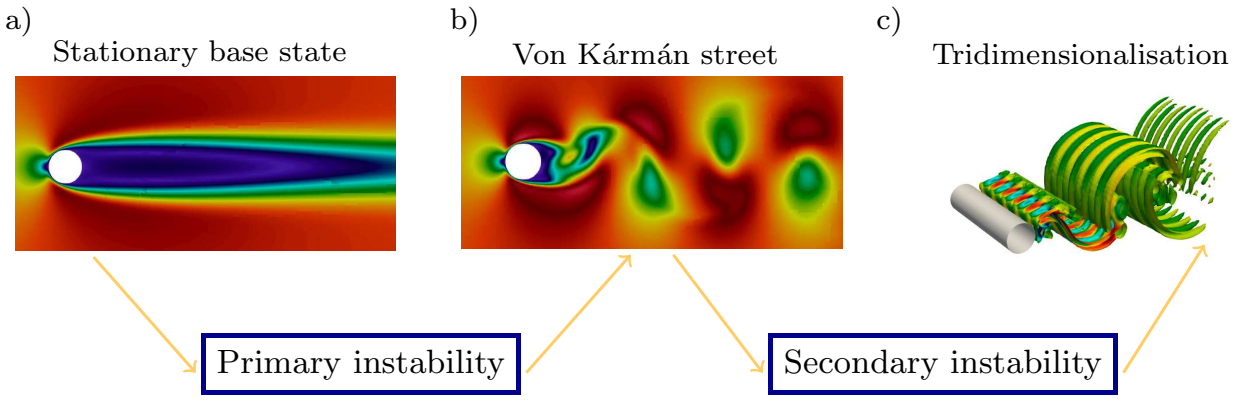

Figure 1.11 – Schematic representation of primary and secondary instabilities development.

instability [102].

1.5 Research objectives and manuscript organization

The aim of this work is to analyze the effects of compressibility on the primary and secondary instability of two canonical bodies, *i.e.* the circular cylinder and the NACA0012 airfoil at different angles of attack. To date, very few studies have addressed stability analysis in this peculiar regime and there is a lack of fundamental knowledge on the physics that drives compressible effects at low Reynolds numbers. To achieve this objective, a linear global stability solver has been developed and coupled to the high order compressible simulation code IC3 of DAEP at ISAE-Supaero.
First of all, we specify how the analysis of the two types of instabilities are treated:

- The primary instability develops on the steady stationary state (figure 1.11.a) and leads to a time periodic regime (figure 1.11.b). The identification of these instabilities needs the computation of a steady stationary base flow (fixed point solution) on which stability analysis is performed.
- The secondary instability develops on the time periodic state (figure 1.11.b) and leads to three-dimensionalisation (figure 1.11.c). This analysis does not require the steady base state computation, but only the time periodic two-dimensional state solution of the Navier–Stokes system (limit cycle solution). Then, a Floquet stability analysis is performed by the same stability solver.

The manuscript is organized as follows. The numerical methods used for the steady base state computation and the stability analysis are presented in Chapter 2, followed by the validation of the developed numerical stability solver on three different test cases: the lid-driven cavity (LDC), the two-dimensional circular cylinder and the NACA0012 airfoil at 16° angle of attack. In Chapter 3, results from DNS and primary instability analysis on the two-dimensional NACA0012 airfoil are discussed for both the incompressible and compressible flow regimes, with angles of attack ranging from $\alpha = 8°$ to $\alpha = 20°$ and Reynolds numbers up to $Re = 1000$. In Chapter 4, secondary instabilities on the three-dimensional circular cylinder wake and three-dimensional NACA0012 airfoil wake are analyzed in both the incompressible and compressible regimes. Conclusions and perspective are presented in Chapter 5.

1.6 Résumé

Ce chapitre introduit d'abord le contexte applicatif qui justifie l'étude des écoulements compressibles à bas nombre de Reynolds. Jusqu'à tout récemment, les analyses de stabilité hydrodynamique portaient principalement sur les conditions atmosphériques terrestres (voir tableau 1.1), où les écoulements à faible nombre de Reynolds sont considérés comme incompressibles. Au cours des dernières décennies, de nombreuses limites technologiques ont été dépassées et des applications comme le vol stratospherique et l'exploration martienne ont suscité un grand intérêt. Les écoulements concernés sont différents des régimes conventionnels et sont typiques des environnements à faible densité/pression (Mars ou stratosphère, voir tableau 1.1) ou des écoulements induits par le déplacement de micro-objets à grande vitesse. Pour ce nombre croissant d'applications, la compréhension des écoulements compressibles à faible nombre de Reynolds devient essentielle, mais une connaissance fondamentale de leur dynamique spécifique fait encore défaut.

La section 1.2 est consacrée à l'établissement des équations régissant l'évolution des écoulements compressibles, ainsi que la définition des nombres adimensionels caractérisant l'écoulement. La section 1.3 présente un rappel général des différentes approches utilisées dans le cadre de l'analyse de stabilité linéaire. Les limites des approches locales temporelles ou spatiales sont exposées au travers de la formulation en analyse locale convective-absolue, avec laquelle l'analyse globale est étroitement liée. Le problème aux valeurs propres résultant de la linéarisation du système de Navier–Stokes est dérivé à l'équation (1.9), permettant ainsi de définir les conditions de stabilité d'un écoulement :

- l'état de base est dit *globalement stable* si $\Re(\omega_j) < 0 \quad \forall j \in \mathbb{N}^*$. Cela signifie que toutes les perturbations sont amorties dans le temps. Dans ce cas, l'écoulement perturbé reviendra toujours à son état d'équilibre initial, appelé état de base ;

- l'état de base est *globalement instable* s'il existe au moins une valeur propre ω_j avec $\Re(\omega_j) > 0$. Cela signifie qu'il existe au moins une perturbation dont l'amplitude croît dans le temps. Dans ce cas, l'écoulement perturbé va diverger de l'état de base, soit indéfiniment, soit en convergeant vers un nouvel état d'équilibre ;

- l'état de base est dit *marginalement stable* si la valeur propre principale ω_j a une partie réelle nulle $\Re(\omega_j) = 0$. Dans ce cas, la perturbation n'est ni amortie ni amplifiée.

La section 1.4 présente les deux premières instabilités rencontrées dans le sillage de certains corps émoussés, comme le cylindre circulaire : la bifurcation de Hopf et la tridimensionalisation de l'écoulement. La bifurcation de Hopf correspond au passage d'une solution stationnaire à un régime périodique bidimensionnel auto-entretenu en formant un sillage de tourbillons plus connu sous le nom d'allée de von Kármán. D'un point de vue mathématique, cette transition est décrite par le passage d'une solution à point fixe instable à une solution de type cycle limite stable (images 1.7 et 1.8). La bifurcation de Hopf correspond au franchissement de l'axe réel par une paire de valeurs propres complexes ($\omega = \omega_r + i\omega_i$ pour le problème aux valeurs propres (1.9)). La tridimensionnalisation a lieu sur le sillage bidimensionnel de von Kármán et correspond à une instabilité du cycle limite périodique. Son analyse nécessite de recourir à une théorie spécifique, appelée théorie de Floquet, qui lie l'étude du cycle limite à celle d'un point fixe.

Jusqu'à présent, très peu d'études ont abordé l'analyse de la stabilité dans ce régime particulier et il y a un manque de connaissances fondamentales des écoulements compressibles à faible nombre de Reynolds. Dans ce cadre, l'objectif de ce travail est d'analyser les effets de la compressibilité sur l'instabilité primaire et secondaire de deux corps canoniques : le cylindre circulaire et l'aile NACA0012

à différentes incidences. Un solveur de stabilité globale linéaire a été développé et couplé au code de simulation compressible d'ordre élevé IC3 du DAEP à l'ISAE-Supaero. Tout d'abord, nous précisons comment l'analyse de ces deux instabilités est traitée :

- l'instabilité primaire se développe sur un état de base stationnaire (figure 1.11.a) et conduit à un régime périodique (figure 1.11.b). L'identification de ces instabilités nécessite le calcul d'un écoulement de base stationnaire (solution point fixe) sur lequel l'analyse de stabilité est effectuée ;
- l'instabilité secondaire se développe sur l'état périodique (figure 1.11.b) et conduit à une tridimensionnalisation de l'écoulement (figure 1.11.c). Cette analyse ne nécessite pas le calcul d'un état de base stationnaire, mais seulement la solution de l'état périodique bidimensionnel, solution du système de Navier–Stokes (solution de type cycle limite). Ensuite, une analyse de stabilité de Floquet est effectuée avec le même solveur de stabilité.

Le manuscrit est organisé comme suit. Les méthodes numériques utilisées pour le calcul de l'état de base stationnaire et l'analyse de stabilité sont présentées au chapitre 2, suivies par la validation du solveur numérique sur trois cas différents : la cavité, le cylindre circulaire et le profil NACA0012 pour une incidence de 16°. Le chapitre 3 présente les résultats de l'analyse DNS et de l'analyse de l'instabilité primaire sur le profil aérodynamique bidimensionnel NACA0012 pour les régimes d'écoulement incompressible et compressible, avec des incidences comprises entre $\alpha = 8°$ et $\alpha = 20°$ et des nombres de Reynolds allant jusqu'à $Re = 1000$. Dans le chapitre 4, les instabilités secondaires tridimensionnelles du cylindre circulaire et de l'aile NACA0012 sont analysées dans les régimes incompressible et compressible. Les conclusions et les perspectives sont présentées au chapitre 5.

Chapter 2

Numerical methods: steady base state computation and stability analysis

Abstract: This chapter is devoted to the numerical methods related to the base state computation and the global stability analysis. The validity of the continuum hypothesis is demonstrated in §2.1. The steady base state calculation methodologies and the modified governing equations for computing the filtered steady solution are introduced in §2.2, while §2.3 focuses on stability analysis and on the resolution of large eigenvalue problems. The numerical methods and code development are validated in §2.4 for the lid-driven cavity, the circular cylinder and the NACA0012 airfoil at an angle of attack $\alpha = 16°$. In §2.5 we summarize the present chapter in French.

Contents:

2.1 Continuum hypothesis

In the context of low Reynolds number compressible flows, due to the low density, the mean free path increases and the validity of the continuum hypothesis, and so the one of the NS equations, must be verified. The Knudsen number Kn, defined as the ratio of particle mean free path over the characteristic length scale, determines whether the medium can be considered as a continuum or not. The NS equations can be used under the assumption of continuum mechanics, i.e. if $Kn \lesssim 0.01$. At higher Knudsen number (rarefied flow), this assumption does not apply anymore and statistical mechanics is needed in order to model it[1].

In figure 2.1, the values of the Knudsen number are given as a function of the Reynolds and Mach number:

$$Kn = \frac{M_\infty}{Re}\sqrt{\frac{\gamma\pi}{2}} \tag{2.1}$$

where γ is the heat capacity ratio.

[1] Or the Navier–Stokes equations may be used with slip conditions in near continuum hypothesis.

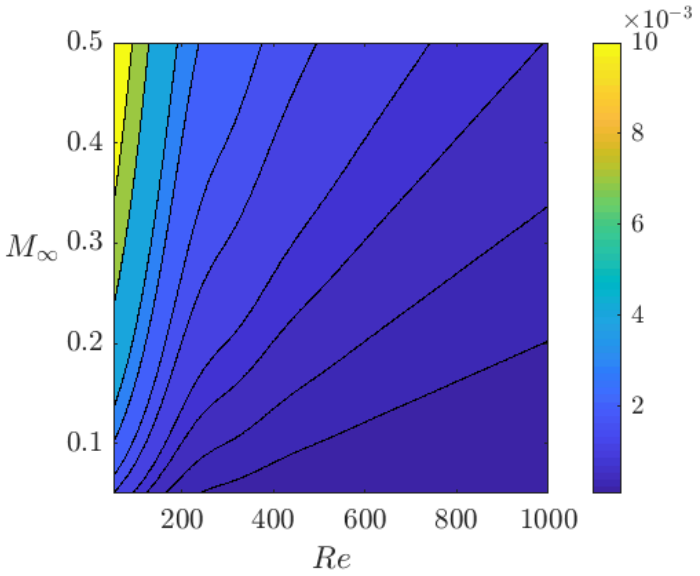

Figure 2.1 – Knudsen number isocontours in the Reynolds-Mach numbers plane, calculated using expression 2.1.

In the range of Reynolds ($Re \in [200; 1000]$) and Mach ($M_\infty \in [0.05; 0.5]$) numbers considered in this work, the maximum Knudsen number is $0.007 < 0.01$, so the continuum hypothesis is valid.

2.2 Steady base state computation

The steady base flow is obtained with the numerical solver IC3, a high order compact solver for the compressible NS equations developed at ISAE-SUPAERO [12, 44, 91]. IC3 is a parallel finite volume based code with explicit Runge–Kutta (RK) scheme for time integration. In this work, the third-order RK and the fourth-order centered [12] schemes have been used respectively for temporal and spatial discretization.

Below the critical threshold of the first bifurcation, the base flow corresponds to a steady solution of the NS equations which is directly obtained from direct numerical simulations (DNS). Above the critical threshold, instead, the numerically simulated flow is naturally unsteady and there are two types of base flow that can be used for the stability analysis. Either it can be chosen as the time-average of the unsteady solution or it can be computed enforcing the steadiness of the numerical solution. The choice of the base state is of crucial importance, since the stability responses are different with respect to the base flow considered. Indeed, as originally found by Barkley [8] in the case of the circular cylinder, before being theoretically proven by Sipp *et al.* [96] and generalized by Turton *et al.* [107], temporal averages of quasi-monochromatic frequency oscillating flows are marginally stable close to critical parameters, rendering the identification of bifurcation threshold very difficult, while the mode frequency matches the natural one. On the other hand, stability analysis performed on enforced steady solutions (obtained either by filtering or imposing symmetry conditions), enables a clear identification of the critical threshold, but the mode frequency diverges from the observed one when moving above the bifurcation threshold. In the present work, since we are interested in the influence of compressibility on bifurcations as well as the instabilities characteristics above the critical thresholds, we opt for the second option and resort to a filtering technique for computing a fixed point solution of the NS equations.

We use the selective frequency damping (SFD) method, first introduced by Åkervik *et al.* [1], which damps the highest temporal frequency by means of a low-pass filter introduced in the NS equations

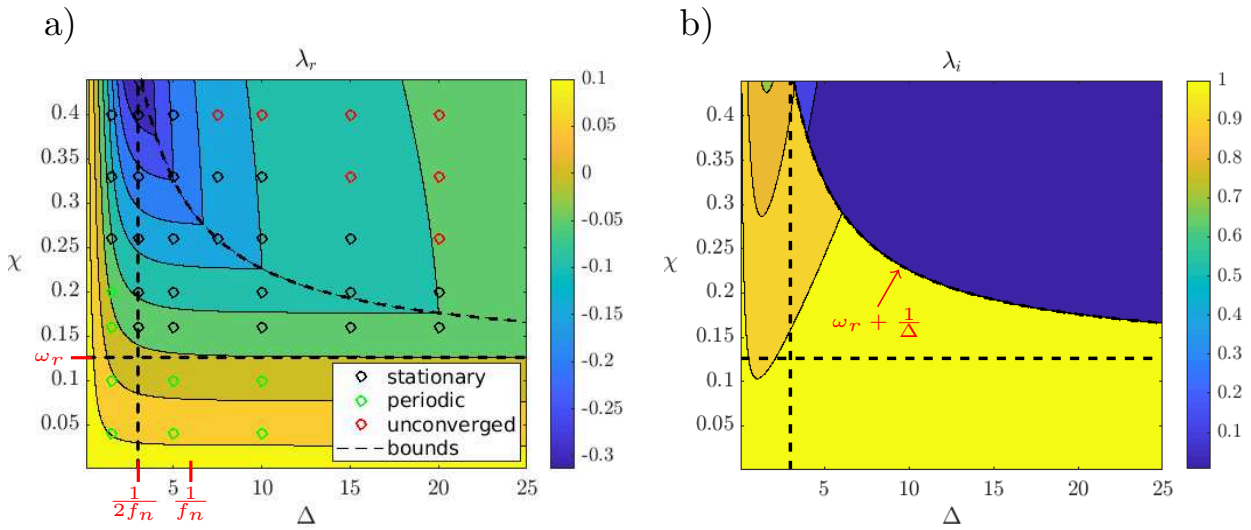

Figure 2.2 – Isocontours of the growth rate $\Re(\lambda^+) = \lambda_r^+$ (a) and the frequency $\Im(\lambda^+) = \lambda_i^+$ (b) in the (Δ, χ) plane as given by equation (2.4). The value of ω is set to $\omega_r + 2\pi f_n i = 0.126 + 1.04i$ which corresponds to the most amplified mode of the two-dimensional circular cylinder at $Re = 100$ and $M_\infty = 0.05$. The open circles represent the outcome of the numerical simulations of (2.2).

(1.2) in the following way:

$$\begin{aligned} \frac{\partial \boldsymbol{q}}{\partial t} &= \mathscr{N}(\boldsymbol{q}) - \chi(\boldsymbol{q} - \bar{\boldsymbol{q}}) \\ \frac{\partial \bar{\boldsymbol{q}}}{\partial t} &= \frac{\boldsymbol{q} - \bar{\boldsymbol{q}}}{\Delta} \end{aligned} \tag{2.2}$$

where $\bar{\boldsymbol{q}}$ is an approximation of the unknown steady solution, while χ and Δ are respectively the gain and the width of the low-pass filter. Both $\boldsymbol{q}$ and $\bar{\boldsymbol{q}}$ converge toward the targeted steady solution $\bar{\boldsymbol{q}}_0$, *i.e.* $\mathscr{N}(\bar{\boldsymbol{q}}_0) = 0$.

The convergence criterion of the steady stationary solution has been set on the L2 norm variation within the last 5 characteristic times as follows:

$$\frac{||\rho \boldsymbol{u}(t) - \rho \boldsymbol{u}(t_f - 5T)||_2}{||\rho \boldsymbol{u}(t_f - 5T)||_2} \leq 0.002 \quad \text{for} \quad t \in [t_f - 5T; t_f]. \tag{2.3}$$

The convergence toward the steady state depends on the chosen values of (Δ, χ). Such a steady state is obtained only if the most unstable eigenvalues $\lambda^\pm$ of the modified system (2.2) are stable, *i.e.* $\Re\{\lambda^\pm\} < 0$. As derived in Appendix A, the two most unstable eigenvalues $\lambda^\pm$ have the following expression:

$$\lambda^\pm = \omega - \chi(1 - \alpha^\pm) \qquad \text{where} \qquad \alpha^\pm = \frac{-1 + \chi\Delta - \Delta\omega \pm \sqrt{(1 - \chi\Delta + \Delta\omega)^2 + 4\chi\Delta}}{2\chi\Delta} \tag{2.4}$$

with ω denoting the most unstable eigenvalue of the unfiltered dynamical system. Figure 2.2 displays the isocontours of both the real and imaginary part of λ^+ in the (Δ, χ) plane, where ω has been set to $\omega_r + 2\pi f_n i = 0.126 + 1.04i$, which corresponds to the most amplified mode of the two-dimensional circular cylinder at $Re = 100$ and $M_\infty = 0.05$. Numerical simulations of system (2.2) have been performed for the circular cylinder with various values of (Δ, χ), starting from uniform initial conditions equal to the upstream quantities on the whole domain[2]. A maximal number of temporal iterations

[2] Another option is to initialize the SFD simulation with the unfiltered unsteady solution of the unmodified NS system.

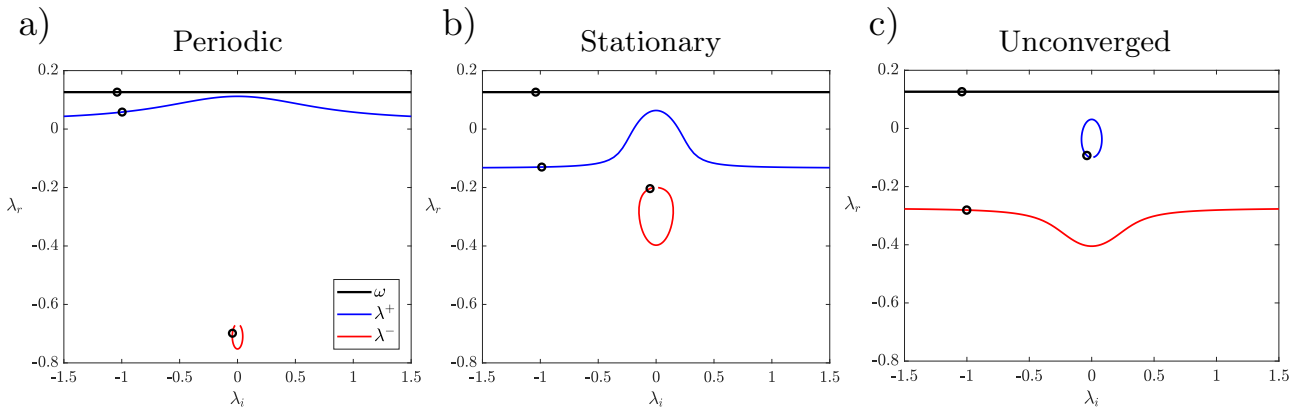

Figure 2.3 – Visualization of the mapping of ω toward $\lambda^{\pm}$ in the three different cases: a) periodic ($\Delta = 1.5, \chi = 0.1$), b) stationary ($\Delta = 5, \chi = 0.26$) and c) unconverged ($\Delta = 15, \chi = 0.4$) solutions. The black circles indicate the eigenvalue corresponding to the most unstable mode of the two-dimensional circular cylinder at $Re = 100$ and $M_\infty = 0.05$, $\omega = \omega_r \pm 2\pi f_n i = 0.126 \pm 1.04i$, and the two corresponding mapped eigenvalues $\lambda^{\pm}$.

has been set in order to stop a simulation which does not convergence. The results of the simulations are represented by the open circles in figure 2.2.a. Their outcome is either a converged stationary solution, a periodic solution or an unconverged solution, depending on the chosen values of (Δ, χ). In the two latter cases, the convergence criterion (2.3) was never satisfied within the maximal number of time-steps allowed.

Therefore, the parameters (Δ, χ) of the low-pass filter must be chosen adequately to ensure the convergence of the numerical simulations. Some theoretical bounds can be derived to set their values. First, the filter cutoff frequency must be chosen below the frequency of the unstable disturbances of the flow:

$$f_c = \frac{1}{\Delta_c} \leq f_n. \tag{2.5}$$

Åkervik *et al.* [1] even suggest that $f_c = \frac{1}{\Delta_c} \leq \frac{f_n}{2}$. Nevertheless, we can see in figure 2.2.a that for

$$f_c = \frac{1}{\Delta_c} \leq 2f_n \tag{2.6}$$

the simulation converges toward the filtered solution. We also remark that for high values of the gain χ, the convergence is achieved even with lower values of Δ. This is mainly due to the uniform initial condition, *i.e.* if the initial condition is taken as the unfiltered unsteady solution, the oscillations are not damped unless Δ satisfies condition (2.5). The gain of the filter χ must be high enough to damp the unstable mode, namely

$$\chi > \omega_r. \tag{2.7}$$

Figure 2.3 displays for three (Δ, χ) couples, the evolution of the two eigenvalues $\lambda^{\pm}$ in the complex plane, according to their analytical expression (2.4). The imaginary part of ω is varied, while its real part is fixed to $\omega_r = 0.126$, which corresponds to the growth rate of the most unstable mode for the circular cylinder at $Re = 100$ and $M_\infty = 0.05$. In the first case, figure 2.3.a, where $\Delta = 1.5$ and $\chi = 0.1$, condition (2.7) is not satisfied and it can be seen that the eigenvalue λ^+ has a lower growth rate with respect to ω, but is still positive. This prevents the modified system to converge towards a steady stationary solution and rather yields a periodic solution. The value of χ is here not high enough to map the eigenvalue ω into the damped part of the spectrum, *i.e.* $\Re(\lambda^+) \leq 0$, and this is why the numerical system leads to an unsteady periodic solution. Another condition recommended by Åkervik

et al. [1] to ensure convergence, or at least a faster convergence, is

$$\omega_r < \chi < \omega_r + \frac{1}{\Delta}. \tag{2.8}$$

In figure 2.3.c, we see that when this condition is not satisfied, *i.e.* $\chi > \omega_r + \frac{1}{\Delta}$, the most unstable mode complex frequency ω is mapped into an eigenvalue λ^+ whose real part $\Re(\lambda^+)$ is negative and imaginary part $\Im(\lambda^+)$ is very close to 0. The negative real part ensures the steadiness of the solution, but the low frequency corresponds to very long oscillation periods, *i.e.* longer temporal scales, inducing the simulation to converge very slowly [1]. Therefore, the fixed number of temporal iterations is not large enough to obtain the stationary solution. We define this case as the unconverged case[3]. When the couple (Δ, χ) is well within the bounds, the system converges towards the stationary solution within the fixed number of temporal iterations, see figure 2.2.b, and corresponds to a fixed point solution of the NS system.

Therefore, despite its ease of implementation, the SFD method should be used with some *a priori* knowledge on the most unstable mode in order to ensure the convergence of the simulations. If the mode characteristics are not known *a priori*, it is possible to use an adaptive algorithm as proposed by Jordi *et al.* [55]: the SFD method is combined with a flow stability analysis, in order to compute an approximation of the most unstable mode for the "partially converged" steady base flow and iteratively find the optimal parameters $(\Delta_{opt}, \chi_{opt})$. Close to the bifurcation threshold, instead, one can consider that $\omega_r \ll f_c$, therefore $\chi = f_c$ stands as a good compromise. In this work, the filter parameters (Δ,χ) are deduced from the unfiltered DNS solutions: $\Delta = \frac{1}{f_n}$ and $\chi = \frac{1}{\Delta}$, where f_n is the natural frequency.

2.3 Stability analysis

As already presented in section 1.2, the dynamics of a perturbation $\boldsymbol{q}' = \tilde{\boldsymbol{q}} e^{\omega t}$, with $\tilde{\boldsymbol{q}} = [\tilde{\rho}, \widetilde{\rho \mathbf{u}}, \widetilde{\rho E}]^T$, in the neighborhood of the base state $\boldsymbol{q}_b$ reads [4]:

$$\frac{\partial \boldsymbol{q}'}{\partial t} = \mathscr{L} \boldsymbol{q}' \tag{2.9}$$

where $\mathscr{L} = \left.\frac{\partial \mathscr{N}(\boldsymbol{q})}{\partial \boldsymbol{q}}\right|_{\boldsymbol{q}_b}$ is the Jacobian matrix of the discretized NS operator computed at the base state $\boldsymbol{q}_b$. In order to find the dominant modes which govern the asymptotic behavior of the perturbation, we have to compute the spectrum of $\mathscr{L}$. However, explicitly assembling the Jacobian matrix of very large-scale dynamical systems can be very expensive and time consuming. For this reason, the so-called matrix-free approaches are becoming very popular nowadays: the coefficients of the Jacobian matrix are not computed explicitly, but rather accessed by evaluating matrix-vector products [65]. A large number of iterative methods used to solve eigenvalue problems allow for a matrix-free implementation, including the Krylov–Schur method [47, 98] which has been chosen here. This method is an improvement of the Arnoldi algorithm and belongs to the class of Krylov projection methods whose aim is to find an approximation of the most relevant eigenvalues and corresponding eigenvectors of a matrix, projecting

[3] In this case, the term unconverged refers to the system that did not reach a solution either stationary or periodic within the fixed number of temporal iterations, and for this reason it does not even satisfy the convergence criterion 2.3. It is different from the periodic solution, for which the convergence criterion 2.3 is not satisfied either, even if the system converged toward a (periodic) solution within the fixed number of temporal iterations.

[4] It should be noticed that, even though the time average solution is usually taken as base state for the stability analysis, it is not a solution of the NS system and it does not satisfy $\dot{\boldsymbol{q}}_b = \mathscr{N}(\boldsymbol{q}_b)$, while the filtered solution does.

the original problem onto an orthonormal basis of the Krylov subspace. Given an eigenproblem

$$A\mathbf{x} = \lambda\mathbf{x}\,, \tag{2.10}$$

the Krylov subspace of m-dimension $\mathscr{K}_m$ is generated by the $n \times n$ matrix A and a n-dimensional vector $\mathbf{b}$ as follows:

$$\mathscr{K}_m(A, \mathbf{b}) = \text{span}\left\{\mathbf{b}, A\mathbf{b}, A^2\mathbf{b}, ..., A^{m-1}\mathbf{b}\right\} \tag{2.11}$$

where $\{\mathbf{b}, A\mathbf{b}, A^2\mathbf{b}, ..., A^{m-1}\mathbf{b}\}$ is called the Krylov sequence. This sequence, under some assumptions, converges towards the eigenvector associated with the largest modulus eigenvalue as $m \to \infty$ (power iteration method). In order to describe the Krylov–Schur procedure, we first have to introduce the Arnoldi algorithm.

2.3.1 The Arnoldi algorithm

Considering problem (2.10) and the Krylov sequence, we can write

$$A\mathscr{K}_m \simeq \mathscr{K}_m \underbrace{[\mathbf{e}_2, \mathbf{e}_3, ..., \mathbf{e}_m, -\boldsymbol{c}]}_{\text{companion matrix}}\,. \tag{2.12}$$

The computation of the companion matrix spectrum is cheaper than that of A and, since it represents the projection of A onto $\mathscr{K}_m$, its eigenpairs approximate those of A. We should note that in (2.12), the equality is achievable only if $\boldsymbol{c} = -\mathscr{K}_m^{-1}A^n b$, which is not convenient to compute; moreover, increasing the Krylov subspace dimension m, the sequence consists of vectors that become almost linearly dependent , making the companion matrix ill-conditioned.

Approximation (2.12) can be reformulated as follows:

$$A\mathscr{V}_m = \mathscr{V}_m\mathscr{H} + \underbrace{\mathbf{r}\,\mathbf{e}_m^T}_{\text{residual}} \tag{2.13}$$

where $\mathscr{V}_m$ is an orthonormal basis of the Krylov subspace, normalized with the euclidean norm. $\mathscr{H}$ is an upper Hessenberg matrix whose spectrum approximates that of A and the residual indicates how far the orthonormal basis is from an invariant subspace of A [47]. Figure 2.4.a visually represents this factorization.

The algorithm can be explicitly summarized as follows:

Algorithm 1 Arnoldi algorithm

Input: $n \times n$ Matrix A, initial vector $\mathbf{v}_1$ of norm 1, number of steps $m \leq n$
Output: $\mathscr{V}_m$, $\mathscr{H}$, $\mathbf{r}$, residual norm β

$\mathscr{H} = [\,]$
$\mathscr{V}_1 = [\mathbf{v}_1]$
for k=1:m-1 **do**
  $\mathbf{r} = \mathrm{A}\ \mathbf{v}_k$
  $\mathbf{h} = \mathscr{V}^T\mathbf{r}$
  $\mathbf{r} = \mathbf{r} - \mathscr{V}\mathbf{h}$
  $\beta = \|\mathbf{r}\|$
  $\mathscr{H} = \begin{bmatrix} \mathscr{H} & \mathbf{h} \\ 0 & \beta \end{bmatrix}$
  $\mathbf{v}_{k+1} = \mathbf{r}/\beta$
  $\mathscr{V}_{k+1} = [\mathscr{V} \quad \mathbf{v}_{k+1}]$
end for
$\mathbf{r} = A\mathbf{v}_m$
$\mathbf{h} = \mathscr{V}_m^T\mathbf{r}$
$\mathscr{H} = \begin{bmatrix} \mathscr{H} & \mathbf{h} \end{bmatrix}$

The procedure ends by computing the eigenpairs of $\mathscr{H}$ and finally the eigenvalues and eigenvectors of A are approaximated by $(\lambda_A, \mathbf{x}_A) \simeq (\lambda_{\mathscr{H}}, \mathscr{V}_m\mathbf{x}_{\mathscr{H}})$. However, the Krylov subspace dimension m required to ensure the convergence of a given number of eigenvalues, may be too large when using the Arnoldi method. This can yield to very large matrices that exceed the available memory and considerably increase the cost of computing $\mathscr{H}_m$-eigenpairs (the cost grows with m^3).

2.3.2 The Krylov–Schur algorithm

The Krylov–Schur method is an extension of the Arnoldi algorithm since it incorporates an effective restarting scheme, which fixes the dimension of the Krylov-subspace, and iteratively applies the Arnoldi factorization. More precisely, if k eigenpairs are needed, the Krylov subspace dimension is fixed so that $m > k$, the m-Arnoldi factorization is called. If k eigenpairs have not converged yet, the unwanted part of the factorization is discarded in order to restart the process with the remaining eigenvectors as the new initial Krylov subspace [47, 65, 98]. The discarding process is achieved after two transformations: a Schur decomposition and a reordering.
The main steps of the algorithm can be described as follows:
Inputs: $n \times n$ matrix A, initial unitary vector $\mathbf{v}_1$, order of the decomposition (dimension of the Krylov subspace) $m < n$, desired eigenpairs $k < m$.

1. Compute the m-Arnoldi factorization getting $\mathscr{V}_m$, $\mathscr{H}$ and check if enough eigenpairs have converged, if not, continue to step 2

2. Compute a QR factorization finding Q_1, orthogonal matrix, such that $\tilde{\mathscr{B}} = Q_1\mathscr{H}Q_1^T$ is in real Schur form (see figure 2.4.b). The approximation (2.14) becomes

$$A\mathscr{V}_m Q_1^T = \mathscr{V}_m Q_1^T \underbrace{Q_1\mathscr{H}Q_1^T}_{\tilde{\mathscr{B}}} + \mathbf{r}\,\underbrace{\mathbf{e}_m^T Q_1^T}_{\tilde{b}^T}. \tag{2.14}$$

3. The eigenpairs of $\tilde{\mathscr{B}}$ are divided in two subsets: the k "wanted"(those with largest module eigenvalues) and the $m - k$ "unwanted" eigenpairs.

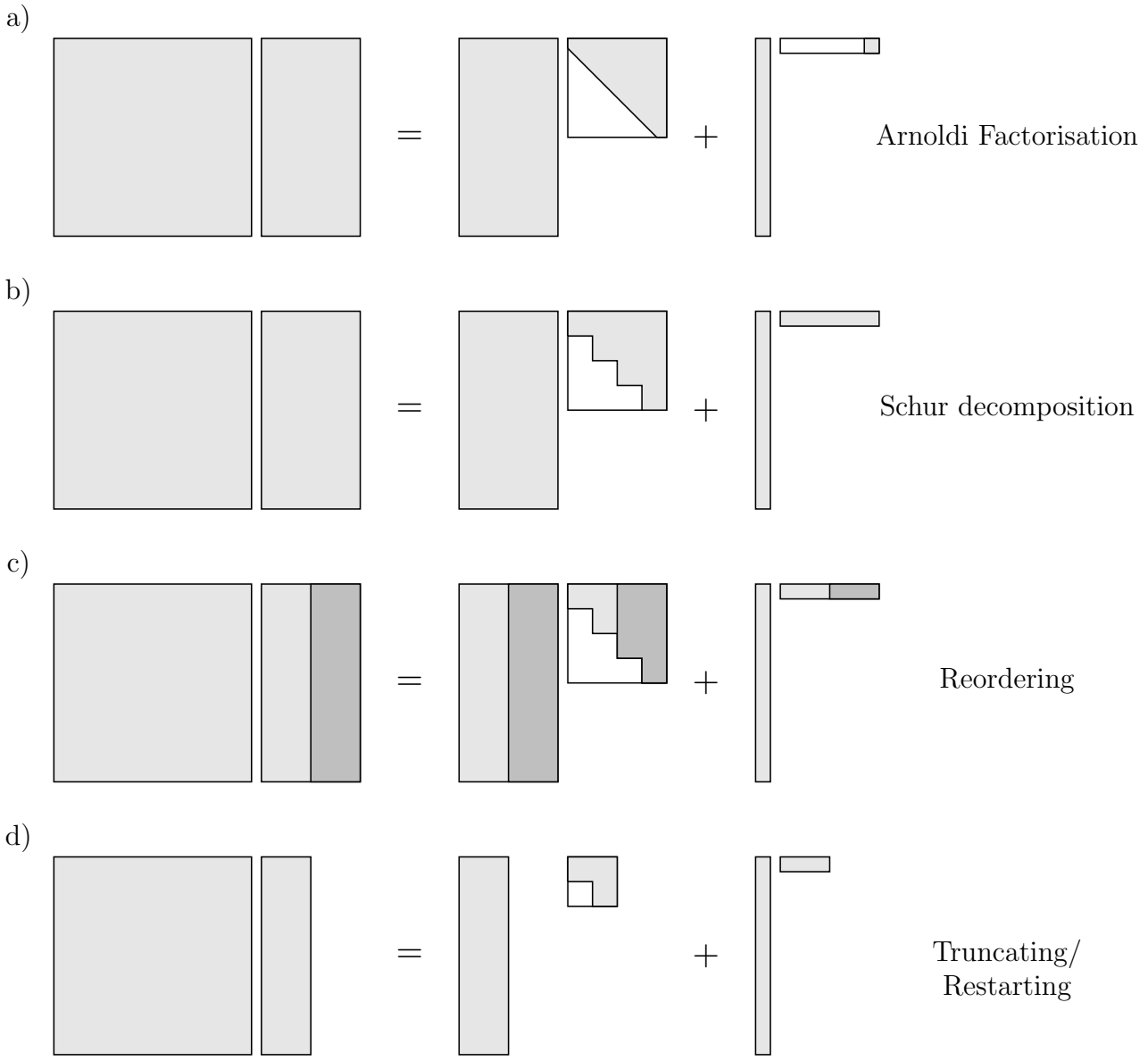

Figure 2.4 – Matrix representation of the Krylov–Schur algorithm.

4. Matrix $\tilde{\mathscr{B}}$ is transformed by another orthogonal matrix Q_2, $\mathscr{B} = Q_2 \tilde{\mathscr{B}} Q_2^T$, in order to have the "wanted" Ritz pairs on the top of $\mathscr{B}$ (see figure 2.4.c). At this stage the problem has the following form:

$$A\mathscr{V}_m Q_1^T Q_2^T = \mathscr{V}_m Q_1^T Q_2^T \underbrace{Q_2 Q_1 \mathscr{H} Q_1 Q_2}_{\mathscr{B}} + \mathbf{r} \underbrace{\mathbf{e}_m^T Q_1^T Q_2^T}_{b^T} \tag{2.15}$$

$$A\mathscr{V}_m Q_1^T Q_2^T = \mathscr{V}_m Q_1^T Q_2^T \begin{bmatrix} \mathscr{B}_{wanted} & * \\ 0 & \mathscr{B}_{unwanted} \end{bmatrix} + \mathbf{r} \begin{bmatrix} \boldsymbol{b}_{wanted}^T & * \end{bmatrix}. \tag{2.16}$$

5. The Krylov–Schur decomposition is truncated, discarding the "unwanted" (smallest module eigenvalues) part (see figure 2.4.d).

$$A\tilde{\mathscr{V}}_k = \tilde{\mathscr{V}}_k \mathscr{B}_{wanted} + \mathbf{r}\, \boldsymbol{b}_{wanted}^T \tag{2.17}$$

where $\tilde{\mathscr{V}}_k$ corresponds to the first $k < m$ columns of $\mathscr{V}_m Q_1 Q_2$.

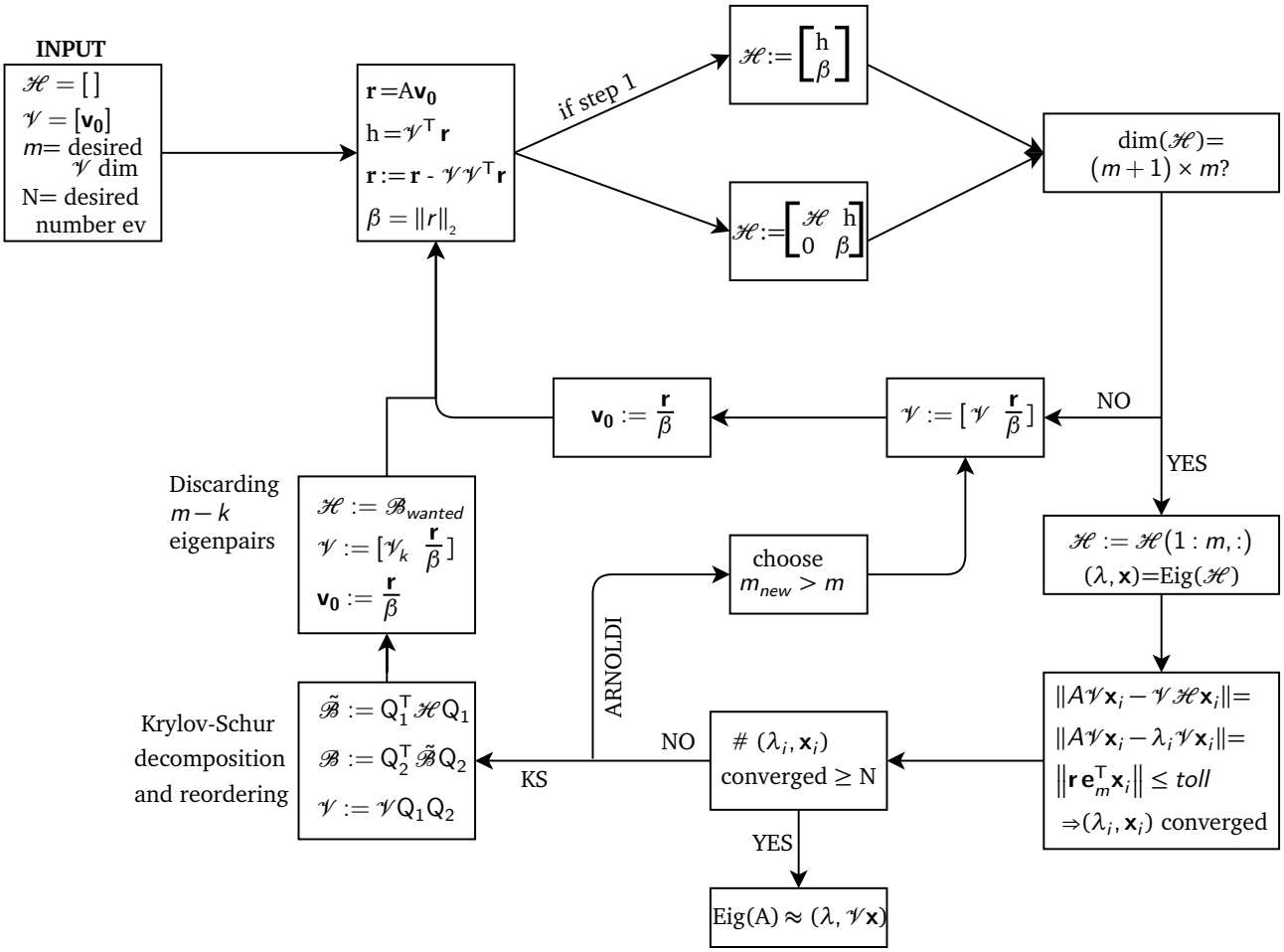

Figure 2.5 – Schematic representation of Arnoldi and Krylov–Schur algorithms.

6. Recall the Arnoldi factorization from k to m, with starting vector $\mathbf{v}_k = \mathbf{r}$ and initial orthogonal basis $\tilde{\mathcal{V}_k}$.

7. Compute the eigenpairs $(\lambda_i, \mathbf{x}_i)_{\mathcal{B}}$ and check convergence for a given tolerance threshold:

$$\begin{aligned} \|A\mathcal{V}_m\mathbf{x}_i - \mathcal{V}_m\mathcal{B}\mathbf{x}_i\| &= \|A\mathcal{V}_m\mathbf{x}_i - \lambda_i\mathcal{V}_m\mathbf{x}_i\| \\ &= \left\|\mathbf{v}_{m+1}\mathbf{b}_{m+1}^T\mathbf{x}_i\right\| \\ &< \text{tol}. \end{aligned} \tag{2.18}$$

8. If enough eigenpairs have not converged, restart from step 2.

A schematic representation of the algorithm is given in figure 2.5.

2.3.3 Matrix-free formulations

The matrix-free formulation can be used in Arnoldi-based algorithms since an explicit representation of the Jacobian matrix, whose eigenvalues are to be calculated, is not necessary. Indeed, only matrix-vector products are needed for the construction of the Krylov subspace. There are mainly two ways for easily achieving this formulation within a CFD code and calculate the Jacobian eigenpairs [43]:

- **Jacobian-free method**
  The Taylor series expansion (1.4) is applied to the NS equations around the steady state q_b.

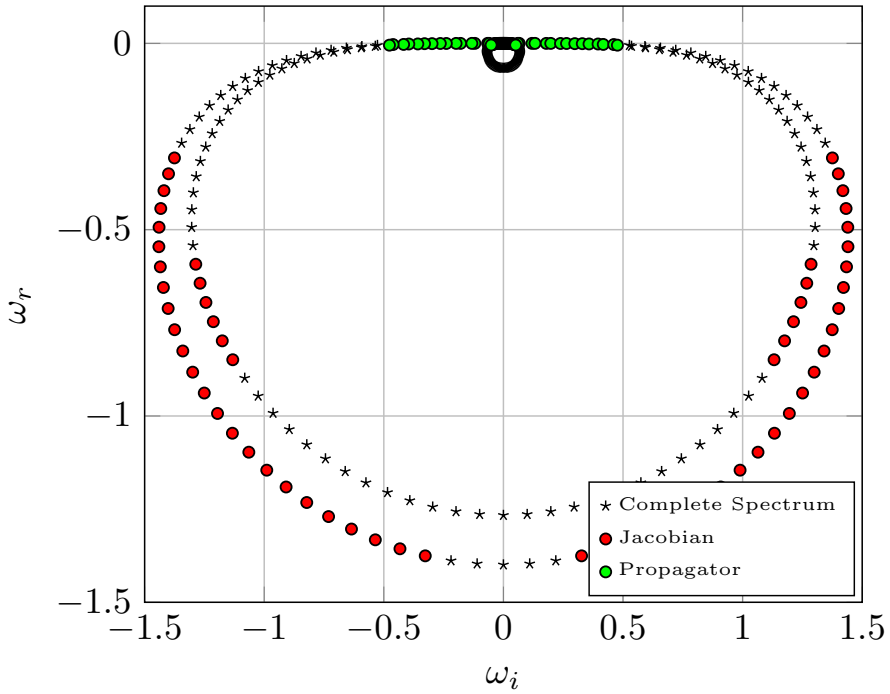

Figure 2.6 – Spectrum of the uniform flow test case.

Therefore, the matrix vector product (*i.e.* the application of the Jacobian matrix onto a given vector) is computed through a finite difference formulation (in this case first order)

$$\mathscr{L}\boldsymbol{q}' = \frac{\mathscr{N}(\boldsymbol{q}_b + \epsilon\boldsymbol{q}') - \mathscr{N}(\boldsymbol{q}_b)}{\epsilon}. \tag{2.19}$$

Higher order finite difference schemes can be implemented as well. This method is usually coupled with the Newton method for computing a stationary solution [19, 58].

- **Time-stepping exponential transformation**
  We now consider the analytic solution of system (2.9), already introduced in section 1.4.2:

$$\boldsymbol{q}'(\tau) = \mathscr{M}\boldsymbol{q}'(0) \tag{2.20}$$

with the propagator $\mathscr{M}$. For a strictly constant operator $\mathscr{L}$, $\mathscr{M}$ is the exponential propagator $\mathscr{M} = e^{\mathscr{L}\tau}$. If $\mathscr{L}$ varies, instead, $\mathscr{M}$ is an average propagator $\mathscr{M} = e^{\bar{\mathscr{L}}\tau}$. The algorithm can be applied on $\mathscr{M}$ instead of $\mathscr{L}$, where the matrix-vector product $\mathscr{M}\boldsymbol{q}'$ corresponds to the perturbation at a certain time $t = \tau$. In Chiba's method [23, 24, 104], $\mathscr{M}\boldsymbol{q}'$ is approximated as follows:

$$\mathscr{M}\boldsymbol{q}' = \frac{\boldsymbol{q}_+^\tau - \boldsymbol{q}_-^\tau}{2\epsilon} \tag{2.21}$$

where $\boldsymbol{q}_+^\tau$ and $\boldsymbol{q}_-^\tau$ are the DNS solutions corresponding to the initial conditions $(\boldsymbol{q}_b + \epsilon\boldsymbol{q}')$ and $(\boldsymbol{q}_b - \epsilon\boldsymbol{q}')$ integrated until τ. The same numerical parameters used for the base state computation, like the Courant-Friedrichs-Lewi coefficient (CFL), and numerical schemes (third-order RK and fourth-order centered schemes) have been used for the computation of $\boldsymbol{q}_+^\tau$ and $\boldsymbol{q}_-^\tau$.

The Krylov sequence takes the following form:

$$\begin{aligned}&\{\boldsymbol{q}'(0), \mathscr{M}\boldsymbol{q}'(0), \mathscr{M}^2\boldsymbol{q}'(0), \mathscr{M}^3\boldsymbol{q}'(0), ..\}\\ =&\{\boldsymbol{q}'(0), \boldsymbol{q}'(\tau), \mathscr{M}\boldsymbol{q}'(\tau), \mathscr{M}^2\boldsymbol{q}'(\tau), ..\}\\ &...\\ =&\{\boldsymbol{q}'(0), \boldsymbol{q}'(\tau), \boldsymbol{q}'(2\tau), \boldsymbol{q}'(3\tau), ..\}.\end{aligned} \tag{2.22}$$

Once the eigenpairs $(\lambda_{\mathscr{M}}, \mathbf{x}_{\mathscr{M}})=(\mu, \widetilde{\boldsymbol{q}}_{\mathscr{M}})$ of $\mathscr{M}$ are computed, the eigenpairs of $\mathscr{L}$ $(\lambda_{\mathscr{L}}, \mathbf{x}_{\mathscr{L}})=(\omega, \widetilde{\boldsymbol{q}}_{\mathscr{L}})$ can be obtained by inverting the exponential transformation:

$$\begin{aligned}\omega &= \frac{\log|\mu| + i\ \arg(\mu)}{\tau}\\ \widetilde{\boldsymbol{q}}_{\mathscr{L}} &= \widetilde{\boldsymbol{q}}_{\mathscr{M}}.\end{aligned} \tag{2.23}$$

An easier exponential transformation can be performed having access to a linearized NS equations solver. In this case the application of $\mathscr{M}$ onto a given vector simply corresponds to the time-marching of the linearized solver [7, 65].

Applying Arnoldi-based algorithms on $\mathscr{M}$ instead of $\mathscr{L}$ is usually preferable, since Arnoldi-based algorithms converge toward the eigenvectors associated with the eigenvalues of largest modulus, that may not correspond to the most amplified modes, *i.e.* the eigenvalues with the largest real part[5]. In figure 2.6 the complete spectrum of a uniform flow test case is presented with the parts of the spectrum computed by the Jacobian and the propagator approach. It can be seen that the two approaches converge toward a different part of the spectrum. Those calculated from the propagator, using the time-stepping approach and relation (2.23), correspond to the most amplified modes, unlike when the method is directly applied to the Jacobian using the Jacobian-free method.

The choice between Jacobian-free and time-stepping exponential transformation can be made for the analysis of primary instabilities, but not for that of secondary instabilities. As introduced in 1.4.2, the Floquet analysis used for computing secondary instabilities requires the evolution of the perturbation after each period T and results in the computation of the eigenvalues of matrix $\mathscr{M}$. Therefore the time-stepping exponential transformation allows to perform Floquet analysis, while the Jacobian-free method does not. In this work, the time-stepping exponential transformation approach has been used for studying both primary and secondary instabilities.

In this formulation, two specific numerical parameters have to be tuned, apart from those of the CFD solver: ϵ and τ. The finite difference parameter ϵ has to be large enough to avoid round-off errors, but not too large to prevent non-linear effects. There is no general rule to set this parameter. For example, Tezuka *et al.* [104] use $\epsilon \in [0.01; 1]$ whereas De Pando *et al.* [36] recommend $\epsilon \in [10^{-8}; 10^{-5}]$. Other authors, like An *et al.* [2] and Mack *et al.* [67] instead, set ϵ as a function depending on both the base state and the perturbation. In our simulations, we have set $\epsilon \approx 10^{-6}$. Regarding the parameter τ, it depends on whether we are computing the primary or secondary instability:

- for primary instabilities, where the base state is a stationary solution, *i.e.* fixed point solution computed by the SFD method 2.2, τ must be smaller than half the oscillation period of the mode, in order to avoid aliasing effects, and large enough to filter out numerical disturbances;
- for secondary instabilities, which develop on the periodic Von Kármán street, the base state is

[5] Considering for example two real eigenvalues $\lambda_1 = -3$ and $\lambda_2 = 1$, the algorithm first converge to λ_1 even if the leading eigenvalue is λ_2. The exponential transformation (propagator) ensures that the less stable eigenvalue is the one with the largest modulus ($e^{\lambda_1} = e^{-3} < e^1 = e^{\lambda_2}$).

taken as the periodic DNS solution of the NS equations (1.1) and $\tau = T$, where T is the oscillation period of the base state.

2.3.4 Stability analysis with IC3

The time-stepping matrix-free exponential transformation using full[6] DNS has been implemented by coupling the software library SLEPc with our CFD solver IC3. This library solves large scale sparse eigenvalue problems and has been shown to perform better than ARPACK [47]. In addition, this library allows a matrix-free implementation, using the so called SHELL Matrix and defining a new operation, *MatMult*, for a generic product computation $\boldsymbol{y} = A\boldsymbol{x}$, where $\boldsymbol{x}$ is the input and $\boldsymbol{y}$ the output of the *MatMult* function. In our case the product is finite difference (2.21).

MatMult is called iteratively for the construction of the Krylov subspace. Except for the first iteration, the input $\boldsymbol{x}$ in *MatMult* corresponds to the normalized output $\boldsymbol{y}$ of the previous iteration. These calls are entirely managed by the library and the perturbation vector is a read-only variable, therefore, it cannot be modified. It would have been useful to have access on this variable in order to modify it, since the normalization performed by the library is done through the L2-norm. The main problem is that, in the vector, all the conservative variables are concatenated ($\boldsymbol{q}' = [\rho'^T \ \rho\boldsymbol{u}'^T \ \rho e'^T]^T$), therefore, the proper norm should be $\|N^{-1}\boldsymbol{q}\|_2$, where

$$N = \begin{bmatrix} \rho_\infty & 0 & 0 \\ 0 & \rho_\infty u_\infty & 0 \\ 0 & 0 & \rho_\infty u_\infty^2 \end{bmatrix} \tag{2.24}$$

In order to address this problem, we have decided to compute a normalized Krylov subspace. This corresponds to the application of the method to the normalized flow $N^{-1}q$, but, as we will see later on, this can be achieved implicitly, avoiding the computation of the normalized flow. In fact, computing the normalized flow would have been overly demanding, since it would have implied the modification of the viscosity and of the gradients calculation in order to be conform to the normalization process.

The main steps of the *MatMult* operation and the Krylov subspace construction[7] are the following:

1. the initial perturbation $\boldsymbol{q}'_0 = \boldsymbol{q}'_0(x, y, z)$ is a white noise;
2. normalization of $\boldsymbol{q}'_0$ by L2 norm $\hat{\boldsymbol{q}}'_0 = \frac{\boldsymbol{q}'_0}{\|\boldsymbol{q}'_0\|_2}$ and $\mathscr{K} = [\hat{\boldsymbol{q}}'_0]$;
3. $\hat{\boldsymbol{q}}'_0$ is the input of the *MatMult* operation;
4. computation of $\boldsymbol{q}^0_+ = \boldsymbol{q}_b + \epsilon N\hat{\boldsymbol{q}}'_0$ and $\boldsymbol{q}^0_- = \boldsymbol{q}_b - \epsilon N\hat{\boldsymbol{q}}'_0$;
5. $\boldsymbol{q}^0_+$ and $\boldsymbol{q}^0_-$ are set as initial conditions for the IC3 time integration and advanced in time until τ, obtaining $\boldsymbol{q}^\tau_+$ and $\boldsymbol{q}^\tau_-$. The same boundary conditions than those for the computation of the base state are used;
6. computation of $\mathscr{M}N\hat{\boldsymbol{q}}'_0$ using equation (2.21);
7. the result is normalized: $\boldsymbol{q}'_1 = N^{-1}\mathscr{M}N\hat{\boldsymbol{q}}'_0$ is the output of *MatMult*;
8. normalization of $\boldsymbol{q}'_1$ by L2 norm $\hat{\boldsymbol{q}}'_1 = \frac{\boldsymbol{q}'_1}{\|\boldsymbol{q}'_1\|_2}$ and $\mathscr{K} = [\mathscr{K} \ \ \hat{\boldsymbol{q}}'_1]$;

[6] Full here refers to the fact that it is a DNS of the non-linear NS equations, instead of a DNS of the linearized NS equations.

[7] Orthonormal basis of the Krylov sequence 2.22

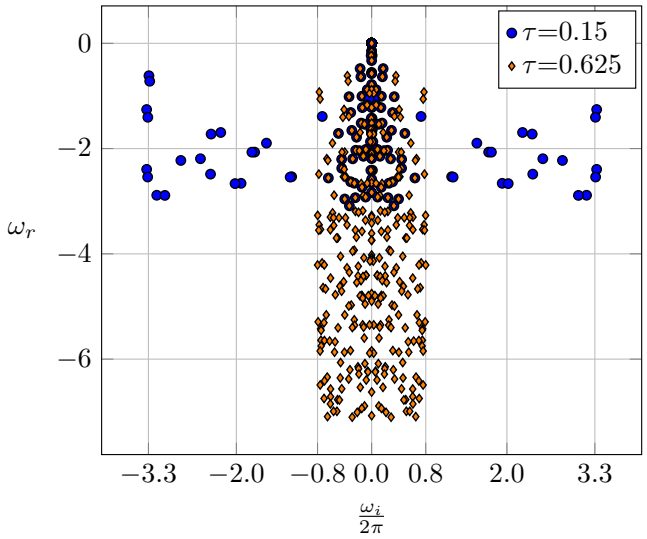

Figure 2.7 – Cutoff effect of τ on the spectrum of the LDC at $Re = 200$ and $M_\infty = 0.05$.

9. $\hat{\boldsymbol{q}}_1'$ is the input of the *MatMult* operation. Restart the process from step 3, considering $\hat{\boldsymbol{q}}_1'$ instead of $\hat{\boldsymbol{q}}_0'$.

Another point that we have taken into account concerns the calculation of the primitive perturbation variables. In order to compute the perturbation pressure and temperature fields, we have linearized the following equations:

$$\begin{aligned} \boldsymbol{u} &= \frac{\rho \boldsymbol{u}}{\rho} \\ e &= \frac{\rho E}{\rho} - 0.5\boldsymbol{u}^2 \\ T &= \frac{e}{c_v} \\ P &= \rho R T \end{aligned} \tag{2.25}$$

Therefore, remembering that $\cdot'$ variables refer to the perturbation, we obtain:

$$\begin{aligned} \boldsymbol{u}' &= \frac{(\rho \boldsymbol{u})'}{\rho} - \frac{\rho \boldsymbol{u}}{\rho^2}\rho' \\ e' &= \frac{(\rho E)'}{\rho} - \frac{\rho E}{\rho^2}\rho' - \boldsymbol{u}\cdot\boldsymbol{u}' \\ T' &= \frac{e'}{c_v} \\ P' &= \rho' R T + \rho R T' \end{aligned} \tag{2.26}$$

2.4 Code validation and parameters dependence

The stability solver has been validated against three two-dimensional test cases presented in this subsection: the lid-driven cavity (LDC), the flow past a circular cylinder and the NACA0012 airfoil at 16° angle of attack. The dependence on the temporal parameters (CFL and τ) and on the Krylov subspace dimension (m) is analyzed on the LDC, while the dependence on the finite difference parameter (ϵ) and the convergence tolerance ($toll$) is investigate on the circular cylinder.

2.4.1 Lid-driven cavity

The lid-driven cavity (LDC) consists of a square box of size L whose upper wall is a moving isothermal no-slip wall with constant tangential velocity U_∞ while the three other sides are fixed adiabatic no-slip walls.

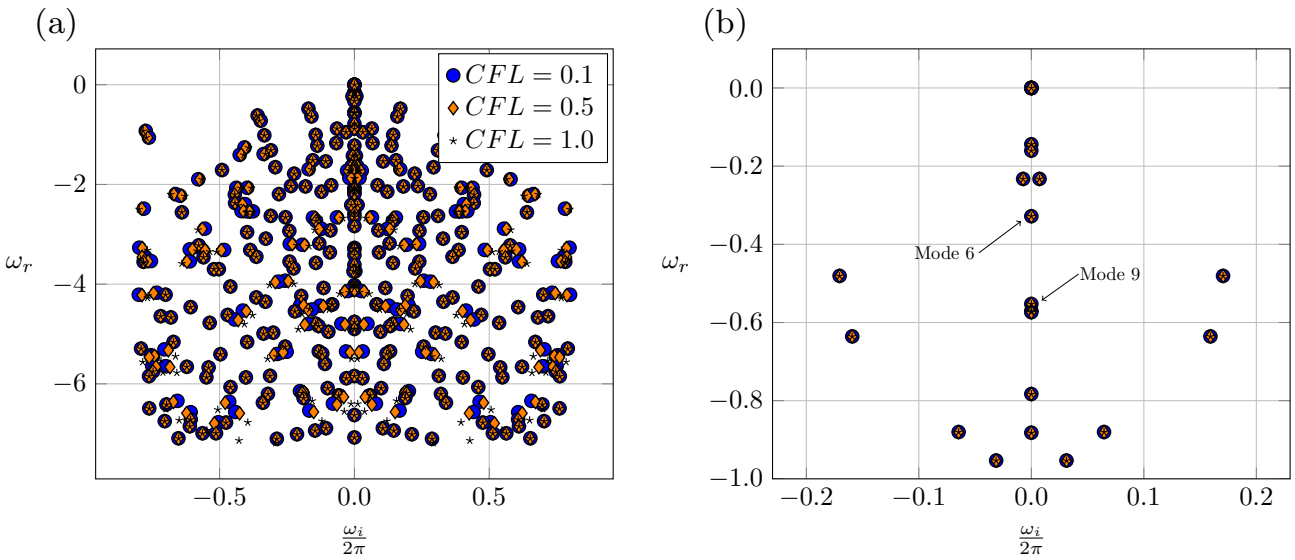

Figure 2.8 – (a) Effect of CFL number on the spectrum of the LDC with $\tau = 0.625$ at $Re = 200$ and $M_\infty = 0.05$ and (b) close-up view on the most relevant part of the spectrum.

All LDC simulations have been performed at $Re = 200$ and $M_\infty = 0.05$ in order to compare our results with those of Gómez *et al.* [42], who investigated the efficiency of the time-stepping approach on the incompressible LDC. To perform grid refinement analysis, three different meshes have been tested. The coarsest M1, medium M2 and finest M3 meshes have 48×48, 64×64 and 94×94 elements, respectively. In figure 2.7, the spectra obtained with mesh M2 and two different values of τ are presented. The cutoff frequency f_c given by

$$|f_c| = \left|\frac{\omega_{i_c}}{2\pi}\right| = \frac{1}{2\tau} \tag{2.27}$$

for a given τ is clearly visible on this figure. Here, there are no mode with frequencies greater than $|f_c|$ ($|f_c| = 3.33$ for $\tau = 0.15$ and $|f_c| = 0.8$ for $\tau = 0.625$).

In figure 2.8.a, the spectra obtained for different values of CFL number show that the time step does not influence the results, especially for the largest growth rates, as it can be seen in the close-up view of the spectrum displayed in figure 2.8.b. The two stationary modes labelled Mode 6 and Mode 9 are those described in Gómez *et al.* [42] and are used for validation. Their growth rates are reported in table 2.1 for the different meshes and are in close agreement with those obtained by Gómez *et al.* [42].

	M1	M2	M3	Gómez *et al.*
Mode 6	-0.3258	-0.3281	-0.3301	-0.3322
Mode 9	-0.5476	-0.5527	-0.5536	-0.5437

Table 2.1 – Growth rate of Mode 6 and Mode 9 obtained with the three different meshes in comparison with the results of Gómez *et al.* [42].

Figure 2.9 presents the mesh convergence based on the growth rate of these two modes together with the asymptotic value as given by the Richardson extrapolation. The values obtained with mesh M3

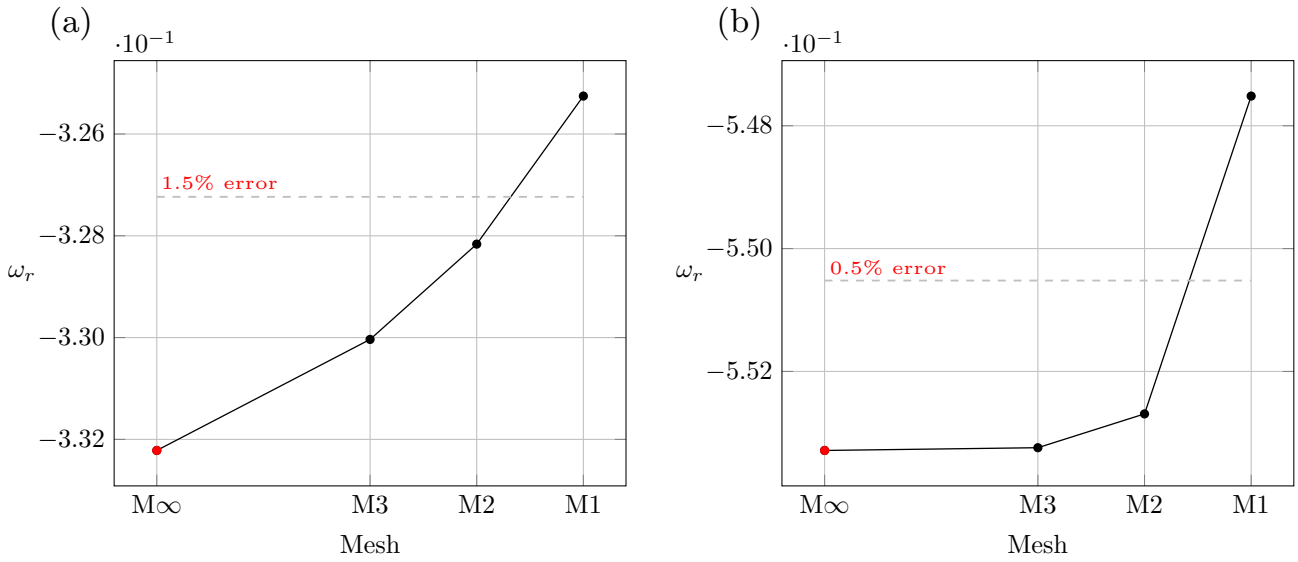

Figure 2.9 – Mesh convergence on the growth rate of (a) Mode 6 and (b) Mode 9. The red dots correspond to the asymptotic values obtained from Richardson extrapolation.

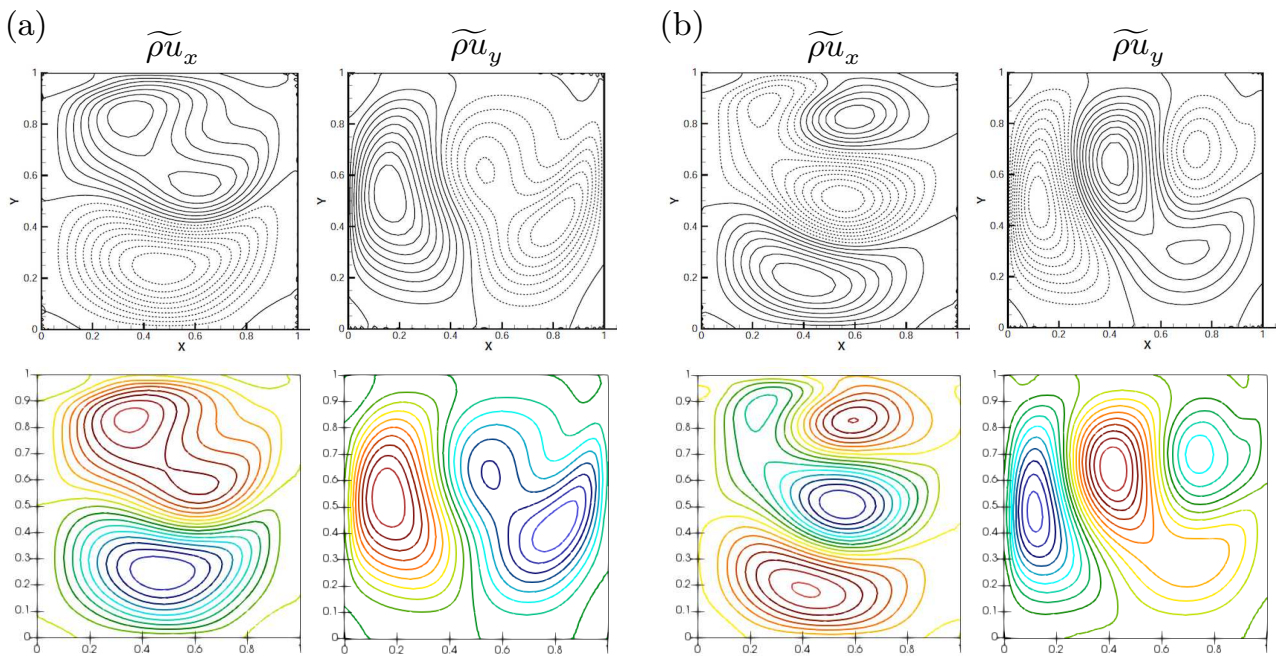

Figure 2.10 – $\widetilde{\rho u_x}/\max(|\widetilde{\rho u_x}|)$ and $\widetilde{\rho u_y}/\max(|\widetilde{\rho u_y}|)$ isocontours of (a) Mode 6 and (b) Mode 9. The first row corresponds to the results of [42] and second row to the present results. 21 levels of contours in the range $[-1; 1]$ are plotted.

are correctly converged and the corresponding order of convergence is p=1.5 and p=6.3 for Mode 6 and Mode 9, respectively. Moreover, the values obtained with mesh M2 differ from the Richardson extrapolation by 1.2% for Mode 6 and by 0.1% for Mode 9. The structures of the modes are presented in figure 2.10 for mesh M2 and compared with those obtained by Gómez *et al.* [42]. The different isocontours accurately match.

In figure 2.11.a, we consider the influence of both the integration time τ and the *CFL* number on the growth rate of Mode 6, for a Krylov subspace of dimension $m = 50$. We can see that, whatever the *CFL*, large values of τ are required to reach convergence, *i.e.* $\tau > 0.6$. In figure 2.11.b, instead, the convergence of the growth rate of Mode 6 is presented for different values of the Krylov subspace

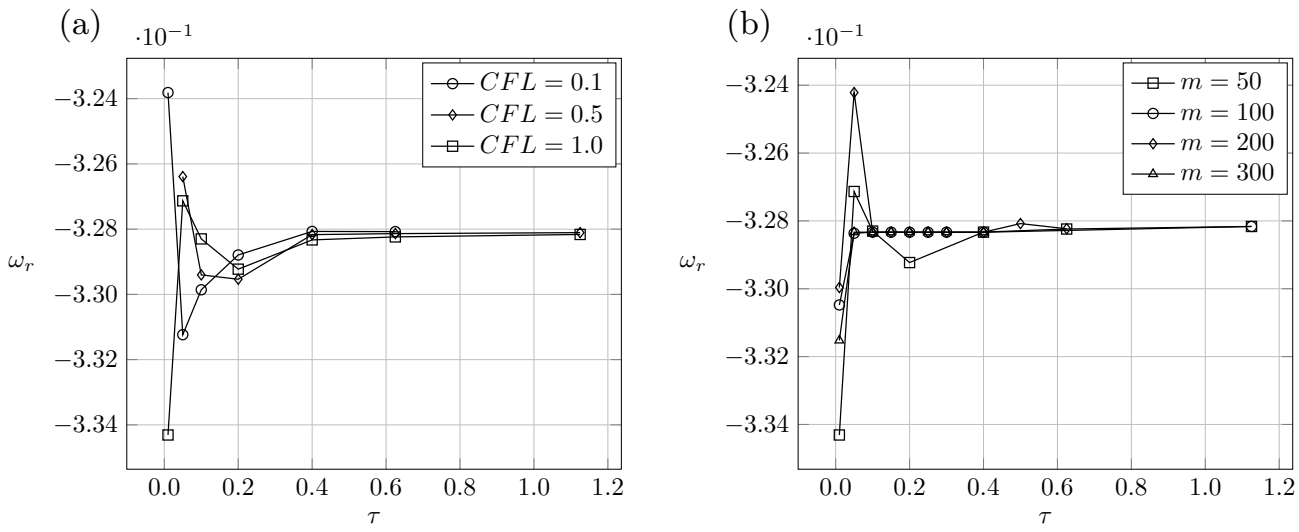

Figure 2.11 – Convergence of the growth rate of Mode 6 with respect to τ for (a) different CFL and $m = 50$ and (b) for different m and $CFL = 1$.

dimension m at $CFL = 1$. For low values of τ, the growth rate is very dependent on the Krylov subspace dimension which is no longer true for higher values of τ.

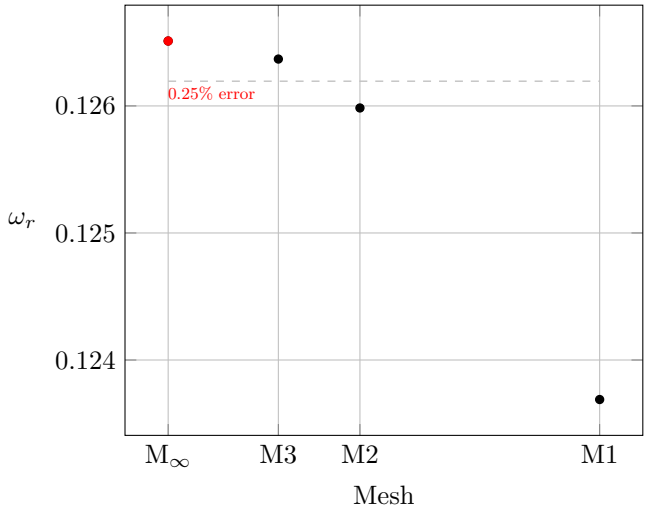

Figure 2.12 – Mesh convergence on the growth rate of the most unstable eigenmode at $Re = 100$ and $M_\infty = 0.05$. The red dot corresponds to the asymptotic value obtained from the Richardson extrapolation.

2.4.2 Circular cylinder

We now analyze the effect of compressibility on the stability of the two-dimensional flow around a circular cylinder for different Reynolds numbers and compare our results with those of Canuto & Taira [20]. In their work, the complex frequency of the most unstable mode was obtained by tracking the early time evolution of the lift coefficient of the unstable steady state, computed with the SFD filtering technique and initially perturbed by a small numerical perturbation.

We firstly performed a mesh and domain sensitivity analysis. Figure 2.13 presents the mesh convergence for the growth rate of the most unstable mode with the asymptotic value as given by the Richardson extrapolation. The value obtained with mesh M3 is correctly converged and differs from the Richardson extrapolation by less than 0.5%.

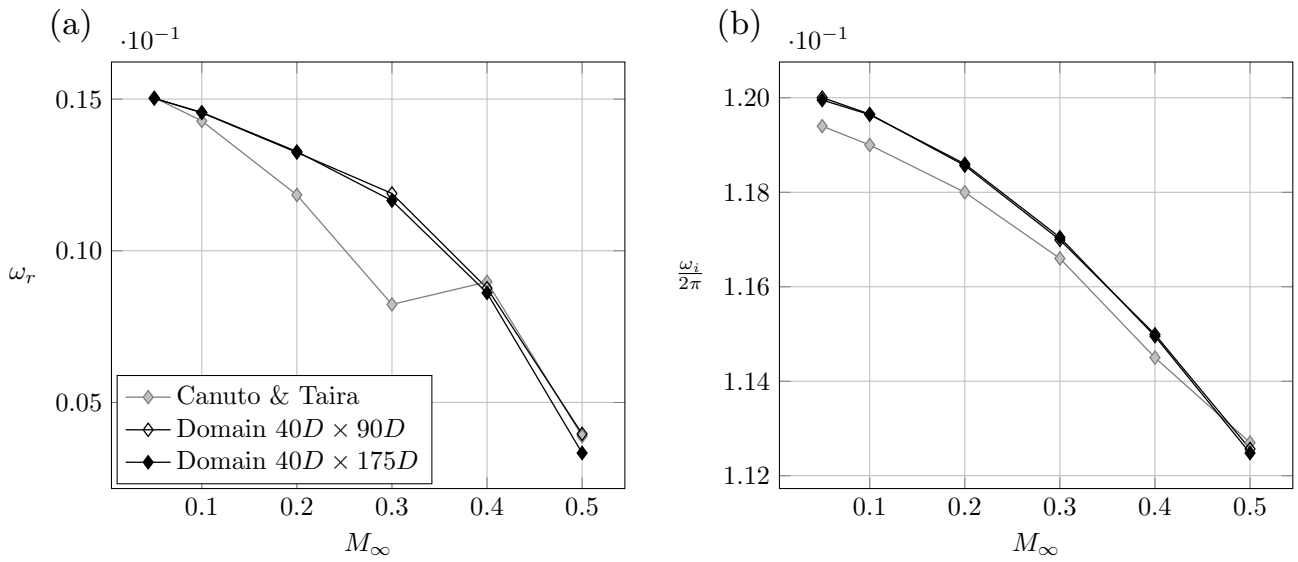

Figure 2.13 – (a) Growth rate and (b) frequency of the most unstable eigenmode with respect to the Mach number at $Re = 50$ for two domain sizes. Results of Canuto & Taira [20] are also reported.

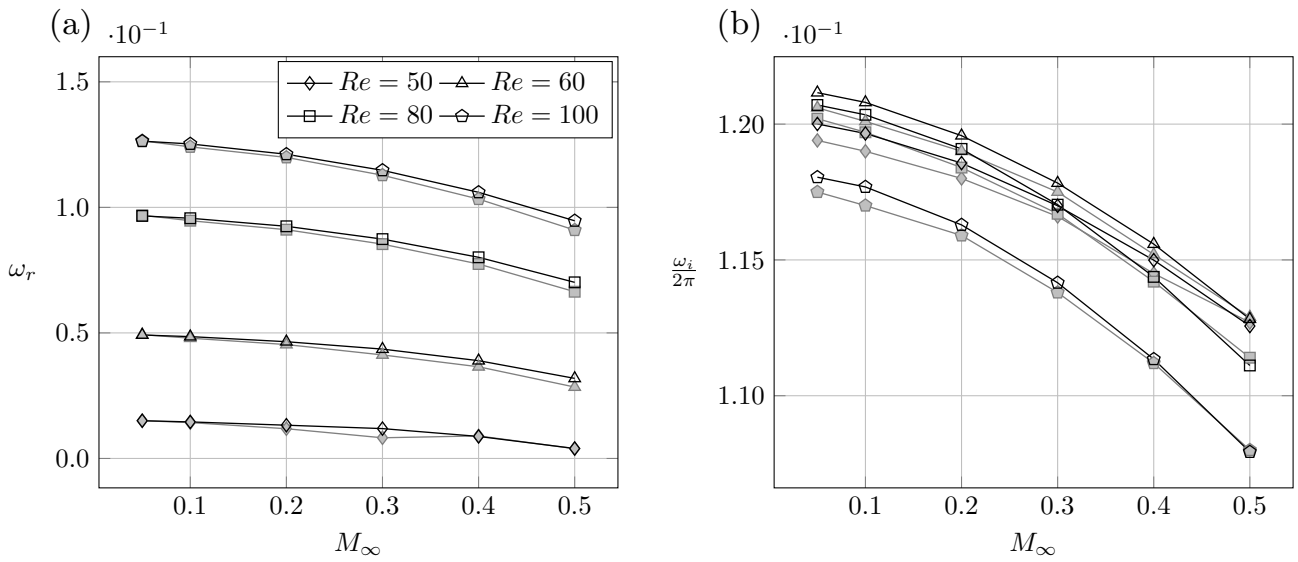

Figure 2.14 – (a) Growth rate and (b) frequency of the most unstable eigenmode with respect to Mach number for different Reynolds numbers. Results of Canuto & Taira [20] have been reported for comparison (grey lines).

Two domains have been considered: a $40D \times 90D$ and a $40D \times 175D$ domain where D is the diameter of the cylinder which is taken as the characteristic length scale, *i.e.* $L = D$. In figure 2.13.a, the difference observed for the growth rates at $M_\infty = 0.2$ and $M_\infty = 0.3$ is liekly to be due to a lack of convergence for the results of Canuto & Taira as indicated by the non monotonic behaviour of their curve. Nevertheless, the characteristics of the most unstable mode obtained with both domains are in good agreement with the overall trend of the reference, in which the domain considered is a $40D \times 60D$ with a sponge zone of $10D$ applied at the outlet. For this reason, the simulations used to validate the compressibility effect have been performed on the $40D \times 90D$ domain. Moreover, the value of τ has been set to half of the characteristic time and the Krylov subspace dimension to $m = 300$.

In figure 2.14.a, the growth rate and frequency of the most unstable eigenmode are reported with respect to Mach number for different Reynolds numbers together with the results of Canuto & Taira [20] in grey lines. Overall, relatively good agreement is shown between both data sets. The stabilizing

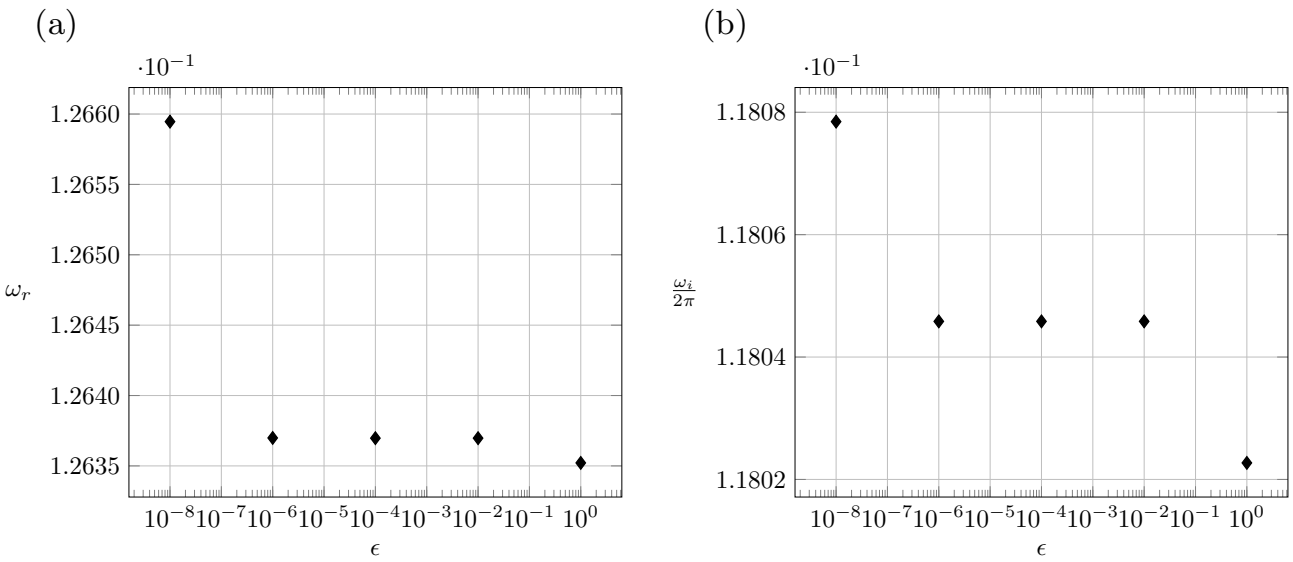

Figure 2.15 – (a) Growth rate and (b) frequency of the most unstable eigenmode with respect to the perturbation amplitude at $Re = 100$ and $M_\infty = 0.05$.

effect of the Mach number is clearly observed for all the Reynolds numbers considered, with growth rates decreasing as M_∞ increases. The mode frequency decreases as well with respect to the Mach number (see figure 2.14.b) and this is found to be correlated with the elongation of the recirculation region that forms behind the cylinder, as observed in the base state, corroborating previous results by Canuto & Taira [20].

This test case has also been used for validating the choice made both on the value of ϵ and the algorithm tolerance parameters. The parameter ϵ is used in the finite difference for the perturbation amplitude in equation (2.21) and its effect on the growth rate and mode frequency dependence can be seen in figure 2.15. We can remark that their values do not vary for $10^{-6} < \epsilon < 10^{-2}$. Moreover, the relative error using an amplitude smaller or greater by one order of magnitude, *i.e.* $\epsilon = 10^{-8}$ and 1, is found to be less than 0.2% with respect to values obtained within the range $10^{-6} < \epsilon < 10^{-2}$. Setting $\epsilon \leq 10^{-10}$, the finite difference (2.21) becomes close to a roundoff-error quotient, while using $\epsilon \geq 1$, the perturbed state vector $(\boldsymbol{q}_b \pm \epsilon \boldsymbol{q}')$ may be not physical, with possibly negative densities. The growth rate and mode frequency dependence on the algorithm tolerance parameter used in equation (2.18) is shown in figure 2.16. The convergence is obtained for tol $\approx 10^{-4}$, nevertheless, the maximum relative error using tol $= 10^{-1}$ is found to be less than 1%. The algorithm tolerance dependence has been performed with a Krylov subspace dimension $m = 40$ and the relative error using tol $= 10^{-1}$ is found to decrease when the Krylov subspace dimension is increased.

2.4.3 NACA0012 at 16° angle of attack

The third test case is represented by the NACA0012 at 16° angle of attack. The configuration of the current simulations and those presented in Chapter 3 is depicted in figure 2.17. The upstream velocity is imposed as $\boldsymbol{U} = U_\infty \cos\alpha\ \boldsymbol{e_x} + U_\infty \sin\alpha\ \boldsymbol{e_y}$, where α is the angle of attack. The airfoil closes at chord $C = 1$, with a sharp trailing edge, and the chord is taken as the characteristic length scale, *i.e.* $L = C$. Both the upper and lower edges of the domain are divergent to allow simulations at different angles of attack. Table 2.2 summarizes the growth rate and mode frequency of the most unstable modes, obtained at different Reynolds numbers for the incompressible case at $\alpha = 16°$ and compared to the results of Zhang & Samtaney [116]. The authors have performed a biglobal stability analysis on the incompressible flow around a NACA0012 profile at $\alpha = 16°$, studying both the 2D and 3D cases by

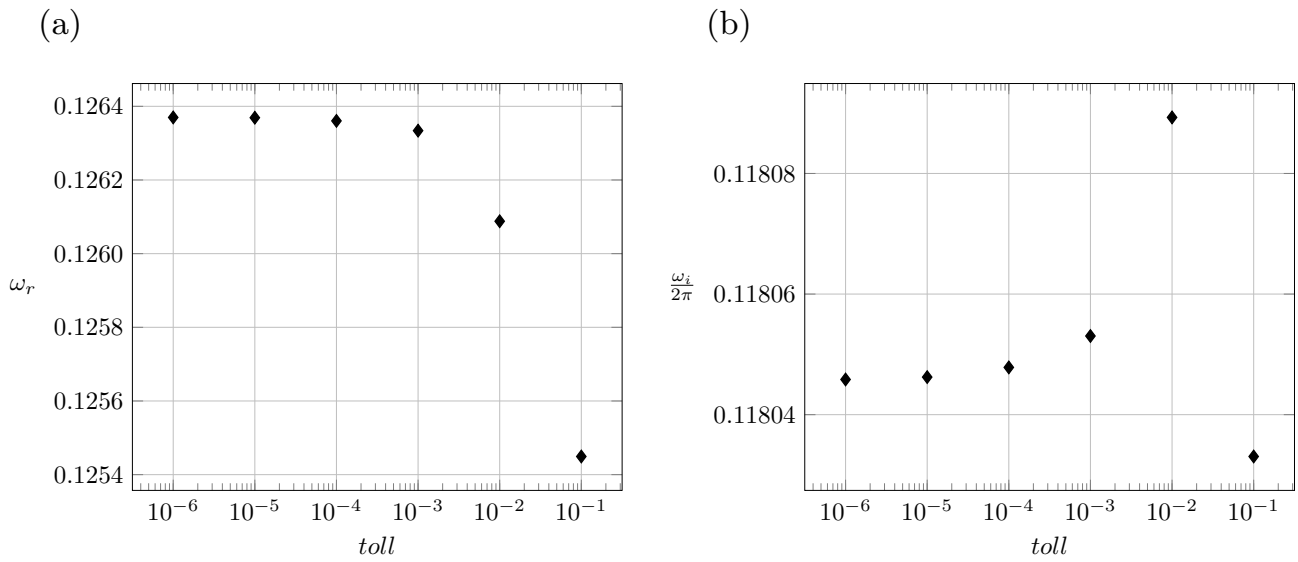

Figure 2.16 – (a) Growth rate and (b) frequency of the most unstable eigenmode with respect to the algorithm tolerance at $Re = 100$ and $M_\infty = 0.05$.

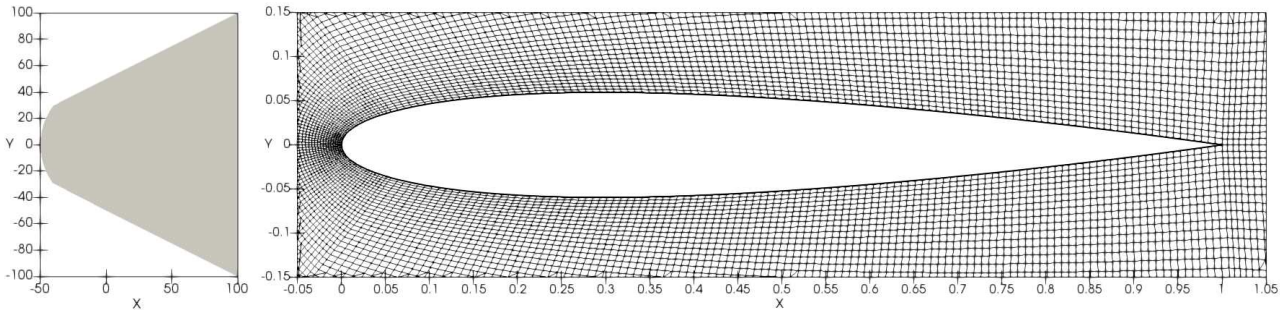

Figure 2.17 – Domain details for simulations around the NACA0012 profile.

varying the transverse wavenumber value. They also conducted a 2D DNS tracking the early time evolution of the cross-stream velocity when the filtered base state is perturbed by a small amplitude perturbation. The comparison shows a good agreement between present results and the reference. For the stability analysis, the value of τ has been set to 0.1 characteristic time and a Krylov subspace of dimension $m = 300$ has been considered.

Re	Current work	2D DNS [116]	Biglobal analysis [116]
400	$0.2591 + 0.4555i$	$0.2754 + 0.4549i$	$0.2956 + 0.4285i$
600	$0.5164 + 0.4468i$	$0.5363 + 0.4459i$	$0.5126 + 0.4264i$
800	$0.6393 + 0.4261i$	$0.6625 + 0.4247i$	$0.6202 + 0.4085i$
1000	$0.6949 + 0.4012i$	$0.7160 + 0.3994i$	$0.6783 + 0.3860i$

Table 2.2 – Growth rate and frequency ($\omega_r + \omega_i i$) with respect to Reynolds number at angle of attack $\alpha = 16°$ compared with reference results.

2.5 Résumé

Ce chapitre est consacré aux méthodes numériques permettant le au calcul de l'état de base et l'analyse de la stabilité globale de cet état.

La validité de l'hypothèse du milieu continu est démontrée dans le §2.1. Le nombre de Knudsen Kn, défini comme le rapport du libre parcours moyen des particules sur l'échelle de longueur caractéristique, détermine si le fluide peut être considéré comme un milieu continu ou non : la mécanique des milieux continus, et donc les équations de NS, peuvent être utilisées si $Kn \lesssim 0{,}01$, inversement, l'écoulement est en milieu raréfié et la mécanique statistique est nécessaire pour le modéliser. Dans la plage des nombres de Reynolds et de Mach considérée dans ce travail, le nombre de Knudsen maximal est de $0{,}007 < 0{,}01$ et l'hypothèse du milieu continu est donc valide.

La section §2.2 présente les méthodologies de calcul de l'état de base stationnaire ainsi que les équations de Navier–Stokes modifiées pour le calcul de l'état de base filtré. L'écoulement de base est obtenu avec le solveur numérique IC3, un code compressible compact d'ordre élevé développé au DAEP à l'ISAE-SUPAERO. IC3 est un code parallèle basé sur les volumes finis avec un schéma de Runge–Kutta (RK) explicite pour l'intégration temporelle. Dans ce travail, le schéma RK du troisième ordre et le schéma centré du quatrième ordre ont été utilisés respectivement pour la discrétisation temporelle et spatiale. En dessous du seuil critique de la première bifurcation, l'écoulement de base correspond à une solution stable des équations de NS qui est directement obtenue à partir des simulations numériques directes (DNS). Au-dessus du seuil critique, par contre, l'écoulement simulé numériquement est naturellement instable et il existe deux types d'écoulement de base qui peuvent être utilisés pour l'analyse de stabilité. Soit il peut être choisi comme la moyenne temporelle de la solution instationnaire, soit la stationnarité de la solution numérique peut être imposée. Le choix de l'état de base est d'une importance cruciale, puisque les réponses de l'analyse de stabilité sont différentes en fonction de l'écoulement de base considéré. En effet, les moyennes temporelles d'écoulements oscillant à une fréquence quasi-monochromatique sont marginalement stables en proximité des paramètres critiques [8, 96, 107], ce qui rend l'identification du seuil de bifurcation très difficile, alors que la fréquence du mode correspond à la fréquence naturelle. D'autre part, l'analyse de stabilité effectuée sur d'autres états de base (obtenus soit par filtrage, soit en imposant des conditions de symétrie), permet une identification claire du seuil critique, mais la fréquence de mode diverge de celle observée lorsqu'on passe au-dessus du seuil de bifurcation. Comme ce travail de thèse se focalise sur l'influence de la compressibilité sur les bifurcations, nous optons pour la seconde option et recourons à une technique de filtrage pour calculer une solution de type point fixe des équations de Navier–Stokes. Cette technique, appellée « *Selective Frequency Damping* » (SFD) [1], amortit la fréquence temporelle la plus élevée au moyen d'un filtre passe-bas introduit dans les équations de Navier–Stokes, comme indiqué dans le systeme (2.2).

La section §2.3 se concentre sur l'analyse de stabilité et la résolution de problèmes aux valeurs propres de grande dimension. Étant donné le problème aux valeurs propres (1.9), le spectre de la matrice Jacobienne $\mathscr{L}$ doit être calculé afin de trouver les modes dominants qui régissent le comportement asymptotique de la perturbation. Néanmoins, l'assemblage explicite de la matrice Jacobienne de systèmes dynamiques de grande taille peut être très coûteux en ressources de calcul et en temps. C'est pourquoi les approches dites « *matrix-free* » deviennent très populaires aujourd'hui : les coefficients de la matrice jacobienne ne sont pas calculés explicitement, mais on y accède plutôt en évaluant des produits matrice-vecteur. La méthode de Krylov–Schur [98], qui permet une implémentation de type « *matrix-free* », a été choisie dans ce travail. Cette méthode est une amélioration de l'algorithme d'Arnoldi et appartient à la classe des méthodes de projection de Krylov dont le but est de trouver

une approximation des valeurs propres de plus grand module et des vecteurs propres associés d'une matrice, en projetant le problème originel sur une base orthonormée du sous-espace de Krylov (2.11). En introduisant la matrice du propagateur $\mathscr{M} = e^{\mathscr{L}t}$, il est généralement préférable d'appliquer les algorithmes basés sur Arnoldi sur $\mathscr{M}$ plutôt que sur $\mathscr{L}$, car ceux-ci convergent vers les vecteurs propres associés aux valeurs propres de plus grand module, qui peuvent ne pas correspondre aux modes les plus amplifiés, c'est-à-dire les valeurs propres ayant la plus grande partie réelle, comme montré sur l'image 2.6. Pour cette raison, le « *time-stepping exponential transformation* » a été utilisée pour le calcul des produits matrice-vecteur. Les méthodes numériques et le développement du code sont validés dans la section §2.4 pour la « lid-driven cavity », le cylindre circulaire et le NACA0012 à incidence $\alpha = 16°$, montrant des résultats en bon accord avec des travaux de la littérature pris comme références.

Chapter 3

NACA0012 airfoil: primary two-dimensional instability

Abstract: In this chapter, we investigate the two-dimensional linear stability of the NACA0012 airfoil wake, whose configuration and validation has been presented in §2.4.3. In §3.1, the state of the art of compressibility effects on the aerodynamics and the two dimensional primary instability of bluff bodies is presented. First, in §3.2 the influence of the angle of attack and Reynolds number is treated in the incompressible regime, then the compressible case is considered in §3.3. In section §3.4, a comparison between the stability analysis response on the filtered and the time-averaged base flow is presented. In §3.5, we summarize the present chapter in French. The most part of this chapter is the object of a paper published in the AIAA Journal [109].

Contents:

3.1 State of the art

Recently, some studies have been conducted on the effect of compressibility on the stability of low Reynolds number flows [20, 72, 92]. In their global stability analysis of axisymmetric two-dimensional wake flows, Meliga *et al.* [72] reported contrasted effects of compressibility in the subsonic regime (up to $M_\infty = 0.7$), depending on the base flow configuration. In the case of an axisymmetric afterbody flow at zero angle of attack, focusing on the secondary Hopf bifurcation, they observed an increase of the critical Reynolds number at which the secondary oscillating helical mode becomes unstable with respect to the Mach number, hence, a stabilizing effect of compressibility. Conversely, they observed a decrease of the same critical Reynolds number with respect to the Mach number, up to $M_\infty \approx 0.63$, for the flow around a sphere. Through an adjoint-based sensitivity analysis, they related this stabilizing/destabilizing behaviour to a change in the longitudinal advection of the perturbation by the base flow within the recirculation zone in the lee of the body. Their analysis questions the previous hypothesis of Bouhadji & Braza [18], who attributed the destabilizing effect of compressibility to an

increase of the length of the recirculation bubble, whereas this last effect (increase of the recirculation zone) was observed for both the afterbody and the sphere in the work of Meliga *et al.* [72].

The increase of the recirculation length with growing Mach number has also been documented by Canuto & Taira [20] for the flow around a circular cylinder and by Sansica *et al.* [92] for the sphere, with a stronger elongation as the critical Reynolds number is approached. In the latter case, the recirculation length is significantly reduced as M_∞ increases above unity (see also Nagata *et al.* [78, 79]). The size variation of the separation regions behind bodies influences the natural frequency of the flow [39, 64, 78, 79], as well as the frequency of the most unstable mode [92]. In both [20] and [92], the frequency of the most amplified eigenmode is found to decrease as the recirculation length increases.

Sansica *et al.* also extended the stability analysis of Meliga for the sphere up to low supersonic regime at $M_\infty = 1.2$, for Reynolds numbers between $Re = 200$ and $Re = 370$. Considering a three-dimensional base flow, they confirmed the non monotonic effect of compressibility but observed a destabilization only in the low subsonic regime up to $M_\infty \approx 0.3$. For higher Mach numbers, the helical oscillating mode is progressively damped until its complete stabilization in the high subsonic regime ($M_\infty \approx 0.7$ for $Re = 280$). They attributed this difference to the base flow axisymmetry assumption used by Meliga *et al.* [72].

This specific regime of compressible low-Reynolds number flows has also been investigated experimentally in the Mars Wind Tunnel at Tohoku University. Anyoji *et al.* [3] compared the aerodynamic characteristics of a flat plate and a NACA0012-34 airfoil at Reynolds numbers $Re \in [4\,300; 41\,000]$ in the low subsonic regime, up to $M_\infty = 0.6$. Effects of compressibility on the aerodynamic coefficients at Reynolds numbers in the range $Re \in [100; 10\,000]$ have been also studied in [31, 77, 101, 115] for flat plates, cambered and triangular airfoils. From these studies, it can be concluded that for Reynolds numbers up to $Re \approx 10\,000$, the influence of compressibility on the drag and lift coefficients is not the same for the different angles of attack tested. In particular, the dynamics of the separated leading edge shear layer at high angles of attack is highly dependent on the Mach number, which affects leading edge vortex formation and the resulting aerodynamic force. Unique features related to the displacement of the shock foot away from the airfoil surface were also put into evidence in the transonic regime [31].

3.2 Incompressible case

3.2.1 Influence of the angle of attack

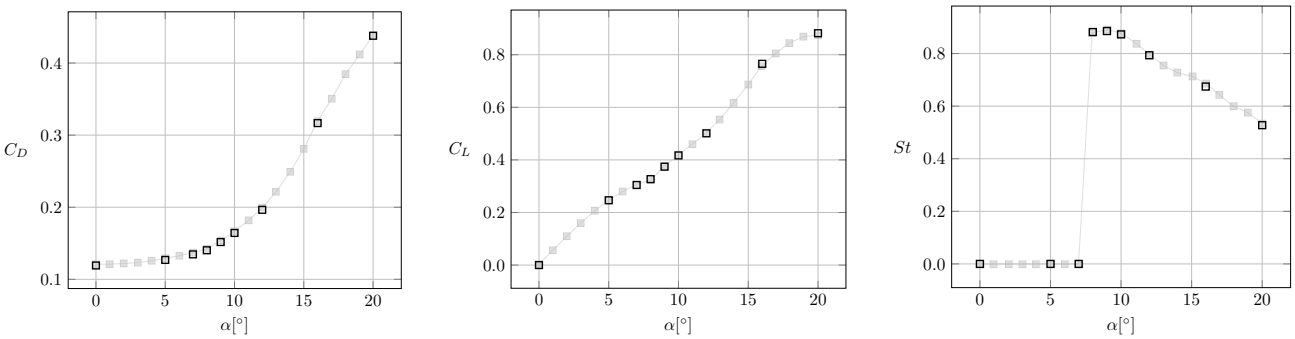

Figure 3.1 – Evolution of the mean values of C_D, C_L and associated Strouhal number St with the angle of attack at $Re = 1000$. Black marks show results of the present work and light gray those of Kurtulus [60].

The incompressible case has been simulated using a Mach number of 0.05. We first consider the unfiltered base flow whose mean aerodynamic coefficients C_D, C_L and corresponding Strouhal number

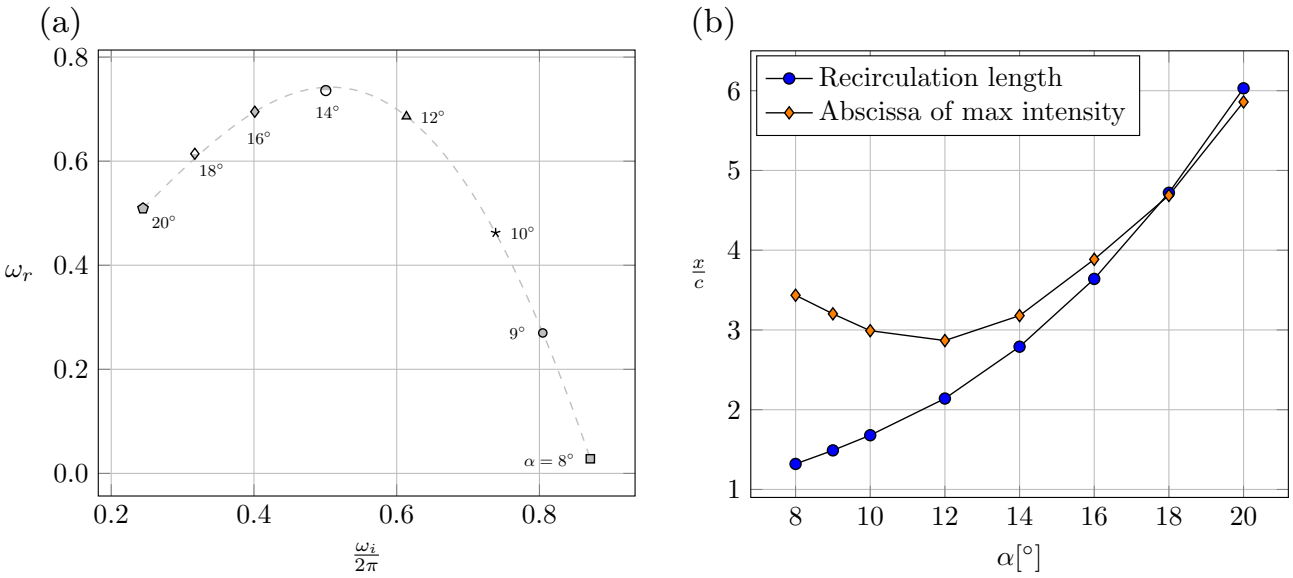

Figure 3.2 – Growth rate as a function of frequency of the most unstable mode (a) and length of the recirculation region and streamwise location of maximal intensity in the spatial structure of the most unstable mode (b), at $Re = 1000$, varying the angle of attack.

St are reported in figure 3.1 for different angles of attack at $Re = 1000$. The results are in very good agreement with those of Kurtulus [60]. It can be observed from the St vs α plot that, at this Reynolds number, the onset of vortex shedding occurs at $\alpha = 8°$. The Strouhal number initially reaches values of the order of 0.9 before decreasing as α increases. This decrease shows that St scales with $C \times \sin\alpha$, where it is reminded that C is the chord of the profile. This quantity corresponds to the vertical distance between leading and trailing edge separated shear layers and hence represents a characteristic length scale for shear layers, cross-wake interactions. The onset of vortex shedding is found to be correlated with an increase in C_L which reflects the separation and roll-up of the leading edge shear layer and the influence of subsequent leading edge vortex formation on the upper surface of the airfoil. Note that this trend of C_L as a function of α is different to that observed at higher Reynolds number, where leading edge separation is generally associated with lift stall. Accordingly, since the leading edge vortex generates a pressure force that acts normal to the surface, C_D is also found to increase greatly for values of α above 8°.

In figure 3.2.a the growth rate versus frequency of the most unstable mode at different angles of attack is presented for $Re = 1000$. It shows a non monotonic behaviour of the growth rate ω_r with respect to α : a sharp increase as the angle of attack increases from 8° to 14° where ω_r is maximal, followed by a decrease for $\alpha \geq 14°$. The frequency of the mode ω_i, instead, constantly decreases. While this appears to correlate with the evolution of the natural frequency (see figure 3.1), we stress the fact that stability analysis is here performed on the filtered base flow. As a consequence, for such a base flow, the frequency of the most unstable mode does not accurately match the vortex shedding frequency away from the stability threshold.

The decrease in ω_i can be correlated with an increase in size of the recirculation region of the base flow, both in the streamwise and transverse directions, hence an increase in the wake characteristic length scale, as depicted in figure 3.3. The length of the recirculation region is here identified using zero streamwise velocity isoline. Moreover, the streamwise wavelength of the most unstable mode increases with the thickening of the recirculation region associated with the increase of the angle of attack. The corresponding streamwise wavenumber is found to be proportional to the mode frequency, leading to a relatively constant phase velocity $v_\phi \approx 0.8$ with respect to α. This value scales with the base flow

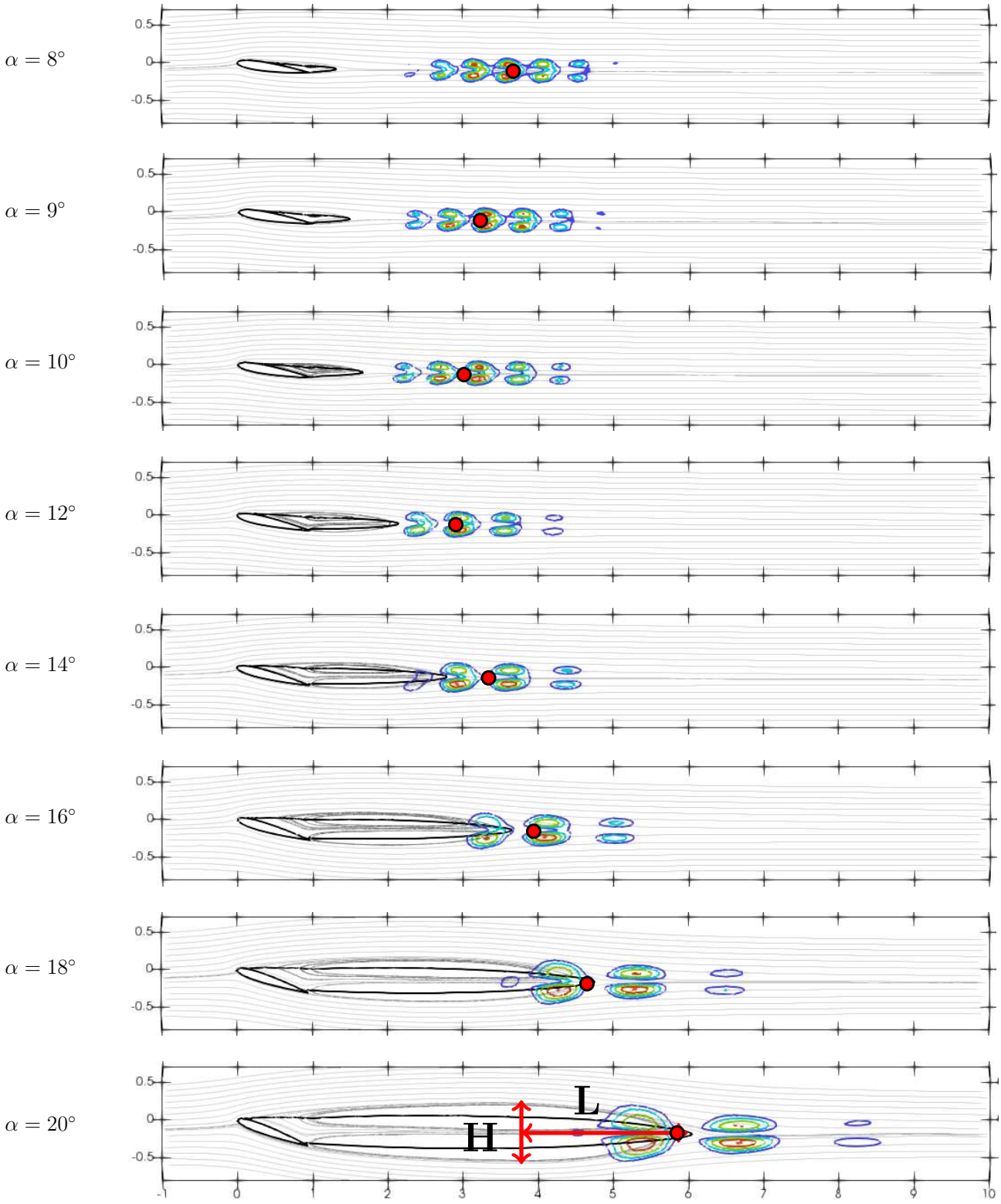

Figure 3.3 – $||\widetilde{\rho\mathbf{u}}||/\max(||\widetilde{\rho\mathbf{u}}||)$ isocontours at different angles of attack, $Re = 1000$ and $M_\infty = 0.05$. 5 levels of contours in the range $[0.5; 1]$ are plotted. The base flow streamlines are in light gray and the solid black line corresponds to the isocontour $u_x = 0$. Red circles indicate the streamwise position of the peak intensity of the mode. The parameters L and H used for the "closing angle" calculation are shown for $\alpha = 20°$.

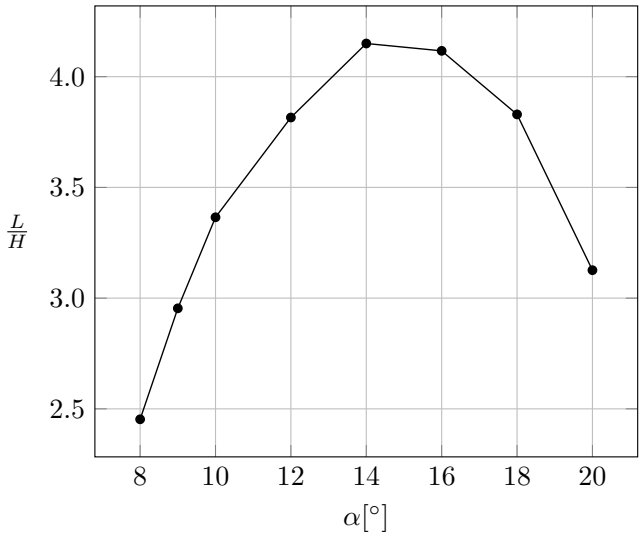

Figure 3.4 – L/H ratio at different angles of attack, $Re = 1000$ and $M_\infty = 0.05$.

mean velocity measured in the wake at a large distance downstream of the recirculation bubble.

Figure 3.3 further shows that the spatial structure of the most unstable mode exhibits larger intensities in the wake downstream of the recirculation region for all angles of attack. The streamwise positions of maximal intensities of the mode are indicated by the red circles and are calculated considering the position of maximal amplitude of the envelope of the signal, *i.e.* the modulus of the complex signal. Yet, it is observed that the relative position of the peak intensity with respect to the recirculation region strongly varies with α. For $\alpha = 8°$, largest intensities are observed far downstream of the recirculation region, quite similarly to what can be observed behind bluff bodies at Reynolds numbers slightly above the stability threshold, *i.e.* slightly above the critical Reynolds number corresponding to the first Hopf bifurcation [69, 116]. The base flow in this region is nearly parallel and the instability can be explained by deficits of streamwise velocity in the wake and the associated inflection points in their cross-stream distribution. The location of maximal intensity in the spatial structure of the most unstable mode and the tail end of the base flow recirculation region get closer as α increases.

This is further highlighted on figure 3.2.b, which plots the streamwise position of the trailing point of the recirculation region and the one of the peak intensity in the spatial structure of the most unstable mode. It is shown that the two regions first exhibit strong correlation at $\alpha \approx 12° - 14°$, where the trend of the peak intensity position changes and starts increasing with respect to α, then both curves join at $\alpha = 18°$. The two regions seem uncorrelated below $\alpha = 14°$ and strongly correlated above. For $\alpha \geq 14°$, the most unstable mode is preferentially located in the non parallel region of the base flow and hence the mechanism driving the instability may differ from that at lower values of α. We note that $\alpha = 14°$ also corresponds to maximal growth rate of the unstable mode (see figure 3.2.a), but it remains unclear at this point whether or not the decrease of growth rate observed for $\alpha \geq 14°$ is due to the interaction between the recirculation region and the mode.

For the flow past square and circular cylinders, Mao & Blackburn [69] attributed the maximum growth rate to the base flow being most parallel at the end of the recirculation region. A measure of parallelism in this region was provided by the "closing angle" of the recirculation region, quantified by the ratio between the streamwise distance from the widest point to the end of the recirculation region (L), and its maximum width (H), as it is shown in figure 3.3. In figure 3.4, we also find that this ratio is maximal (*i.e.* the flow is most parallel at the end of the recirculation region) when the growth rate is

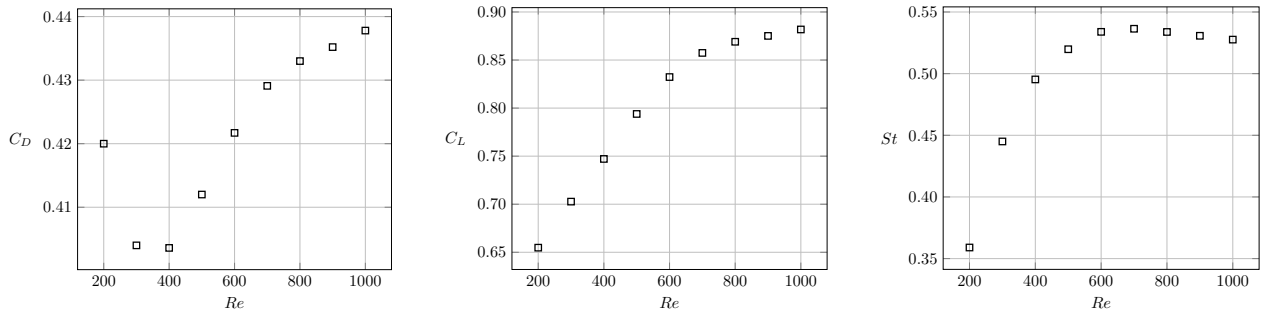

Figure 3.5 – Evolution of the mean values of C_D, C_L and associated Strouhal number St with the Reynolds number at $\alpha = 20°$.

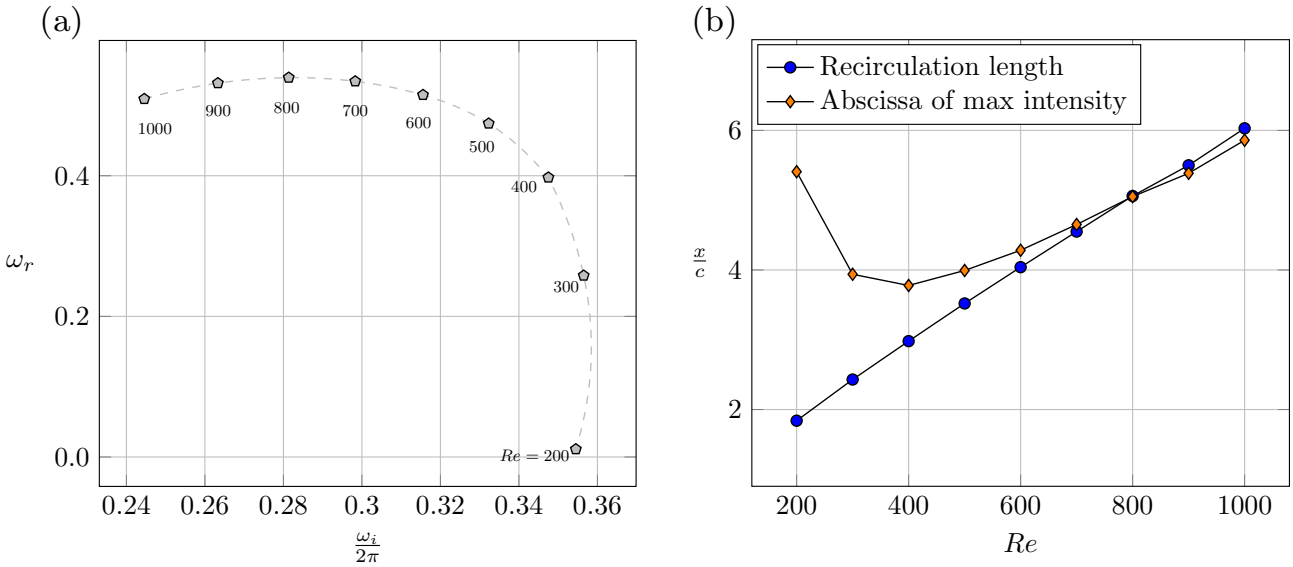

Figure 3.6 – Growth rate as a function of frequency of the most unstable mode (a) and length of the recirculation region and streamwise location of maximal intensity in the spatial structure of the most unstable mode (b), for $\alpha = 20°$, varying the Reynolds number.

maximal, which seems to corroborate previous observations of Mao & Blackburn. However, we will see in the next section that this correlation may not strictly hold for all cases.

3.2.2 Influence of Reynolds number

We first consider the unfiltered base flow whose mean aerodynamic coefficients C_D, C_L and corresponding Strouhal number St are reported in figure 3.5 for different Reynolds numbers at $\alpha = 20°$. Due to a decrease of the viscous contribution, the drag coefficient C_D first decreases with increasing Reynolds number up to $Re = 400$. Beyond, it increases because of the growing contribution of the pressure drag. The lift coefficient increases, while the associated Strouhal number presents a maximum at $Re \approx 700$.

The evolution of ω_r as a function of ω_i for the most unstable mode at different Reynolds numbers and for $\alpha = 20°$ is displayed in figure 3.6.a. The mode frequency slightly increases close to the stability threshold, *i.e.* from $Re = 200$ to $Re = 300$; this is probably due to the thinning of the shear layers, caused by the decrease of viscosity, which at those very low Reynolds numbers may impact the frequency more than the elongation of the recirculation region. Beyond $Re = 300$, instead, the mode frequency decreases, and the growth rate exhibits a non monotonic trend with a maximum observed around $Re = 800$.

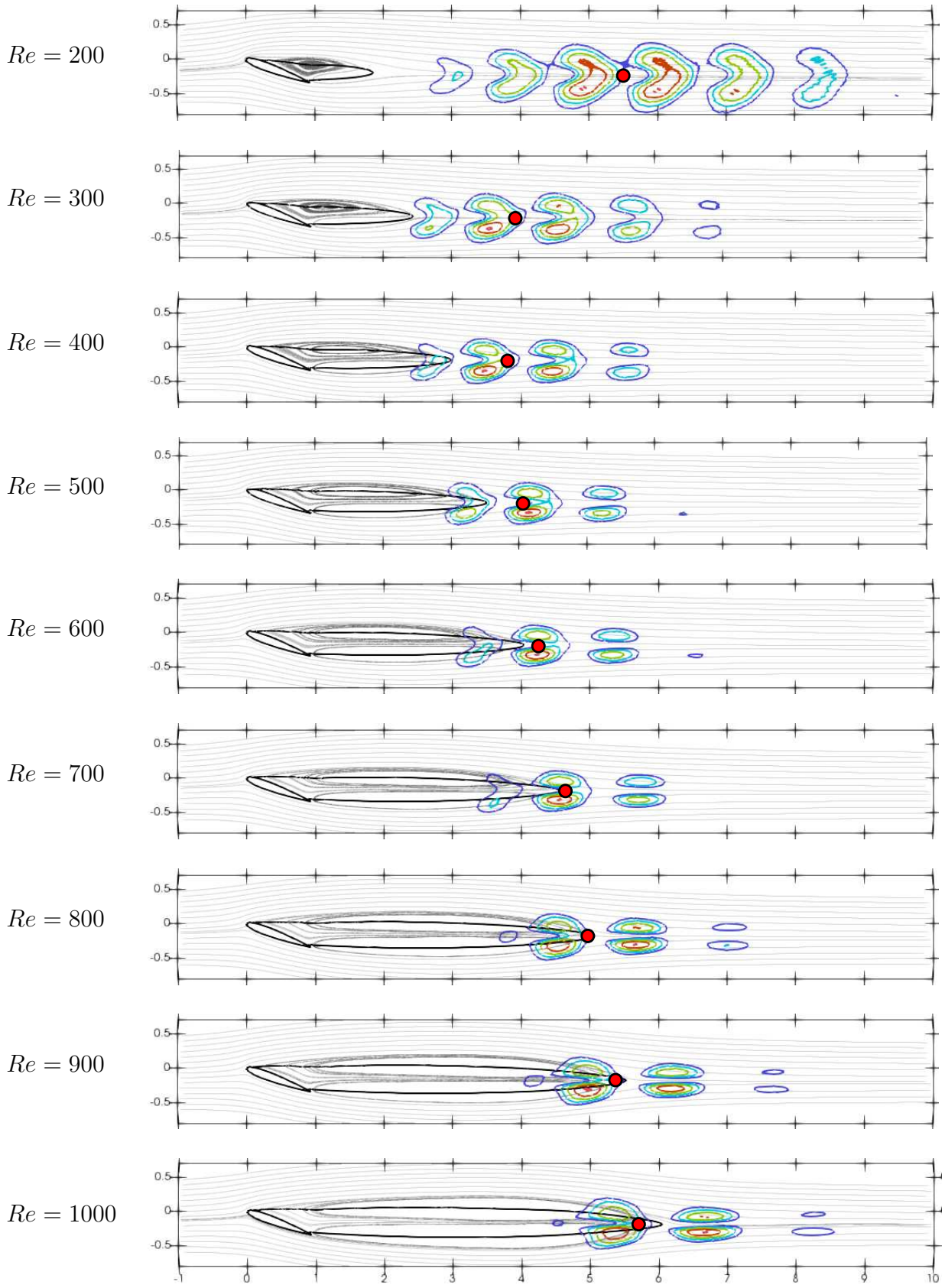

Figure 3.7 – $||\widetilde{\rho\mathbf{u}}||/\max(||\widetilde{\rho\mathbf{u}}||)$ isocontours at different Reynolds numbers, $\alpha = 20°$ and $M_\infty = 0.05$. 5 levels of contours in the range $[0.5; 1]$ are plotted. The base flow streamlines are in light gray and the solid black line corresponds to the isocontour $u_x = 0$. Red circles indicate the streamwise position of the peak intensity of the mode.

It can be observed from figure 3.7 that the recirculation region extends further downstream with increasing Re, which is in line with previous observations on circular and square cylinders [69] and on the NACA0012 airfoil at $\alpha = 16°$ [116]. This supports the idea that the characteristic length scale of the recirculation region drives ω_i. The evolution of the streamwise wavenumber with respect to Re is also in line with the results of Mao & Blackburn [69] for the square cylinder: it slightly increases close to the stability threshold and drops as the Reynolds number is further increased. The wavenumber is proportional to the mode frequency, leading to a constant phase velocity $v_\phi \approx 0.8$, which is similar to what has been observed at constant $Re = 1000$ for the different angles of attack. Overall, figures 3.6.b and 3.7 indicate that the evolution of the most unstable modes with Re is somewhat similar to that with α.

Figure 3.7 further shows that the end of the recirculation region and the streamwise abscissa of maximal intensity in the spatial structure of the mode, indicated by the red circles, are clearly separated at $Re = 200$ and then get closer to one another as Re is increased. Figure 3.6.b shows that the Reynolds number at which both locations first exhibit strong correlation is $Re \approx 400 - 500$, but the peak intensity joins the recirculation region at $Re = 800$, which corresponds to the maximum growth rate. This suggests that the interaction between the recirculation region and the far wake instability is a necessary condition, but not (solely) responsible for the change in the trend of ω_r as we move away from the stability threshold. The relation between the maximum growth rate and the abscissa of maximum intensity has been confirmed by further calculations at lower angles of attack. As for the $\alpha = 20°$ case, the maximum growth rate has been reached when the peak intensity of the mode becomes coincident with the end of the recirculation region (see Appendix C). On the other hand, we find again that the maximum growth rate is obtained when the base flow is most parallel at the end of the recirculation region, as measured by the "closing angle" defined previously.

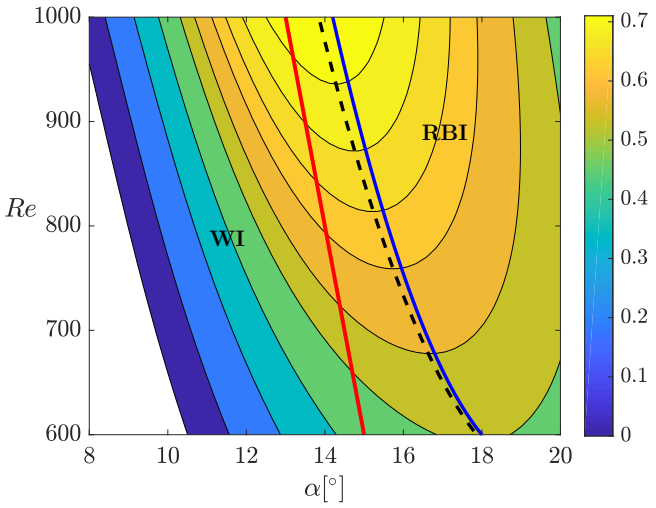

Figure 3.8 – Growth rate isocontours for the most unstable mode in the plane (α, Re). The dashed line corresponds to the maximum growth rate at each Re. The thick red line separates regions of Wake Instability (WI) from the region of Recirculation Bubble Instability (RCI). The thick blue line corresponds to the maximum L/H ratio.

Figure 3.8 summarizes these results in the form of contours of ω_r in the plane (α, Re). WI and RBI labels are added to denote regions of the parameter space where the dominant instability is located far downstream (Wake Instability) or at the end of the recirculation region (Recirculation Bubble Instability) of the base flow. The thick red line delimits the two regions and is obtained by considering when the length of the recirculation region and the location of the mode peak intensity first exhibit strong correlation. The dashed black line marks the maximum growth rate obtained at each Re (as α

is varied). For this range of Reynolds number and angles of attack, the maximum growth rate is always reached within the RBI region. The blue thick line indicates when the base flow is most parallel at the end of the recirculation zone, measured by the maximum L/H ratio at each Re. This maximum is relatively close to that of the growth rate within the range of Re and α tested. Hence, figure 3.8 shows that ω_r reaches a maximum for all Re and that the angle of attack at which this value is obtained increases as Re decreases. Accordingly, the angle of attack at which the mode transitions from the WI to the RBI type increases as Re decreases. Moreover, it appears that within this range of Reynolds numbers, ω_r does not reach a maximum for all α and additional cases at higher Re should be computed to clarify whether ω_r continuously rises with Re or drops at some point. We note that the continuous increase in ω_r with Re is in line with previous results of Zhang & Samtaney [116] obtained on the NACA0012 airfoil at $\alpha = 16°$ and $Re \in [400 - 1000]$. Finally, it can be observed that the variability of ω_r with α increases with the Reynolds number.

3.3 Compressibility effects in the subcritical regime

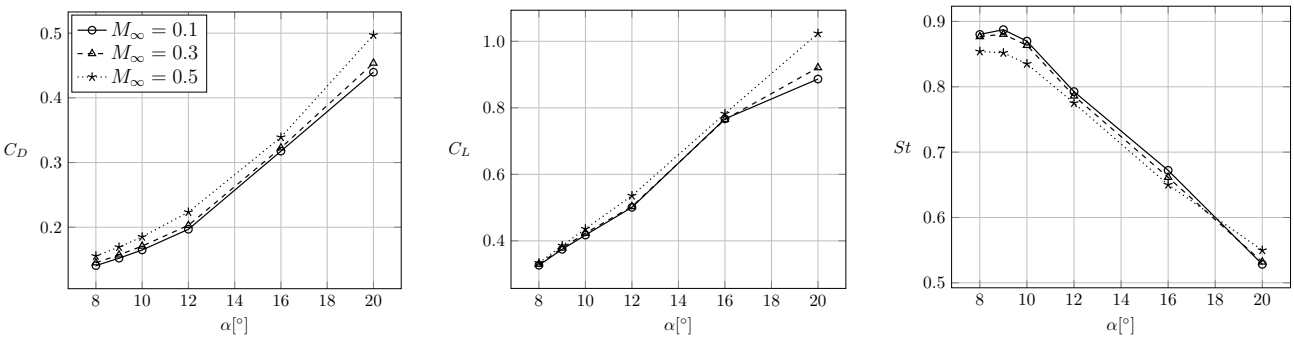

Figure 3.9 – Drag coefficient C_D, lift coefficient C_L and Strouhal number St as a function of the angle of attack at $Re = 1000$ and for various values of the Mach number.

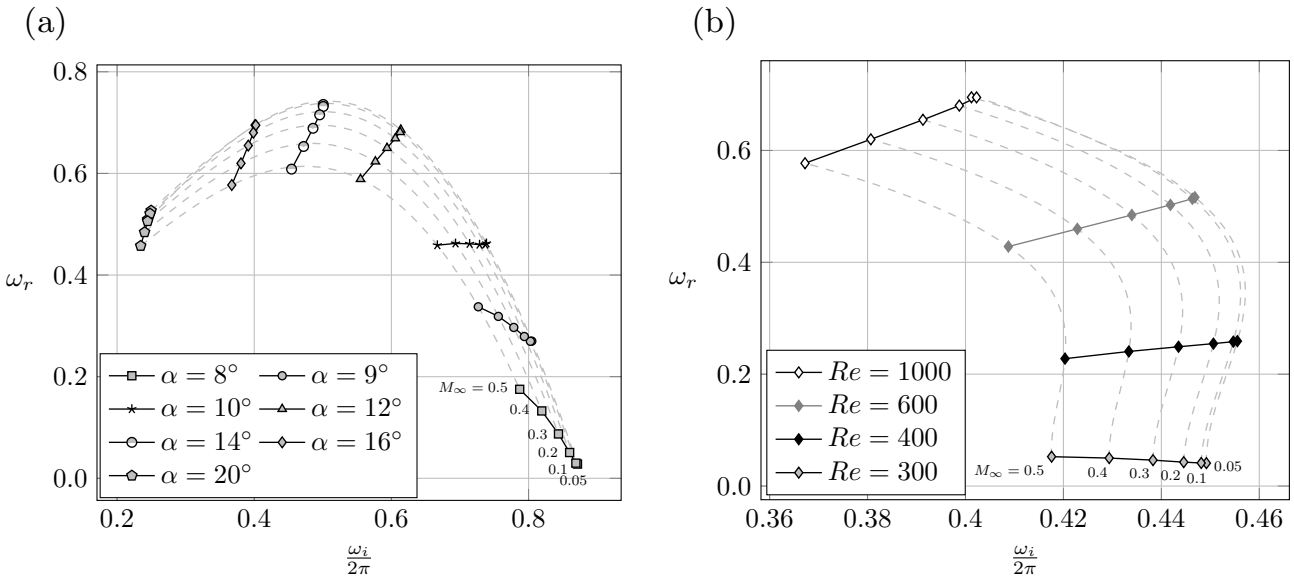

Figure 3.10 – Most unstable mode evolution in the complex plane (a) with respect to α and Mach number at $Re = 1000$ and (b) with respect to Re and Mach number at $\alpha = 16°$. Dashed lines represent the interpolation curves at iso-Mach number.

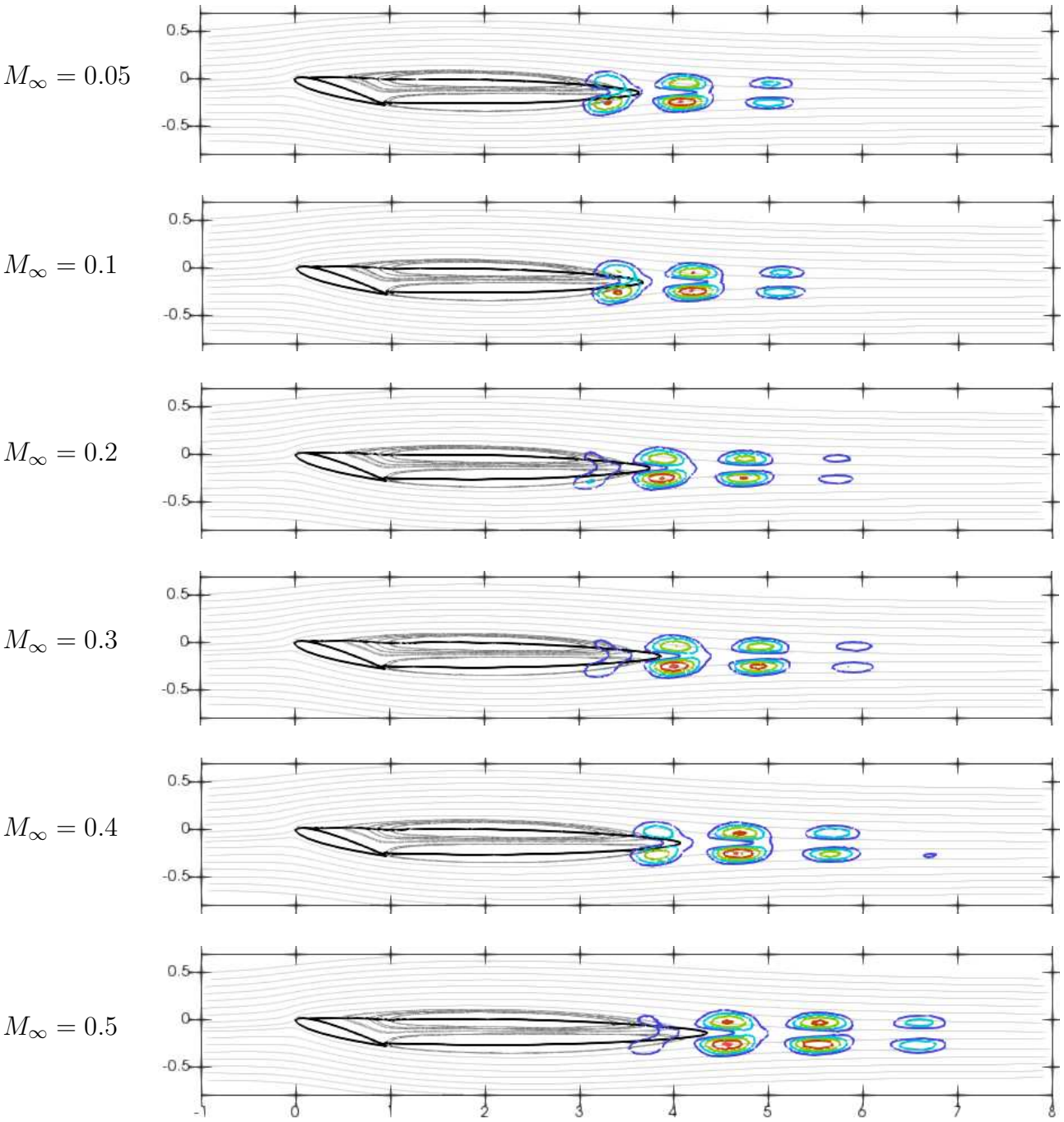

Figure 3.11 – $||\widetilde{\rho\mathbf{u}}||/\max(||\widetilde{\rho\mathbf{u}}||)$ isocontours at different Mach numbers, $\alpha = 16°$ and $Re = 1000$. Contours are from 0.5 to 1 across 5 levels. The base flow streamlines are in light gray and the solid black line corresponds to the isocontour $u_x = 0$.

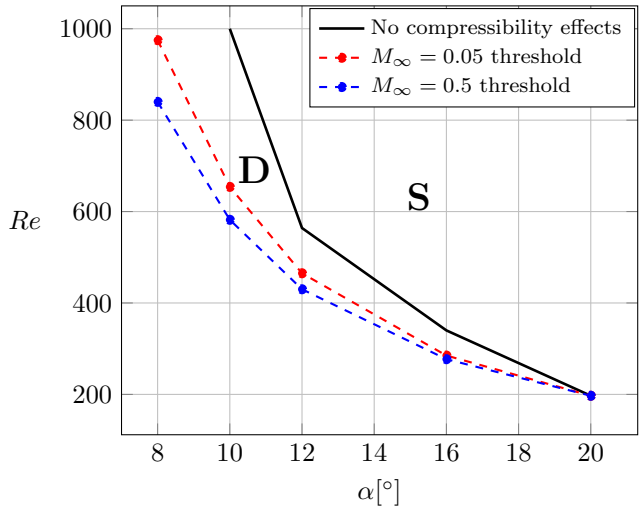

Figure 3.12 – Compressibility effects on the most amplified mode in the (α, Re) plane. The solid black line separates regions where compressibility has a stabilizing (S) effect from those where it has a destabilizing (D) effect. The dashed lines correspond to the critical Reynolds number at $M_\infty = 0.05$ and $M_\infty = 0.5$.

The effect of compressibility on the aerodynamic coefficients is shown in figure 3.9 for a Reynolds number of $Re = 1000$ and various angles of attack. Both the drag and lift coefficients increase with the Mach number. This increase is more noticeable at high angles of attack and steepens with the Mach number, as expected. The Strouhal number, instead, decreases with the increase of M_∞ for all the tested angles of attack, except for $\alpha = 20°$ for which it increases with respect to the Mach number.

In figure 3.10.a, the growth rate of the most amplified mode is shown as a function of its frequency at $Re = 1000$ for different angles of attack α and Mach number varying between 0.05 and 0.5. First, the frequency ω_i of this oscillatory mode decreases with α for all M_∞, which generalizes previous results on the incompressible case to the compressible one. In addition, ω_i decreases with M_∞ for all α. As discussed previously in the incompressible case, there is no strict correlation between the evolution of St and that of ω_i with respect to the Mach number, which can be attributed to our approach based on the filtered base state (rather than on the time-averaged base state). The decrease in ω_i with increasing M_∞ is consistent with previous works on bluff bodies [20, 72, 78, 79, 92] and can again be related to the elongation of the recirculation region. As illustrated in figure 3.11 for $\alpha = 16°$, the recirculation region of the base flow, depicted by the zero streamwise velocity contour in thick black line, elongates as the Mach number is increased.

On the other hand, the influence of compressibility on the growth rate of the most unstable mode depends on the angle of attack. For $\alpha = 8°$ and 9°, the growth rate increases with the Mach number, indicating a destabilizing effect of compressibility that is clearly less pronounced for $\alpha = 9°$ than for $\alpha = 8°$. At $\alpha = 10°$, compressibility does not change the growth rate, while further increasing the angle of attack leads to a decrease of the growth rate with increasing Mach number, hence a stabilizing effect of compressibility. This figure further shows that the maximum growth rate (as α is varied) decreases with increasing M_∞ and it is achieved at slightly lower angles of attack compared to the incompressible case. The transition between the stabilizing and destabilizing effects of compressibility is also shown in figure 3.10.b, where the characteristics of the leading mode are presented at $\alpha = 16°$ for different Reynolds numbers. Compressibility has a stabilizing effect at $Re = 1000, 600$ and 400 while it has a destabilizing effect at $Re = 300$, *i.e.* as one gets closer to the critical Reynolds number ($Re_c \approx 285$) corresponding to the first Hopf bifurcation. Figure 3.12 summarizes the effect of compressibility on the

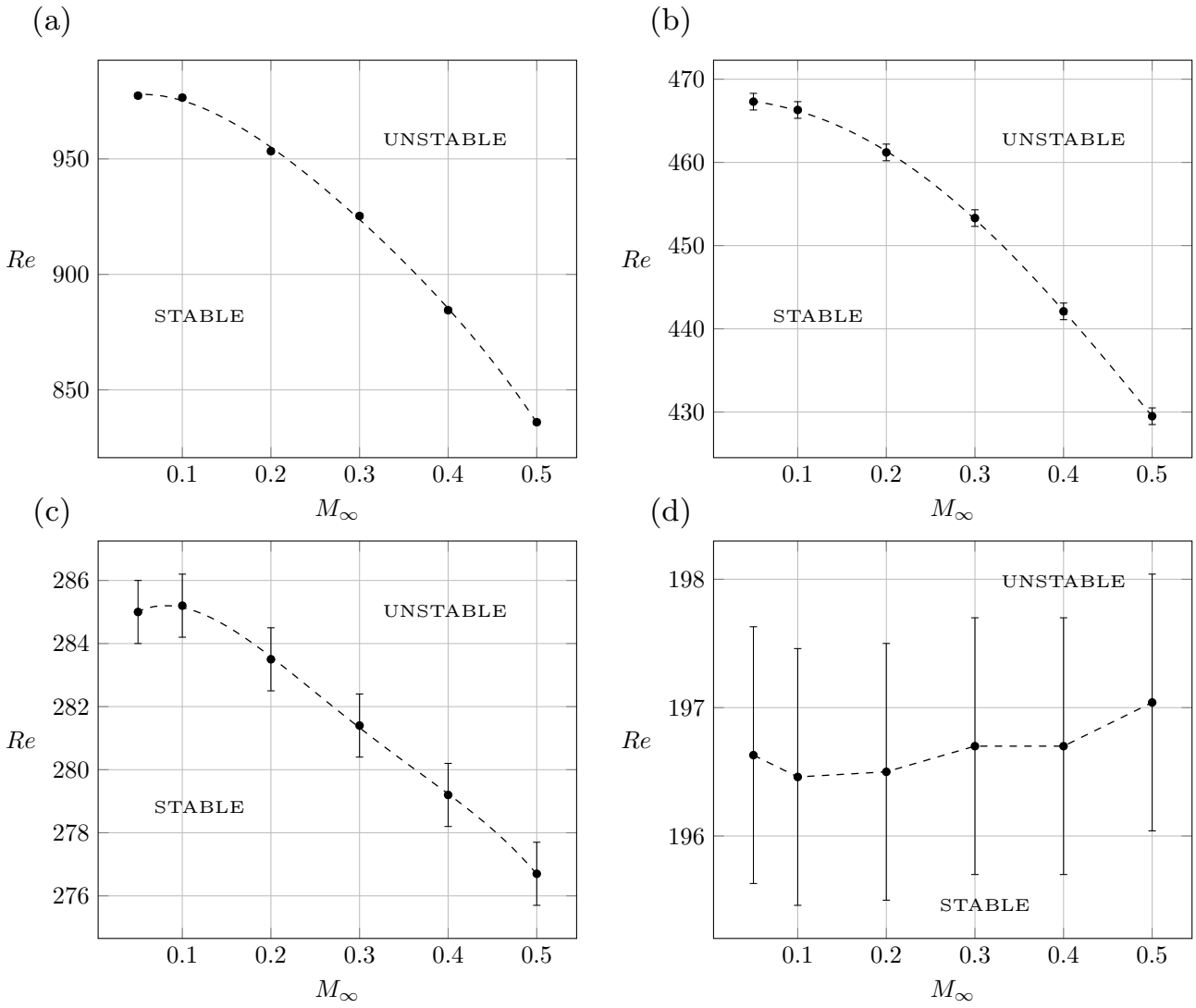

Figure 3.13 – Neutral stability curves in the (M_∞, Re) plane for (a) $\alpha = 8°$, (b) $\alpha = 12°$, (c) $\alpha = 16°$ and (d) $\alpha = 20°$.

most amplified mode in the plane (α, Re). The solid black line separates regions where compressibility has a stabilizing (S) effect from those where it has a destabilizing (D) effect. This limit goes from high to low Reynolds numbers as the angle of attack is increased and it also shows that the destabilizing effect of the upstream Mach number is observed close to the critical threshold only.

In figure 3.13, the critical Reynolds number Re_c is presented as a function of the Mach number. Compressibility brings the first Hopf bifurcation forward for all the angles of attack considered here. Nevertheless, the intensity of the destabilization (the variation of ΔRe_c with M_∞) weakens as α increases: $\Delta Re_c = Re_c(M_\infty = 0.5) - Re_c(M_\infty = 0.05)$ represents 15%, 8% and 3% for $\alpha = 8°, 12°$ and 16° respectively, up to $\alpha = 20°$ where compressibility does not influence the transition ($\Delta Re_c \approx 0$).

The analysis of the incompressible regime in section 3.2 has shown a correlation between the variation of the growth rate of the most unstable mode and the relative position between the peak intensity of the mode and the end point of the recirculation region, as well as with the “closing angle”. We now examine whether these two properties of the base flow can similarly be responsible for the growth rate variation in the compressible regime, and thus explain the stabilizing/destabilizing effect of compressibility.

As the compressibility lengthens the recirculation region, the abscissa of maximal intensity is also

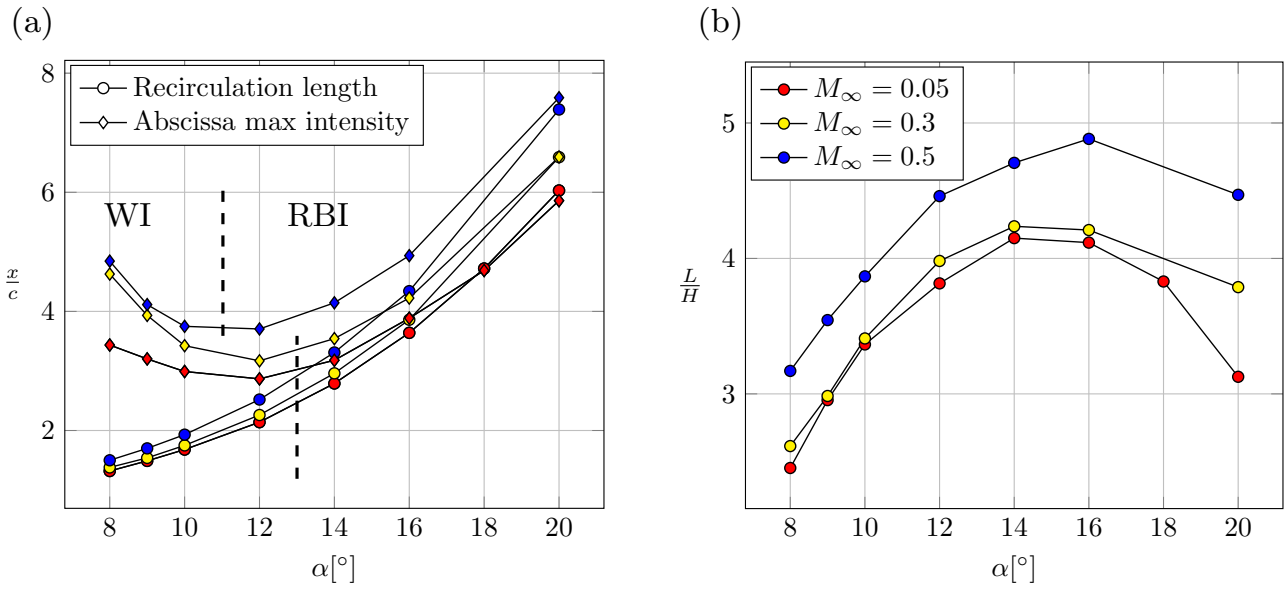

Figure 3.14 – Length of the recirculation region and streamwise location of maximal intensity in the spatial structure of the most unstable mode, with boundaries between WI and RBI regions (a) and L/H ratio (b) at different angles of attack, $Re = 1000$ and three different Mach numbers $M_\infty = 0.05$ (red), 0.3 (yellow) and 0.5 (blue).

found to move downstream for all the angles of attack, as it can be seen in figure 3.14.a for three different Mach numbers. In particular, the peak of maximal intensity of the mode joins the recirculation region at higher angles of attack when the Mach number is increased: at $\alpha = 18°$ for $M_\infty = 0.05$ and $\alpha = 20°$ for $M_\infty = 0.3$, while for $M_\infty = 0.5$ it has not reached the recirculation region yet within the range of α explored here.

As defined in section 3.2.1, we consider that the angle of attack at which the recirculation region and the far wake instability first exhibit strong correlation corresponds to the change in trend of the abscissa of maximal intensity of the mode. This specific angle of attack is seen to slightly decrease when the Mach number increases: $\alpha \approx 10° - 12°$ for $M_\infty = 0.5$, against the $\alpha \approx 12° - 14°$ for $M_\infty = 0.05$, as indicated by the dashed black separation lines in figure 3.14.a. We can remark that, when increasing the Mach number, the downstream shift of the abscissa of maximal intensity of the mode compared to the lengthening of the recirculation region, is stronger at low angles of attack (WI region). In other words, when increasing the Mach number, the relative distance between the peak of maximal intensity of the mode and the end of recirculation region increases more strongly in the WI region than in the RBI one. Nevertheless, the destabilizing/stabilizing effect of compressibility changes at $\alpha = 10°$, which is in the WI region. Hence, this criterion does not seem to explain the stabilizing/destabilizing effect of compressibility.

However, looking at the effect of the angle of attack for a given Mach number, the growth rate is observed to reach its maximum value at $\alpha \approx 14°$ for all the Mach numbers considered here (see figure 3.10.a), which corresponds to the RBI region. Therefore, the interaction between the recirculation region and the far wake instability is a necessary but not sufficient condition to explain the change in the trend of ω_r, for a constant Mach number, as in the compressible regime.

The lengthening of the recirculation region induced by compressibility also increases the "closing angle" for each angle of attack, as we can see in figure 3.14.b where the L/H ratio is shown for three different Mach numbers. This suggests that the "closing angle" criterion cannot be used to explain the destabilizing/stabilizing effect of compressibility, since there is no difference in its variation with the Mach number between angles of attack $\alpha < 10°$ and $\alpha > 10°$. Furthermore, as the Mach number

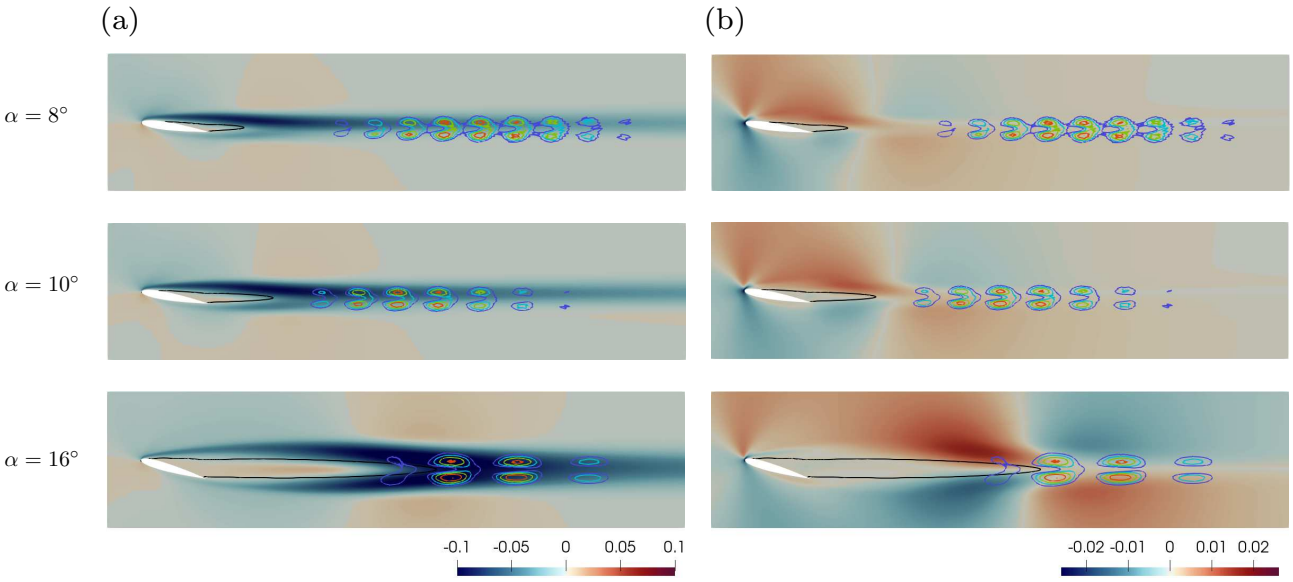

Figure 3.15 – Momentum variation of the base state with respect to the Mach number for different angles of attack at $M_\infty = 0.5$ and $Re = 1000$. Streamwise component $\partial \rho u_x / \partial M_\infty$ in column (a) and cross-stream component $\partial \rho u_y / \partial M_\infty$ in column (b). The solid black line corresponds to the isocontour $u_x = 0$. $||\widetilde{\rho \mathbf{u}}||/\max(||\widetilde{\rho \mathbf{u}}||)$ isocontours are shown from 0.5 to 1 across 5 levels.

increases, the maximum L/H ratio is observed for values of the angle of attack greater than that for which the maximum growth rate is measured: $\alpha = 14°$ for $M_\infty = 0.05$ and $\alpha = 16°$ for $M_\infty = 0.5$ to be compared with $\alpha \approx 14°$. The explanation of the maximum growth rate by the degree of parallelism of the base flow at the end of the recirculation region, is no longer valid in the compressible regime.

Through an adjoint-based sensitivity analysis, Meliga *et al.* [72] have analyzed the stabilizing/ destabilizing effects of the Mach number on axisymmetric wake flows (sphere and afterbody) by considering the competition between the production, cross-stream and streamwise advection of the disturbance by the base flow. In particular they have hypothesized that the destabilization is governed by the streamwise advection and is promoted when blockage effects are strong, *i.e.* when the width of the recirculation region is large compared to the characteristic length of the body. Yet, in our case, we find that blockage increases with α and that the intensity of destabilization (with increasing M_∞) decreases, see figure 3.13.

Nevertheless, the relation between blockage and the role of streamwise and crosswise advection may not be as straightforward. Figure 3.15 shows the spatial distribution of the base flow momentum variation with respect to the Mach number at $Re = 1000$. The streamwise momentum variation is negative downstream of the recirculation region, which promotes advection of the instability toward the recirculation bubble (destabilizing effect) for all the angles of attack. Its absolute value increases with α. The cross-stream momentum variation, instead, is significant only close to the recirculation bubble and tends to convect the instability away from the recirculation region (stabilizing effect). Looking at the location of the unstable mode relatively to the base flow recirculation region, the cross-stream momentum variation is likely to induce a stabilizing effect for $\alpha > 10°$ since the structure of the leading eigenmode is localized close to the recirculation region, even if at $\alpha = 10°$ they do not exhibit strong correlation yet. Conversely, for lower angles of attack, the instability is located far downstream of the recirculation region and is presumably not affected by such stabilizing effects. In a similar way, stabilizing effects due to crosswise advection may not play a significant role at Reynolds numbers close to stability threshold, where the unstable mode is located far downstream of the recirculation region, at least for $\alpha < 20°$.

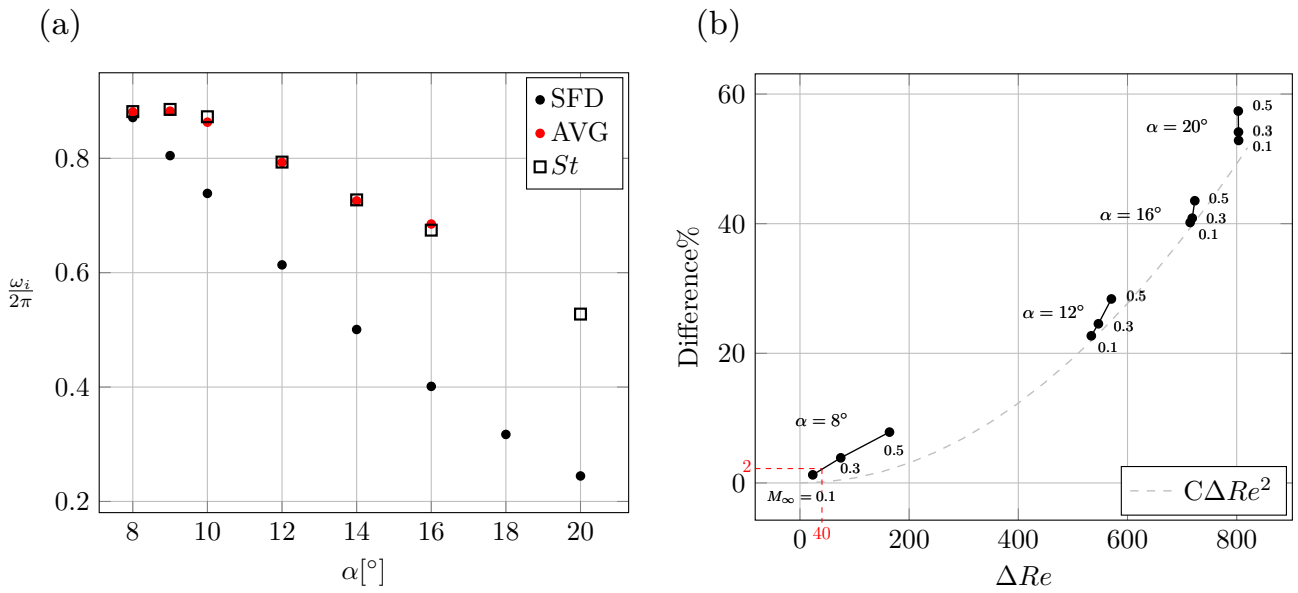

Figure 3.16 – Frequency of the most unstable mode of the filtered (SFD) and of the time-averaged base flow (AVG) at $Re = 1000$ and $M_\infty = 0.05$ for different angles of attack (a). Percentage difference between vortex shedding frequency (St) and frequency of the most unstable mode of the filtered base flow with respect to the gap from the stability threshold for three Mach numbers and four angles of attack (b).

3.4 Filtered vs time-averaged base flow

The response of the stability analysis has been seen to depend on the base flow choice [8, 68, 92, 96]. In some cases, the time-averaged flow has been found to be marginally stable, *i.e.* the growth rate of the most unstable mode being close to zero $\omega_r \approx 0$ above the stability threshold, while its frequency accurately predicts the one of the nonlinear periodic flow. Therefore, its use is not adequate for determining numerically the critical Reynolds number. Conversely, performing stability analysis on fixed point solutions enables the identification of the critical threshold, but the frequency of the most unstable mode diverges from the natural one as the Reynolds number is increased above the stability threshold.

The different responses of stability analysis performed on the fixed point solution and on the time-averaged flow have been described by Mantič-Lugo *et al.* [68], for the two dimensional cylinder, through the saturation process of the vortex shedding, *i.e.* the evolution from the fixed point solution to the periodic solution, and by Turton *et al.* [107]. The latter showed that those different responses between fixed point and time-averaged flow, were characteristic of systems with traveling wave solutions, *i.e.* quasi-monochromatic frequency oscillating flows. On the contrary, in systems with standing waves solutions, the time-averaged flow was found to be unstable and the predicted frequency differed from the natural one, as it has been observed for open cavities [96].

The present results for the NACA0012 airfoil confirms that the frequency of the most unstable mode given by the stability analysis for the fixed point solution, diverges from the nonlinear vortex shedding frequency, while stability analysis on the time-averaged base state leads to a mode frequency that accurately matches the vortex shedding one. This is shown in figure 3.16.a, where the mode frequency predicted by the stability analysis performed on both the filtered and the time-averaged base flow, are compared with the nonlinear Strouhal number for different angles of attack at $Re = 1000$ in the incompressible regime. The stability analysis performed on the time-averaged base flow accurately captures the variation of the Strouhal number with an increasing angle of attack, while the one

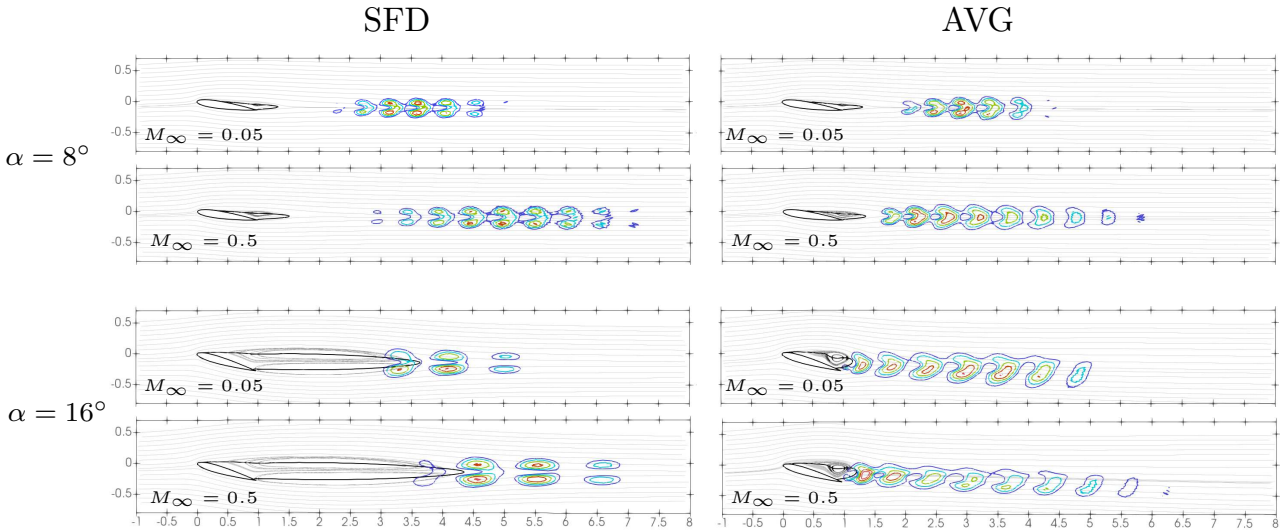

Figure 3.17 – $||\widetilde{\rho\mathbf{u}}||/\max(||\widetilde{\rho\mathbf{u}}||)$ isocontours at two different Mach numbers, $\alpha = 16°$ and $\alpha = 8°$ at $Re = 1000$ for the filtered (SFD) and time-averaged (AVG) base flows. Contours are from 0.5 to 1 across 5 levels. The base flow streamlines are in light gray and the solid black line corresponds to the isocontour $u_x = 0$.

performed on the filtered base flow only approaches the Strouhal number for $\alpha = 8°$. This is due to the fact that the chosen value of the Reynolds number $Re = 1000$ is very close to the critical Reynolds number of $\alpha = 8°$, which is $Re_c \approx 980$.

The relative error between the mode frequency of the filtered base flow and the Strouhal number of the nonlinear solution, $(St - \omega_i/2\pi)/St * 100$, is reported in figure 3.16.b as a function of the distance from the critical Reynolds number, $\Delta Re = (Re - Re_c) = (1000 - Re_c)$, for various angles of attack $\alpha = 8°$, 12°, 16° and 20° and Mach numbers $M_\infty = 0.1$, 0.3 and 0.5. The relative error is found to be quadratic with respect to ΔRe at iso-Mach number, while it increases linearly with the Mach number for a given angle of attack. Nevertheless, the way the frequency predicted by the stability analysis on the filtered solution diverges from the vortex shedding frequency, is found to be case dependent. Sansica *et al.* [92] have reported a difference of approximately 3% for $\Delta Re = 40$ in the case of the flow around a sphere, which is much lower than the difference of 25% measured in the case of the two-dimensional cylinder [8, 92] for the same ΔRe. In our case, the interpolation for $\alpha = 8°$ in figure 3.16.b yields to a difference close to 2% for $\Delta Re = 40$.

Figure 3.17 compares the spatial structure of the most unstable mode of the time-averaged base flow with the one of the filtered base flow for two angles of attack at $Re = 1000$ and Mach numbers of $M_\infty = 0.05$ and 0.5. In the incompressible case ($M_\infty = 0.05$), the spatial structures of the modes at $\alpha = 8°$ are similar to each other whereas they significantly differ for $\alpha = 16°$. This is due to the fact that the filtered and the time-averaged base flow are very different at $\alpha = 16°$, which is not the case for $\alpha = 8°$. Indeed, the recirculation region of the filtered solution expands downstream as the angle of attack increases, in contrast with the one of the time-averaged flow which, instead, shortens. Since the decrease of the mode frequency is related to the lengthening of the recirculation zone, this may explain why the mode frequencies of the filtered base flow are substantially smaller than the natural ones. Furthermore, the lengthening of the recirculation region also limits the asymmetry of the filtered base flow with respect to the streamwise direction, which is in contrast with the strong asymmetry of the time-average base flow. The difference in the base flows structure is also transferred to the mode structure. Indeed, the mode structure is almost symmetric with respect to the streamwise direction for the filtered case, while it is asymmetric and expands obliquely for its time-average counterpart.

Nevertheless, there are some similarities between the two cases. First, the mode switches from a WI type to a RBI type when the angle of attack is increased from $\alpha = 8°$ to $\alpha = 16°$. Second, the compressibility induces an extension of the mode structure along the streamwise direction in both cases.

3.5 Résumé

Dans ce chapitre, nous effectuons l'analyse de stabilité linéaire de l'écoulement bidimensionnel autour d'un profil NACA0012, dont la configuration et la validation ont été présentées au paragraphe §2.4.3. La plupart des résultats de ce chapitre font l'objet d'un article publié dans le *AIAA Journal* [109].

Dans la section §3.1, l'état de l'art des effets de la compressibilité sur l'aérodynamique et l'instabilité primaire bidimensionnelle du sillage de corps émoussés est présentée. Quelques études récentes ont été menées à propos de l'influence de la compressibilité sur la stabilité des écoulements à faible nombre de Reynolds [20, 72, 92]. Dans leur analyse de stabilité globale d'écoulements de sillage bidimensionnels axisymétriques, Meliga *et al.* [72] ont rapporté des effets contrastés de la compressibilité dans le régime subsonique (jusqu'à $M_\infty = 0.7$), selon l'écoulement considéré. Dans le cas de l'écoulement axisymétrique autour d'une ogive à culot droit, en se concentrant sur la bifurcation de Hopf secondaire, ils ont observé une augmentation du nombre de Reynolds critique auquel le mode hélicoïdal oscillant secondaire devient instable lorsque le nombre de Mach augmente, ce qui correspond à un effet stabilisateur de la compressibilité. Inversement, ils ont observé une diminution du même nombre de Reynolds critique en augmentant le nombre de Mach, jusqu'à $M_\infty \approx 0.63$, pour l'écoulement autour d'une sphère. Grâce à une analyse de sensibilité basée sur l'opérateur adjoint, ils ont relié ce comportement stabilisant/déstabilisant à un changement dans l'advection longitudinale de la perturbation par l'écoulement de base dans la zone de recirculation se développant directement à l'aval du corps. Sansica *et al.* ont étendu l'analyse de stabilité de Meliga pour la sphère jusqu'au régime supersonique à $M_\infty = 1.2$, pour des nombres de Reynolds compris entre $Re = 200$ et $Re = 370$. En considérant un écoulement de base tridimensionnel, ils ont confirmé l'effet non monotone de la compressibilité mais ont observé une déstabilisation seulement dans le régime subsonique jusqu'à $M_\infty \approx 0.3$. Pour des nombres de Mach plus élevés, le mode oscillant hélicoïdal est progressivement amorti jusqu'à sa stabilisation complète dans le régime subsonique élevé ($M_\infty \approx 0.7$ pour $Re = 280$). Ils ont attribué cette différence à l'hypothèse d'axisymétrie de l'écoulement de base utilisée par Meliga *et al.* .

Dans la section §3.2, l'influence de l'incidence et du nombre de Reynolds est traitée dans le régime incompressible. La variation de l'incidence à un nombre de Reynolds constant et la variation du nombre de Reynolds à incidence constante révèlent un comportement non monotone sur le taux de croissance du mode le plus instable. À $Re = 1000$, le taux de croissance du mode augmente fortement lorsque l'incidence passe de 8° à 14° où il atteint sa valeur maximale, suivi d'une diminution pour $\alpha \geq 14°$ (voir figure 3.2.a). La fréquence du mode ω_i, en revanche, diminue constamment, en raison de l'allongement de la bulle de recirculation. De même en variant le nombre de Reynolds à incidence fixe $\alpha = 20°$ (figure 3.6.a), le taux de croissance présente une évolution non monotone avec un maximum observé autour de $Re = 800$. La fréquence du mode augmente légèrement à proximité du seuil de stabilité, c'est-à-dire de $Re = 200$ à $Re = 300$; ceci est probablement dû à l'amincissement des couches de cisaillement, causé par la diminution de la viscosité qui, à ces nombres de Reynolds très bas, peut avoir un impact sur la fréquence plus important que l'allongement de la zone de recirculation. Au-delà de $Re = 300$, au contraire, la fréquence du mode diminue. Dans les deux cas, le taux de croissance maximal est atteint lorsque l'écoulement de base est le plus parallèle à la fin de la zone de recirculation. De plus, on constate que le taux de croissance maximal, en variant le nombre de Reynolds, est observé lorsque le point d'intensité maximale du mode coïncide avec la fin de la bulle de recirculation.

Le cas compressible est considéré dans la section §3.3. Comme synthétisé par la figure 3.12, un effet stabilisant ou déstabilisant de la compressibilité est observé en fonction de l'angle d'incidence et du nombre de Reynolds. Pour $\alpha < 20°$, la compressibilité a un effet déstabilisant près du seuil critique, qui se traduit par une bifurcation de Hopf plus précoce, tandis que l'augmentation du nombre de Mach

entraîne toujours une diminution du taux de croissance du mode lorsqu'on se situe bien au delà du seuil critique. Comme suggéré par Meliga *et al.* [72], nous avons lié l'effet stabilisant/déstabilisant de la compressibilité à une modification de l'écoulement de base, plus particulièrement en lien avec la distribution spatiale de la variation de la quantité de mouvement de l'écoulement de base par rapport au nombre de Mach. La variation de quantité de mouvement longitudinale est négative en aval de la région de recirculation, ce qui favorise l'advection de l'instabilité vers la bulle de recirculation (effet déstabilisant), ce quelle que soit l'incidence. La variation de la quantité de mouvement verticale, au contraire, n'est significative qu'à proximité de la bulle de recirculation et à pour effet d'éloigner l'instabilité de la zone de recirculation (effet stabilisant). Si l'on considère l'emplacement du mode instable par rapport à la région de recirculation de l'écoulement de base, la variation de quantité de mouvement verticale est susceptible d'induire un effet stabilisant pour $\alpha > 10°$ puisque l'instabilité est proche de la région de recirculation. Inversement, pour des incidences plus faibles, l'instabilité est située loin en aval de la région de recirculation et n'est vraisemblablement pas affectée par de tels effets stabilisants.

Dans la section §3.4, une comparaison entre la réponse de l'analyse de stabilité sur l'état de base filtré et l'état de base moyenné temporellement est présentée. L'analyse de stabilité sur l'écoulement de base moyenné dans le temps capture bien la variation du nombre de Strouhal, alors que celle sur l'écoulement de base filtré, ne s'approche du nombre de Strouhal qu'à $\alpha = 8°$ (figure 3.16), incidence pour laquelle le nombre de Reynolds considéré $Re = 1000$ est très proche du nombre de Reynolds critique $Re_c \approx 980$. La différence entre la fréquence prédite par l'analyse de stabilité sur l'écoulement de base SFD et celle de l'écoulement non-linéaire s'avère augmenter quadratiquement par rapport à $\Delta Re = Re - Re_c$ à iso-nombre de Mach, tandis que, pour chaque incidence, cette différence augmente linéairement en augmentant le nombre de Mach. Des différences sont également observées sur la structure du mode. En particulier, la forte asymétrie de l'écoulement de base moyenné dans le temps à $\alpha = 16°$ se transpose sur la structure du mode qui se développe de manière oblique dans le sillage (figure 3.17).

Chapter 4

Three-dimensional secondary instabilities

Abstract: In this chapter, we investigate the three-dimensional linear stability of bluff bodies periodic wakes. In §4.1, prior knowledge on the process that leads to the three-dimensionalization of the wake is introduced and discussed, with a description of modes A and B secondary instabilities of the circular cylinder periodic wake. In §4.2 the influence of Reynolds and Mach numbers on the two-dimensional periodic wake of the circular cylinder and on the properties of modes A and B is assessed. Section §4.3 presents a comparison between the stability analysis response on the filtered, time-averaged and periodic base flows for the circular cylinder wake. In section §4.4 preliminary results on compressibility effects on the three-dimensionalization of the NACA0012 airfoil periodic wake at 20° angle of attack are introduced. Section §4.5 summarizes the present chapter in French.

Contents:

4.1 Three-dimensionalization of the wake

Within the periodic regime, the amplitude of the oscillation increases when increasing the Reynolds number. Then, a second bifurcation occurs, which triggers the three-dimensionalization of the flow. The three-dimensional structures are due to the deformation of the von Kármán vortex street in the near wake [63, 105, 112]. The three-dimensional transition involves two consecutive steps, each characterized by a discontinuity in the Strouhal–Reynolds numbers relationship that can be seen in figure 4.1 at points 2 and 3 for the circular cylinder. These discontinuities are caused by the emergence of the so called mode A and mode B secondary three-dimensional instabilities, respectively, whose time periodicity is the same of the base state [37, 111, 113]. These modes can be characterized by their symmetry properties [15, 17], characteristic spanwise wavelengths and their structure with respect to the base flow. Indeed, two different regions can be identified in the two dimensional flow, as shown in figure 4.2: the elliptic and the hyperbolic regions, that are related to the instability mechanisms of these two modes.

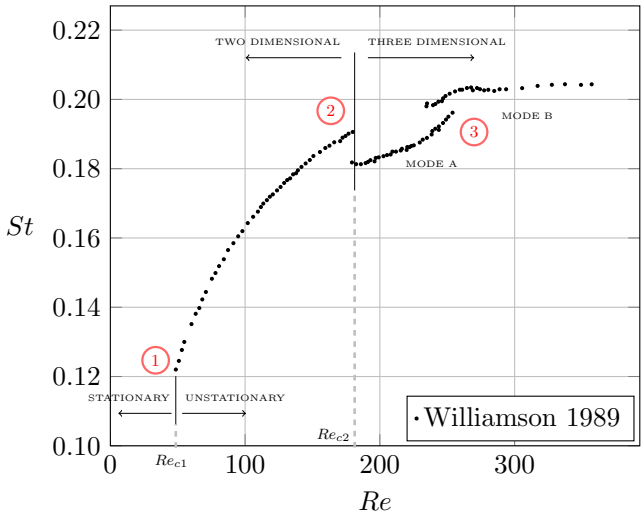

Figure 4.1 – Reynolds-Strouhal relation at low Reynolds numbers for the cylinder wake.

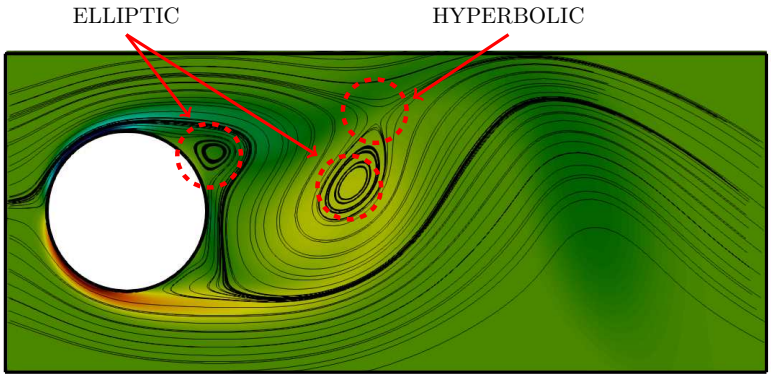

Figure 4.2 – Vorticity field with streamlines of the two-dimensional cylinder wake showing the elliptic and hyperbolic regions.

The first one, mode A, appears around $Re \approx 180 - 190$ and is associated with an elliptic instability of the primary vortex cores [62, 105], which start to deform along the spanwise direction pulling back the base flow spanwise vorticity upstream at some points [112] (see figure 4.3), leading to the development of large scale transverse structures of characteristic wavelength $\lambda_z \sim 4D$.

Moreover, this mode preserves the half-period symmetry, $\mathbf{Hu}(\mathbf{x}, t) = \mathbf{u}(\mathbf{x}, t)$, of the base state, expressed in terms of velocity and vorticity as follows:

$$\begin{aligned} \mathrm{H}(u_x, u_y, u_z)(x, y, z, t) &= (u_x, -u_y, u_z)(x, -y, z, t + \frac{T}{2}) \\ \mathrm{H}(\omega_x, \omega_y, \omega_z)(x, y, z, t) &= (-\omega_x, \omega_y, -\omega_z)(x, -y, z, t + \frac{T}{2}) \end{aligned} \tag{4.1}$$

The second one, mode B, which arises around $Re \approx 230 - 260$, is instead associated with a hyperbolic instability. It develops in the stretched braid region, which develops in between two-consecutive counter-rotating von Kármán vortices and is related to the formation of finer scale structures of characteristic wavelength $\lambda_z \sim 1D$. This mode breaks the half-period symmetry of the base state:

$$\mathbf{Hu}(\mathbf{x}, t) = -\mathbf{u}(\mathbf{x}, t) \tag{4.2}$$

In figure 4.4 the iso-surfaces of the three vorticity components show, for mode A, a concentration of vorticity in the vortex cores that persist downstream, also visible in the (x, y)-plane, while mode

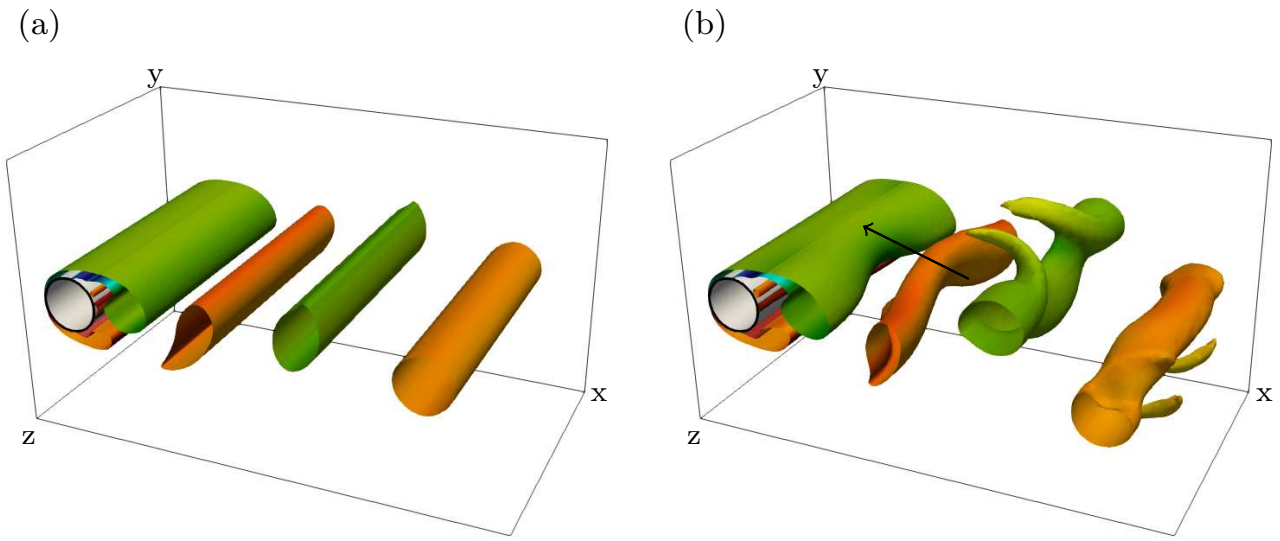

Figure 4.3 – Vorticity iso-surfaces of the two dimensional flow (a) compared to the first stage mechanism of vortex deformation with base flow spanwise vorticity pulled back upstream (b). DNS at $Re = 250$.

B vorticity is concentrated in the braid region and does not persist downstream as far as mode A. Nevertheless, both modes involve the generation of vorticity located in the braid connecting the primary von Kármán vortices. Yet, in accordance with the half-period symmetry, the streamwise and spanwise vorticity of mode A change sign passing from a primary vortex to the next. Conversely, for mode B, the streamwise and spanwise vorticity have the same sign between two consecutive primary vortices. We can also remark that both mode A and mode B present the same transverse shift of $\lambda_z/4$ of spanwise vorticity $\tilde{\omega}_z$ with respect to $\tilde{\omega}_x$ and $\tilde{\omega}_y$ which are instead in phase.

Passing from mode A to mode B, the instability shifts from the vortex core towards the braid (*i.e.* from the elliptic to the hyperbolic region). This has also been observed in round jets and mixing layers and is actually a typical feature of open shear flows[1] [6, 71, 80, 84].

At higher Reynolds number $Re \approx 380$ [17], a third secondary mode is found to become unstable, this mode is referred to as the Quasi-Periodic (QP) mode, whose characteristic wavelength lies in between those of modes A and B and whose time-periodicity is almost twice the one of the base state [17]. This mode will not be addressed in this work but is worth to be mentioned here to give a complete view.

Although the occurrence of modes like A, B and QP in the three-dimensionalization process of the circular cylinder wake can be thought to represent the generic transition to three-dimensional motions of any von Kármán vortex street, this seems to be true only for flows with $Z_2 \times O(2)$ symmetry[2], and only looking at these modes with respect to their symmetry properties [15, 17]. Indeed, in $Z_2 \times O(2)$ symmetric flows, the correlation between preserving/breaking symmetry and large/short wavelength instabilities, as observed in case of the cylinder, is not generic. Considering these modes with respect to their symmetry properties rather then their physical characteristics (such as their wavelength), provides a more general statement: flows with a $Z_2 \times O(2)$ symmetry bifurcate to a three-dimensional state via the emergence of two synchronous (same time periodicity as the base state) modes, one preserving the base state H-symmetry and one breaking it, together with a quasi-periodic mode. In

[1] This only refers to the transition from large scale structures localized in the vortex core to small scale structures localized in the braid, not to symmetric/antisymmetric properties, since these characteristics are related to the time periodicity

[2] Z_2 refers to half-period spatio-temporal symmetry, while $O(2)$ refers to the fact that the wake is symmetric for arbitrary translations or reflections.

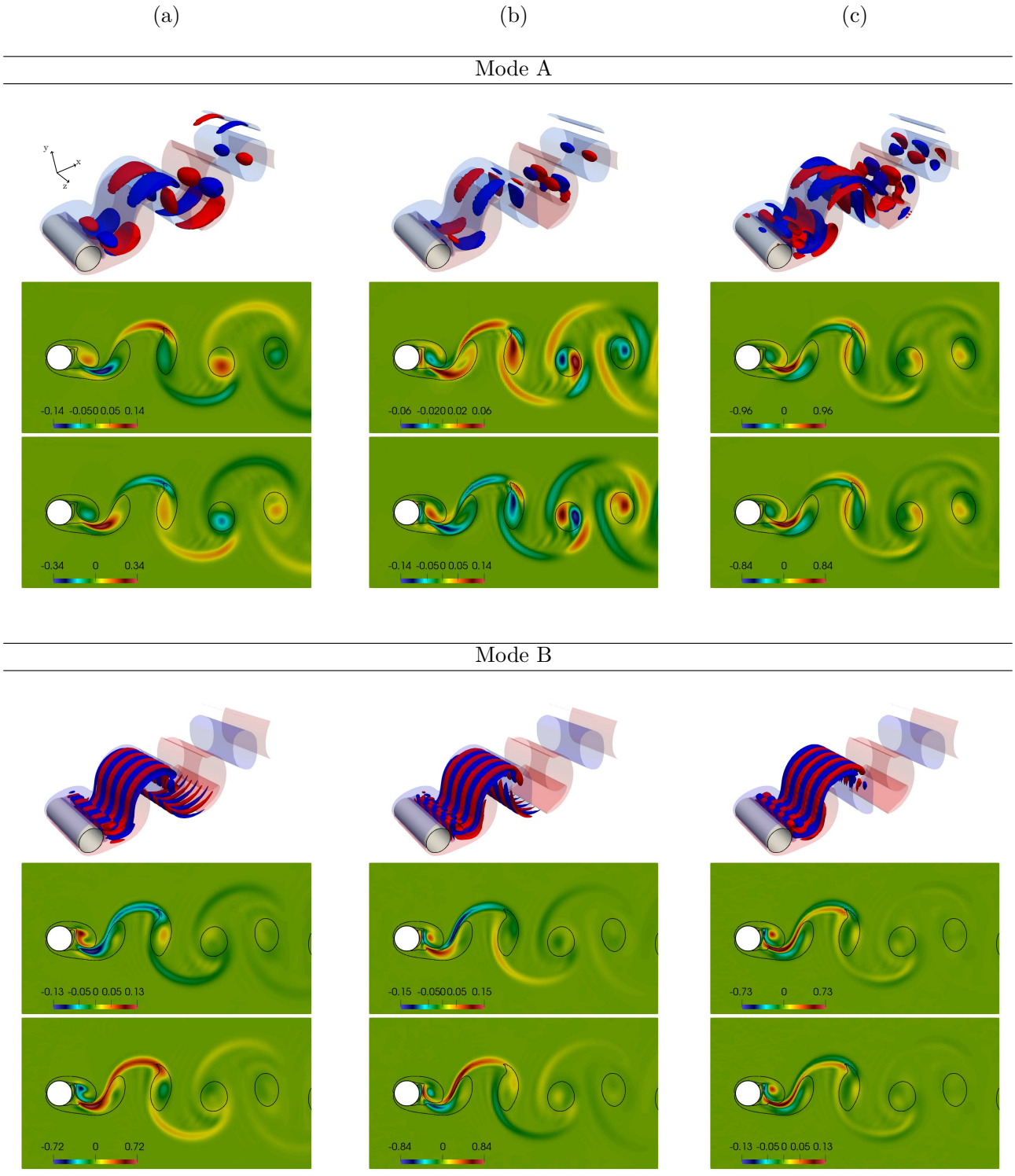

Figure 4.4 – Mode vorticity $\widetilde{\boldsymbol{\omega}}/\max(||\widetilde{\boldsymbol{\omega}}||)$ of mode A and mode B with wavelength $\lambda_z = 3D$ at $Re = 250$ and $0.75D$ at $Re = 300$, respectively: (a) streamwise, (b) cross-stream and (c) spanwise component. Three-dimensional iso-surfaces at levels ± 0.1 (positive in red, negative in blue) superposed to translucent iso-surfaces at level ± 0.01 of base flow vorticity. Spatial variation on the (x, y)-plane at two different spanwise locations ($z = 1.4D$ and $z = 1.4D + \lambda_z/4$) superposed to base flow vorticity contour at ± 0.05 (black line).

fact, other $Z_2 \times O(2)$ symmetric flows have been found to transition to a three-dimensional state with the same type of modes (in terms of symmetries) but they can correspond to different wavelengths, or their chronology in the flow history may be different to what has been observed in the circular

cylinder case [17, 70, 89]. For example, the flow past a square cylinder flow has been found to become three-dimensional via the occurrence of the same types of modes: the first mode to emerge is a long wavelength one, $\lambda_z \approx 5.03L$, which preserves the base flow symmetry, the second is a short wavelength one, $\lambda_z \approx 1.11L$, which breaks the base flow symmetry and the third one is a quasi periodic one [85]. However, for the wake developing downstream a flat plate, the two synchronous modes have similar wavelength [56]. In the flow past a high aspect ratio elliptic cylinder at zero angle of attack, instead, the symmetry-breaking mode has been found to become unstable before the symmetry-preserving one [62]. Moreover, the wavelengths of both modes are found to increase with the aspect ratio of the elliptic cylinder[3]. Finally, in the non-autonomous driven cavity, the chronology differs under certain conditions[4]: either the QP mode or the symmetry-breaking mode, which in this case corresponds to large wavelengths (unlike the cylinder case), appears first while the symmetry-preserving mode, corresponding to short wavelengths, emerges later [15, 16, 17].

Before linking the three-dimensionalization process of the cylinder wake to that of generic time-periodic wake flows[5], some clarifications are needed. The flow around the cylinder belongs to the class of $Z_2 \times O(2)$ flows and therefore satisfies the symmetry about the half-period $T/2$ (H-symmetry) given by expression (4.1). As a consequence, the Floquet analysis can be performed for the half-period $T/2$ instead of the full period T [15, 17]. Thereby, the symmetry-preserving mode would become unstable by crossing the unit circle in the complex plane with a Floquet exponent $\mu_{\mathrm{H}} = 1$, the QP mode with a complex one μ_{H} and the symmetry-breaking mode with $\mu_{\mathrm{H}} = -1$, which corresponds to a period doubling bifurcation (see figure 1.10) of the base flow half-period, resulting in a period T. Hence, one may consider that the symmetry-preserving mode has a period of $T/2$, but this periodicity only refers to the H-symmetry. Applying the half-period H-symmetry twice, which corresponds to a Floquet analysis on the whole period, we obtain the following identity:

$$\mathbf{u}(\mathbf{x}, t) = \mathrm{H}^2\mathbf{u}(\mathbf{x}, t) = \mathrm{I}\mathbf{u}(\mathbf{x}, t + T) = \mathbf{u}(\mathbf{x}, t + T) \tag{4.3}$$

which correspond to a T-periodicity. Hence, the Floquet multipliers μ_{P} obtained by considering the whole period T are the square of those obtained by the Floquet analysis performed on the half-period: $\mu_{\mathrm{P}} = (\mu_{\mathrm{H}})^2$. Therefore, both modes A and B become unstable by crossing the unit circle with a Floquet exponent $\mu_{\mathrm{P}} = \mu_{\mathrm{H}}^2 = 1$, which corresponds to T-periodic modes.

For flows past canonical bodies which do not satisfy the half-period symmetry, Floquet analysis can only be performed for the whole period T. For these flows, a different instability may arise [90, 94]. In particular, the so-called mode C, has been observed and found to be the leading three-dimensional mode in several configurations [21, 54, 94, 114]. Mode C is a period doubling mode corresponding to a marginal Floquet multiplier of $\mu = -1$, hence, its periodicity is twice that of the base state. In the last section of this Chapter, where the three-dimensionalization of the NACA0012 airfoil is briefly addressed, we will refer to this mode as the period doubling mode instead of mode C.

In symmetric flows, since $\mu_{\mathrm{P}} = (\mu_{\mathrm{H}})^2$, the only way to obtain a period doubling mode, $\mu_{\mathrm{P}} = -1$, *i.e.* a mode whose period is $2T$, would be with $\mu_{\mathrm{H}} = \pm i$, *i.e.* a quadrupling of the half period. However, as pointed out in section 1.4.2, this solution is in resonance with the period doubling $\mu_{\mathrm{H}} = -1$ solution (the symmetry-breaking mode). This explains why, in general, the period doubling mode is suppressed in symmetric flows [102], while it can emerge in non-symmetric ones.

[3] Leontini *et al.* [62] give other names to these modes ($\hat{A}$ and $\hat{B}$ modes respectively) which they justify by the increase of their wavelength and the slight differences observed on the structures, even if their symmetries are the same as modes A and B.

[4] In particular changing the length of the cavity

[5] The limit cycle solution of these flows is not necessarily symmetric, while periodic solutions of $Z_2 \times O(2)$ represent a symmetric limit cycle.

Brief discussion on the period doubling mode

It is reasonable to wonder if the period doubling mode of non-symmetric flows can be seen as the equivalent of either the symmetry-breaking mode or the QP mode arising in symmetric flows. In symmetric flows such as the circular cylinder wake, the first instability that appears (mode A) breaks the spanwise homogeneity (transition from a 2D to a 3D flow), while the second instability (mode B), which in the half period corresponds to a period doubling bifurcation, breaks the spatio-temporal half-period symmetry given by equation (4.1). For non-symmetric flows, the first mode to appear (at least at high angles of attack) is the period doubling one, which breaks both the spanwise homogeneity and time periodicity of the base flow, likewise the mode B with respect to the half-period in the case of the cylinder flow.

For the elliptic cylinder or the non-autonomous driven cavity [17, 62], changing other parameters than the Reynolds number, such as the aspect ratio or the cavity length, gives rise to a different chronology in the occurrence of the modes. For example, decreasing the angle of attack in the flow around a NACA airfoil or other symmetric bodies would induce a more symmetric flow and the emergence of a synchronous mode as the first secondary instability. This has been shown for the square cylinder wake by varying the angle of attack [14, 95] and for the wake of two circular cylinders in staggered arrangements by varying their relative position [21], while it has not been explored so far for NACA airfoils. Nevertheless, He *et al.* [45], in their stability analysis of flows around different NACA airfoils, reported the emergence of a synchronous long wavelength instability ($\lambda_z \approx 2\pi C$), much less unstable that the period doubling mode, but they attributed this mode to numerical artifacts, while Deng *et al.* [29] attributed this mode to mode A.

On the other hand, a complex mode has been also observed for NACA airfoil wakes [45, 73], but associated with a Floquet exponent not close to $\mu = \pm|\mu|i$ as for the circular cylinder[6]. For the NACA0015 airfoil, for example, $\mu \approx |\mu| e^{\pm i\bar{\omega}_i 0.1}$ at $Re = 500$ [7] [45]. Nevertheless, when increasing the Reynolds number, the ratio between the frequency of the complex mode and the one of the base flow increases to ≈ 0.15 (this ratio should be ≈ 0.25 if it corresponds to a period quadrupling, *i.e.* a complex mode with $\mu = \pm i$). Therefore, one may think that it would be interesting to perform a Floquet analysis over two periods of the base flow (intersection with the Poincaré section every $2T$) at higher Reynolds number to see if a period doubling (doubling of $2T$, hence $4T$) is observed. But, in this case the Floquet multiplier of such a mode would be the square of the one given by the Floquet analysis performed on a single period of the base flow. A preserving periodicity mode $\mu = (-1)^2 = 1$ would appear together with a mode with a period of $8T$, *i.e.* a Floquet exponent of $\mu = \pm i$, in resonance with the -1 mode, corresponding to the $4T$ period mode. This process corresponds to the period doubling cascade to chaos. These successive period doubling bifurcations can be identified in the power spectra of time series of both the lift [33] and velocities [87]. In particular, Pulliam *et al.* [87] observed this phenomenon up to 32 periods for the NACA0012 airfoil at $\alpha = 20°$. They also measured the limit of the ratio between each bifurcation ($Re_c \approx 1400$ for $4T$, $Re_c \approx 1525$ for $8T$, $Re_c \approx 1575$ for $16T$ and $Re_c \approx 1580$ for $32T$) finding a Feigenbaum number[8] of $\delta = \frac{Re_{c,n-1} - Re_{c,n-2}}{Re_{c,n} - Re_{c,n-1}} \approx 4.5$ and a first accumulation point at $Re \approx 1583$. Above this Reynolds number, the system response presents *"a series of chaotic states interspersed with period windows"* [87] . Each periodic window is characterized by another period doubling cascade which ends, again, in an accumulation point. In particular the

[6] And for this reason it has not been refered to as a QP mode in [45], while in [73] the mode is refered to as QP.

[7] The 0.1 value at the exponent corresponds to the the ratio between the period of the base flow T and that of the complex mode, while $\bar{\omega}_i = 2\pi/T$.

[8] The Feigenbaum number takes its name from the physicist Mitchell J. Feigenbaum, who first demonstrated that the successive period doubling bifurcations presented an accumulation point, with a limit of the ratio between successive bifurcations that he found to be constant ($\delta \approx 4.67$) for many nonlinear systems.

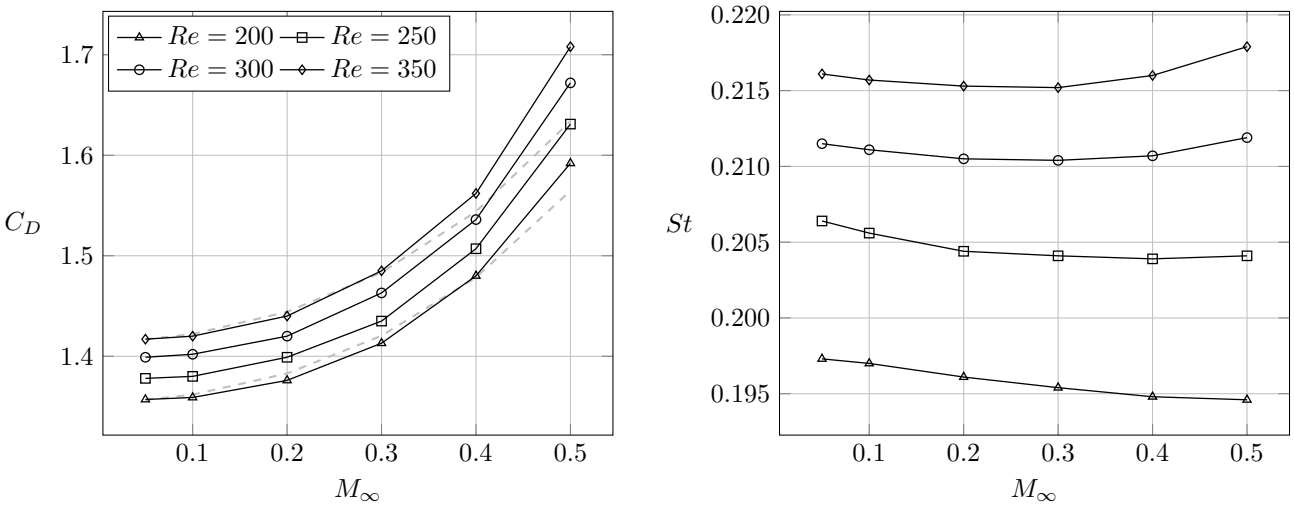

Figure 4.5 – Mean drag coefficient and Strouhal number of the two-dimensional flow. Dashed line superposed to the drag coefficient curves are the theoretical predictions given by the Prandtl–Glauert transformation for $Re = 200$ and 350.

successive three periodic windows are period-doubling cascades of 14, 10 and 6 periods, respectively.

4.2 3D circular cylinder

In order to perform three-dimensional stability analysis, the 3D mesh and base flow have been generated by extruding the two-dimensional grid and the DNS solution along the spanwise direction. The mesh convergence study is reported in Appendix D.

4.2.1 Base flow characterization

The mean drag coefficient and Strouhal number of the two-dimensional flow, used as base state for the stability analysis, are reported in figure 4.5 for the range of Reynolds and Mach numbers considered in this chapter. The drag coefficient increases when increasing the Reynolds number[9] and, as previously found for Reynolds numbers up to $Re = 100$ [20], it also increases due to compressibility effects as the Mach number is increased. In their work on compressibility effects on the two-dimensional flow around a circular cylinder up to $Re = 100$, Canuto & Taira [20] observed that, for a Reynolds number equal to 20, the Prandtl–Glauert theoretical prediction

$$C_D\left(M_\infty\right) = \frac{C_{D,M_\infty=0.05}}{\sqrt{1-M_\infty^2}} \tag{4.4}$$

overestimates the drag coefficient when increasing the Mach number, but the overestimation decreases when the Reynolds number is increased up to $Re = 100$, where the Prandtl–Glauert transformation gives a correct approximation of the drag increase. Figure 4.5 shows that, in the range of Reynolds numbers considered here *i.e.* $Re \in [200; 350]$, the Prandtl–Glauert provides a good estimation of the drag coefficient up to a given Mach number, which decreases with increasing Reynolds number (from $M_\infty = 0.4$ at $Re = 200$ to $M_\infty = 0.3$ at $Re = 350$), before diverging from the real values with an underestimation increasing with Re.

[9] This trend is different to the one observed at lower Reynolds numbers, where the decrease of the viscous drag term is stronger than the increase of the pressure drag term, which results in a decrease of the drag coefficient with the Reynolds number.

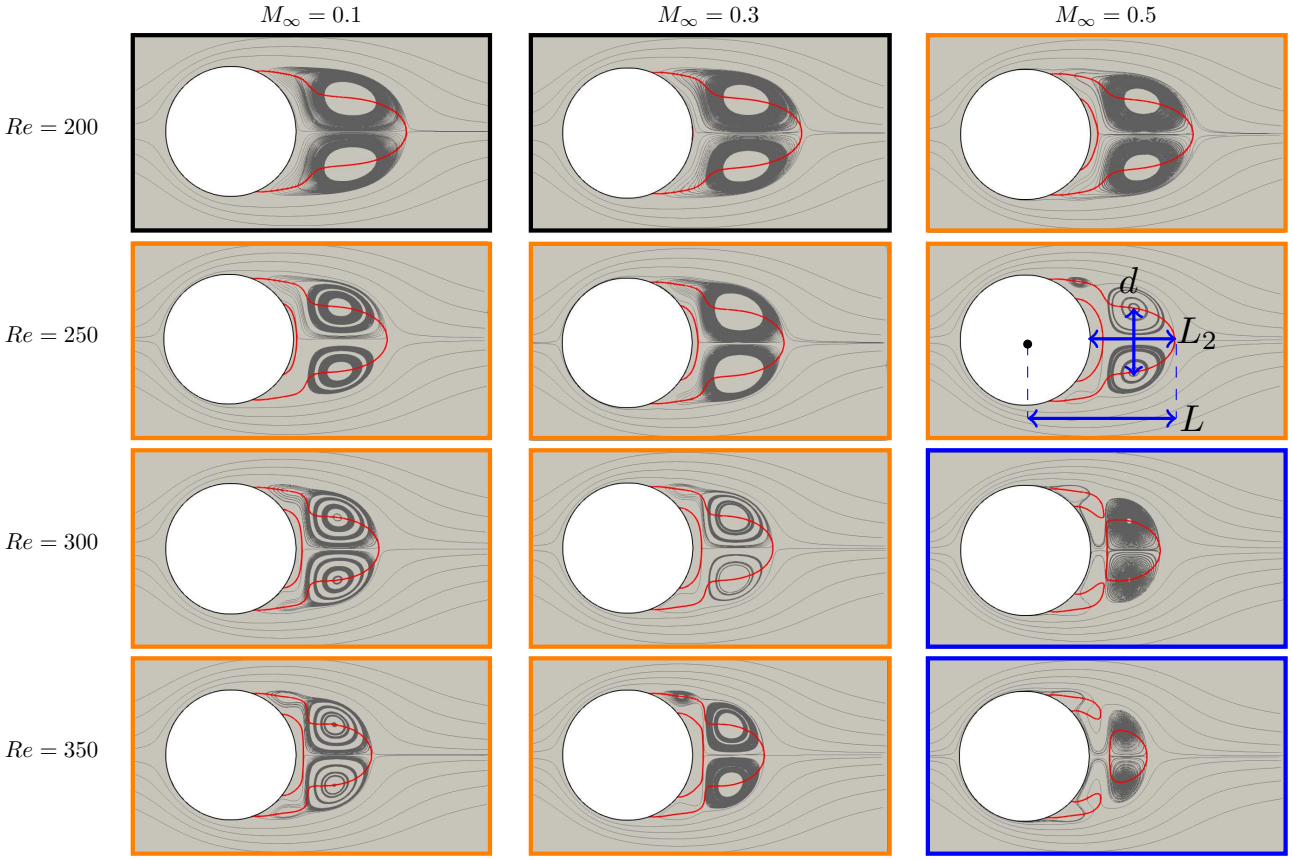

Figure 4.6 – Structure of the time-averaged base flow. Streamlines are shown in gray color and red line is the isocontour of time averaged longitudinal velocity $\bar{u}_x = 0$. Characteristic lengths of the recirculation region are indicated for $Re = 250$ and $M_\infty = 0.5$. Black, orange and blue frames indicate different structure types.

The Strouhal number exhibits a monotonic decrease with the increase of the Mach number, up to $Re = 250$. This trend is similar to the one reported for lower Reynolds numbers [20], with a decreasing relative difference: $(St_{M_\infty=0.05} - St_{M_\infty=0.5})/St_{M_\infty=0.05} = 8\%$ at $Re = 50$, 3.5% at $Re = 100$ and 1.5% at $Re = 200$. For Reynolds numbers higher than $Re = 250$, the Strouhal number decreases for low Mach number values, before increasing with compressibility. A similar trend has been observed for the NACA0012 airfoil wake at $Re = 1000$ by increasing the angle of attack, see figure 3.9. Since the percentage of variation is less than 2%, a further investigation at higher Reynolds numbers is needed to confirm this trend.

The structure of the time-averaged flow, reported in figure 4.6 which shows the streamlines and the zero longitudinal velocity contour, is found to strongly vary within the range of Reynolds and Mach numbers considered. This mainly depends on three steps of the vortex shedding: the development of an opposite sign vorticity region, the vorticity pulled upstream by the forming vortex and the vorticity rolled up/entrained by the opposite sign main vortex [39]. Three different mean flow structures can be hence identified:

- The first structure (type 1), which corresponds to cases with $Re = 200$ and $M_\infty \in [0.05; 0.3]$, exhibits a unique recirculation region downstream of the cylinder with two time averaged counter-rotating symmetrical vortices (figure 4.6 with black frame). Instantaneous vorticity flow fields in figure 4.7.a, show that vorticity with opposite sign to the one of the forming vortex is stagnating at the base of the cylinder ($t = T/8$). This vorticity is due to the interaction between the forming vortex and the cylinder wall at $t = 0$, which is indicated by the arrow at $t = T/2$ for the

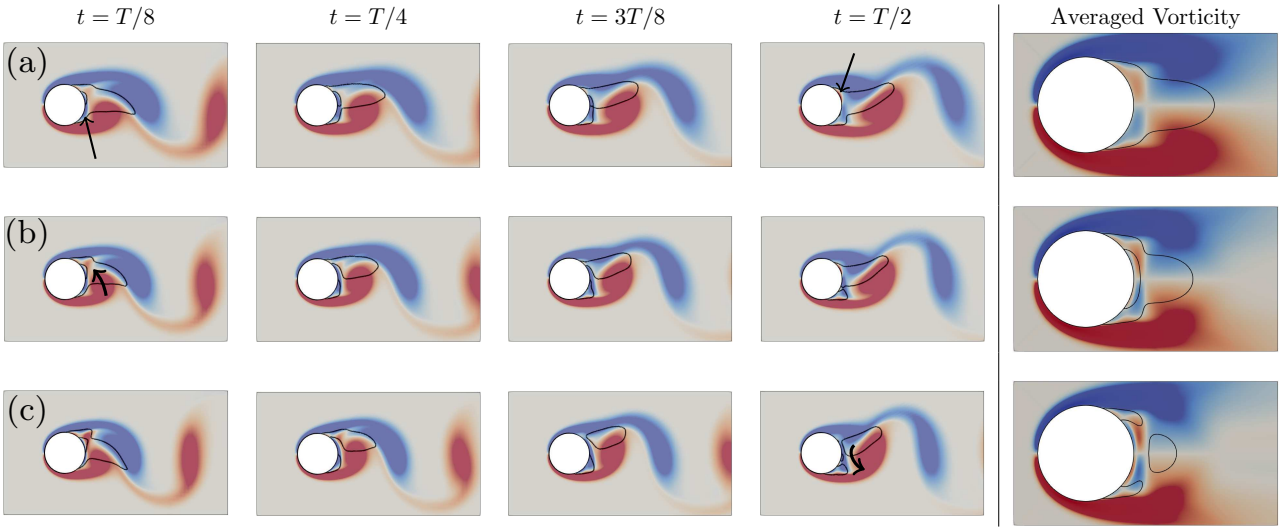

Figure 4.7 – Evolution of both the instantaneous positive (red) and negative (blue) vorticity saturated at 10% of the maximum and the isocontour of longitudinal velocity $u_x = 0$ (black line) during the first half-period of vortex shedding. The corresponding time-averaged vorticity is given at the extreme right for comparison. (a) Structure of type 1 for $Re = 200$ and $M_\infty = 0.1$, (b) Structure of type 2 for $Re = 300$ and $M_\infty = 0.3$, (c) Structure of type 3 for $Re = 350$ and $M_\infty = 0.5$.

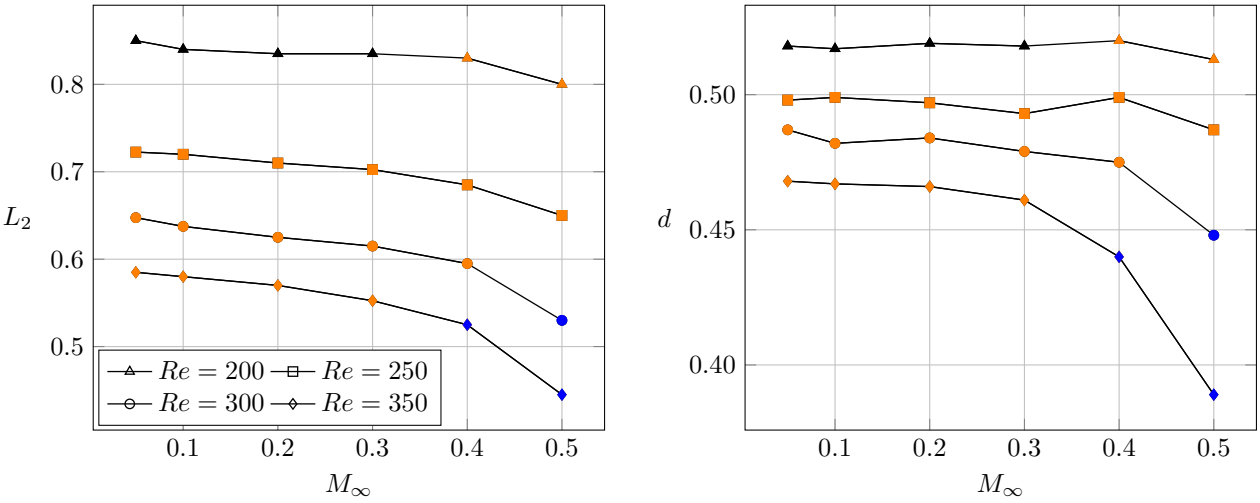

Figure 4.8 – Evolution of the time-averaged flow characteristic lengths with respect to the Mach number for the different the Reynolds numbers. Black, orange and blue symbols indicate the different base flow structures (type 1, 2 and 3) as illustrated in figure 4.6.

opposite sign forming vortex. This vorticity region, which stagnates at the rear of the cylinder ($t = T/8, T/4, 3T/8$) until it is feed by the same sign vortex at $t = T/2$, is not that strong to produce a mean recirculation region.

- The second structure (type 2), which corresponds to cases from $Re = 200$ and $M_\infty = 0.4$ to $Re = 300$ and $M_\infty = 0.4$ and $Re = 350$ and $M_\infty \in [0.05; 0.3]$, exhibits a mean second recirculation region downstream of the cylinder (figure 4.6 with yellow frame), with two additional counter-rotating vortices in the time-averaged flow. The induced vorticity and the feeding by the forming vortex (figure 4.7.b at $t = T/8$) are stronger compared to the first case.

- The third structure (type 3) corresponds to cases at $Re = 300$ and $M_\infty = 0.5$ and $Re = 350$ and $M_\infty \in [0.4; 0.5]$ (figure 4.6 with blue frame). In this case, the induced vorticity and the feeding

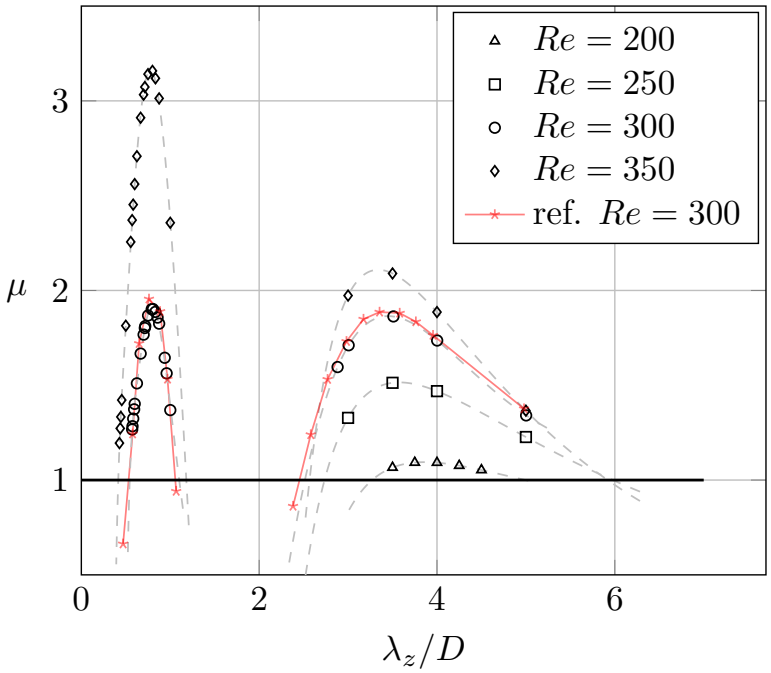

Figure 4.9 – Floquet multiplier μ of the secondary instabilities as a function of the spanwise wavelength λ_z for different Reynolds numbers. For comparison, the red lines correspond to results from Leontini *et al.* [62] at $Re = 300$. Dashed lines represent the interpolation curves for a given Reynolds number.

by the forming vortex are stronger compared to the previous cases (figure 4.7.c at $t = T/8$). Moreover, the entrainment of the vortices (figure 4.7.c at $t = T/2$) produces positive signed velocity in a more extended area, in particular enlarging the second recirculation zone. This makes the two mean recirculation regions to approach one another until they split in three distinct regions.

We can define two main characteristic lengths from the time average flow to characterize the recirculation region: the streamwise extent of the recirculation region (L_2) and the cross-stream separation distance between the two main counter-rotating vortices (d), as indicated in figure 4.6 for $Re = 250$ and $M_\infty = 0.5$. Their variation with respect to the Reynolds and Mach numbers is reported in figure 4.8, with the different time-averaged flow structures indicated by the respective colors. We can see that both the length of the recirculation region and the vortex separation distance decrease when the Reynolds number is increased. The length of the recirculation region is also decreasing with increasing compressibility. The length reduction is more pronounced for the higher Reynolds numbers and particularly when the time-averaged base flow switches from a type 2 to a type 3 structure. The separation distance between the main vortex centers is affected by compressibility at Reynolds number above $Re = 300$ and its reduction due to compressibility is more pronounced when the time-averaged base flow switches from a type 2 to a type 3 structure. Interestingly, the change in trend of the Strouhal number at $Re = 300$ and 350 (figure 4.5) also occurs when switching from type 2 to type 3 structure. We will see that these characteristic length scales might also correlate with the characteristic wavelengths of the three-dimensional instabilities.

4.2.2 Incompressible regime

In figure 4.9 the Floquet multipliers μ of the secondary instabilities are reported as a function of the spanwise wavelength λ_z for different Reynolds numbers. In this case, since both mode A and mode B have positive real Floquet multiplier, $|\mu|$ coincides with its real part. Results for $Re = 300$ show a

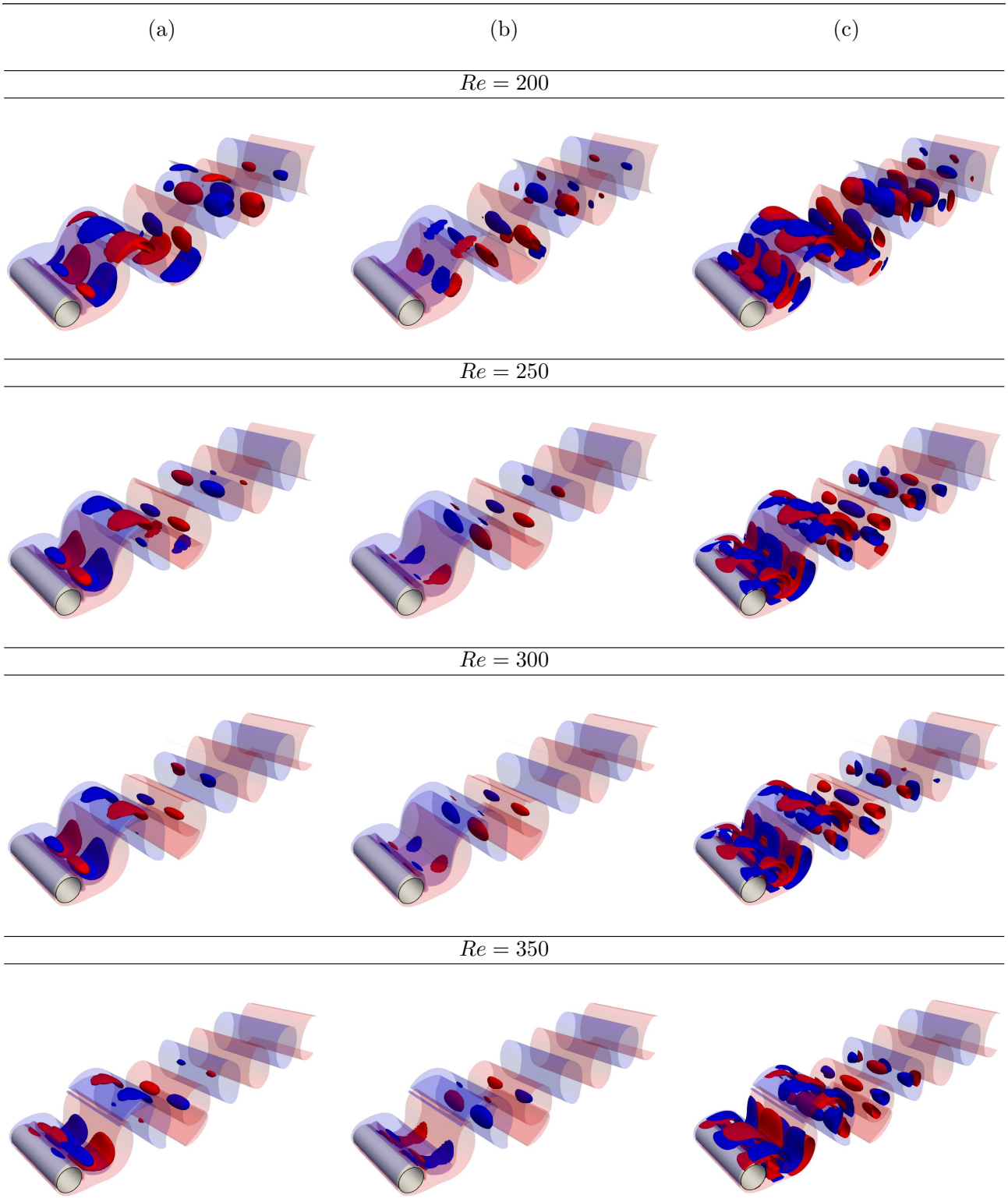

Figure 4.10 – Vorticity $\widetilde{\boldsymbol{\omega}}/\max(||\widetilde{\boldsymbol{\omega}}||)$ of mode A for a spanwise wavelength of $\lambda_z = 4D$ at different Reynolds numbers: (a) streamwise, (b) cross-stream and (c) spanwise component. Red and blue iso-surfaces correspond respectively to positive and negative values of ± 0.1. The translucent iso-surfaces represent the base flow vorticity at level ± 0.01.

good agreement with previous analysis by Leontini *et al.* [62]. For the Reynolds numbers considered, we see that mode B becomes unstable at a Reynolds number between $Re = 250$ and $Re = 300$[10], while mode A has already emerged at $Re = 200$, with a wavelength of $\lambda_z \approx 3.8D$. Both modes A and

[10]Experimentally mode B is observed at lower Reynolds numbers, since it develops on mode A.

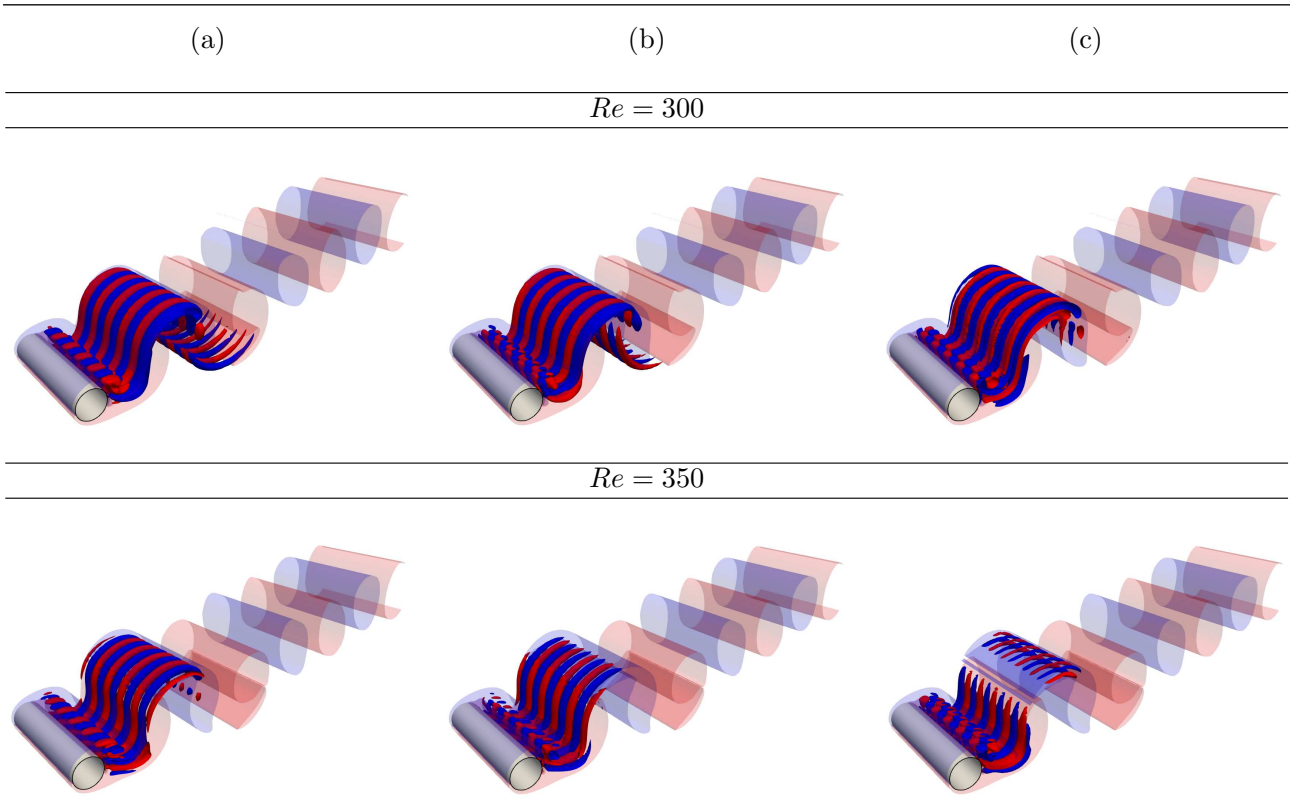

Figure 4.11 – Mode vorticity $\widetilde{\boldsymbol{\omega}}/\max(||\widetilde{\boldsymbol{\omega}}||)$ of mode B for a spanwise wavelength of $\lambda_z = 0.8D$ at different Reynolds numbers: (a) streamwise, (b) cross-stream and (c) spanwise component. Same conventions as in figure 4.10.

B have their growth rate which increases and spans a wider range of unstable spanwise wavelength when the Reynolds number is increased. Regarding mode A, the wavelength of maximum Floquet multiplier slightly moves toward lower values with increasing Reynolds number, passing from $\lambda_z \approx 3.8D$ at $Re = 200$ to $\lambda_z \approx 3.2D$ at $Re = 350$. The most amplified wavelength for mode B, instead, remains constant around $\lambda_z \approx 0.8D$. Mode B is more sensitive to the increase of the Reynolds numbers since its Floquet multiplier grows faster than the one of mode A: μ_B experiences an increase of 80% from $Re = 300$ to 350, while μ_A only increases by 10%. Therefore, mode B becomes the dominant mode for Reynolds numbers above $Re = 300$.

Figures 4.10 and 4.11 display iso-surfaces of streamwise, cross-stream and spanwise vorticity of modes A and B, respectively, superimposed on the iso-surfaces of the base flow vorticity magnitude. As visible on the three vorticity components of the modes, the localization of both instabilities is progressively concentrated in the most upstream part of the two-dimensional wake as the Reynolds number is increased. Looking at the distribution of each component, one can see that there is a strong anisotropy for mode A, the cross-stream vorticity component being the less intense and the spanwise component the most intense, while for mode B, the three components have comparable intensities. As shown in Appendix E, the choice of the initial instant within the period of the base flow does not affect these general considerations on the mode characteristics.

As also evidenced in figure 4.4, the structure of mode A is localized both in the braid region and in the vortex core of the base flow while the structure of mode B is essentially distributed in the braid region. If the streamwise and spanwise vorticity components of mode A are localized in both regions of the base flow, the cross-stream vorticity component progressively concentrates in the vortex core as the wavelength increases, as visible in figure 4.12, where the mode vorticity is reported for two different wavelengths. Moreover, the cross-stream vorticity presents dipoles in the vortex core at low wavelegths

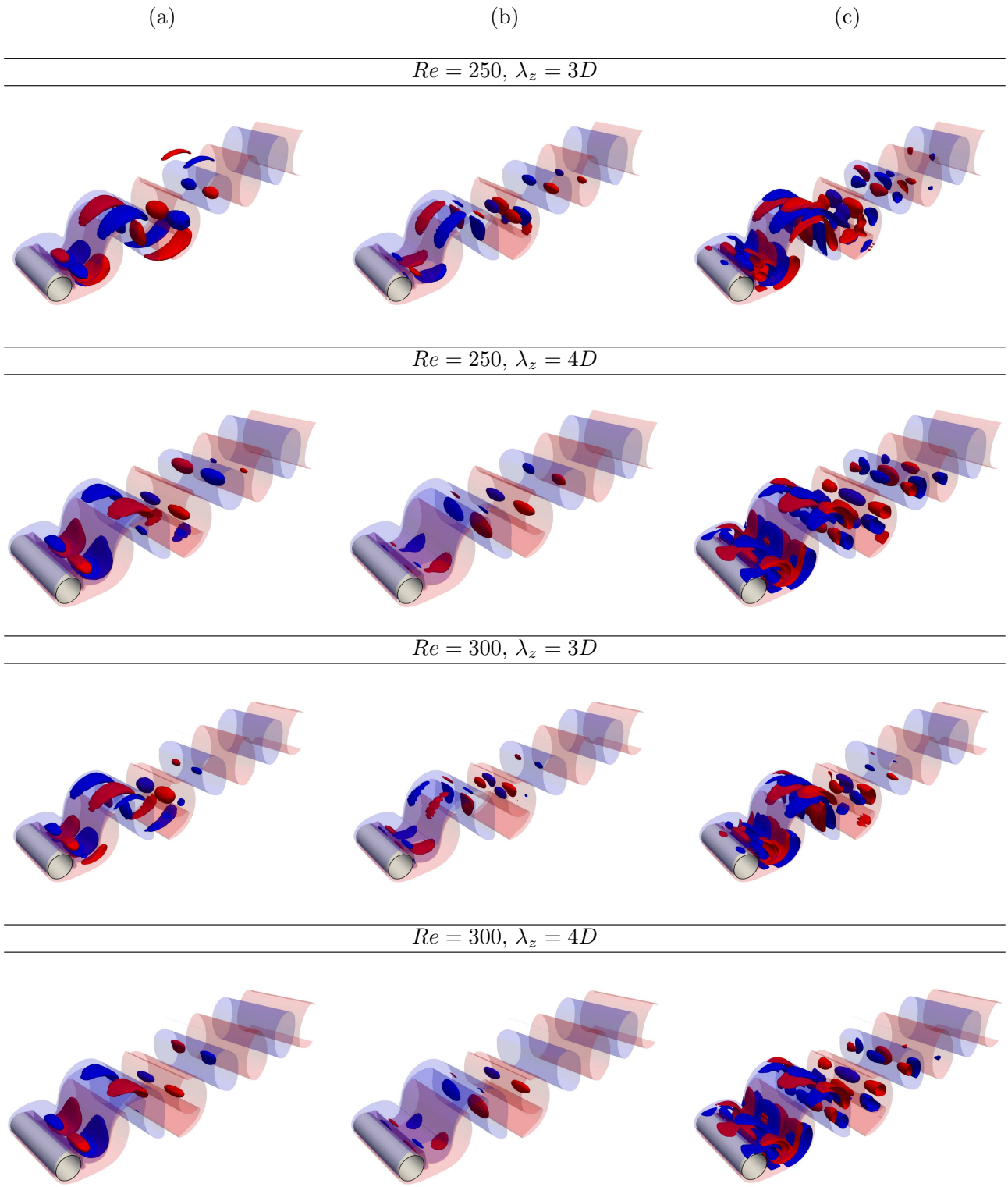

Figure 4.12 – Mode vorticity $\widetilde{\boldsymbol{\omega}}/\max(||\widetilde{\boldsymbol{\omega}}||)$ of mode A for two spanwise wavelengths of $\lambda_z = 4D$ and $\lambda_z = 3D$ at Reynolds numbers $Re = 250$ and 300: (a) streamwise, (b) cross-stream and (c) spanwise component. Same conventions as in figure 4.10.

that are not present at higher ones.

4.2.3 Compressible regime

In figure 4.13, compressibility effects on the Floquet multiplier μ as a function of the spanwise wavelength is shown for the different Reynolds numbers. Likewise in the incompressible case, mode A

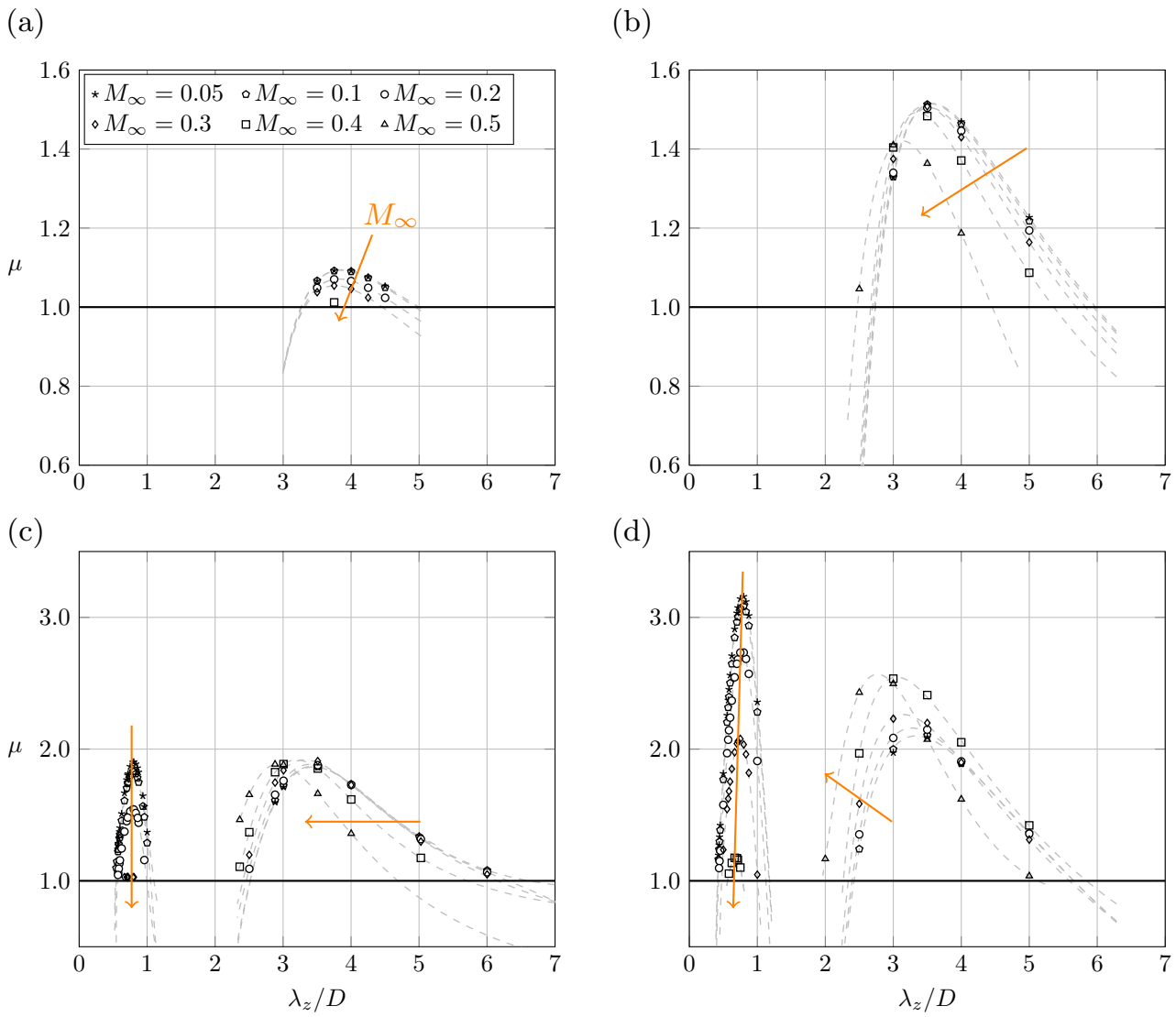

Figure 4.13 – Floquet multiplier μ of the secondary instabilities as a function of the spanwise wavelength λ_z at Reynolds number $Re = 200$ (a), $Re = 250$ (b), $Re = 300$ (c) and $Re = 350$ (d) for different Mach numbers. Dashed lines represent the interpolation curves for a given Mach number.

is the only unstable mode at Reynolds $Re = 200$ and 250 when the Mach number is increased up to $M_\infty = 0.5$. At these Reynolds numbers, compressibility has a stabilizing effect on mode A, delaying the three-dimensional transition, so that at $Re = 200$ and $M_\infty = 0.5$ the flow has not transitioned yet. At this Reynolds number, the spanwise wavelength relative to the maximum Floquet multiplier does not change with the Mach number and remains the same as its value in the incompressible regime, *i.e.* $\lambda_z \approx 3.8D$. At $Re = 250$, compressibility has also a stabilizing effect, but the critical threshold has been reached even for $M_\infty = 0.5$ and the most amplified wavelength is slightly shifted toward a smaller value for $M_\infty = 0.5$, *i.e.* $\lambda_z \approx 3.2D$. At $Re = 300$, compressibility does not change the level of amplification for mode A but rather induces a progressive shift of the unstable range toward smaller wavelengths, with the most amplified wavelength going from $\lambda_z \approx 3.5D$ at $M_\infty = 0.05$ to $\lambda_z \approx 2.9D$ at $M_\infty = 0.5$. Finally at $Re = 350$, compressibility has a destabilizing effect on mode A with a substantial increase of the maximum Floquet multiplier together with a similar shift of the unstable range of wavelengths.

Regarding mode B, it becomes unstable at low Mach numbers for Reynolds numbers above $Re = 300$, indicating that the incompressible critical threshold lies in between $Re = 250$ and $Re = 300$.

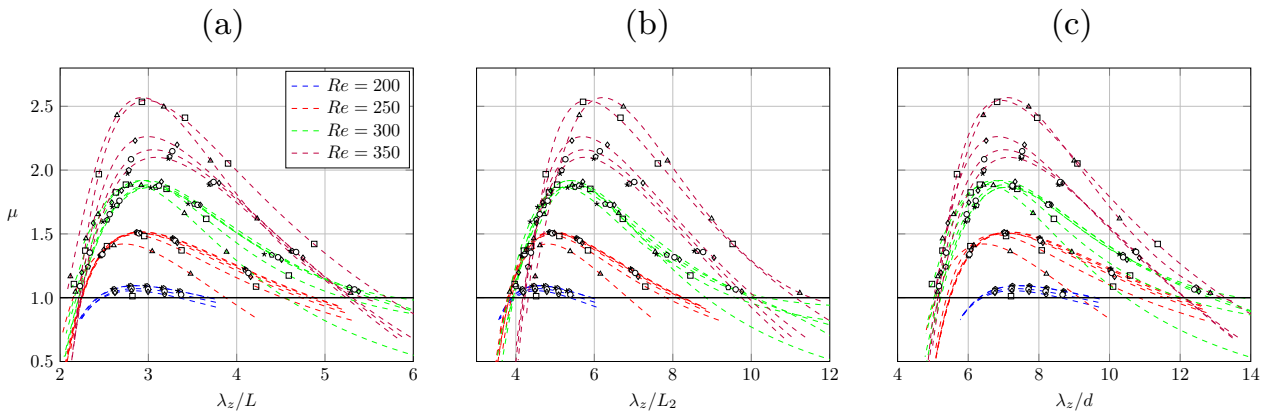

Figure 4.14 – Values of Floquet multipliers shown in figure 4.13, for all the Reynolds and Mach numbers considered, as a function of the wavelength normalized by the characteristic lengths of the time-averaged base flow: (a) L, (b) L_2 and (c) d. The different symbols indicate the Mach numbers with the same convention as in figure 4.13.

Compressibility has a stabilizing effect on this mode since the amplification levels are significantly reduced as the Mach number is increased, the mode becoming marginally stable at $M_\infty = 0.3$. However, the most amplified wavelength is not sensitive to the change in Mach number, with a constant value of $\lambda_z \approx 0.8D$ as in the incompressible regime. The effect of compressibility on mode B remains quite similar at $Re = 350$, except that mode B is now unstable up to $M_\infty = 0.4$ and that the most unstable wavelength is slightly decreased going from $\lambda_z \approx 0.8D$ at $M_\infty = 0.05$ to $\lambda_z \approx 0.6D$ at $M_\infty = 0.4$.

When normalizing the mode A wavelengths by the different characteristic lengths of the time-averaged base flow introduced in 4.2.1 rather than by the cylinder diameter D, the Floquet multipliers exhibit a maximum at an almost constant wavelength of $\lambda_z \approx 2.7L - 3L$ and $\lambda_z \approx 6.8d - 7.2d$, while a constant low wavelength cut-off is observed at $\lambda_z \approx 3.8L_2$ when normalized by L_2.

Figure 4.15 and 4.16 display iso-surfaces of streamwise, cross-stream and spanwise vorticity of mode A and B with wavelength $\lambda_z = 4D$ and $\lambda_z = 0.66D$, respectively, superimposed to iso-surfaces of vorticity magnitude of the base flow for the different Mach numbers at $Re = 350$. The three components of vorticity of the modes are normalized by the maximum vorticity magnitude, and contours are set to ± 0.1. The vorticity anisotropy of mode A evidenced in the incompressible regime is enhanced when the Mach number is increased. The intensity of streamwise vorticity component decreases strongly with the Mach number with levels below $\tilde{\omega}_x < 0.1||\tilde{\boldsymbol{\omega}}||$ almost everywhere for $M_\infty = 0.4$ and 0.5. In agreement with observations made in the incompressible case (see section 4.2.2), the intensity of the cross-stream vorticity is weaker than the one of the spanwise vorticity whatever M_∞ and its contribution to the vorticity magnitude does not depend on the Mach number. Therefore, the vorticity essentially concentrates into the spanwise component and this concentration gets stronger as the Mach number is increased. With growing effect of compressibility, the spatial distribution of the spanwise vorticity component is found to vary within the braid and the vortex core with the formation of opposite sign vorticity layers mainly concentrated in the base flow hyperbolic region where stretching is intense due to high velocity and vorticity gradients. However, the strong vorticity anisotropy in favor of the spanwise component and the formation of the opposite sign vorticity layers when the Mach number is increased, are only observed at largest wavelength, while they are not promoted at the lowest ones, as we can see from the evolution of iso-surfaces of streamwise, cross-stream and spanwise vorticity of mode A with the Mach number at $Re = 350$, $\lambda_z = 3D$ and $Re = 250$, $\lambda_z = 3D, 4D$ reported in Appendix F.

For mode B the vorticity is equally distributed among its three components as in the incompressible

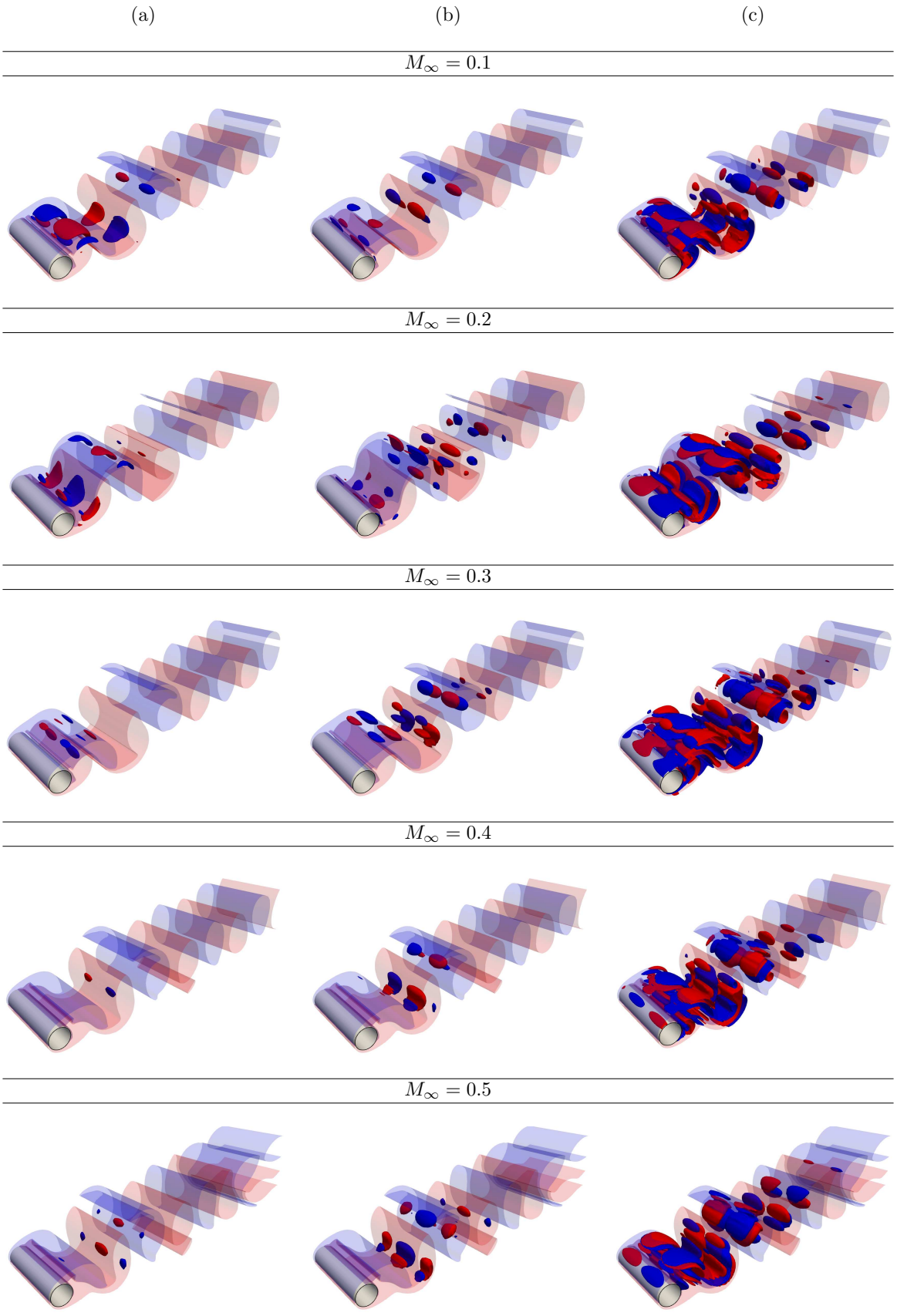

Figure 4.15 – Vorticity $\widetilde{\boldsymbol{\omega}}/\max(||\widetilde{\boldsymbol{\omega}}||)$ of mode A at a wavelength of $\lambda_z = 4D$ and $Re = 350$ for different Mach numbers: (a) streamwise, (b) cross-stream and (c) spanwise component. Same conventions as in figure 4.10.

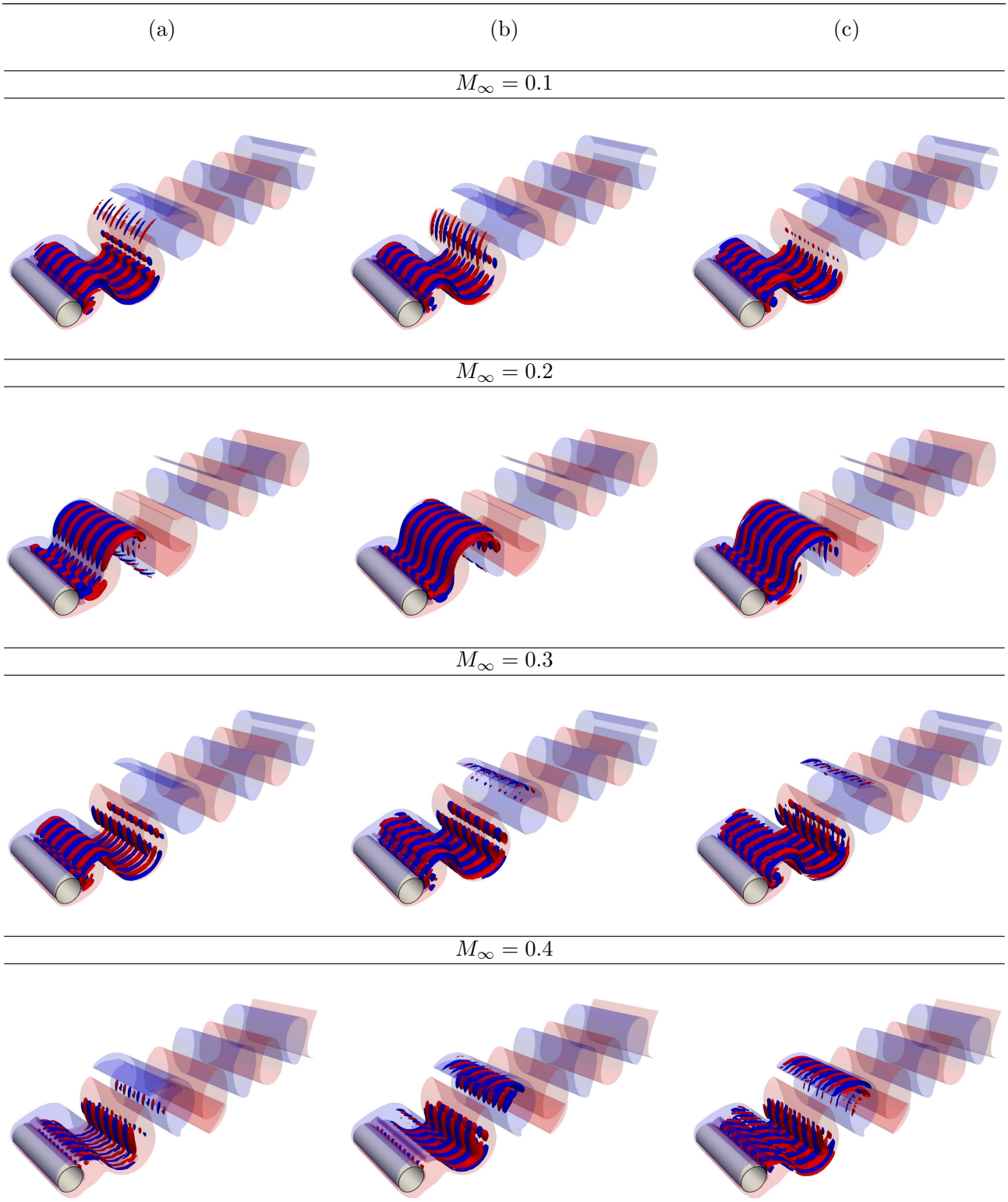

Figure 4.16 – Vorticity $\widetilde{\boldsymbol{\omega}}/\max(||\widetilde{\boldsymbol{\omega}}||)$ of mode B at a wavelength of $\lambda_z = 0.66D$ and $Re = 350$ for different Mach numbers: (a) streamwise, (b) cross-stream and (c) spanwise component. Same conventions as in figure 4.10.

case: the Mach number does not have a significant influence on the spatial structure of the mode.

4.2.4 Linearized vorticity equation

In order to understand the origin of the different vorticity responses, we investigate the linearized version of the vorticity equation, which reads

$$\frac{\partial \boldsymbol{\omega}'}{\partial t} + \overbrace{\boldsymbol{u}\cdot\boldsymbol{\nabla}\boldsymbol{\omega}' + \boldsymbol{u}'\cdot\boldsymbol{\nabla}\boldsymbol{\omega}}^{\text{transport}} = \overbrace{\boldsymbol{\omega}'\cdot\boldsymbol{\nabla}\boldsymbol{u} + \boldsymbol{\omega}\cdot\boldsymbol{\nabla}\boldsymbol{u}'}^{\text{stretching/tilting}} - \overbrace{\boldsymbol{\omega}'(\boldsymbol{\nabla}\cdot\boldsymbol{u}) - \boldsymbol{\omega}(\boldsymbol{\nabla}\cdot\boldsymbol{u}')}^{\text{expansion/contraction}} + \boldsymbol{b} + \underbrace{\frac{1}{Re\rho}(\boldsymbol{\Delta}\boldsymbol{\omega}' - \frac{\rho'}{\rho}\boldsymbol{\Delta}\boldsymbol{\omega} - \boldsymbol{\phi}_{\rho} - \boldsymbol{\phi}_{\rho'})}_{\text{diffusion}}, \tag{4.5}$$

where $\boldsymbol{b}$ is the linearised baroclinic torque:

$$\boldsymbol{b} = \frac{1}{\rho}\boldsymbol{\nabla}\rho \times \left(\frac{1}{\rho}\boldsymbol{\nabla}p' - \frac{\rho'}{\rho^2}\boldsymbol{\nabla}p\right) + \boldsymbol{\nabla}\left(\frac{\rho'}{\rho}\right) \times \frac{1}{\rho}\boldsymbol{\nabla}p. \tag{4.6}$$

$\boldsymbol{\phi}_{\rho}$ and $\boldsymbol{\phi}_{\rho'}$ are diffusion terms involving a coupling between the base flow density field and the perturbation diffusion and the coupling between the perturbation density field and the base flow diffusion, respectively. They are defined as follows:

$$\boldsymbol{\phi}_{\rho} = \frac{1}{\rho}\boldsymbol{\nabla}\rho \times \left(\boldsymbol{\Delta}\boldsymbol{u}' + \frac{1}{3}\boldsymbol{\nabla}(\boldsymbol{\nabla}\cdot\boldsymbol{u}') - \frac{\rho'}{\rho}(\boldsymbol{\Delta}\boldsymbol{u} + \frac{1}{3}\boldsymbol{\nabla}(\boldsymbol{\nabla}\cdot\boldsymbol{u}))\right), \tag{4.7}$$

$$\boldsymbol{\phi}_{\rho'} = \boldsymbol{\nabla}\left(\frac{\rho'}{\rho}\right) \times (\boldsymbol{\Delta}\boldsymbol{u} + \frac{1}{3}\boldsymbol{\nabla}(\boldsymbol{\nabla}\cdot\boldsymbol{u})), \tag{4.8}$$

We now analyze the different terms of stretching/tilting and expansion/contraction in order to identify those that may be major contributors to the mode vorticity evolution. The expression of stretching/tilting, expansion/contraction are derived as follow:

$$\boldsymbol{\omega}'\cdot\boldsymbol{\nabla}\boldsymbol{u} + \boldsymbol{\omega}\cdot\boldsymbol{\nabla}\boldsymbol{u}' = \begin{bmatrix} \omega'_x\frac{\partial u_x}{\partial x} + \omega'_y\frac{\partial u_x}{\partial y} + \cancel{\omega'_z\frac{\partial u_x}{\partial z}} \\ \omega'_x\frac{\partial u_y}{\partial x} + \omega'_y\frac{\partial u_y}{\partial y} + \cancel{\omega'_z\frac{\partial u_y}{\partial z}} \\ \cancel{\omega'_x\frac{\partial u_z}{\partial x}} + \cancel{\omega'_y\frac{\partial u_z}{\partial y}} + \cancel{\omega'_z\frac{\partial u_z}{\partial z}} \end{bmatrix} + \begin{bmatrix} \cancel{\omega_x\frac{\partial u'_x}{\partial x}} + \cancel{\omega_y\frac{\partial u'_x}{\partial y}} + \omega_z\frac{\partial u'_x}{\partial z} \\ \cancel{\omega_x\frac{\partial u'_y}{\partial x}} + \cancel{\omega_y\frac{\partial u'_y}{\partial y}} + \omega_z\frac{\partial u'_y}{\partial z} \\ \cancel{\omega_x\frac{\partial u'_z}{\partial x}} + \cancel{\omega_y\frac{\partial u'_z}{\partial y}} + \omega_z\frac{\partial u'_z}{\partial z} \end{bmatrix} \tag{4.9a}$$

$$-\boldsymbol{\omega}'(\boldsymbol{\nabla}\cdot\boldsymbol{u}) - \boldsymbol{\omega}(\boldsymbol{\nabla}\cdot\boldsymbol{u}') = -\begin{bmatrix} \omega'_x(\frac{\partial u_x}{\partial x} + \frac{\partial u_y}{\partial y} + \cancel{\frac{\partial u_z}{\partial z}}) \\ \omega'_y(\frac{\partial u_x}{\partial x} + \frac{\partial u_y}{\partial y} + \cancel{\frac{\partial u_z}{\partial z}}) \\ \omega'_z(\frac{\partial u_x}{\partial x} + \frac{\partial u_y}{\partial y} + \cancel{\frac{\partial u_z}{\partial z}}) \end{bmatrix} - \begin{bmatrix} \cancel{\omega_x(\frac{\partial u'_x}{\partial x} + \frac{\partial u'_y}{\partial y} + \frac{\partial u'_z}{\partial z})} \\ \cancel{\omega_y(\frac{\partial u_x}{\partial x} + \frac{\partial u_y}{\partial y} + \frac{\partial u'_z}{\partial z})} \\ \omega_z(\frac{\partial u'_x}{\partial x} + \frac{\partial u'_y}{\partial y} + \frac{\partial u'_z}{\partial z}) \end{bmatrix} \tag{4.9b}$$

Taking into account the two-dimensional nature of the base flow, it is possible to cancel the terms that are null, *i.e.* those crossed out in blue in expressions (4.9).

From these equations, we can first consider the incompressible regime, where the expansion/contraction terms are null. Therefore, the stretching/tilting term is the only active source term. An increase of

the mode spanwise vorticity component due to the stretching term (expressed by the term in the green box in equation 4.9a) would be associated to an increase of both the mode streamwise and cross-stream velocity components, whose variation along the spanwise direction produce streamwise and cross-stream vorticity due to the stretching term (yellow boxes in equation 4.9a). They are associated to an increase of the mode spanwise velocity whose spanwise gradient produces spanwise vorticity through the stretching term in green. This (simplified) path, at the origin of the three-dimensionalization process expresses a *circular causality* and gives an idea of how, once the instability is triggered, the mode growth is self-sustained.

In the compressible regime, where the expansion/contraction terms cannot be neglected, we can hypothesize the following growth mechanism that could explain the vorticity anisotropy in favor of the spanwise vorticity component observed for mode A when the Mach number is increased. The divergence term ($\boldsymbol{\nabla} \cdot \boldsymbol{u}'$), which grows in magnitude with increasing compressibility, has an impact only on the spanwise vorticity of the mode (red box in equation 4.9b). As a consequence, the spanwise vorticity (ω_z') would grow and induce a self-sustained growth via the other expansion/contraction term (yellow box in equation 4.9b. However, it would not directly impact the two other vorticity components, since all other terms involving ω_z' are null due to the two-dimensional nature of the base flow. Nevertheless, an increase of the mode spanwise vorticity is correlated to an increase on the streamwise and cross-stream velocity components, which can produce in return ω_x' and ω_y' due to the stretching terms in yellow boxes in equation 4.9a.

The observed vorticity anisotropy in favour of the spanwise vorticity component for mode A at $Re = 350$, could be explained by the fact that mode A mainly develops in regions where the expansion/compression terms and the base flow vorticity are higher, *i.e.* in the vortex cores. For mode B, which instead develops in the hyperbolic region, the three vorticity component contribute to the vorticity magnitude even increasing the Mach number. This analysis provides a possible explanation for the influence of compressibility on the mode structure. A quantitative analysis of the contribution of each term of equation (4.5) is nevertheless necessary to confirm this analysis and is left for future work.

4.2.5 Base flow aperiodicity

As introduced in section 1.4.2, the main assumption underlying Floquet theory is the periodicity of the base state. This assumption allows to consider the periodic limit cycle as a fixed point on the Poincaré section and therefore to have a constant Jacobian matrix at each period T. In wake flows, such as the cases discussed in this work, the base state is indeed periodic near the object as a consequence of vortex shedding, with period $T = 1/St$. However, in the far wake, where vortex pairing can occur (figure 4.17.a), the base state may no longer be T-periodic, as shown by the velocity field difference between the unsteady solution at time t and $t + T$ in figure 4.17.b.
Recently, some works have been devoted on how to overcome this limitation and have a base state that respects the T-periodicity in the whole domain. This can be achieved by reconstructing the base flow solution and limiting the downstream domain for the stability calculation [52], as well as by computing and using phase-averaged or stabilized base flows [53], which are a modification of the unsteady solution. However, Chiba's method, adopted in this works for the stability analysis, limits the use of such approaches, since the base flow is integrated in time with the perturbation (eq. 2.21). Nevertheless, valuable stability analysis can be performed even if the base flow is approximately periodic. In fact, in order to investigate the effect of the far wake base flow aperiodicity, in figure 4.18 results of Floquet analysis are reported at two Reynolds and Mach numbers using base flows computed at different periods. These spectra highlight the fact that Mode A and Mode B ($\mu_r > 0$ and $\mu_i = 0$)

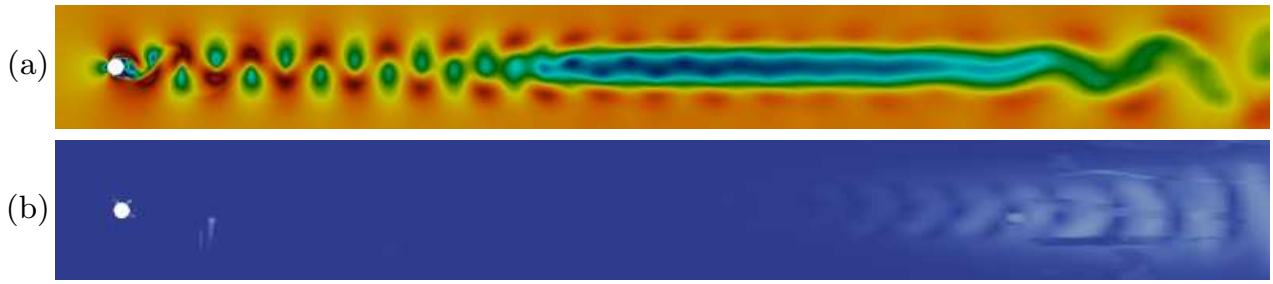

Figure 4.17 – (a) Base flow velocity magnitude distribution at time t and (b) velocity magnitude field difference between base flow at time t and $t+T$.

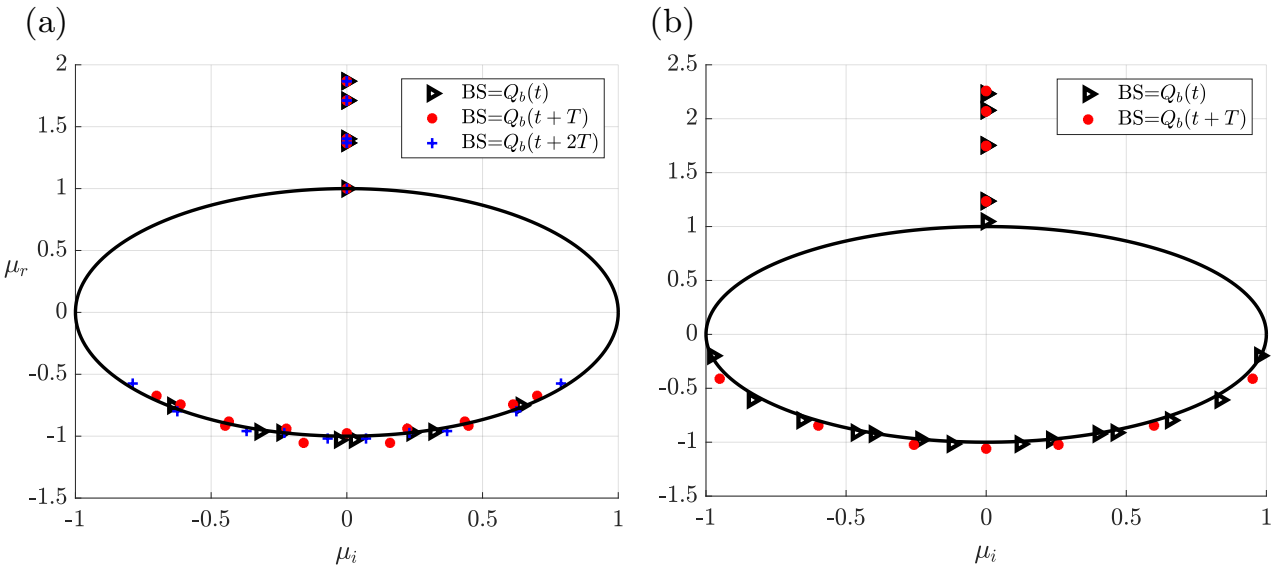

Figure 4.18 – Spectra obtained with different base states periods at (a) $Re = 300$, $M_\infty = 0.05$ and (b) $Re = 350$, $M_\infty = 0.3$. Solid black line indicates the unitary circle.

are not affected by the the far wake aperiodicity, since Floquet results do not vary for the different base state and the spatial structures show that these modes arise in the well periodic near wake region. Conversely, the other part of the spectrum ($\mu_r < 0$) shows a dependence on the base flows. Their spatial structures show that these modes, indeed, emerge in the far wake where the base flow is not T-periodic. Hence, in order to analyze the far wake instabilities, which have not been considered in this work, approaches like those cited above should be used.

4.3 Comparison between filtered, time-averaged and periodic base states

Many works have recently been devoted to the three-dimensional stability analysis performed on the fixed point solution rather than on the periodic limit cycle, among them we can cite [41, 45, 116]. As done in section 3.4 for the two-dimensional case, we provide an analysis on the differences between those approaches. First of all, we should remind that three-dimensional stability analysis aims to find three-dimensional secondary instabilities if performed on the periodic limit cycle (here denoted as VK), while it aims to find three-dimensional primary instabilities if performed on the fixed point solution (SFD). Interestingly, Noack *et al.* [81], found for the circular cylinder, that the fixed point solution and the periodic solution become three-dimensional simultaneously. We also report comparisons with

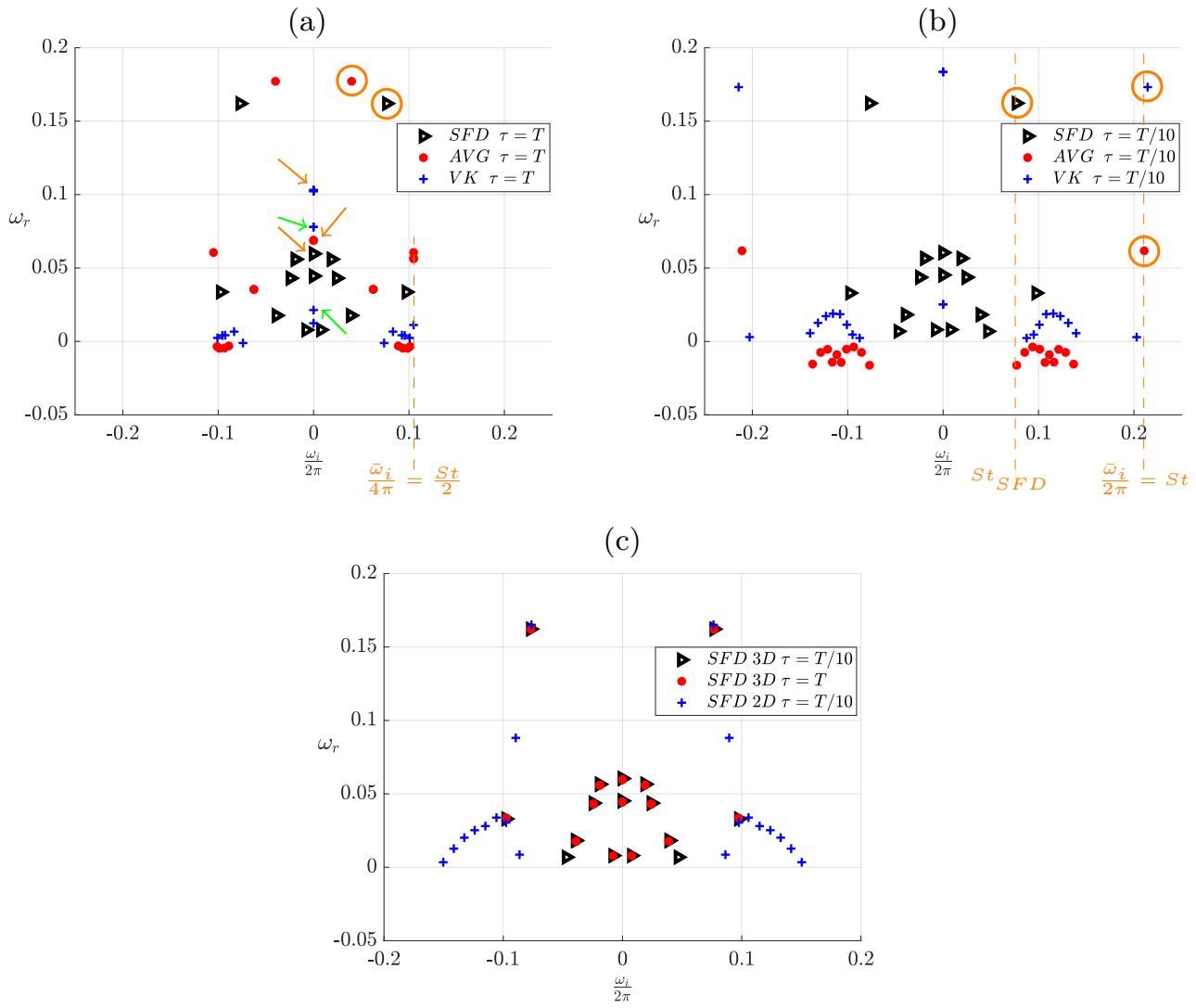

Figure 4.19 – Comparison of the spectra obtained when using different base states with $\tau = T$ (a) and $\tau = T/10$ (b) for $Re = 300$ and $M_\infty = 0.05$. Comparison of the 3D-SFD response with the 2D case (c). The transverse length of the domain is fixed to $L_z = 4D$ for all 3D cases.

respect to three-dimensional stability analysis performed on the time-averaged solution (AVG). In this section, results of the stability analysis are reported in terms of growth rate and mode frequency of the Jacobian matrix[11] instead of Floquet multipliers, since the concept of Floquet analysis is relevant only for periodic base flows, while the growth rate is more generic[12]. Since we are interested in a comparison of the different approaches, rather than the precise computations of the modes, these results have been obtained with simulations on the coarsest (x, y)-resolution (mesh M1) and $\Delta_z = D/8$ (see Appendix D). The transverse length of the computational domain is $L_z = 4D$.

In figures 4.19.a and 4.19.b the spectra obtained at $Re = 300$ and $M_\infty = 0.05$ with the different base states are reported for $\tau = T$ and $\tau = T/10$, respectively, where T is the shedding period of the periodic solution. Imposing $\tau = T$, stationary modes appear for the three base states, as indicated by the yellow arrows in figure 4.19.a, and they all have the same wavelength $\lambda_z = 4D$. Their structures, reported

[11] As done in Chapter 3, we consider $\omega = \omega_r + i\omega_i$.

[12] We could also report results in terms of eigenvalues of the propagator matrix, which in the particular case of $\tau = T$, is equivalent to the Floquet multipliers, but whenever $\tau \neq T$ it is misleading to call them Floquet multipliers.

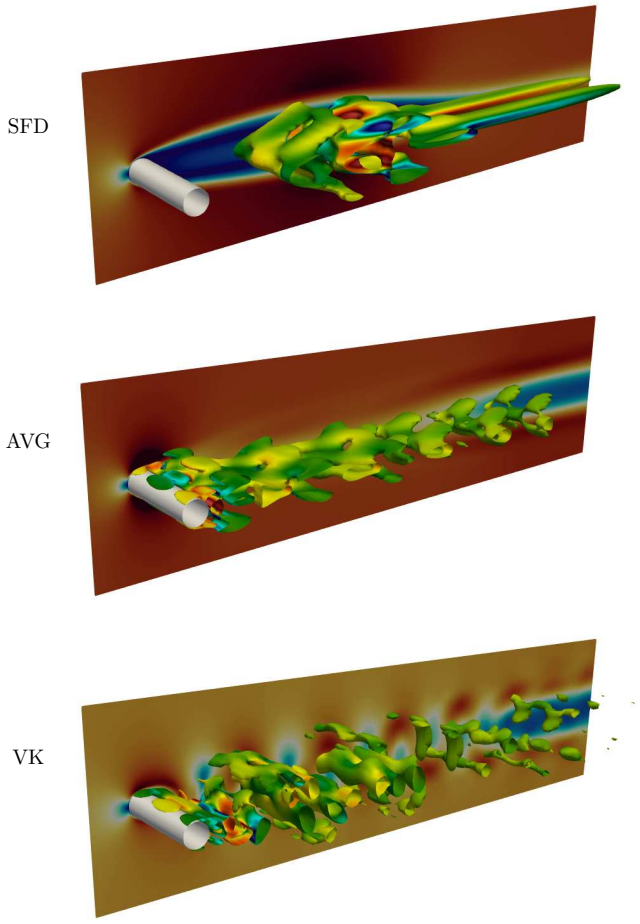

Figure 4.20 – Q-criterion contours colored by spanwise vorticity. The slice shows the base state velocity magnitude.

in figure 4.20, are quite different. In particular, the stationary mode of the SFD base flow develops at the center of the recirculation region, which extends far downstream similarly to the NACA0012 airfoil, see Chapter 3. The AVG and VK stationary modes also differ from each other, but present a similar structure on the cylinder surface and same downstream extension. It would be interesting to time-average the VK stationary mode calculated at different instants of the shedding cycle and compare it to the AVG stationary mode. Mode B only emerges for the VK base flow (indicated by the green arrows) with wavelengths $\lambda_z = 0.8D$ and $\lambda_z = 0.66D$, while the other stationary mode of the SFD in again a $\lambda_z = 4D$ mode.

With $\tau = T/10$, the VK base flow presents a more unstable stationary mode, but its wavelength is $\lambda_z = 2D$, different from the one of the mode calculated with $\tau = T$. The SFD, instead, converges toward the same stationary mode. Indeed, τ does not influence the three-dimensional stability response of the SFD base flow, as shown in figure 4.19.c where the different spectra of the SFD are presented. Comparison with the two-dimensional stability response is also shown to distinguish three-dimensional from two-dimensional modes.

As discussed in the two dimensional analysis, the SFD and AVG base flows present two-dimensional modes associated with the primary von Kármán instability. The AVG mode frequency coincides with the natural frequency ($St = 0.21$, Appendix D), while the one of the SFD is lower. Interestingly, for this low value of τ, also the VK base flow presents a two-dimensional mode at a frequency close to the natural one. These modes are indicated by the orange circles in figure 4.19.b. Those indicated by the orange circles in figure 4.19.a, are also two-dimensional modes. The one corresponding to the SFD

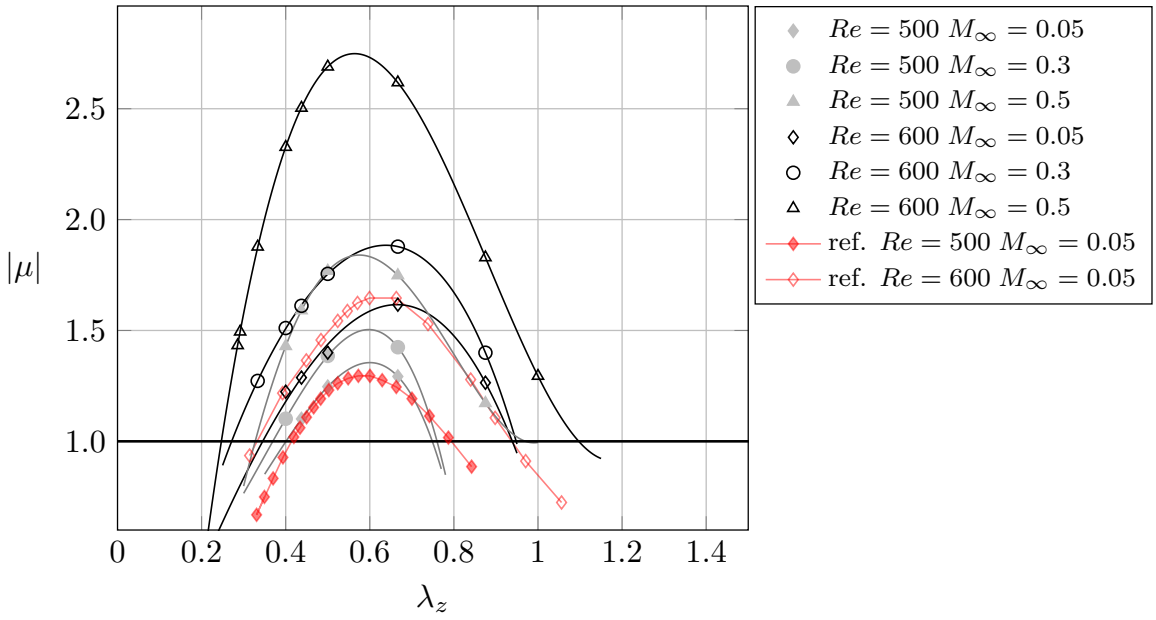

Figure 4.21 – Absolute values of the Floquet multiplier μ as a function of the wavelength λ_z at Reynolds number $Re = 500$ and $Re = 600$ at $\alpha = 20°$ for different Mach numbers. Reference values in red are taken from Meneghini *et al.* [73].

base flow is the same as the one obtained with $\tau = T/10$, whereas the one obtained for the AVG base flow has a different structure with respect to the two-dimensional mode found with $\tau = T/10$. Due to the cut-off frequency imposed by the value of τ (see section 2.4.1 and figure 2.7), it is not surprising that the stability analysis performed with $\tau = T$ has filtered out the AVG two-dimensional mode associated to the von Kármán instability, which instead appears for $\tau = T/10$. This is not the case for the SFD base flow, for which the von Kármán instability has not been filtered out since its frequency, $St_{SFD} = 0.076$, is lower than half the natural one $1/2T$ and satisfies the condition for avoiding aliasing effects $\tau = T < 1/(2 \cdot St_{SFD})$.

Finally, it is worth mentioning that the spectra obtained with $\tau = T$, presents period doubling modes both for the AVG and VK base flows ($\omega_i/2\pi = St/2$). Two period doubling modes appear for the AVG base flow at wavelengths of $\lambda_z = 4D$, likewise the stationary mode, and $\lambda_z = 2D$, while the one corresponding to the VK base flow is two-dimensional and essentially localized in the far wake. This might be related to the development of the secondary vortex street [34] in the far wake in proximity to the outflow boundary. We stress that these simulations have been performed on the coarsest mesh, hence the quantitative values of the modes might be questioned. These modes are unlikely to be the quasi periodic mode (QP) which usually appears for symmetric flows (as mentioned is section 4.1) with a wavelength in between those of mode A and mode B, since the critical threshold of this mode is $Re_c = 380$ for the periodic cylinder wake [17], while the present simulations have been performed at $Re = 300$.

4.4 3D NACA0012

In this section, we briefly address preliminary results on the three-dimensional stability analysis of the periodic wake behind a NACA0012 at angle of attack $\alpha = 20°$. In order to perform three-dimensional stability analysis, the 3D mesh and base flow have been generated by extruding the two-dimensional grid and the DNS unsteady solution along the spanwise direction. The mesh convergence study is reported in Appendix G.

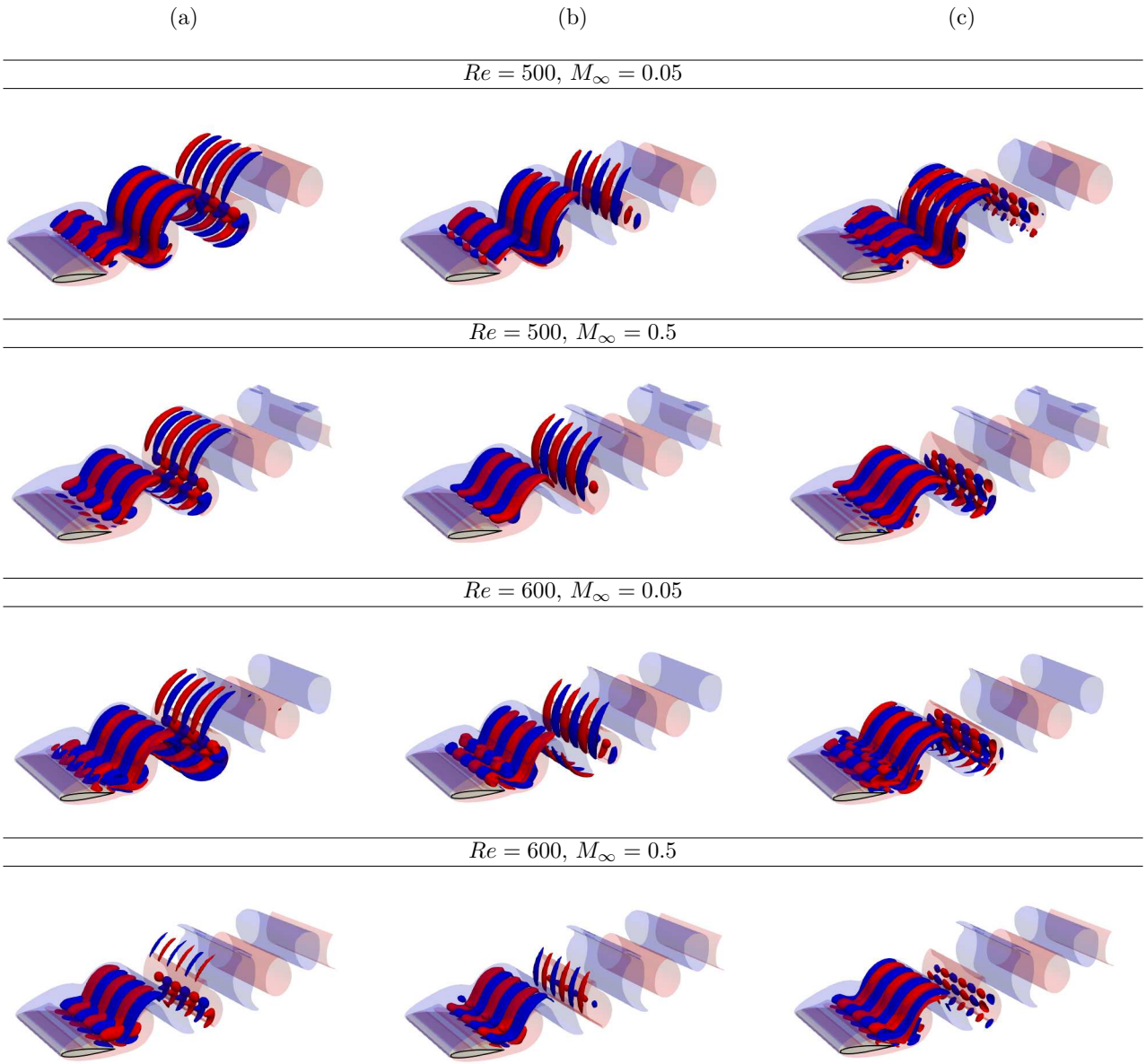

Figure 4.22 – Vorticity $\tilde{\boldsymbol{\omega}}/\max(||\tilde{\boldsymbol{\omega}}||)$ of the period doubling mode for a spanwise wavelength $\lambda_z = 0.66C$ at $Re = 500, 600$ and $M_\infty = 0.05, 0.5$: (a) streamwise, (b) cross-stream and (c) spanwise component. Same conventions as in figure 4.10.

As discussed in section §4.1, periodic wake flows which do not present an half-period symmetry, have been found to become three-dimensional through a period doubling bifurcation. Examples include periodic wake flows past airfoils which have been addressed in the incompressible regime [29, 41, 45, 73]. The NACA0012 periodic wake flow has been virtually unexplored using three-dimensional stability analysis, perhaps with the exception of Meneghini *et al.* [73] and Tsiloufas *et al.* [106] who investigated the stability of the flow past a NACA0012 airfoil at $\alpha = 20°$.

Figure 4.21 shows the evolution of the Floquet multiplier module[13] as a function of the characteristic wavelength for $\alpha = 20°$, at two different Reynolds numbers, with Mach numbers in the range $[0.05 : 0.5]$. Results from Meneghini *et al.* [73] obtained in the incompressible regime are shown for comparison. The critical Reynolds number of the incompressible case is $Re_c \approx 456$ [73]. That is, Reynolds numbers 500 and 600 addressed in this section are relatively close to the stability threshold in the

[13]For period doubling modes, the Floquet multipliers are all real negative numbers (see figure 1.10)

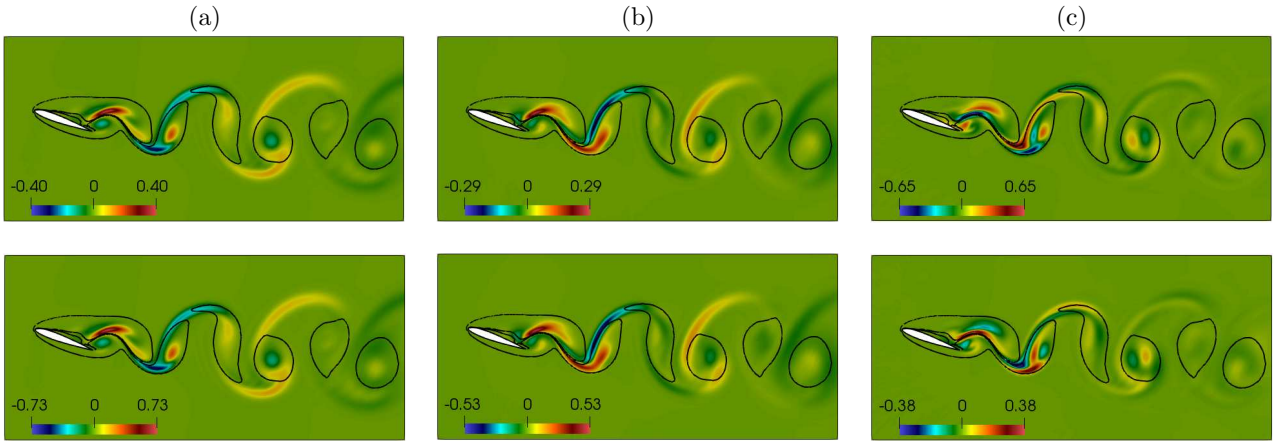

Figure 4.23 – Spatial variation in the (x, y)-plane of the mode vorticity $\widetilde{\boldsymbol{\omega}}/\max(||\widetilde{\boldsymbol{\omega}}||)$ at $\lambda_z = 0.66C$: (a) streamwise, (b) cross-stream and (c) spanwise component, superposed to base flow vorticity contour at ± 0.01 (black line). Two different spanwise locations separated by a quarter period (*i.e.* z and $z + \lambda_z/4$) are shown.

incompressible regime, but may be farther away in the compressible regime. Figure 4.21 indicates that the Floquet multipliers increase when increasing the Mach number, at both Reynolds numbers and for all unstable wavelengths. This is in contrast with previous results on the circular cylinder wake where it was found that compressibility may stabilize or destabilize the flow at different wavelengths, depending on the Reynolds number. Furthermore, the destabilization of the flow becomes stronger as the Reynolds number is increased, with a relative increment in the maximum Floquet multiplier ($(\mu_{max}(M_\infty = 0.5) - \mu_{max}(M_\infty = 0.05))/\mu_{max}(M_\infty = 0.05)$) of $\approx 40\%$ at $Re = 500$ against $\approx 70\%$ at $Re = 600$. Finally, it is observed that the wavelength of the maximum Floquet multiplier does not significantly vary with changes in Reynolds and Mach numbers and remains approximately constant at $\lambda_z \approx 0.6C$, where C is the airfoil chord. This value of $\lambda_z = 0.6C$ has also been found by Meneghini *et al.* [73] for the most amplified mode at $Re_c \approx 456$ in the incompressible regime.

Figure 4.22 displays iso-surfaces of streamwise, cross-stream and spanwise vorticity of the period doubling mode, superimposed on iso-surfaces of the base flow vorticity magnitude, for Reynolds numbers 500 and 600 and Mach numbers 0.05 and 0.5. The structure and the spatial localization of the mode are very similar to those of mode B observed for the circular cylinder wake, with the mode mainly developing in the braids of the base flow. Likewise mode B, the three vorticity components have comparable intensities and the largest intensities are observed in the hyperbolic regions. There is nevertheless a difference with mode B of the circular cylinder wake in that streamwise vorticity layers localized in between two consecutive base flow vortices change sign at each period T 4.23. This is similar to mode A of the circular cylinder wake where streamwise vorticity layers change sign with respect to the half period $T/2$, as shown in figure 4.4.

The localization of the mode is progressively concentrated in the most upstream part of the two-dimensional wake when both the Reynolds and Mach numbers are increased. This is related to the destabilization of the mode, as previously observed for both modes A and B for the circular cylinder wake when increasing the Reynolds number.

It has been observed that a second bifurcation of the periodic wake of NACA airfoils occurs with a critical wavelength longer than the one of the period doubling mode [41, 45, 73]. For the NACA0012 airfoil, the second bifurcation occurs at $Re_c \approx 600$ with $\lambda_z \approx 2.1C$. This mode emerges with a complex conjugate Floquet multiplier, hence, the flow undergoes a Neimark–Sacke (secondary Hopf) bifurcation,

but it has not been observed in our preliminary calculations.

4.5 Résumé

Dans ce chapitre, nous analysons la stabilité linéaire tridimensionelle de l'écoulement periodique bidimensionnel autour du cylindre circulaire et autour du profil NACA0012 à une incidence de 20°.
Dans la section §4.1, nous décrivons d'abord le processus conduisant à la tridimensionnalisation de l'écoulement périodique autour du cylindre, *via* l'apparition succéssive de deux modes d'instabilité transverse, communément appelés modes A et B. Le premier mode (mode A) apparaît vers $Re \approx 180-190$ et est associé à une instabilité elliptique des tourbillons primaires [62, 105] dont la déformation transverse résulte d'un déplacement, en certains points, de la vorticité du champs de base vers l'amont [112] (voir figure 4.3). Cette déformation conduit au développement de structures transversales à grande échelle de longueur d'onde caractéristique $\lambda_z \sim 4D$. Le mode A préserve la symétrie de demi-période de l'état de base, qui peut se traduire par l'équation 4.1.
Le deuxième mode (mode B) apparaît autour de $Re \approx 230 - 260$ et est au contraire associé à une instabilité hyperbolique. Il se forme dans la région hyperbolique qui se développe entre deux tourbillons de von Kármán contrarotatifs consécutifs et est lié à la formation de structures d'échelle plus fine de longueur d'onde caractéristique $\lambda_z \approx 1D$. Ce mode brise la symétrie de demi-période de l'état de base, qui peut se traduire par l'équation 4.2. A un nombre de Reynolds plus élevé, $Re \approx 380$ [17], un troisième mode secondaire devient instable. Ce mode est communément désigné ~~le~~ mode Quasi-Périodique (QP), et sa longueur d'onde caractéristique se situe entre celles des modes A et B. Par ailleurs, sa périodicité temporelle est presque le double de celle de l'état de base.
En général, les écoulements présentant une symétrie $Z_2 \times O(2)$ bifurquent vers un état tridimensionnel via l'émergence de deux modes synchrones (même périodicité temporelle que l'état de base), l'un préservant la symétrie H de l'état de base et l'autre la brisant, et d'un mode quasi-périodique. Pour les écoulements autour des corps canoniques qui ne vérifient pas la symétrie de demi-période, une instabilité différente peut apparaître [90, 94]. En particulier, le mode C a été observé et s'est avéré être le mode tridimensionnel principal dans plusieurs configurations, telles que [54, 94, 114]. Le mode C est un mode dit de doublement de période correspondant à un multiplicateur de Floquet marginal $\mu = -1$, *i.e.* sa périodicité est deux fois celle de l'état de base.

Dans la section §4.2, l'influence des nombres de Reynolds et de Mach sur les propriétés des modes A et B est analysé. Dans un premier temps, nous caractérisons l'état de base périodique bidimensionnel. Il apparaît que le coefficient de traînée moyen augmente en augmentant les nombres de Reynolds et de Mach et que la transformation de Prandtl–Glauert fournit une bonne estimation du coefficient de traînée jusqu'à un nombre de Mach donné, qui diminue avec l'augmentation du nombre de Reynolds (voir figure 4.5). Par ailleurs, le nombre de Strouhal diminue de façon monotone avec l'augmentation du nombre de Mach pour $Re \leq 250$, alors qu'il présente une évolution non-monotone pour $Re > 250$ (avec une diminution puis une augmentation pour un nombre de Mach croissant). Il est observé que la structure de l'écoulement moyenné dans le temps, représentée sur la figure 4.6, varie fortement dans la gamme des nombres de Reynolds et de Mach considérés. En particulier, nous identifions trois types de structure dont les longueurs caractéristiques semblent corrélées aux longueurs d'onde caractéristiques des instabilités tridimensionnelles. Dans un second temps, nous procédons à l'analyse de stabilité tridimensionnelle de l'écoulement de base. L'effet du nombre de Reynolds sur les instabilités tridimensionnelles est d'abord traité dans le régime incompressible. On constate que le support spatial des modes se déplace vers l'amont lorsque le mode devient plus instable avec l'augmentation du nombre de Reynolds. De plus, l'analyse de la distribution de chaque composante de vorticité du mode révèle une forte anisotropie pour le mode A (les composantes de vorticité transversale et verticale étant les plus et moins intenses, respectivement) alors que des intensités comparables sont mises en évidence

pour le mode B (figures 4.10 and 4.11).
L'effet de la compressibilité sur les instabilités tridimensionnelles est ensuite abordé. De manière intéressante, on constate qu'une augmentation du nombre de Mach a toujours un effet stabilisant sur le mode B, alors qu'il peut avoir un effet stabilisant ou déstabilisant pour le mode A, en fonction du nombre de Reynolds, voir figure 4.13. En particulier, il est observé que la compressibilité a un effet stabilisant sur le mode A, près du seuil critique, alors qu'elle a un effet déstabilisant à un nombre de Reynolds plus élevé, avec un déplacement des longueurs d'onde critiques vers des valeurs plus petites. L'analyse du champs de vorticité du mode A obtenus pour différents nombres de Mach à $Re = 350$ (figure 4.15) révèl que la compressibilité accentue l'anisotropie de la vorticité du mode, avec toujours une principale contribution de la composante transversale à la voriticté totale. Ceci contraste avec le mode B pour lequel les trois composantes de la vorticité présentent des intensités comparables (figure 4.16).
Dans la section §4.3, une comparaison entre la réponse de l'analyse de stabilité tridimensionelle conduite sur l'état de base filtré, l'état de base moyenné temporellement et l'état de base periodique de l'écoulement autour du cylindre de section circulaire est présentée. De manière identique à l'écoulement de base périodique, avec un temps d'integration $\tau = T$, l'écoulement filtré et l'écoulement moyenné temporellement sont instables aux perturbations tridimensionnelles. En particulier, un mode stationnaire apparaît, dont la longueur d'onde est identique à celle obtenue sur l'écoulement de base périodique (voir figure 4.19). Néanmoins, lorsque le temps d'intégration diminue, l'état de base moyenné dans le temps ne présente pas de modes instables stationnaires.

Conclusions and perspectives

Conclusions

Interest in low-Reynolds-number compressible flows has recently emerged together with prospective applications like stratospheric flight, Mars exploration and vactrains. Up to date, very few studies have addressed this peculiar regime and there is a lack of fundamental knowledge on the physics that drives compressible effects at low Reynolds numbers. In this thesis, the effect of compressibility on the circular cylinder and NACA0012 airfoil wakes is analyzed using linear stability analysis and direct numerical simulations.

A global linear stability solver, based on the finite volume spatial discretisation of the compressible Navier–Stokes equations and Chiba's time-stepping approach, has been developed. This approach does not need the linearization of the equations and allows to perform stability analysis on both stationary and periodic base states. Global stability analysis has been performed to gain insight into the mechanisms that govern primary and secondary instabilities developing in the two-dimensional wake behind a NACA0012 airfoil and a circular cylinder in the low Reynolds number compressible flow regime. Stationary base flows for detecting primary instabilities are obtained through two-dimensional direct numerical simulations using the Selective Frequency Damping method, while the unfiltered two-dimensional periodic numerical solutions have been used as base flows for detecting secondary instabilities emerging on the periodic limit cycle.

First, the two-dimensional primary instabilities behind a NACA0012 airfoil at different angles of attack and Reynolds numbers have been analyzed, starting with the incompressible case ($M_\infty = 0.05$). Our results indicate that the frequency of the most unstable mode decreases as α or Re increases, which is related to the elongation of the recirculation region of the (filtered) base flow, as previously observed on bluff bodies. Moreover, it has been observed that the growth rate of the most unstable mode first increases beyond the stability threshold with α or Re, before eventually decreasing. As α or Re are increased, the instability is first localized far downstream of the recirculation region and the position of maximal intensity in the spatial structure of the mode moves upstream closer to the airfoil, until the mode starts to interact with the recirculation region and then moves back downstream, following the elongation of the recirculation zone: the mode transitions from a Wake Instability (WI) to a Recirculation Bubble Instability (RBI). Nevertheless, the relative distance between the end of the recirculation region and the location of maximal intensity of the mode keeps decreasing. When Re is varied, the maximum growth rate is obtained when the peak intensity of the mode enters the recirculation zone. However, this is not as clear when α is varied, as the entry of the peak intensity into the recirculation zone is observed after the growth rate has reached its maximum value. On the

other hand, when both α and Re are varied, the maximum growth rate is observed when the base flow at the end of the recirculation region is most parallel and the instability is of RBI type.
We then have investigated the effects of compressibility up to $M_\infty = 0.5$. Our results show that the general trends observed in the incompressible case hold for the subcritical regime. In particular, for all the Mach numbers investigated, the frequency of the most unstable mode decreases with α and Re, which is again related to the elongation of the recirculation region of the base flow. Similar observations are made as M_∞ increases. Peak values in growth rate are found to occur when maximal intensities in the spatial structure of the most unstable mode are close to or on the recirculation region (RBI type). Moreover, it has been shown that the Mach number may have a stabilizing or destabilizing effect depending on α and Re. Following the hypothesis of Meliga *et al.* [72], we have seen that the destabilizing effect of compressibility with the Mach number is due to an increase of the negative streamwise advection (backward) of the disturbance by the base flow, within and downstream the recirculation region, while the stabilizing effect results from an increase in crosswise advection in the recirculation region. Consequently, destabilizing effects are always non-negligible, while stabilizing effects are significant in (or near) the RBI state, hence for Reynolds numbers and angles of attack far from critical values. This has been further supported by Re vs M_∞ neutral stability curves obtained at different angles of attack.

Second, the three-dimensional secondary instabilities that arise on the two-dimensional periodic wake of the circular cylinder and the NACA0012 airfoil have been analyzed. Our attention has first focused on the circular cylinder wake at Reynolds and Mach numbers up to $Re = 350$ and $M_\infty = 0.5$. The two-dimensional periodic base state is found to exhibit time-averaged properties that substantially vary within the range of Reynolds and Mach numbers considered. Specifically, three different types of time-averaged flow structure are identified when varying both Reynolds and Mach numbers.

In the incompressible case, mode A and mode B three-dimensional secondary instabilities are investigated at different wavelengths and Reynolds numbers. The increase in the Floquet multiplier, *i.e.* the destabilizing effect induced by an increase in Reynolds number, is associated with an upstream displacement toward the cylinder body of the zones of maximum vorticity concentration. At constant Reynolds number, instead, the vorticity distribution of mode A is found to vary depending on the wavelength. In particular, the cross-stream vorticity presents dipoles in the vortex core at lower wavelengths that are not present at higher ones.

In the compressible case, our results indicate that the increase of Mach number has a stabilizing effect on both the modes close to the critical thresholds, delaying the three-dimensional transition, without modifying the transverse wavelengths at which the flow becomes unstable. Conversely, above the critical thresholds, compressibility still has a stabilizing effect on mode B but progressively becomes destabilizing for mode A as the Reynolds number is further increased. In addition, the range of unstable wavelengths does not change with M_∞ for mode B, while it shifts toward lower values for mode A as M_∞ is increased. Interestingly, the normalization of the spanwise wavelengths of the modes with the characteristic length scales of the time-averaged recirculation region of the base flow highlights a possible correlation between properties of the unstable modes and those of the time-averaged flow field. The spatial support of the modes is found to strongly vary with the Mach number at the highest Reynolds number. In particular, the contributions of streamwise and cross-stream vorticity components to the overall vorticity magnitude of mode A decrease as the Mach number is increased. In that case the spanwise vorticity component of mode A exhibits a layered-structure and is the main contributor to the overall vorticity magnitude of the mode. These characteristics of mode A significantly differ from those of mode B.

Finally, preliminary results on the three-dimensionalisation of the NACA0012 airfoil periodic wake

at angle of attack $\alpha = 20°$ are discussed. It is shown that compressibility has a destabilizing effect on the period doubling mode for all the critical wavelengths. The period doubling mode structure has been found to present similarities with both modes A and B of the circular cylinder wake.

Future works

Based on the results and numerical development of this work, the following directions of research are recommended for future works.

Numerical improvements and developments

On the numerical aspects, we identify three main points:

- deriving and implementing the adjoint-operator [82]. The enhancement of the existing global stability solver to a direct/adjoint one would help gain further fundamental insight into the mechanisms driving the first transitions from stationary to three-dimensional wake flows and open the path towards efficient flow control strategies;
- extending the investigation of the Krylov–Schur parameters dependence for the solution of the EVP, in order to find the optimum combination between tolerance, Krylov subspace dimension and time integration τ;
- extending the global stability solver to spectral element spatial discretisation, already present in IC3;

Flow physics

The present thesis provided evidence that compressibility may have a strong effect on the scenario that leads to the destabilization of bluff body wakes, from a two-dimensional steady state to a three-dimensional unsteady state. However, further investigations should be provided in order to generalize present conclusions to a wider variety of fluid flows. In particular :

- the criteria for detecting the threshold between stabilizing and destabilizing effect of compressibility, in the context of primary two-dimensional instabilities, should be clarified. This may be achieved by refining the boundary between the Wake Instability (WI) and Recirculation Bubble Instability (RBI) regions, for example through analyzing the global adjoint stability response;
- the influence of compressibility on the three-dimensional instabilities developing on the two-dimensional filtered base state, as performed by Zhang & Samtaney [116] for the NACA0012 airfoil in the incompressible regime, should be explored. In particular, the investigation of the link between three-dimensional stationary mode developing on the fixed point solution and those developing on the periodic solution, which, for the circular cylinder wake, have been found to simultaneously bifurcate [81], could be of interest;
- in the case of the cylinder wake, extending this work to higher Reynolds numbers $Re > 350$ could help generalize our results. In particular, the effect of compressibility on the QP mode developing on the cylinder wake should be analyzed;
- further extension of this work to supercritical regimes could be addressed, as performed by Sansica *et al.* for the flow around a sphere [92].

- further extension of this work to the three-dimensional stability analysis of other bluff body wakes, such as the elliptic and square cylinders, the axisymmetric afterbody or other airfoils, should be addressed.

Conclusions

De récentes applications impliquant le déplacement d'objet de petite taille à grande vitesse ou le déplacement d'objet dans des environnements basse pression, telles que le vol stratosphérique et l'exploration martienne, ont conduit à l'étude des écoulements compressibles à bas nombre de Reynolds. Ce régime d'écoulement particulier n'a été que très peu abordé dans la litérature scientifique et il existe manifestement un manque de connaissances fondamentales sur l'influence de la compressibilité à faible nombre de Reynolds. En ce sens, l'objectif de cette thèse est de contribuer à une meilleure compréhension des phénomènes physiques mis en jeu dans la transition des sillages de corps canoniques de type cylindre circulaire et profil NACA0012 en régime compressible, à faible nombre de Reynolds, par la mise en oeuvre de calcul de stabilité linéaire globale et simulations numériques directes (DNS).

Un code de stabilité linéaire globale, basé sur la discrétisation spatiale en volumes finis des équations compressibles de Navier-Stokes et l'approche temporelle de Chiba, a été développé. Cette approche ne nécessite pas la linéarisation des équations et permet d'effectuer une analyse de stabilité sur les états de base stationnaire et périodique. Une analyse de stabilité globale a été réalisée afin de mieux comprendre les mécanismes qui régissent les instabilités primaires et secondaires se développant dans le sillage bidimensionnel à l'aval d'un profil NACA0012 et d'un cylindre de section circulaire, dans le régime d'écoulement compressible à faible nombre de Reynolds. Les écoulements de base stationnaires employés pour l'identification des instabilités primaires sont générés par la méthode dite de Selective Frequency Damping, tandis que les solutions périodiques bidimensionnelles des simulations non-linéaires (DNS) sont employées pour l'identification des instabilités secondaires du cycle limite périodique

Dans un premier temps, les instabilités primaires bidimensionnelles se développant dans le sillage d'un profil NACA0012 ont été étudiées, d'abord pour le cas incompressible ($M_\infty = 0.05$) à différents angles d'incidence et nombres de Reynolds. Nos résultats indiquent que la fréquence du mode le plus instable diminue lorsque α ou Re augmente, ce qui est lié à l'allongement de la bulle de recirculation de l'écoulement de base (filtré), comme cela a été précédemment observé pour les corps émoussés. Par ailleurs, il a été observé que le taux de croissance du mode le plus instable augmente avec α et Re en proximité du seuil critique, avant de diminuer. L'instabilité (dont la localisation est définie ici par la position de l'intensité maximale dans la structure spatiale du mode), d'abord localisée loin en aval de la bulle de recirculation, se déplace vers l'amont (vers le profil) avec l'augmentation de α ou Re jusqu'à ce qu'elle intéragisse avec la bulle de recirculation, puis vers l'aval avec l'allongement de la zone de recirculation : le mode passe d'une instabilité de sillage (WI) à une instabilité de bulle de recirculation (RBI). Néanmoins, la distance relative entre l'extrémité de la zone de recirculation et l'emplacement de l'intensité maximale du mode diminue continûment.Avec l'augmentation de Re, le taux de croissance maximal est obtenu lorsque l'intensité maximale du mode entre dans la zone de recirculation. Cette corrélation n'est toutefois pas aussi évidente avec l'augmentation de α, l'entrée de l'intensité maximale dans la zone de recirculation étant observée après que la valeur maximale du taux de croissance ait été atteinte. Cependant, dans les deux cas, le taux de croissance maximal semble corrélé à la parallélité de l'écoulement de base à l'extrémité de la zone de recirculation, dans une configuration de type RBI.

Nous avons ensuite étudié les effets de la compressibilité jusqu'à $M_\infty = 0.5$. Nos résultats montrent que les tendances générales observées dans le cas incompressible sont valables pour le régime sous-critique. En particulier, pour tous les nombres de Mach étudiés (*i.e.* jusqu'à 0,5), la fréquence du mode le plus instable diminue avec α et Re, ce qui est à nouveau lié à l'allongement de la bulle de recirculation de l'écoulement de base. Des observations similaires sont faites lorsque M_∞ augmente. On constate que les valeurs maximales du taux de croissance sont obtenues lorsque les intensités maximales de la structure spatiale du mode le plus instable sont proches de la zone de recirculation (type RBI).

De plus, il a été démontré que le nombre de Mach peut avoir un effet stabilisateur ou déstabilisateur en fonction de α et Re. Suivant l'hypothèse de Meliga *et al.* [72], nous avons vu que l'effet déstabilisant de la compressibilité est dû à une augmentation, avec le nombre de Mach, de l'advection longitudinale négative (vers l'amont) de la perturbation par l'écoulement de base, à l'intérieur et en aval de la zone de recirculation, tandis que l'effet stabilisant résulte d'une augmentation de l'advection transversale dans la zone de recirculation. Par conséquence, les effets déstabilisants sont toujours non négligeables, tandis que les effets stabilisants sont significatifs dans (ou près de) l'état RBI, c'est à dire pour des nombres de Reynolds et des angles d'incidence éloignés des valeurs critiques. Ceci a été confirmé par les courbes de stabilité neutre Re vs M_∞ obtenues à différents angles d'incidence.

Dans un second temps, les instabilités secondaires tridimensionnelles se développant dans le sillage périodique bidimensionnel à l'aval d'un cylindre de section circulaire et d'un profil NACA0012 ont été étudiées. Le cas du cylindre circulaire pour une gamme de nombres de Reynolds et de Mach allant jusqu'à $Re = 350$ et $M_\infty = 0.5$ a d'abord été considéré. Les résultats ont mis en évidence la dépendance des propriétés moyennes de l'état de base périodique bidimensionnel aux nombres de Reynolds et de Mach. En particulier, trois types différents de structures d'écoulements moyens ont été observés.
Dans le cas incompressible, la structure des modes A et B a été analysée pour différentes longueurs d'onde et différents nombres de Reynolds. L'augmentation du multiplicateur de Floquet, c'est-à-dire l'effet déstabilisant induit par une augmentation du nombre de Reynolds, est associée à un déplacement vers l'amont des zones de concentration maximale de vorticité. Au contraire, à nombre de Reynolds constant, la distribution de la vorticité du mode A varie en fonction de la longueur d'onde. En particulier, il a été observé que la vorticité verticals du mode s'organise en dipôles au cœur des tourbillons du champs de base pour les faibles longueurs d'onde, ce qui n'est pas observé aux plus grandes longueurs d'onde.

Dans le cas compressible, nous avons constaté que l'augmentation du nombre de Mach a un effet stabilisateur sur les modes A et B proche des seuils critiques, retardant la transition du sillage vers un état tridimensionnel, sans modifier les longueurs d'onde transversales auxquelles l'écoulement devient instable. Inversement, plus loin des seuils critiques, la compressibilité a toujours un effet stabilisant sur le mode B mais devient progressivement déstabilisante pour le mode A avec l'augmentation du nombre de Reynolds. Si la gamme des longueurs d'onde instables ne change pas avec M_∞ pour le mode B, celle des longueurs d'onde instables pour le mode A se déplace vers des valeurs plus faibles. Par ailleurs, la normalisation des longueurs d'onde transverses des modes A et B par les longueurs caractéristiques de la zone de recirculation moyenne du champs de base a révélé une corrélation entre les propriétés des modes transverses et celles du camps de base moyenné en temps. Il a pu également être mis en évidence la dépendance de la distribution spatiale de la vorticité du mode A au nombre de Mach, pour le nombre de Reynolds le plus élevé. En particulier, les contributions des composantes de vorticité longitudinale et verticale à la vorticité totale diminuent avec l'augmentation du nombre de Mach. La composante de voriticité transverse présente alors une structure en feuillets et constitue le principale contirbution à la vorticité totale, ce qui diffère notablement du mode B.

Enfin, les résultats préliminaires sur la tridimensionnalisation du sillage périodique du profil NACA0012 à angle d'incidence $\alpha = 20°$ montrent un effet déstabilisant de la compressibilité sur le mode de doublement de période pour toutes les longueurs d'onde critiques. La structure du mode de doublement de période présente des similitudes avec les modes A et B du sillage du cylindre de section circulaire.

Perspectives

Sur la base des résultats et du développement numérique de ce travail, les directions de recherche suivantes sont recommandées pour les travaux futurs.

Améliorations et développements numériques

Sur les aspects numériques, nous identifions trois points principaux :

- dériver et implémenter l'opérateur adjoint [82]. L'amélioration du code de stabilité globale existant vers un code direct/adjoint conduira à une meilleure compréhension des mécanismes fondamentaux qui régissent les premières transitions conduisant un écoulement stationnaire vers un état instationnaire tridimensionnel ;
- investiguer de manière plus approfondie la dépendance de la solution du problème aux valeurs propres aux paramètres de Krylov–Schur, afin de trouver la combinaison optimale entre tolérance, dimension du sous-espace de Krylov et intégration temporelle τ ;
- étendre le code de stabilité globale à la discrétisation spatiale par éléments spectraux, déjà présent dans le code IC3 ;

Physique des écoulements

Ce travail a permis de mettre en évidence l'influence de la compressibilité dans le processus de déstabilisation d'un sillage de corps émoussé, d'un état stationnaire vers un état instationnaire tridimensionnel. Toutefois, des investigations plus approfondies doivent être conduite en vue d'évaluer dans quelle mesure ces résultats sont généralisables à une plus grande variété d'écoulements. En particulier :

- les propriétés physiques de l'écoulement responsables de la transition entre l'effet stabilisant et déstabilisant de la compressibilité, dans le contexte des instabilités primaires bidimensionnelles, doivent être clarifiées. Mieux caractériser la frontière entre les régions d'instabilité de sillage (WI) et d'instabilité de bulle de recirculation (RBI) peut aider en ce sens, par exemple *via* l'analyse de la réponse globale de l'opérateur adjoint ;
- l'influence de la compressibilité sur les instabilités tridimensionnelles se développant sur l'état de base filtré bidimensionnel, comme présenté par exemple par Zhang & Samtaney [116] pour le NACA0012 dans le régime incompressible, devrait être explorée. En particulier, l'étude du lien existant entre le mode stationnaire tridimensionnel se développant sur la solution du point fixe et ceux se développant sur la solution périodique, qui, pour le sillage du cylindre de section circulaire, se sont avérés devenir simultanément instables [81], pourrait être intéressante ;
- dans le cas du sillage du cylindre, étendre ce travail à des nombres de Reynolds plus élevés $Re > 350$ permettrait de généraliser nos résultats. En particulier, l'effet de la compressibilité sur le mode QP se développant sur le sillage du cylindre devrait être analysé ;
- l'extension de ce travail aux régimes supercritiques pourrait également être considérée, comme abordé par Sansica *et al.* pour l'écoulement autour d'une sphère [92].
- l'extension de l'analyse de stabilité tridimensionnelle de sillages d'autres corps émoussés, tels que les cylindres de section elliptiques et carrés, l'arrière-corps axisymétrique ou différents profils d'aile, pourrait également être considérée.

Appendix A

Floquet multipliers and frequency perturbation

$$\mu = e^{\omega T} = e^{(\omega_r + i\omega_i)T} = \overbrace{e^{\omega_r T}\cos(\omega_i T)}^{\mu_r} + i\overbrace{e^{\omega_r T}\sin(\omega_i T)}^{\mu_i}$$
$$\bar{\omega}_i = \frac{2\pi}{T}$$

There are different mode types:

- μ is real and positive:

$$\begin{cases}\mu_r > 0\\ \mu_i = 0\end{cases} \qquad \begin{cases}e^{\omega_r T}\cos(\omega_i T) > 0\\ e^{\omega_r T}\sin(\omega_i T) = 0\end{cases}$$

$$\begin{cases}\omega_i T \in [-\frac{\pi}{2};\frac{\pi}{2}] + 2k\pi, \quad k \in \mathbb{Z}\\ \omega_i T = k\pi\end{cases} \qquad \begin{cases}\omega_i \in [-\frac{\bar{\omega}_i}{4};\frac{\bar{\omega}_i}{4}] + k\bar{\omega}_i\\ \omega_i = k\frac{\bar{\omega}_i}{2}\end{cases}$$

- μ is real and negative:

$$\begin{cases}\mu_r < 0\\ \mu_i = 0\end{cases} \qquad \begin{cases}e^{\omega_r T}\cos(\omega_i T) < 0\\ e^{\omega_r T}\sin(\omega_i T) = 0\end{cases}$$

$$\begin{cases}\omega_i T \in [\frac{\pi}{2};\frac{3\pi}{2}] + 2k\pi\\ \omega_i T = k\pi\end{cases} \qquad \begin{cases}\omega_i \in [\frac{\bar{\omega}_i}{4};\frac{3\bar{\omega}_i}{4}] + k\bar{\omega}_i\\ \omega_i = k\frac{\bar{\omega}_i}{2}\end{cases}$$

- μ is complex:

$$\begin{cases}\mu_r < 0, \mu_r > 0\\ \mu_i \neq 0\end{cases} \qquad \begin{cases}e^{\omega_r T}\cos(\omega_i T) < 0, e^{\omega_r T}\cos(\omega_i T) > 0\\ e^{\omega_r T}\sin(\omega_i T) \neq 0\end{cases}$$

$$\begin{cases}\omega_i T \in [-\pi;\pi] + 2k\pi\\ \omega_i T \neq k\pi\end{cases} \qquad \begin{cases}\omega_i \in [-\frac{\bar{\omega}_i}{2};\frac{\bar{\omega}_i}{2}] + k\bar{\omega}_i\\ \omega_i \neq k\frac{\bar{\omega}_i}{2}\end{cases}$$

Appendix B

Selective frequency damping

The linearized system of equations (2.2) can be cast into the following matrix form:

$$\begin{pmatrix} \dot{\boldsymbol{q}}' \\ \dot{\bar{\boldsymbol{q}}}' \end{pmatrix} = \underbrace{\begin{pmatrix} \mathscr{L} - \chi I & \chi I \\ \frac{I}{\Delta} & -\frac{I}{\Delta} \end{pmatrix}}_{\mathscr{D}} \begin{pmatrix} \boldsymbol{q}' \\ \bar{\boldsymbol{q}}' \end{pmatrix} \tag{B.1}$$

In order to understand the effect of the SFD, we should now compute the eigenpairs $(\lambda, \boldsymbol{\psi})$ of the modified matrix $\mathscr{D}$, therefore the solutions of

$$\mathscr{D}\boldsymbol{\psi} - \lambda\boldsymbol{\psi} = 0 \tag{B.2}$$

Let us now consider $(\omega, \boldsymbol{\phi})$ the eigenpairs of matrix $\mathscr{L}$. The form of matrix $\mathscr{D}$ suggests that the eigenvectors $\boldsymbol{\psi} = [\boldsymbol{\phi}; \alpha\boldsymbol{\phi}]$ [1]. From equation (B.2) and considering the form of $\boldsymbol{\psi}$, we obtain:

$$\begin{cases} \mathscr{L}\boldsymbol{\phi} - \chi\boldsymbol{\phi} - \lambda\boldsymbol{\phi} + \alpha\chi\boldsymbol{\phi} = 0 \\ \frac{1}{\Delta}\boldsymbol{\phi} - (\frac{1}{\Delta} + \lambda)\alpha\boldsymbol{\phi} = 0 \end{cases} \tag{B.3}$$

As already said $(\omega, \boldsymbol{\phi})$ are the eigenpairs of matrix $\mathscr{L}$, therefore $\mathscr{L}\boldsymbol{\phi} = \omega\boldsymbol{\phi}$. This yields to the following:

$$\begin{cases} \omega - \chi - \lambda + \alpha\chi = 0 \\ \frac{1}{\Delta} - (\frac{1}{\Delta} + \lambda)\alpha = 0 \end{cases} \tag{B.4}$$

From the second one:

$$\lambda = \frac{1}{\Delta}\left(\frac{1}{\alpha} - 1\right) \tag{B.5}$$

Substituting in the first one, we derive an expression for α

$$\begin{aligned} &\omega - \chi - \frac{1}{\alpha\Delta} + \frac{1}{\Delta} + \alpha\chi = 0 \\ &\alpha\Delta\omega - \alpha\chi\Delta - 1 + \alpha + \Delta\chi\alpha^2 = 0 \\ &\underbrace{\Delta\chi}_{a}\,\alpha^2 + \alpha\underbrace{(1 - \chi\Delta + \Delta\omega)}_{b} - \underbrace{1}_{c} = 0 \end{aligned}$$

$$\alpha^{\pm} = \frac{-1 + \chi\Delta - \Delta\omega \pm \sqrt{(1 - \chi\Delta + \Delta\omega)^2 + 4\chi\Delta}}{2\chi\Delta} = \frac{-b \pm \sqrt{b^2 - 4ac}}{2a} \tag{B.6}$$

We now substitute $\alpha^{\pm}$ in (B.5):

$$
\begin{aligned}
\lambda =& \frac{1}{\Delta}\left(\frac{2a}{-b \pm \sqrt{b^2-4ac}} - 1\right) \\
=& \frac{1}{\Delta}\left(\frac{2a+b \mp \sqrt{b^2-4ac}}{-b \pm \sqrt{b^2-4ac}} \cdot \frac{-b \mp \sqrt{b^2-4ac}}{-b \mp \sqrt{b^2-4ac}}\right) \\
=& \frac{1}{\Delta}\left(\frac{-b\cdot(2a+b) \mp \sqrt{b^2-4ac}\cdot(2a+b-b) + \sqrt{b^2-4ac}^2}{b^2-b^2+4ac}\right) \\
=& \frac{1}{\Delta}\left(\frac{-2ab-b^2 \mp \sqrt{b^2-4ac}\cdot 2a + b^2 - 4ac}{4ac}\right) \\
=& \frac{1}{\Delta}\left(\frac{-2ab \mp \sqrt{b^2-4ac}\cdot 2a - 4ac}{4ac}\right) \\
=& \frac{1}{\Delta} a \left(\frac{-b-b+b \mp \sqrt{b^2-4ac} - 2c}{2ca}\right) \\
=& \frac{a}{\Delta}\left(\frac{-2b+b \mp \sqrt{b^2-4ac} - 2c}{c2a}\right) \\
=& \frac{a}{\Delta}\left(\frac{-b-c}{ca} - \frac{\alpha^{\pm}}{c}\right) \\
=& \frac{\Delta\chi}{\Delta}\left(\frac{-1+\chi\Delta-\Delta\omega+1}{-\Delta\chi} + \alpha^{\pm}\right) \\
=& \omega - \chi(1-\alpha^{\pm})
\end{aligned}
$$

Appendix C

Influence of the Reynolds number at $\alpha = 14°$ and $18°$

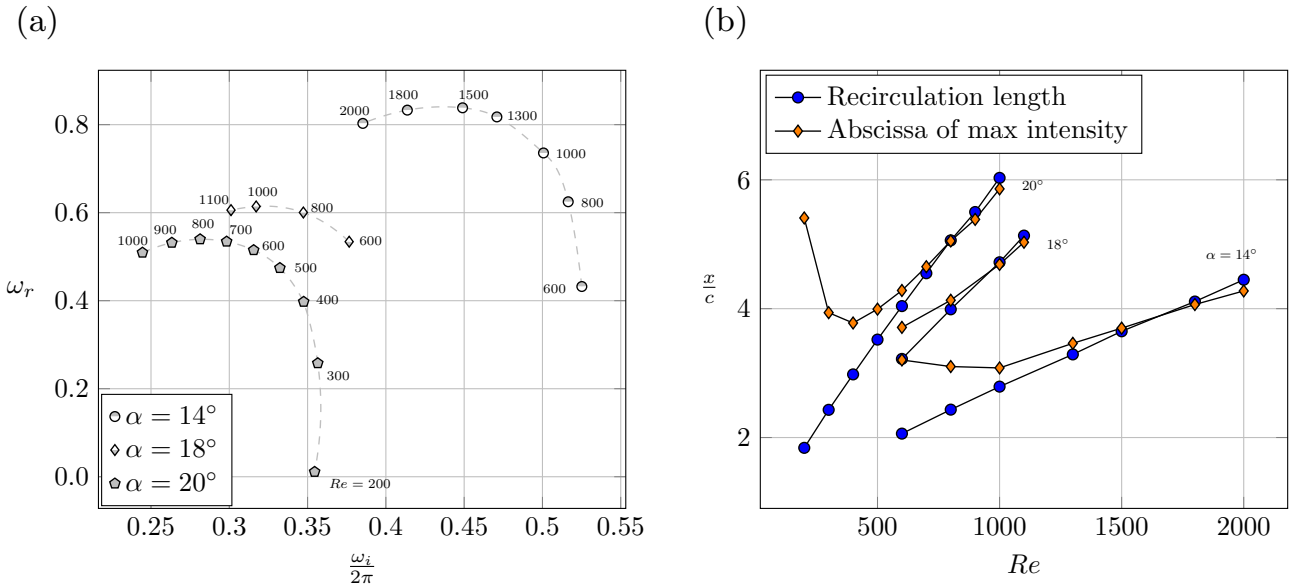

Figure 3.1 – Growth rate as a function of frequency of the most unstable mode (a) and length of the recirculation region and streamwise location of maximal intensity in the spatial structure of the most unstable mode (b), for $\alpha = 14°, 18°$ and $20°$, varying the Reynolds number.

We performed additional stability calculations at two lower values of the angle of attack: $\alpha = 18°$ and $\alpha = 14°$. The results given in figure 3.1.a show a similar evolution of the mode characteristics with the Reynolds number than the one obtained at $\alpha = 20°$, the only difference is that the largest growth rate is obtained for an increasing Reynolds number when the angle of attack is decreased, *i.e.* $Re \approx 1000$ for $\alpha = 18°$ and $Re \approx 1500$ for $\alpha = 14°$. As illustrated in figure 3.1.b, this maximal growth rate occurs, again, when the abscissa of the peak of maximal intensity of the mode coincides with the end of the base flow recirculation region.

Appendix D

Mesh convergence for the three-dimensional cylinder

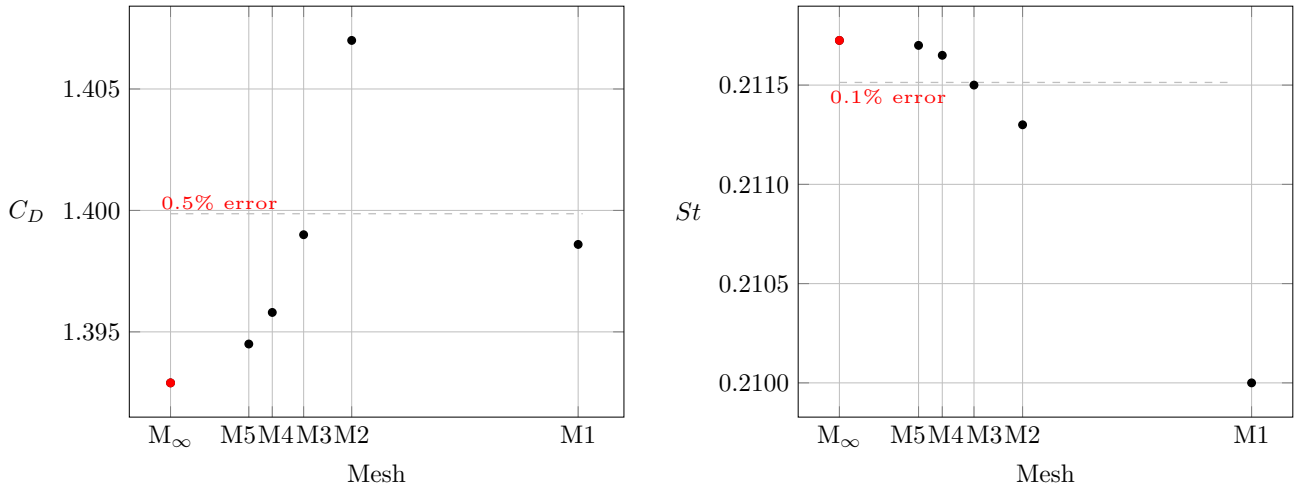

Figure 4.1 – Convergence on drag coefficient C_D and Strouhal number St with respect to 5 different meshes at $Re = 300$. M1 is the coarsest, M5 the most refined. M_∞ (red dots) represent the asymptotic value as given by Richardson extrapolation. Henderson [46] reported $C_D \approx 1.4$

Figure 4.1 shows the two-dimensional flow convergence on coefficient C_D and Strouhal number St with respect to the grid characteristic size $(1/N_{cells})$ of five different meshes, from M1 the coarsest to M5 the most refined. M3 has been chosen for the two dimensional resolution showing less then 0.5% of error with respect to the extrapolated value (red dot) on the drag coefficient and a 0.1% error on the Strouhal number. In the convergence study of Kanaris *et al.* [57], they reported a convergence of the three-dimensional flow at a spanwise cell length of $\Delta_z = 0.2D$, hence, we started with a spanwise discretisation of $\Delta_z = 0.125D$. Values of the Floquet exponent μ with respect to the two-dimensional ((x, y) plane) discretisation and $\Delta_z = 0.125D$ are shown in figure 4.2. Results obtained with mesh M3 differ by less than 1% for the mode A and 3% for mode B. In table 4.1 results for modes A and B at other wavelengths are also reported, including the influence of the spanwise discretisation. The relative error for mode A between mesh M2 with $\Delta_z = D/4$ and M4 with $\Delta_z = D/16$ is $\approx 0.5\%$, while that for mode B between mesh M2 with $\Delta_z = D/4$ and M4 with $\Delta_z = D/32$ is $\approx 3\%$. The higher relative error of mode B is due to the shorter wavelength of this mode compared to the one of mode A. Based on these results, mesh M3 with $\Delta_z = D/8$ has been chosen.

		xy refinement				
		M1	M2	M3	M4	M5
Mode A $\lambda_z = 4D$	$\Delta_z = D/8$	1.635	1.721	1.736	1.742	1.743
Mode A $\lambda_z = 3D$	$\Delta_z = D/4$	-	1.710	-	-	-
	$\Delta_z = D/8$	-	-	1.711	-	-
	$\Delta_z = D/16$	-	-	-	1.718	-
	$\Delta_z = D/32$	-	-	-	-	-
Mode B $\lambda_z = 0.8D$	$\Delta_z = D/8$	1.629	1.889	1.902	1.924	1.938
Mode B $\lambda_z = 0.75D$	$\Delta_z = D/4$	-	1.868	-	-	-
	$\Delta_z = D/8$	-	-	1.836	-	-
	$\Delta_z = D/16$	-	-	-	1.811	-
	$\Delta_z = D/32$	-	-	-	-	1.835

Table 4.1 – Floquet exponents for mode A at a wavelength $\lambda_z = 4D, 3D$ and mode B at $\lambda_z = 0.8D, 0.75D$ with respect to different resolutions at $Re = 300$ and $M_\infty = 0.05$.

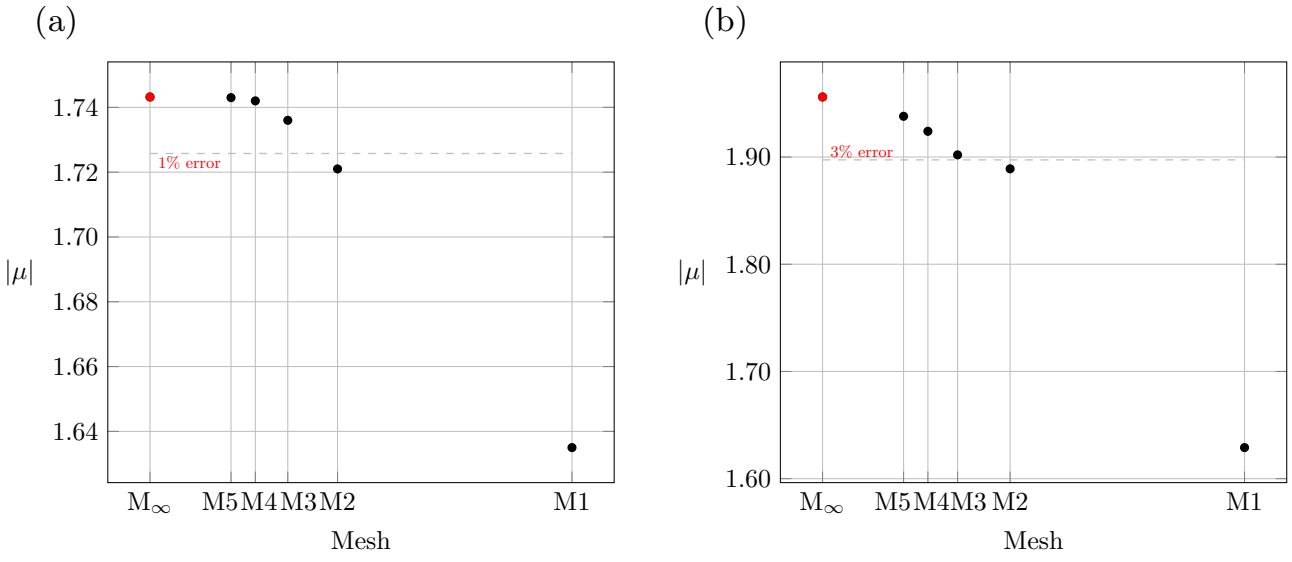

Figure 4.2 – Convergence on the Floquet exponents for (a) mode A at a wavelength $\lambda_z = 4D$ and (b) mode B at a $\lambda_z = 0.8D$ with respect to 5 different (x, y)-resolutions and $\Delta_z = 0.125D$ at $Re = 300$ and $M_\infty = 0.05$. Red dots correspond to the Richardson extrapolation.

Appendix E

Base flow starting point influence

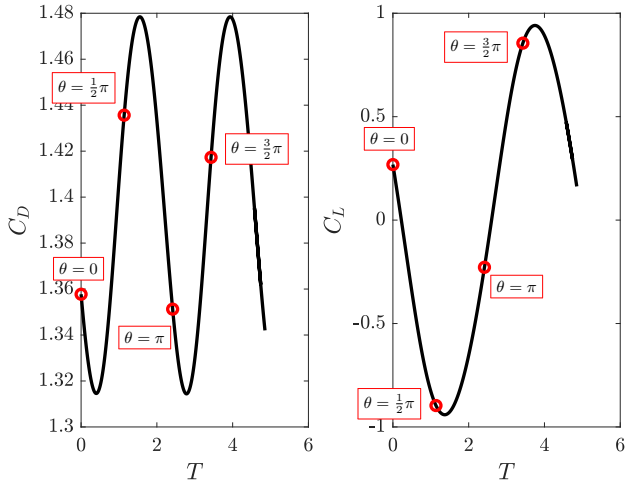

Figure 5.1 – Time variation of drag and lift coefficient at $Re = 300$ and $M_\infty = 0.05$. Red dots are four different instants corresponding to the four stability analysis calculation.

The mode structure resulting from the Floquet stability analysis depends on the starting base flow instant. For this reason, we show in figure 5.2 and 5.3 the mode structure evolution with respect to the base flow, in a complete shedding cycle. The base flow instants of the different simulations are shown on the drag and lift signals in figure 5.1, indicated by red dots as a shift in phase θ.
We can remark that the general characteristics of the mode structure (like the downstream extension or vorticity intensities) do not change that much with respect to the base flow starting instant, only the mode adaptation on the base flow starting instant presents remarkable changes. In particular we can notice that the cross-stream vorticity is present in the braid region close to the cylinder, only when the vortex is about to detach from the body. This is coherent to the fact that at that instant the strain rate in the braid region close to the cylinder is is the maximal. Moreover in the streamwise vorticity we notice that there are intermediate primary vortexes in which mode streamwise vorticity has strongly decreased (the ± 0.1 isosurfaces are not present).
The influence of the initial instant of base flow on the Floquet multiplier, on the other hand, seems to give the multiplier a sinusoidal behavior that follows that of the drag coefficient (presenting two periods in a complete shedding). However, its fluctuations are less than 0.5% around the mean value. These specific simulations have been performed on the coarsest mesh M1 with $\Delta_z = D/8$.

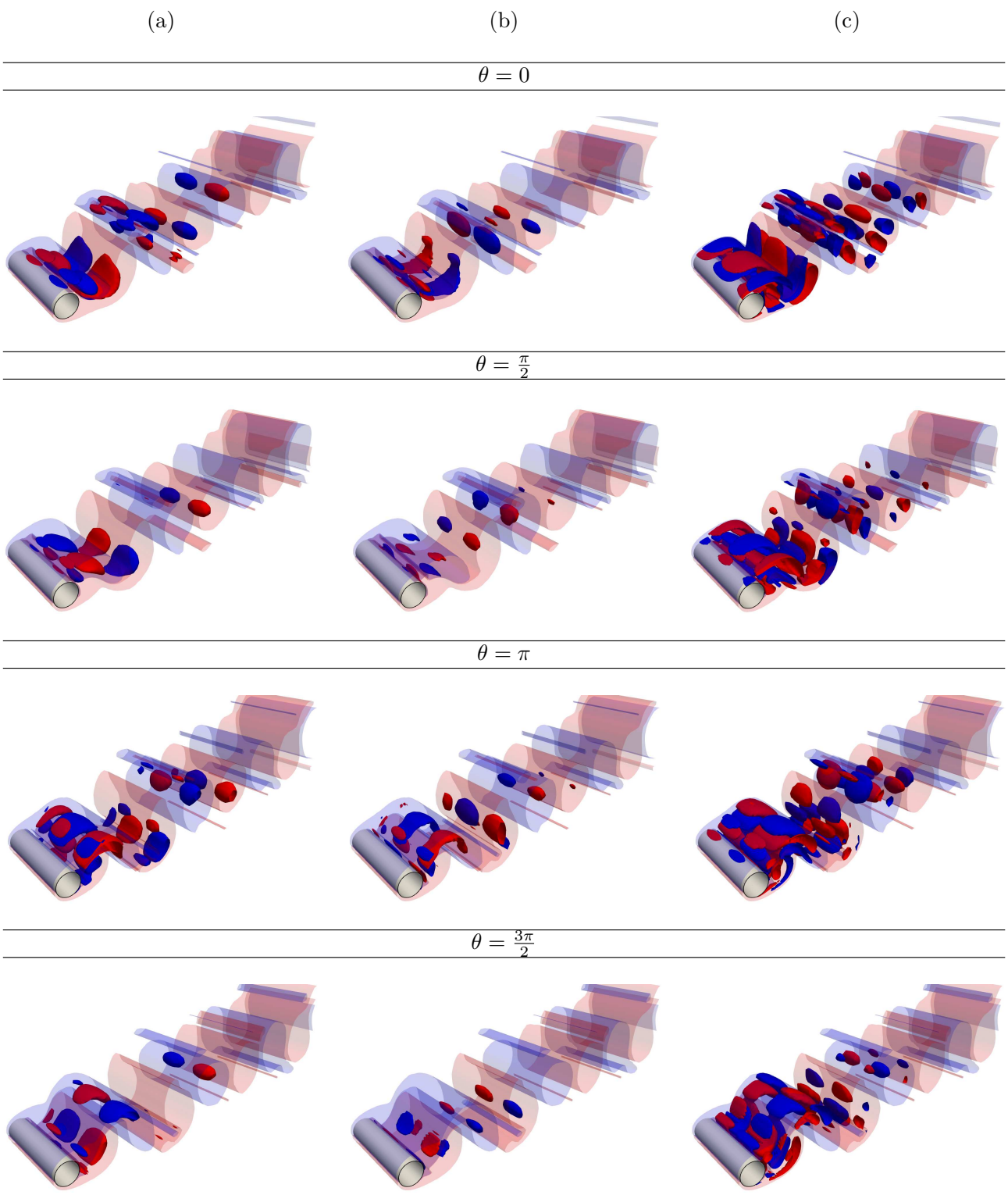

Figure 5.2 – Vorticity $\widetilde{\omega}/\max(||\widetilde{\omega}||)$ of mode A with wavelength $\lambda_z = 4D$ at $Re = 300$ and $M_\infty = 0.05$ for different base flow instants θ: (a) streamwise, (b) cross-stream and (c) spanwise component. Iso-surfaces at levels ± 0.1 (positive in red, negative in blue) superposed to translucent iso-surfaces of base flow vorticity at level ± 0.01.

Figure 5.3 – Vorticity $\widetilde{\omega}/\max(||\widetilde{\omega}||)$ of mode B with wavelength $\lambda_z = 0.8D$ at $Re = 300$ and $M_\infty = 0.05$ for different base flow instants θ: (a) streamwise, (b) cross-stream and (c) spanwise component. Iso-surfaces at levels ± 0.1 (positive in red, negative in blue) superposed to translucent iso-surfaces of base flow vorticity at level ± 0.01.

Appendix F

Mach evolution of mode A vorticity

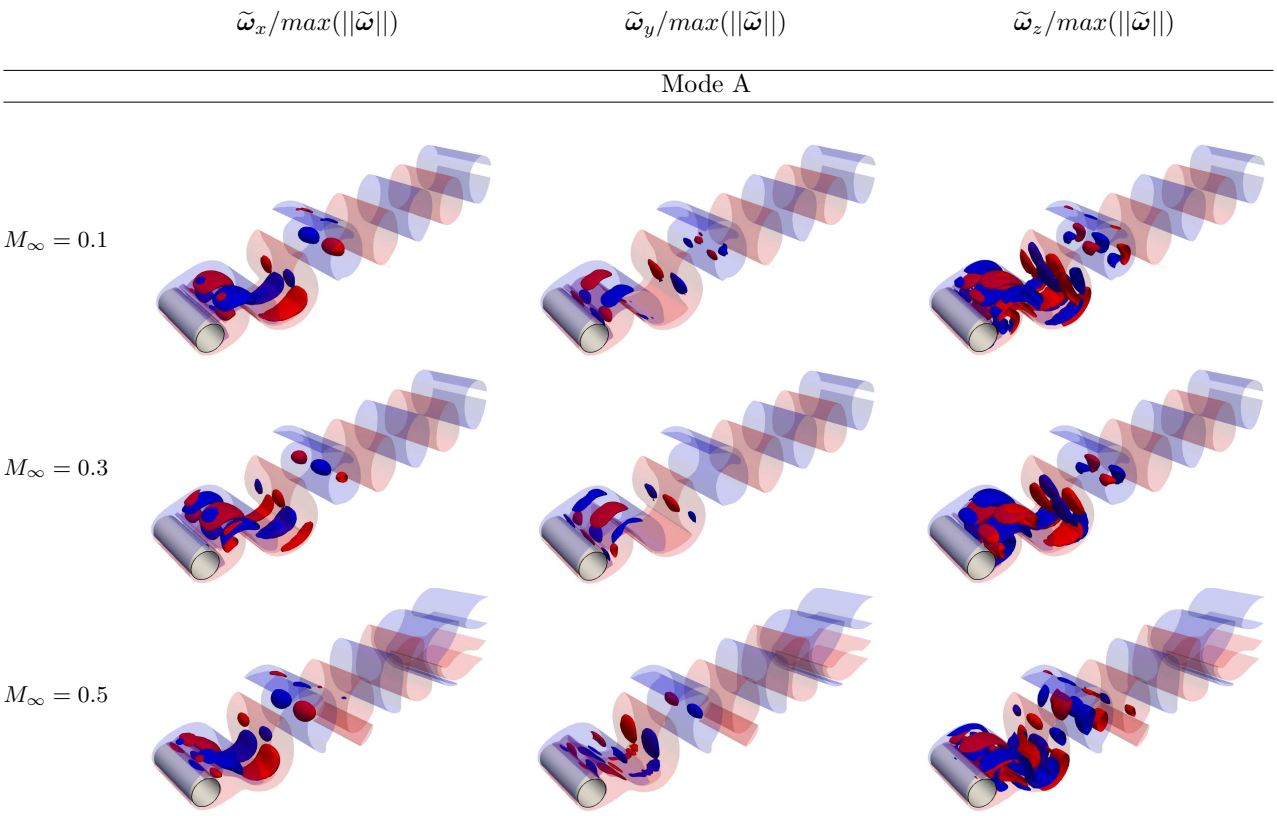

Figure 6.1 – Mach evolution of mode A vorticity $\widetilde{\boldsymbol{\omega}}/\max(||\widetilde{\boldsymbol{\omega}}||)$, with wavelength $\lambda_z = 3D$ and $Re = 350$. Iso-surfaces at levels ± 0.1 (positive in red, negative in blue) superposed to translucent iso-surfaces of base flow vorticity at level ± 0.01.

Figure 6.1 and 6.2 show iso-surfaces of streamwise, cross-stream and spanwise vorticity of mode A at wavelength $\lambda_z = 3D$ and $Re = 250, 350$. Conversely to largest wavelengths (figure 6.3), the contribution of the streamwise and cross-stream components to the vorticity magnitude does not change with the increase in Mach number and spanwise vorticity layers observed at $\lambda_z = 4D$ are not visible.

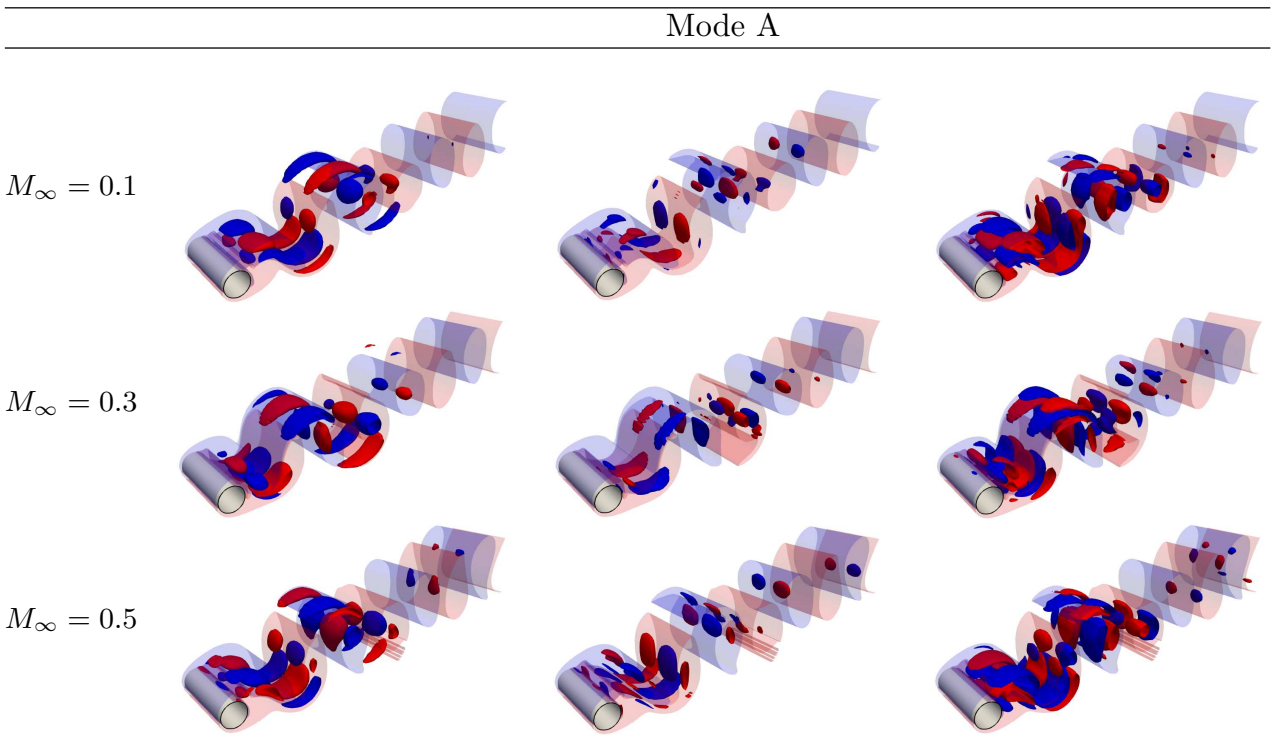

Figure 6.2 – Mach evolution of mode A vorticity $\widetilde{\boldsymbol{\omega}}/\max(||\widetilde{\boldsymbol{\omega}}||)$, with wavelength $\lambda_z = 3D$ and $Re = 250$. Same convention as in figure 6.1.

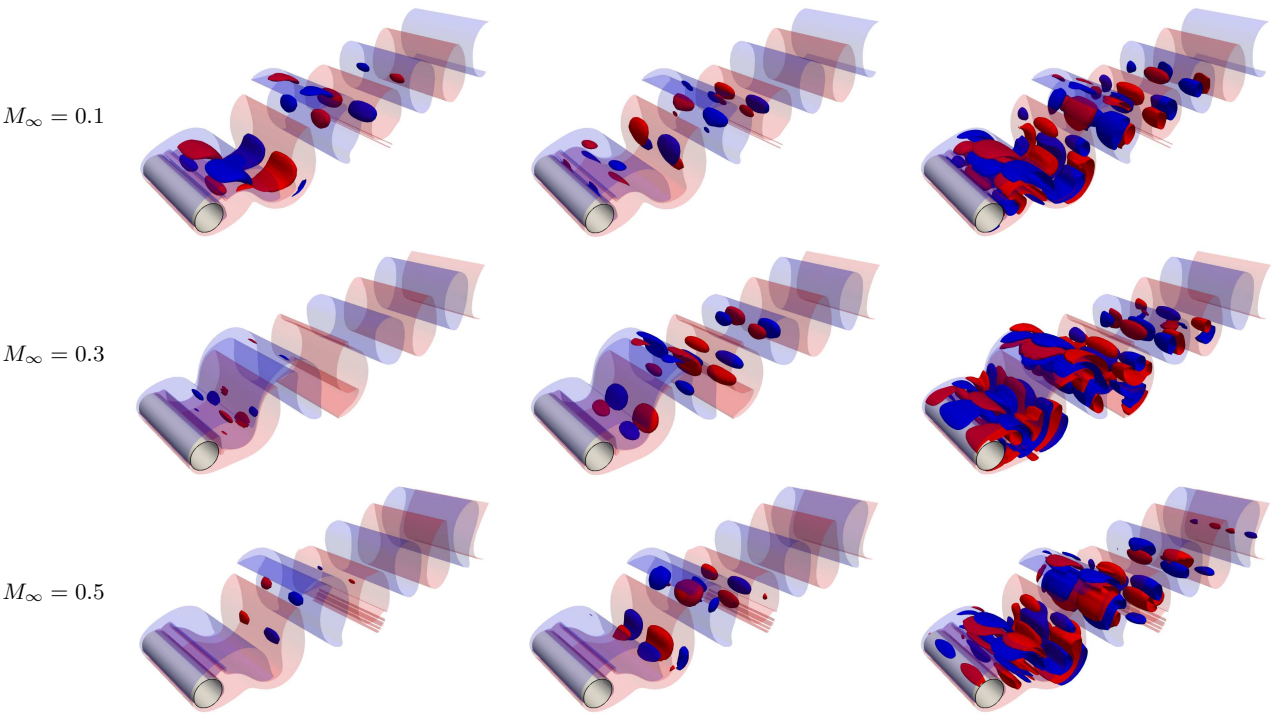

Figure 6.3 – Mach evolution of mode A vorticity $\widetilde{\boldsymbol{\omega}}/\max(||\widetilde{\boldsymbol{\omega}}||)$, with wavelength $\lambda_z = 4D$ and $Re = 250$. Same convention as in figure 6.1.

Appendix G

Mesh convergence for the three-dimensional NACA0012 airfoil

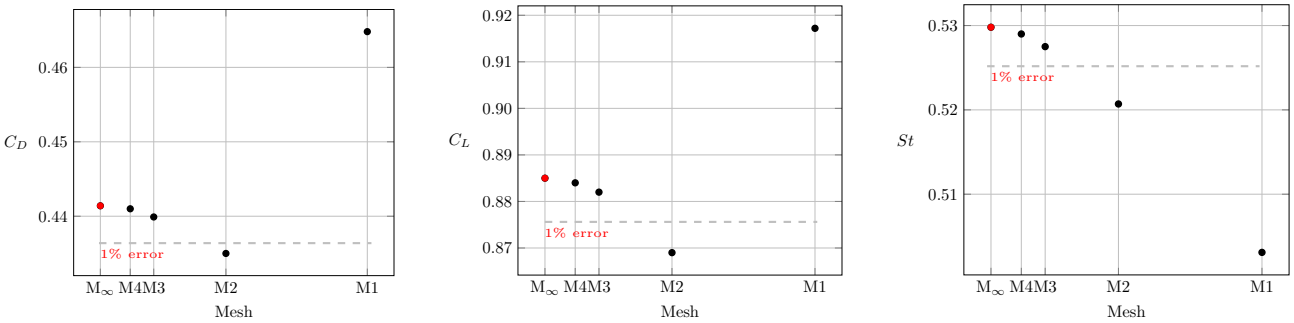

Figure 7.1 – Convergence on mean drag, lift and Strouhal coefficients with respect to 4 different meshes for the NACA0012 airfoil at $\alpha = 20°$, $Re = 1000$ and $M_\infty = 0.05$. M1 is the coarsest, M4 the most refined. M$_\infty$ represents the asymptotic value, computed thought a Richardson extrapolation.

Figure 7.1 shows the two-dimensional flow convergence on the drag and lift coefficients as well as on the Strouhal number with respect to the grid characteristic size ($1/N_{cells}$) for four different meshes, from M1 the coarsest to M4 the most refined. When using mesh M3, the two-dimensional resolution shows less than 1% of error with respect to the extrapolated value (red dot) on each quantity. Values of the Floquet exponent μ with respect to the two-dimensional (x, y) discretisation and different spanwise resolutions Δ_z are reported in table 7.1 for the period doubling mode with wavelength $\lambda_z = 0.66C$, where C indicates the airfoil chord. We can remark that the two-dimensional refinement has much more influence than Δ_z, with a maximum relative error with mesh M4 and the different spanwise discretizations of $\approx 1.6\%$. Based on these results, mesh M4 with $\Delta_z = D/16$ has been chosen. It is

		(x, y) refinement			
		M1	M2	M3	M4
PD $\lambda_z = 0.66C$	$\Delta_z = 1/8$	-1.2361	-	-	-1.5896
	$\Delta_z = 1/16$	-	-1.4127	-1.5950	-1.6164
	$\Delta_z = 1/32$	-	-1.4056	-1.5898	-1.6114
	$\Delta_z = 1/64$	-	-1.4015	-1.5865	-

Table 7.1 – Floquet exponents for the period doubling (PD) mode of wavelength $\lambda_z = 0.66D$ with respect to different resolutions at $\alpha = 20°$, $Re = 600$ and $M_\infty = 0.05$. Reference value from Meneghini *et al.* [73] is $\mu \approx -1.64$.

worth mentioning, that a stronger impact of spatial refinement on stability results compared to that on the aerodynamic coefficients is observed. This issue has been examined in [35].

Bibliography

[1] E. Åkervik, L. Brandt, D. S. Henningson, J. Hœpffner, O. Marxen, & P. Schlatter. Steady solutions of the Navier-Stokes equations by selective frequency damping. *Physics of fluids*, 18(6): 068102, 2006.

[2] H.-B. An, J. Wen, & T. Feng. On finite difference approximation of a matrix-vector product in the Jacobian-free Newton–Krylov method. *Journal of Computational and Applied Mathematics*, 236(6):1399–1409, 2011.

[3] M. Anyoji, K. Nose, S. Ida, D. Numata, H. Nagai, & K. Asai. Low Reynolds Number Airfoil Testing in a Mars Wind Tunnel. In *40th Fluid Dynamics Conference and Exhibit*. AIAA Paper 2010-4627, June 2010.

[4] M. Anyoji, M. Okamoto, K. Fujita, H. Nagai, & A. Oyama. Evaluation of aerodynamic performance of Mars airplane in scientific balloon experiment. *Fluid Mech. Res. Int*, 1(3):1–7, 2017.

[5] H. Aref, M. Brøns, & M. A. Stremler. Bifurcation and instability problems in vortex wakes. In *Journal of Physics: Conference Series*, volume 64, page 012015. IOP Publishing, 2007.

[6] C. Arratia, C. P. Caulfield, & J.-M. Chomaz. Transient perturbation growth in time-dependent mixing layers. *J. Fluid Mech.*, 717:90–133, 2013.

[7] S. Bagheri, E. Åkervik, L. Brandt, & D. S. Henningson. Matrix-free methods for the stability and control of boundary layers. *AIAA journal*, 47(5):1057–1068, 2009.

[8] D. Barkley. Linear analysis of the cylinder wake mean flow. *EPL (Europhysics Letters)*, 75(5): 750, 2006.

[9] D. Barkley & R. D. Henderson. Three-dimensional Floquet stability analysis of the wake of a circular cylinder. *Journal of Fluid Mechanics*, 322:215–241, 1996.

[10] O. A. Bauchau & Y. G. Nikishkov. An implicit Floquet analysis for rotorcraft stability evaluation. *Journal of the American Helicopter Society*, 46(3):200–209, 2001.

[11] C. M. Bender & S. A. Orszag. *Advanced mathematical methods for scientists and engineers I: Asymptotic methods and perturbation theory*. Springer Science & Business Media, 2013.

[12] I. Bermejo-Moreno, L. Campo, J. Larsson, J. Bodart, D. Helmer, & J. Eaton. Confinement effects in shock wave/turbulent boundary layer interactions through wall-modelled large-eddy simulations. *Journal of Fluid Mechanics*, 758:5–62, 2014. doi: 10.1017/jfm.2014.505.

[13] A. Bers. Space-time evolution of plasma instabilities-absolute and convective. In *Basic plasma physics. 1.* 1983.

[14] H. Blackburn & G. Sheard. On quasiperiodic and subharmonic Floquet wake instabilities. *Physics of Fluids*, 22(3):031701, 2010.

[15] H. Blackburn, F. Marques, & J. Lopez. On three-dimensional instabilities of two-dimensional flows with a Z2 spatio-temporal symmetry. *J. Fluid Mech., submitted for publication*, 2004.

[16] H. M. Blackburn & J. M. Lopez. On three-dimensional quasiperiodic Floquet instabilities of two-dimensional bluff body wakes. *Physics of Fluids*, 15(8):L57–L60, 2003.

[17] H. M. Blackburn, F. Marques, & J. M. Lopez. Symmetry breaking of two-dimensional time-periodic wakes. *Journal of Fluid Mechanics*, 522:395–411, 2005.

[18] A. Bouhadji & M. Braza. Organised modes and shock–vortex interaction in unsteady viscous transonic flows around an aerofoil Part I: Mach number effect. *Computers & fluids*, 32(9): 1233–1260, 2003.

[19] P. N. Brown, H. F. Walker, R. Wasyk, & C. S. Woodward. On using approximate finite differences in matrix-free Newton–Krylov methods. *SIAM Journal on Numerical Analysis*, 46(4):1892–1911, 2008.

[20] D. Canuto & K. Taira. Two-dimensional compressible viscous flow around a circular cylinder. *Journal of Fluid Mechanics*, 785:349–371, 2015.

[21] B. S. Carmo, S. J. Sherwin, P. W. Bearman, & R. H. Willden. Wake transition in the flow around two circular cylinders in staggered arrangements. *Journal of Fluid Mechanics*, 597:1–29, 2008.

[22] F. Charru. *Instabilités hydrodynamiques*. EDP Sciences, 2021.

[23] S. Chiba. Global stability analysis of incompressible viscous flow. *J. Jpn. Soc. Comput. Fluid Dyn*, 7:20–48, 1998.

[24] S. CHIBA. Three-dimensional global stability analysis for the time-periodic cylinder wake. *Theoretical and Applied Mechanics*, 50:321–326, 2001.

[25] J. Chomaz. Linear and non-linear, local and global stability analysis of open flows. *Comptes-rendus de l'École des Houches Turbulence in Spatially Extended Systems*, 1993.

[26] J. Chomaz, P. Huerre, & L. Redekopp. Bifurcations to local and global modes in spatially developing flows. *Physical review letters*, 60(1):25, 1988.

[27] J.-M. Chomaz. Global instabilities in spatially developing flows: non-normality and nonlinearity. *Annu. Rev. Fluid Mech.*, 37:357–392, 2005.

[28] J.-M. Chomaz, P. Huerre, & L. G. Redekopp. A frequency selection criterion in spatially developing flows. *Studies in applied mathematics*, 84(2):119–144, 1991.

[29] J. Deng, L. Sun, & X. Shao. Floquet stability analysis in the wake of a NACA0015 airfoil at post-stall angles of attack. *Physics of Fluids*, 29(9):094104, 2017.

[30] T. Desert. *Étude aéropropulsive d'un micro-drone à voilure tournante pour l'exploration martienne*. PhD thesis, UNIVERSITE DE TOULOUSE, 2019.

[31] T. Désert, T. Jardin, H. Bézard, & J.-M. Moschetta. Numerical predictions of low reynolds number compressible aerodynamics. *Aerospace Science and Technology*, 92:211–223, 2019.

[32] P. G. Drazin. *Introduction to Hydrodynamic Stability*. Cambridge University Press, sep 2002. doi: 10.1017/cbo9780511809064.

[33] D. Durante, E. Rossi, & A. Colagrossi. Bifurcations and chaos transition of the flow over an airfoil at low Reynolds number varying the angle of attack. *Communications in Nonlinear Science and Numerical Simulation*, 89:105285, 2020.

[34] G. Y. Dynnikova, Y. A. Dynnikov, & S. Guvernyuk. Mechanism underlying Kármán vortex street breakdown preceding secondary vortex street formation. *Physics of Fluids*, 28(5):054101, 2016.

[35] P. Fernandez & Q. Wang. Lyapunov spectrum of the separated flow around the NACA 0012 airfoil and its dependence on numerical discretization. *Journal of Computational Physics*, 350: 453–469, 2017.

[36] M. Fosas de Pando, D. Sipp, & P. J. Schmid. Efficient evaluation of the direct and adjoint linearized dynamics from compressible flow solvers. *Journal of Computational Physics*, 231(23): 7739–7755, 2012.

[37] R. Gabbai & H. Benaroya. An overview of modeling and experiments of vortex-induced vibration of circular cylinders. *Journal of Sound and Vibration*, 282(3-5):575–616, 2005.

[38] M. Gaster. Growth of disturbances in both space and time. *The Physics of Fluids*, 11(4):723–727, 1968.

[39] J. Gerrard. The mechanics of the formation region of vortices behind bluff bodies. *Journal of fluid mechanics*, 25(2):401–413, 1966.

[40] F. Giannetti & P. Luchini. Structural sensitivity of the first instability of the cylinder wake. *Journal of Fluid Mechanics*, 581:167–197, 2007.

[41] R. Gioria, W. He, J. M. Perez, & V. Theofilis. Modal and non-modal global instability analyses of low-re massively separated flow around a NACA0015 airfoil. In *46th AIAA Fluid Dynamics Conference*, page 3778, 2016.

[42] F. Gómez, R. Gómez, & V. Theofilis. Coupling time-stepping numerical methods and standard aerodynamics codes for instability analysis of flows in complex geometries. In *6th Theoretical Fluid Mechanics Conference*. AIAA Paper 2011-3753, June 2011.

[43] F. J. Gómez Carrasco. *Matrix-free time-stepping methods for the solution of TriGlobal instability problems*. PhD thesis, School of Aeronautics, Universidad Politécnica de Madrid, 2013.

[44] A. Grébert, J. Bodart, S. Jamme, & L. Joly. Simulations of shock wave/turbulent boundary layer interaction with upstream micro vortex generators. *International Journal of Heat and Fluid Flow*, 72:73–85, 2018.

[45] W. He, R. d. S. Gioria, J. M. Pérez, & V. Theofilis. Linear instability of low Reynolds number massively separated flow around three NACA airfoils. *Journal of Fluid Mechanics*, 811:701–741, 2017.

[46] R. D. Henderson. Details of the drag curve near the onset of vortex shedding. *Physics of Fluids*, 7(9):2102–2104, 1995.

[47] V. Hernández, J. E. Román, A. Tomás, & V. Vidal. Krylov-schur methods in SLEPc. *Universitat Politecnica de Valencia, Tech. Rep. STR-7*, 2007.

[48] H. Hochstadt. *Differential equations*. Courier Corporation, 2014.

[49] P. Huerre. Spatio-temporal instabilities in closed and open flows. In *Instabilities and nonequilibrium structures*, pages 141–177. Springer, 1987.

[50] P. Huerre. Open shear flow instabilities. *Perspective in Fluid Dynamics: Collective Introduction to Current Research*, pages 159–229, 2000.

[51] P. Huerre & P. A. Monkewitz. Local and global instabilities in spatially developing flows. *Annu. Rev. Fluid Mech.*, 22(1):473–537, 1990.

[52] D. L. Jacono, J. S. Leontini, M. C. Thompson, & J. Sheridan. Modification of three-dimensional transition in the wake of a rotationally oscillating cylinder. *Journal of Fluid Mechanics*, 643: 349–362, 2010.

[53] H. Jiang. Three-dimensional wake transition of a diamond-shaped cylinder. *Journal of Fluid Mechanics*, 918, 2021.

[54] H. Jiang & L. Cheng. Transition to chaos in the cylinder wake through the Mode C flow. *Physics of Fluids*, 32(1):014103, 2020.

[55] B. E. Jordi, C. J. Cotter, & S. J. Sherwin. An adaptive selective frequency damping method. *Physics of Fluids*, 27(9):094104, 2015.

[56] S. Julien, J. Lasheras, & J.-M. Chomaz. Three-dimensional instability and vorticity patterns in the wake of a flat plate. *Journal of Fluid Mechanics*, 479:155–189, 2003.

[57] N. Kanaris, D. Grigoriadis, & S. Kassinos. Three dimensional flow around a circular cylinder confined in a plane channel. *Physics of Fluids*, 23(6):064106, 2011.

[58] D. A. Knoll & D. E. Keyes. Jacobian-free Newton–Krylov methods: a survey of approaches and applications. *Journal of Computational Physics*, 193(2):357–397, 2004.

[59] W. Koch. Local instability characteristics and frequency determination of self-excited wake flows. *Journal of Sound and vibration*, 99(1):53–83, 1985.

[60] D. F. Kurtulus. On the unsteady behavior of the flow around NACA0012 airfoil with steady external conditions at re= 1000. *International journal of micro air vehicles*, 7(3):301–326, 2015.

[61] S. Le Dizès, P. Huerre, J.-M. Chomaz, & P. A. Monkewitz. Linear global modes in spatially developing media. *Philosophical Transactions of the Royal Society of London. Series A: Mathematical, Physical and Engineering Sciences*, 354(1705):169–212, 1996.

[62] J. S. Leontini, D. L. Jacono, & M. C. Thompson. Stability analysis of the elliptic cylinder wake. *Journal of Fluid Mechanics*, 763:302–321, 2015.

[63] T. Leweke & C. H. Williamson. Three-dimensional instabilities in wake transition. *European Journal of Mechanics-B/Fluids*, 17(4):571–586, 1998.

[64] Z. Liu & G. A. Kopp. A numerical study of geometric effects on vortex shedding from elongated bluff bodies. *Journal of wind engineering and industrial aerodynamics*, 101:1–11, 2012.

[65] J.-C. Loiseau, M. A. Bucci, S. Cherubini, & J.-C. Robinet. Time-stepping and Krylov methods for large-scale instability problems. In *Computational Modelling of Bifurcations and Instabilities in Fluid Dynamics*, pages 33–73. Springer, 2019.

[66] W. T. Lord Kelvin. XLVI. Hydrokinetic solutions and observations. *Philos. Mag.*, 42(281): 362–377, 1871.

[67] C. J. Mack, P. J. Schmid, & J. L. Sesterhenn. Global stability of swept flow around a parabolic body: connecting attachment-line and crossflow modes. *Journal of Fluid Mechanics*, 611:205–214, 2008.

[68] V. Mantič-Lugo, C. Arratia, & F. Gallaire. A self-consistent model for the saturation dynamics of the vortex shedding around the mean flow in the unstable cylinder wake. *Physics of Fluids*, 27 (7):074103, 2015.

[69] X. Mao & H. Blackburn. The structure of primary instability modes in the steady wake and separation bubble of a square cylinder. *Physics of Fluids*, 26(7):074103, 2014.

[70] F. Marques, J. M. Lopez, & H. M. Blackburn. Bifurcations in systems with Z2 spatio-temporal and O (2) spatial symmetry. *Physica D: Nonlinear Phenomena*, 189(3-4):247–276, 2004.

[71] E. Meiburg, J. C. Lasheras, & W. T. Ashurst. Topology of the vorticity field in three-dimensional shear layers and wakes. *Fluid Dynamics Research*, 3(1-4):140, 1988.

[72] P. Meliga, D. Sipp, & J.-M. Chomaz. Effect of compressibility on the global stability of axisymmetric wake flows. *Journal of Fluid Mechanics*, 660:499–526, 2010.

[73] J. Meneghini, B. Carmo, S. Tsiloufas, R. Gioria, & J. Aranha. Wake instability issues: from circular cylinders to stalled airfoils. *Journal of fluids and structures*, 27(5-6):694–701, 2011.

[74] P. Monkewitz & L. Nguyen. Absolute instability in the near-wake of two-dimensional bluff bodies. *Journal of Fluids and Structures*, 1(2):165–184, 1987.

[75] P. A. Monkewitz. The absolute and convective nature of instability in two-dimensional wakes at low Reynolds numbers. *The Physics of fluids*, 31(5):999–1006, 1988.

[76] P. A. Monkewitz, P. Huerre, & J.-M. Chomaz. Global linear stability analysis of weakly non-parallel shear flows. *Journal of Fluid Mechanics*, 251:1–20, 1993.

[77] P. M. Munday, K. Taira, T. Suwa, D. Numata, & K. Asai. Nonlinear lift on a triangular airfoil in low-Reynolds-number compressible flow. *Journal of Aircraft*, 52(3):924–931, 2015.

[78] T. Nagata, T. Nonomura, S. Takahashi, Y. Mizuno, & K. Fukuda. Investigation on subsonic to supersonic flow around a sphere at low reynolds number of between 50 and 300 by direct numerical simulation. *Physics of Fluids*, 28(5):056101, 2016.

[79] T. Nagata, T. Nonomura, S. Takahashi, Y. Mizuno, & K. Fukuda. Direct numerical simulation of flow past a sphere at a reynolds number between 500 and 1000 in compressible flows. In *2018 AIAA Aerospace Sciences Meeting*, page 0381, 2018.

[80] G. Nastro, J. Fontane, & L. Joly. Optimal perturbations in viscous round jets subject to Kelvin–Helmholtz instability. *J. Fluid Mech.*, 900:A13, 2020.

[81] B. R. Noack & H. Eckelmann. A global stability analysis of the steady and periodic cylinder wake. *Journal of Fluid Mechanics*, 270:297–330, 1994.

[82] Y. Ohmichi & K. Yamada. Matrix-free TriGlobal adjoint stability analysis of compressible Navier–Stokes equations. *Journal of Computational Physics*, 437:110332, 2021.

[83] M. M. Opgenoord & P. C. Caplan. Aerodynamic design of the hyperloop concept. *Aiaa Journal*, 56(11):4261–4270, 2018.

[84] S. Ortiz & J.-M. Chomaz. Transient growth of secondary instabilities in parallel wakes: Anti lift-up mechanism and hyperbolic instability. *Phys. Fluids*, 23(11):114106, 2011.

[85] D. Park & K.-S. Yang. Flow instabilities in the wake of a rounded square cylinder. *Journal of Fluid Mechanics*, 793:915–932, 2016.

[86] R. Pierrehumbert. Local and global baroclinic instability of zonally varying flow. *Journal of Atmospheric Sciences*, 41(14):2141–2162, 1984.

[87] T. H. Pulliam & J. A. Vastano. Transition to chaos in an open unforced 2D flow. *Journal of Computational Physics*, 105(1):133–149, 1993.

[88] R. Rayleigh. On the stability or instability of certain fluid motions (iii.). *Proceedings of the London Mathematical Society*, 1(1):5–12, 1895.

[89] J. Robichaux, S. Balachandar, & S. Vanka. Three-dimensional Floquet instability of the wake of square cylinder. *Physics of Fluids*, 11(3):560–578, 1999.

[90] K. Ryan, M. C. Thompson, & K. Hourigan. Three-dimensional transition in the wake of bluff elongated cylinders. *Journal of fluid mechanics*, 538:1–29, 2005.

[91] G. Saez-Mischlich. *High order numerical methods for unstructured grids and sliding mesh.* PhD thesis, UNIVERSITE DE TOULOUSE, 2021.

[92] A. Sansica, J.-C. Robinet, F. Alizard, & E. Goncalves. Three-dimensional instability of a flow past a sphere: Mach evolution of the regular and Hopf bifurcations. *Journal of Fluid Mechanics*, 855:1088–1115, 2018.

[93] P. J. Schmid. Nonmodal Stability Theory. *Annu. Rev. Fluid Mech.*, 39(1):129–162, 2007.

[94] G. J. Sheard, M. C. Thompson, & K. Hourigan. Subharmonic mechanism of the mode C instability. *Physics of Fluids*, 17(11):111702, 2005.

[95] G. J. Sheard, M. J. Fitzgerald, & K. Ryan. Cylinders with square cross-section: wake instabilities with incidence angle variation. *Journal of Fluid Mechanics*, 630:43–69, 2009.

[96] D. Sipp & A. Lebedev. Global stability of base and mean flows: a general approach and its applications to cylinder and open cavity flows. *Journal of Fluid Mechanics*, 593:333–358, 2007.

[97] K. Sreenivasan, P. Strykowski, & D. Olinger. Hopf bifurcation, landau equation, and vortex shedding behind circular cylinders. In *Forum on unsteady flow separation*, volume 1, pages 1–13. ASME New York, 1987.

[98] G. W. Stewart. A Krylov–Schur algorithm for large eigenproblems. *SIAM Journal on Matrix Analysis and Applications*, 23(3):601–614, 2002.

[99] P. P. Stumpf, Z. Sütő, & I. Nagy. Research in Nonlinear Dynamics Triggered by R&D Experiences. 2011.

[100] J.-Q. Sun & A. C. Luo. *Bifurcation and chaos in complex systems*. Elsevier, 2006.

[101] T. Suwa, K. Nose, D. Numata, H. Nagai, & K. Asai. Compressibility effects on airfoil aerodynamics at low Reynolds number. In *30th AIAA Applied Aerodynamics Conference*, page 3029, 2012.

[102] J. W. Swift & K. Wiesenfeld. Suppression of period doubling in symmetric systems. *Physical review letters*, 52(9):705, 1984.

[103] E. H. Teets Jr, E. J. Carter, L. Firnspiegel, & C. Kings Beach. Atmospheric conditions of stratospheric mountain waves: Soaring the perlan aircraft to 30 km. In *Proceedings of the 10th Conference on Aviation, Range, and Aerospace Meteorology (American Meteorological Society, 2002)*, pages 195–198. Citeseer, 2002.

[104] A. Tezuka & K. Suzuki. Three-dimensional global linear stability analysis of flow around a spheroid. *AIAA journal*, 44(8):1697–1708, 2006.

[105] M. C. Thompson, T. Leweke, & C. H. Williamson. The physical mechanism of transition in bluff body wakes. *Journal of Fluids and Structures*, 15(3-4):607–616, 2001.

[106] S. Tsiloufas, R. Gioria, B. Carmo, & J. Meneghini. Stability analysis of the flow around an airfoil in stalled configuration. In *6th AIAA Theoretical Fluid Mechanics Conference*, page 3296, 2011.

[107] S. E. Turton, L. S. Tuckerman, & D. Barkley. Prediction of frequencies in thermosolutal convection from mean flows. *Physical Review E*, 91(4):043009, 2015.

[108] M. Van Dyke & M. Van Dyke. *An album of fluid motion*, volume 176. Parabolic Press Stanford, 1982.

[109] L. Victoria Rolandi, T. Jardin, J. Fontane, J. Gressier, & L. Joly. Stability of the low Reynolds number compressible flow past a NACA0012 airfoil. *AIAA Journal*, pages 1–15, 2021.

[110] H. von Helmholtz. *Über discontinuirliche Flüssigkeits-Bewegungen*. Akademie der Wissenschaften zu Berlin, 1868.

[111] C. Williamson. The existence of two stages in the transition to three-dimensionality of a cylinder wake. *The Physics of fluids*, 31(11):3165–3168, 1988.

[112] C. H. Williamson. Three-dimensional vortex dynamics in bluff body wakes. *Experimental Thermal and Fluid Science*, 12(2):150–168, 1996.

[113] C. H. K. Williamson. Vortex Dynamics in the Cylinder Wake. *Annual Review of Fluid Mechanics*, 28(1):477–539, 1996.

[114] D. Yang, V. D. Narasimhamurthy, B. Pettersen, & H. I. Andersson. Three-dimensional wake transition behind an inclined flat plate. *Physics of Fluids*, 24(9):094107, 2012.

[115] H. Yang & R. K. Agarwal. CFD Simulations of a Triangular Airfoil for Martian Atmosphere in Low-Reynolds Number Compressible Flow. In *AIAA Aviation 2019 Forum*, 2019.

[116] W. Zhang & R. Samtaney. BiGlobal linear stability analysis on low-Re flow past an airfoil at high angle of attack. *Physics of Fluids*, 28(4):044105, 2016.

THÈSE

DOCTORAT DE L'UNIVERSITÉ DE TOULOUSE

Délivré par : *l'Institut Supérieur de l'Aéronautique et de l'Espace (ISAE-SUPAERO)*
École doctorale/spécialité : *MEGEP : Dynamique des fluides*
Unité de recherche : *ISAE-ONERA EDyF Énergétique et Dynamique des Fluides*

Présentée et soutenue le *13/12/2021* **par :** **Laura Victoria Rolandi**

Titre : Stabilité des écoulements compressibles à bas nombres de Reynolds

Mots-clefs : instabilités primaires, instabilités secondaires, instabilités globales, compressibilité, faibles nombres de Reynolds, matrix free

Title : Stability analysis of compressible flows at low Reynolds numbers

Keywords : primary instabilities, secondary instabilities, global instabilities, compressibility, low Reynolds numbers, matrix free